Magnetism in correlated electron systems

A DISSERTATION

SUBMITTED TO THE FACULTY OF THE GRADUATE SCHOOL

OF THE UNIVERSITY OF MINNESOTA

BY

Mengxing Ye

IN PARTIAL FULFILLMENT OF THE REQUIREMENTS

FOR THE DEGREE OF

Doctor of Philosophy

(Physics)

Advisor: Andrey V. Chubukov

August, 2019

Acknowledgements

First of all, I would like to thank my advisor, Andrey Chubukov. My development as a scientist has been greatly influenced by his invaluable guidance. I am inspired by his passion, his mastery of mathematical techniques together with sharp insights as a physicist. I benefited a lot from the discussions on the bigger pictures besides specific projects, which deepened my view and shaped my own way of thinking. I am also indebted a lot to his encouragement to pursue my own thoughts and learn new things, and his generous suggestions and help. I hope our collaboration continues beyond the confines of graduate school.

I would also like to thank Leon Balents for his generous support and advice, especially during the my stay at KITP, Santa Barbara, where part of the dissertation was completed.

I have greatly benefitted from working with my other collaborators as well, including Fiona Burnell, Rafael Fernandes, Gábor B. Halász, Natasha Perkins, and Lucile Savary.

My thanks also go to Rafael Fernandes, Martin Greven and Bharat Jalan for serving on my committee and providing valuable feedback.

I would like to thank my M.S. advisor Kai Sun at University of Michigan, for introducing me to the field of condensed matter theory and guiding me through my first research project. I am also grateful to my undergraduate mentor Ming-xing Luo at Zhejiang University, in particular for introducing to me special functions and the physics behind, which spurred my interest in theoretical physics.

I am grateful to Henriette Elvang, Ratindranath Akhoury, Finn Larsen, Paul Berman (University of Michigan), Andrey Chubukov and Alex Kamenev (University of Minnesota) for their inspiring lectures as well as the fruitful discussions after class.

I also learned a lot from discussions with the junior colleagues. I owe special thanks to Jian Kang, for his readiness to discuss physics and patience answering my questions since we first met in the 2014 Boulder summer school. I also thank the past and present graduate students and postdocs I have overlapped with, especially those

sincere joiners of the UMN student CMT journal club: Dmitry Chichinadze, Laura Classen, Tianbai Cui, Han Fu, Maria Navarro Gastiasoro, Avi Klein, Dan Phan, Ioannis Rousochatzakis, Dan Schubring, Michael Sammon, Qianhui Shi, Xiaoyu Wang, Yiming Wu, Ruiqi Xing, Xuzhe Ying, and etc. Other people I met outside UMN also have had important impacts on me: Xiao Chen, Chunxiao Liu, Laimei Nie, Hassan Shapourian, Yuxuan Wang and Zhentao Wang.

I couldn't imagine how to get over the tough times and share the happy moments during my Ph.D. study without the love and support from my beloved family and dear friends.

I would like to thank Maria for accompanying me with lots of fun biking and concert activities in Minneapolis, which enriched my life in the summer and lightened it in the winter! I thank Qiaoyuan, Xiyu and Yuanyuan for their help as I first came to the US, as well as Qiaoyuan's suggestions when I moved from Michigan to Minnesota to continue graduate school. I also thank my old friends, Ran, Dan, Yizhen, Butian, Xiaowan, Yue, and Suying, back in the middle/high school, whose perseverance both in class and in the sports field made me feel empowered as a teenager. True friendship never fades away with distance, and I cannot help smiling to myself every time I think of the fun moments with them.

My special thanks go to Zhengkang, my best friend and brilliant partner in life, for his constant love and support through this journey as well as the everyday fun discussions in physics and beyond. I also thank my "little sister" Diandian, for her love and trust, that continue to empower me despite her physical absence.

Last but not the least, I thank my dad Weiguo and Mom Jinzhi for their unconditional love and sacrifice. I cannot imagine how much time and efforts they have devoted in my growth, and cannot feel so firmed with every important decision without their encouragement and trust. I also feel lucky to have my dad as my first science teacher, who took my curiosity has a child seriously and guided me in the exploration with fun experiments at home.

The work in this dissertation was funded in part by the NSF DMR-1523036, U.S. Department of Energy grant DE-SC0014402, KITP graduate fellowship program under Grant No. NSF PHY-1748958, the Anatoly Larkin Fellowship, and the Louise Dosdall Fellowship from the University of Minnesota.

To my beloved parents

Table of Contents

List of Tables

List of Figures

Chapter 1

Introduction

1.1 Magnetism

A major theme in condensed matter physics is to understand emergent quantum phenomena of a macroscopic number of particles due to the interplay between kinetic energy (KE) and potential energy (U) in correlated electronic systems, where the ground state and its collective excitations are fundamentally different from that of the free Fermi gas. Despite the diverse exotic phases realized in correlated electronic systems, the microscopic Hamiltonian can be written in a simple and quite generic form, known as the Hubbard model, in terms of $H = H_K + H_U$, that

$$\begin{aligned} H_K =& \sum_{i,j;\sigma} (t_{ij} - \mu\delta_{ij}) c^\dagger_{i\sigma} c_{j\sigma} + h.c., \\ H_U =& \frac{U}{2} \sum_i \hat{n}_i(\hat{n}_i - 1) = U \sum_i \hat{n}_{i\uparrow}\hat{n}_{i\downarrow}, \end{aligned} \tag{1.1}$$

where $c_{j\sigma}$ is the annihilation operator for an electron with spin σ at site j, $\hat{n}_i$ is the electron density operator, U is the Hubbard repulsion, μ is the chemical potential that is determined self-consistently by the filling fraction of the electrons. Importantly, the kinetic energy H_K tends to delocalize the electron while the potential energy H_U tends to localize the electron.

Besides the charge degree of freedom apparent in the Hubbard model, another ingredient that drives a plethora of emergent quantum phases is magnetism when the spin degree of freedom and quantum mechanics (Pauli exclusion) meet [1]. While H_K

describes independent motion of electrons with spin σ, H_U, rewritten as

$$H_U = \frac{U}{2}\sum_i \hat{n}_i - \frac{2U}{3}\sum_i \hat{S}_i^2, \text{ where } \hat{S}_i = \frac{1}{2}c_i^\dagger \vec{\sigma} c_i, \tag{1.2}$$

tends to develop local spin moment in addition to localize the charge degree of freedom.

The emergent phases related with magnetism in correlated electronic systems can be seen in two ways.

In the strong coupling limit, i.e., $t \ll U$, charge degree of freedom is frozen at half integer filling. The low energy effective Hamiltonian can be expressed in terms of spin operators, e.g. through superexchange process, as [1, 2]

$$H_{eff} = \sum_{ij} J_{ij}\, \hat{S}_i \cdot \hat{S}_j + \dots\,, \tag{1.3}$$

where ... stands for perturbations to the Heisenberg terms, which are generally small if the spin-orbit-coupling is weak. Eq. (1.3) have been extensively studied over decades for various configurations of $\{J_{ij}\}$, which are determined by the lattice structure and range of the couplings. Various magnetic phases arise as the ground state of the Heisenberg model, such as magnetic dipole ordered state, valence bond solid, quantum spin liquid, and etc. [3–6] "Frustration" plays an essential role in realizing different types of exotic magnetic phases, where the classical ground state configurations are extensively degenerate [3].

In the weak coupling limit when $t \gtrsim U$, analyzing the electron band theory from H_K is a good starting point. Due to some Fermi surface instability, the ground state can be different from an ordinary Fermi liquid. The specific form of the instability that develops at the highest transition temperature depends to a large extent on the band structure and the interactions between fermions not far from the Fermi surface (compared to the band width). Strong effective attraction in some particular channel leads to instabilities, such as superconductivity, charge/spin density wave order, or even some "hidden" order that couples to the electromagnetic field at higher orders [7–24]. Importantly, even if the ground state is not magnetic, magnetic fluctuations can play an essential role to drive the system into exotic phases.

It is also important to note that magnetic fluctuation plays an important role in the strong coupling limit in the transition between a Mott insulator with magnetic order and a normal metal by varying certain external parameter, such as temperature or doping level away from half-filling. For example, there have been a lot of discus-

sions on the driving physics for the normal state pseudogap behavior in cuprates near optimal doping. There are two types of theories. One class of theories approach from the Heisenberg antiferromagnetism and study the evolution of the system with electron/hole doping, where the effective coupling gets smaller due to electron screening [26–28]. Another class of theories examine the coupling effects of Fermi liquid (stable on the overdoped side) with its collective bosonic fluctuations, which gets stronger with decreasing doping from the overdoped side [29, 30]. Developing a self-consistent theory that properly incorporate the key ingredient is challenging for both directions of thinking.

In the remaining part of the introduction, I will expand the discussions of the last three paragraphs, which lay the foundation of my Ph.D. researches. Due to the lack of space and my research experience, some important aspects of magnetism in correlated electronic systems will not be discussed in the introduction, such as Kondo physics in heavy fermion compounds, quantum phase transition between different magnetic phases and metal-insulator transition driven by magnetic fluctuations. We also note that while Eq. (1.1) has been proven to be a good approximation for transition metal compounds from $3d$ series, the orbital degrees of freedom and spin-orbit coupling have been shown to drive interesting new physics in $4d$ and $5d$ compounds [31]. The discussion will be limited to Kitaev materials in Chapter 3.

1.2 Frustrated Magnetism

Frustrated magnets refer to magnet systems whose classical ground state configurations (labeled as $\mathcal{G}_{cl}$) are extensively degenerate, though accidental rather than a consequence of symmetries. There are generally two origins for the frustration. *First*, the geometrical structure of the lattice, such as the kagome lattice formed by corner sharing triangles and the pyrochlore lattice built from corner sharing tetrahedra, leads to macroscopic degeneracy even for the simplest nearest neighbor Heisenberg antiferromagnetic coupling. *Second*, competing interactions that favor orders in different patterns, such as the Heisenberg J_1-J_2 triangular antiferromagnet with J_1 (J_2) refers to the nearest (next-nearest) neighbor coupling, can also lead to classical ground state (GS) degeneracy.

Due to the GS degeneracy, thermal and quantum fluctuations play important roles in determining both the statistical mechanics and dynamical properties of the system, and they give rise to very different physics from that in the unfrustrated magnets.

The most appealing feature for comparison could be the dependence on temper-

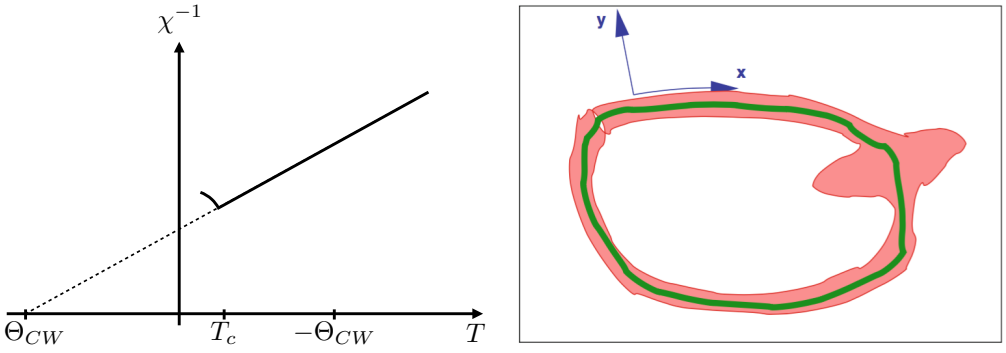

(a) (b)

Figure 1.1: (a) Typical inverse magnetic susceptibility v.s. temperature plot in frustrated magnets. (b) Schematic view of the phase space for low energy fluctuations. The green curve indicates the accidental ground state degeneracy $\mathcal{G}_{cl}$, arrows along x and y indicate two types of low energy modes. See discussions below Chapter 1.2.1. Figure adapted from [3].

ature T of the magnetic susceptability χ, which at high temperature have the linear form

$$\chi^{-1} \propto T - \Theta_{CW} \tag{1.4}$$

where the Curie-Weiss temperature Θ_{CW} characterizes the sign and strength of interactions. In an antiferromagnet $\Theta_{CW} \sim -JS^2$, where J is some characteristic coupling energy, S is the spin value of the model. Without frustration, e.g. in a nearest neighbor Heisenberg antiferromagnet on a square lattice, the magnetic order appears [signaled by a cusp in χ^{-1}, see Fig. 1.1 (a)] below the Neel temperature $T_N \sim \Theta_{CW}$, which is the *classical* energy gap above the ground state. In a frustrated antiferromagnet, ordering or spin freezing can appear at a lower temperature T_c, i.e., the ratio $f \equiv |\Theta_{CW}|/T_c$ can very large.

While f can be large in frustrated magnets, the question is how ordering can develop despite the extensive classical ground state degeneracy at low T. This requires studying the effects of quantum or thermal fluctuations, which either lift the degeneracy and select some particular ordering pattern through the "order from disorder" mechanism [32–35], or destroy any local order parameter but introduce coherence between the classical ground state configurations [4, 36].

In practice, perturbations to the Hamiltonian may lift the accidental ground state degeneracy classically, so order inevitably develop at a low temperature determined by the strength of perturbations. On the other hand, an unambiguous manifestation

of the quantum fluctuations also requires a low temperature study. In this respect, searching for the fingerprints of "order from disorder" or quantum spin liquid in a phase with some ordered ground state due to perturbations to the ideal model Hamiltonian at proper temperatures and energy scales is valuable to guide the research [37].

1.2.1 Order from disorder

The "order from disorder" mechanism is based on the distinction between energetic and entropic contributions to the free energy [see Fig. 1.1 (b)]. At low temperature, there are two types of low energy modes, one comes from the accidental ground state degeneracy $\mathcal{G}_{cl}$ [labeled as x-direction in Fig. 1.1 (b)] and another comes from the fluctuations orthogonal to $\mathcal{G}_{cl}$ around a given point in it [labeled as y-direction in Fig. 1.1 (b)]. Importantly, as $\mathcal{G}_{cl}$ is accidental rather than protected by certain symmetry, the fluctuations of the latter type can be very different around each point in $\mathcal{G}_{cl}$, and softer fluctuations reduce the entropic Free energy [see the red puddle in Fig. 1.1 (b)]. As a result, ordering can develop when the entropic free energy wins over the energetic one.

In the following, we focus on quantum fluctuations. Its effect can be formulated precisely in the large S limit, where the zero point fluctuations around a given point $\mathbf{x} \in \mathcal{G}_{cl}$ gives

$$\mathcal{H}_{eff}(\mathbf{x}) = \frac{1}{2} \sum_{l} \hbar\, \omega_l(\mathbf{x}). \tag{1.5}$$

As $\omega_l \sim JS$, the temperature that the ordering potentially develop is at $T_c \sim JS$, much smaller than $\Theta_{CW} \sim JS^2$ in unfrustrated magnets.

Practically, minimizing Eq. (1.5) is an optimization problem, which in general requires large computation costs. Physical insights and some guiding principles in finding the ordering pattern that minimize the free energy would be valuable. As an example, the isotropic Heisenberg antiferromagnet on a triangular lattice in a magnetic field has classical ground state degeneracy for any field $h \neq 0$. In Chapter 2, I show that quantum fluctuations lead to a cascade of field induced magnetic phase transitions and a half-magnetization plateau in a broad range of interaction regime. The origin of such complex behavior is a competition between long- and short-wavelength quantum fluctuations of magnons, that favor different symmetry breaking ordering patterns [38].

It is important to note that while the "order from disorder" mechanism is accu-

rately defined only in the large S limit, where the harmonic and anharmonic fluctuations are well separated in powers of S, practically, it works well in identifying the ordering pattern even for frustrated magnets with $S = 1/2$ if the order actually develops [39].

1.2.2 Quantum spin liquids

On the other hand, developing conventional order is not the *only* fate of a frustrated magnet. For example, as the *anharmonic* fluctuations are not perturbatively small when $S = 1/2$, they may introduce quantum coherence between states in $\mathcal{G}_{cl}$ strongly enough that no local order develops even at $T \to 0$. The mathematical languages to describe such quantum coherence have been developed over the past two decades, and is still thriving with a plethora of new ideas formulated along the way, such as topological order, quantum entanglement in solid state systems [6, 40]. A fundamental difference between a quantum spin liquid and an ordinary paramagnet is the nature of the excitations, that the latter is local, such as magnon, while the former is fractionalized and non-local, meaning any local operation to the ground state, say $\hat{S}|GS\rangle$, must create a pair of fractional excitations that may propagate with their own momenta.

To understand how the conventional ordered state becomes unstable as the spin value changes from large S to $S = 1/2$, in Chapter 2, we show the phase diagram of a triangular lattice J_1-J_2 Heisenberg antiferromanget for arbitrary spin in a magnetic field right below the saturation value. By obtaining the magnon spectrum renormalized by strong interactions in the presence of a small magnon condensate, we show that for $S = 1/2$ and $S = 1$, the transverse magnetic order is melted by quantum fluctuations in a range of interactions. This opened new avenues to search for spin liquid states or some exotic ordered states in further numerical and analytical studies [41].

On the experimental side, it is still an open question in identifying the smoking gun evidence of a quantum spin liquid state. The challenges are two folds. *First*, materials that can realize the quantum spin liquid state described by the theoretical model, which is either too simple or too artificial, are scarce. However, there is been rapid progress along this line in recent years, with the systematic route to realize the Kitaev honeycomb model and its variants to be a prominent example [42, 43]. *Second*, experimental technique that can probe the fractionalized excitation *directly* has not been developed. Instead, a combination of various probes in terms of spectroscopy (e.g. neutron scattering, X-ray scattering, nuclear magnetic resonance), thermodynamics

(e.g. specific heat, magnetic susceptibility) and transport (e.g. thermal conductivity), serve to reveal the nature of a candidate quantum spin liquid material from multiple facets.

Making further progress in search for quantum spin liquids require combined theoretical and experimental efforts. Proposals for experiment probe are highly desirable [44–48]. Also, as other factors, such as disorder, lattice vibration, may affect the experimental observation significantly, critical examination of the data is demanding [49, 50].

Notably, the observation of quantized thermal Hall conductivity can serve as a smoking gun evidence of a chiral spin liquid state. Recently, observation of quantization of the thermal Hall conductivity at small Hall angle in "Kitaev material" α-$RuCl_3$ has been reported [51]. However, the small Hall angle, i.e., $\kappa_{xx} \gg \kappa_{xy}$, suggests that the spin-lattice coupling, which is the only portal to generate simultaneous non-zero κ_{xx} and κ_{xy} must be considered to explain the observation critically. In Chapter 3, we show the consequence of mixing of energy propagation between chiral edge modes and bulk phonons in the observation of thermal Hall conductivity [49].

1.3 Magnetism in a weak-coupling theory

Weakly interacting Fermi liquid may develop instability in certain particle-particle or particle-hole channel when the interactions are attractive in the proper channel and strong enough.

To the zero-th order approximation, the two most plausible instability channels are superconductivity and magnetism. An arbitrary weak attraction in the particle-particle channel leads to superconducting instability with $T_c \sim e^{-E_f/\lambda}$. In a Fermi liquid with Galilean invariance in two dimension (2D), according to the Kohn-Luttinger mechanism, attractive particle-particle interaction channel must be present for at least large enough angular momentum pairing [15, 52]. However, it does not necessarily work in a lattice model when continuous rotation symmetry is broken. On the other hand, spin density wave (SDW) is generally the *only* attractive channel from bare Coulomb repulsion following a similar calculation as in Eq. (1.2). But different from superconductivity, magnetic fluctuations from fermions near the Fermi surface are generally non-singular, demanding a strong enough interaction to develop the SDW instability. On the other hand, if the Fermi surface geometry is such that particle-hole fluctuations with certain momentum $\mathbf{Q}$ are enhanced, namely the Fermi surface is (nearly) nested, the system tend to develop magnetic instability with

wave vector $\mathbf{Q}$ at weak coupling. Moreover, as the particle-hole fluctuation is logarithmically singular when the Fermi surface is perfectly nested, an arbitrary weak attraction in the spin channel stabilizes SDW state. Examples of Fermi surface (near) nesting include the nearest neighbor tight binding model on a square lattice [25] or a honeycomb lattice at proper electron fillings [53, 54], and compensated metals in e.g. parent compound of iron-based superconductors [55] and some transition metal dichalcogenides (TMDs) [56].

Importantly, there can be multiple the nesting vectors $\mathbf{Q}$ related by the lattice symmetry, and linear combinations of the order parameter fields give rise to distinct SDW ordering patterns. In addition to breaking time-reversal symmetry, some space group symmetries may be broken in a particular SDW phase, and the magnetic/electronic properties and quantum/thermal phase transitions show interesting behaviors. For example, in the hole doped iron pnictides, there are two ordering vectors at $\mathbf{Q}_1 = (0, \pi)$ and $\mathbf{Q}_2 = (\pi, 0)$ in the Fe-only Brillouin zone. Two types of SDW order has been found in different compounds. One is the stripe order at single ordering wave vector, which breaks the Z_2 symmetry that relate the x and y directions. Another is the biaxial (double-$\mathbf{Q}$) SDW order that may break Z_4 translation symmetry. Interestingly, for both phases, the phase transition is shown to take two steps at $T > 0$: The system first recovers time-reversal symmetry, and second recovers lattice symmetry (Z_2 or Z_4) as temperature increases [57, 58]. The multi-wave-vector SDW ordering may also introduce effective spin-orbit-coupling, which leads to interesting electronic behavior. For example, there are three ordering vectors in 1/4 or 3/4 doped graphene near the van-Hove momenta. A tetrahedra SDW order has been shown to minimize the Free energy and fully gap out the Fermi surface. The new spectrum is shown to have non-zero Chern number and exhibit anomalous quantum Hall effect [53]. In Chapter 4, I show another example in a compensated metal on a triangular lattice, whose Fermi surface has two electron pockets around the Brillouin zone corners $\pm\mathbf{K}$, and a hole pocket around the Brillouin zone center. A 120° SDW order is shown to minimize the Free energy, and it introduces effective Ising type spin-orbit coupling such that the remaining electron pockets at $\pm\mathbf{K}$ has opposite spin component [59].

The SDW order responds to a Zeeman magnetic field quite differently from that in the localized spin picture even when the ordering patterns are the same. Chapter 4 shows the analysis for the 120° ordered state, which found an imaginary spin bond order that doesn't break time-reversal symmetry induced by the field in the presence of SDW order. The underlining mechanism should also work for other compensated

metals that develop SDW order. Such imaginary spin/charge bond orders have been proposed in recent years from different mechanism, such as induced by spin-orbit-coupling in the SDW state [60], stabilized due to electronic correlations particularly on a hexagonal lattice [56, 59], or as a finite temperature vestigial phase [61]. Identifying its real space pattern and observing unambiguously in experiments are still open questions.

To close this section, we note that phase diagram can be more complicated and interesting in the following two scenarios. *First*, the above simple reasoning ignored other complicities such as spin-orbit coupling and momentum dependence of fermion interactions beyond onsite Coulomb repulsion. Taken these into consideration, other phases can be stabilized as the leading instability [62]. *Second*, the interactions between low energy fermions can be strongly renormalized in the nesting scenario, where particle-hole and particle-particle fluctuations should be treated on equal footings. Remarkably, couplings in different channels may flip sign due to renormalization from the high energy fermions, new instabilities besides superconductivity and SDW are possible as the fixed point of the theory. In Chapter 4, the above mentioned model in a compensated metal on a triangular lattice is analyzed, and a intriguing imaginary charge bond ordered state is found as a fixed point of the theory [59].

1.4 Pseudogap physics in correlated electron systems

The pseudogap behavior, observed in several classes of materials, most notably the copper-based high temperature superconductors (cuprates), remains one of the mostly debated phenomenon in correlated electron systems. The term "pseudogap" was suggested by Nevill Mott in 1968 [63] to name a minimum in the electronic density of states of liquid mercury at the Fermi level.

We first summarize the experimental anomalies associated with pseudogap behavior in cuprates [64].

Cuprates are a family of layered compounds with a common structural element of copper-oxygen planes (CuO_2), which are believed to be responsible for the exotic physical properties. In the undoped materials, the chemical valence of copper and oxygen is Cu^{2+} and O^{2-}, respectively. While the outer shell of O^{2-} is fully filled, the magnetic ion Cu^{2+} is in $3d^9$ configuration. Due to crystal field splitting, the $d_{x^2-y^2}$ orbital is half-filled. The stoichiometric material can be electron or hole doped, and

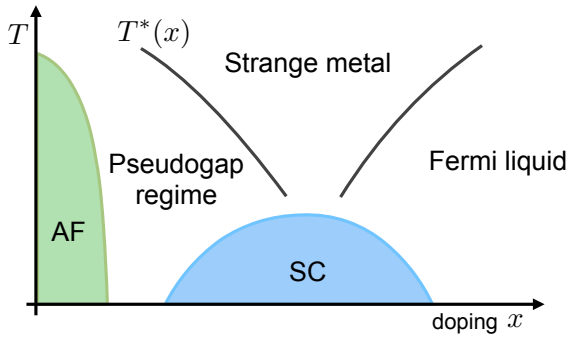

Figure 1.2: Schematic phase diagram of cuprates.

the single band Hubbard model on a square lattice with nearest- (t) and next-nearest- (t') neighbor hopping [see Eq. (1.1)] is generally considered to be sufficient to capture the essential electronic properties of cuprates.

All cuprates possess a similar phase diagram, schematically shown in Fig. 1.2. On the hole doped side, the long range commensurate antiferromagnetic order (AF) [with wave vector $\mathbf{Q} = (\pi, \pi)$] is stable up to $3\% \sim 5\%$ of doping. The phase diagram exhibit a few distinct phases. Upon about 27% of doping, the system is a conventional Fermi liquid. In between, in addition to the high transition temperature and $d_{x^2-y^2}$ symmetry of their superconducting state (SC), the cuprates possess a remarkable range of normal state anomalies. There are two puzzles here. The first one is in the underdoped up to optimal doped region, shown as "pseudogap regime" in the Figure. The second one is in the fan region above optimal doping, shown as "strange metal" regime. In contrast to T^2 scaling of resistivity in a Fermi liquid, the strange metal exhibits linear in temperature scaling of resistivity.

In the undoped sample, the AF long range order is stable up to $T_N \sim 300K$ due to the weak interlayer coupling $J_\perp$, and the Heisenberg exchange coupling within the CuO_2 plane is $J \sim 0.1\text{eV} \sim 1000K$. Due to the Mermin-Wigner theorem, the long range AF order disappears for any $T > 0$ in a pure two-dimensional system. So when $T_N < T < 1000K$, the system displays of two dimensional antiferromagnetic physics. The pseudogap refers to a few anomalies seen in charge response (i.e., dc and optical transport, Raman), spin response (i.e., nuclear magnetic resonance, inelastic neutron scattering), scanning-tunneling microscopy and angle-resolved photoemission (ARPES) experiments. A hump at high energy is observed in spectral weight and charge response measurements, even when the long range AF order vanishes. An increase of magnetic correlation length as temperature decreases is observed in spin response measurements. In particular, ARPES measurement of the momentum

resolved spectral function shows Fermi liquid like feature along the Brillouin zone diagonal and a transfer of spectral weight from zero energies to high energies near the antinodal points, e.g. $(\pi, 0)$.

There are two key theoretical scenarios of the pseudogap, each supported by a set of experiments. One is that the pseudogap is a finite temperature realization of a distinct state of matter with some order, which is either bilinear in fermions (e.g., loop current order [65, 66]), or a four-fermion composite order (e.g., a spin nematic [57, 67, 68]), or a topological order that cannot be easily expressed via fermionic operators [69]. Within this scenario, the experimentally detected onset temperature of a pseudogap, T_p, is a phase transition temperature. The other scenario is that the pseudogap is a precursor to an ordered state – SDW magnetism [29, 70–73], superconductivity [74–77], or both, with the relative strength of the two precursors set by doping/temperature (a precursor to SDW is the dominant one at smaller doping/higher temperature, and a precursor to superconductivity is the dominant one at larger doping/lower temperature). Within this scenario, the system retains a dynamical memory about the underlying order in some temperature range where the order is already destroyed, and this memory gradually fades and disappears at around T_p. At around this temperature the behavior of the spectral function crosses-over to that in a (strange) metal. A similar but not equivalent scenario, is for pseudogap as a precursor to Mott physics [78].

While the AF order has vanished in the pseudogap regime, there are a few supporting evidence that magnetic fluctuations may be the driving force. On the experimental side, the collective short range magnetic fluctuations persist in a wide range of doping as seen from spin response measurements [79, 80]. There have also been extensive numerical efforts in understanding the underlining mechanism of pseudogap in the 2D Hubbard model on a square lattice (see e.g. [78, 81, 82]). The fluctuation diagnostics method have identified the static antiferromangetic fluctuation as the dominant contribution that gives rise to pseudogap behavior at $T > 0$ [81]. Another favorable feature of the magnetic scenario is that near half-filling, the spin fluctuation exchange is known to give rise to an attraction in a $d_{x^2-y^2}$ channel [83], consistent with the $d_{x^2-y^2}$ SC paring symmetry observed in cuprates [84, 85].

It is convenient to separate the contributions from thermal and quantum fluctuations in the analysis. At $T = 0$, it remains an open question to get a precursor behavior due to magnetic fluctuations. The key theoretical challenge lies in the fact that approaching from the overdoped Fermi liquid side, the quantum corrections to the self-energy due to magnetic fluctuations are generally non-singular, disfavoring

a depletion of spectral weight at low energy. On the other hand, at $T > 0$ when quasi-static thermal fluctuations dominant, previous studies of quasi-2D systems on a square lattice have found that the pseudogap does develop in some T range above the critical T_N towards the AF order [70, 71, 73]. In Chapter 5, we address whether pseudogap is a generic property of a system near a magnetic ordered state, or there are situations (e.g. for different lattice geometries) when magnetic thermal fluctuations are logarithmically singular, but do not give rise to pseudogap behavior [86].

1.5 Organization of the thesis

The body of the thesis consists of three parts. We first discuss the frustrated magnets with localized spins, with Chapter 2 and 3 devoted to the magnetic phase diagram and theoretical interpretation of thermal transport experiment, respectively. Next, Chapter 4 covers the unconventional magnetism in the weak coupling limit. Finally, we show several aspects of the magnetic precursor scenario in understanding the pseudogap physics in Chapter 5. An outline of each chapter is given in the following.

Chapter 2: Phase diagram of a triangular Heisenberg antiferromagnet in a magnetic field

Motivated by the discovery of a quantum spin liquid state from numerical simulations of a 2D isotropic Heisenberg antiferromagnet on a triangular lattice with nearest-neighbor and next-nearest-neighbor interactions, in collaboration with Andrey Chubukov, we study the phase diagram of the model in a magnetic field. In particular, we show that the magnetic dipole order transverse to the field is melted by semiclassical spin wave fluctuations when the magnetic field is right below the saturation value (above which all spins are polarized along the field). We also find a cascade of field induced magnetic transitions and a half-magnetization plateau over a large range of magnetic interaction regimes.

Chapter 3: Quantization of thermal Hall conductivity at small Hall angles

The large longitudinal thermal conductivity and nearly quantized thermal Hall conductivity observed in the putative chiral spin liquid phase begs for a careful analysis of the mixing of energy propagation between bulk phonons and edge chiral Majorana fermions. In collaboration with Gábor B. Halász, Lucile Savary and Leon Balents, we find that not only does the quantization persist in the presence of the phonons, but

it relies upon them. We also discuss situations where the quantization breaks down and predict notable experiments to test them.

Chapter 4: Unconventional magnetism and other ordered states from itinerant fermions on a triangular lattice

In collaboration with Andrey Chubukov, we explore several interesting and unique aspects of magnetism in a multi-band electronic system, which shows different behavior compared to a single band Hubbard model. We study the magnetic order patterns determined by fermion interactions, and the interplay between magnetism, other density wave orders and superconductivity. We also show that a time reversal symmetric imaginary-spin-bond order can be stabilized when a Zeeman field is applied on a spin-density-wave state, and vice versa.

Chapter 5: Pseudogap due to spin-density-wave fluctuations

The underlying mechanism of pseudogap in correlated electron systems has been debated for decades. In collaboration with Andrey Chubukov, we calculate the fermionic spectral function in the spiral spin-density-wave (SDW) state of the Hubbard model on a quasi-2D triangular lattice at small but finite temperature. We find that the spiral nature of the SDW order introduces a control parameter, by which one can vary the strength of the pseudogap behavior. We show that, except for a certain value of the control parameter, the system does develop the pseudogap due to singular magnetic fluctuations.

Chapter 2

Phase diagram of a triangular Heisenberg antiferromagnet

We present the zero temperature phase diagram of a Heisenberg antiferromagnet on a frustrated triangular lattice with nearest neighbor (J_1) and next nearest neighbor (J_2) interactions, in a magnetic field. We show that the classical model has an accidental degeneracy for all J_2/J_1 and all fields, but the degeneracy is lifted by quantum fluctuations.

We first show that at large S, for $J_2/J_1 < 1/8$, quantum fluctuations select the same sequence of three sublattice co-planar states in a field as for $J_2 = 0$, and for $1/8 < J_2/J_1 < 1$, the phase diagram is rich due to competition between competing four-sublattice quantum states which break either $\mathbb{Z}_3$ orientational symmetry or $\mathbb{Z}_4$ sublattice symmetry. At small and high fields, the ground state is a $\mathbb{Z}_3$-breaking canted stripe state, but at intermediate fields the ordered states break $\mathbb{Z}_4$ sublattice symmetry. The most noticeable of such states is "three up, one down" state in which spins in three sublattices are directed along the field and in one sublattice opposite to the field. Such a state breaks no continuous symmetry and has gapped excitations. Consequently, the magnetization has a plateau at exactly one half of the saturation value. We identify gapless states, which border the "three up, one down" state and discuss the transitions between these states and the canted stripe state.

We then study the model with arbitrary S, including $S = 1/2$, near the saturation field by exploring the fact that near saturation the density of bosons is small for all S. We show that for $S > 1$, the transition remains first order, with a finite hysteresis width, but for $S = 1/2$ and, possibly, $S = 1$, there appears a new intermediate phase, likely without a spontaneous long-range order.

2.1 Introduction

The Heisenberg antiferromagnet on a triangular lattice is considered as one of the paradigmatic model in the study of frustrated magnetism. Frustration is believed to weaken the system's tendency to form conventional long range orders. Quite a few models of FM systems on a triangular lattice have been proposed as candidates to possess exotic quantum phases, both magnetically ordered and disordered, such as spin nematic phase [87, 88], magnetization plateau state [89–95], valence bond solid phase [96], spin density wave phase [93, 97], and quantum spin liquid phase [36, 98, 99].

In this work, we study Heisenberg antiferromagnet on a triangular lattice with nearest neighbor (J_1) and next nearest neighbor (J_2) interactions in the regime $J_2 < J_1$. This system is highly frustrated in two aspects. First, triangular lattice is geometrically frustrated and does not support a collinear antiferromagnetic order. This generally increases the strength of quantum fluctuations. Indeed, although the ground state of the nearest neighbor Heisenberg model on a triangular lattice is magnetically ordered, the order structure (120° Neel order) is non-collinear [100–103], and the magnetization is substantially suppressed from its classical value due to quantum fluctuations (by about 50% for $S = 1/2$ [102–105]). Second, as the next nearest neighbor coupling J_2 increases to around $J_1/8$, the spin order in zero field changes from the 120° Neel order to stripe order. At large spin S, the transition between 120° state and stripe state is first order [34, 106], but for $S = 1/2$ recent numerical studies [107–111] based on coupled cluster method, density matrix renormalization group (DMRG), and variational Monte Carlo, found that, at least for $S = 1/2$, there exists an intermediate quantum-disordered state in between the two ordered states, though the nature of the non-magnetic phase is not yet fully determined. The width of the quantum-disordered phase was identified numerically as $0.06 \lesssim J_2/J_1 \lesssim 0.17$ [109].

Our studies focus on the model in an external magnetic field. The model is described by

$$\mathcal{H} = J_1 \sum_{\langle i,j \rangle} \boldsymbol{S}_i \cdot \boldsymbol{S}_j + J_2 \sum_{\langle\langle i,j \rangle\rangle} \boldsymbol{S}_i \cdot \boldsymbol{S}_j - S\boldsymbol{h} \cdot \sum_i \boldsymbol{S}_i \tag{2.1}$$

where $\langle i, j \rangle$ and $\langle\langle i, j \rangle\rangle$ run over all the nearest and next nearest neighbor bonds [See Fig. 2.1 (a)].

The goal of these studies is two-fold. *First*, we want to understand what kind of spin order emerges in the large S model in a finite field, and, in particular, how the stripe order, detected at $J_2 > J_1/8$ in zero field, evolves as field increases. As we will

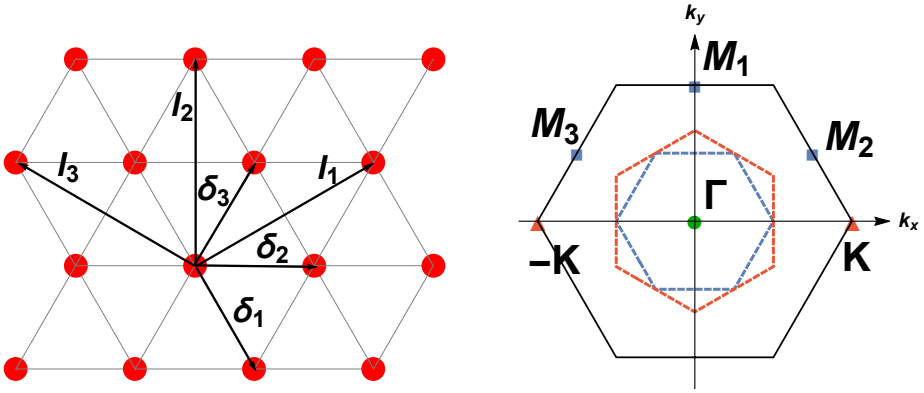

(a) (b)

Figure 2.1: (a) The nearest-neighbor ($\boldsymbol{\delta}_i$) and next-nearest-neighbor ($\boldsymbol{l}_i$) bonds on a triangular lattice. (b) Brillouin zone of the triangular lattice. Black solid line: single sublattice. Blue (Red) dashed line: four (three) sublattice.

see, there is an infinite set of classically degenerate ordered states in a finite field, and the selection of the actual order is done by quantum fluctuations via order from disorder mechanism [34, 112]. *Second*, near a saturation field we take advantage of the fact that spins are almost polarized in a direction selected by the field and the density of Holstein-Primakoff bosons is small at arbitrary S [113, 114], and search for a possible spin state without a spontaneous long-range order for $S = 1/2$, and possibly, larger spins.

2.2 Quantum phase transition near the saturation field

In this section, we analyze the nature of the quantum phase transition near $J_2/J_1 = 1/8$ right below the critical saturation field above which the system is a ferromagnet, where the controlled perturbative calculation can be achieved. The phase transition from ferromagnet to a nearly ferromagnetic spin ordered phase can be described by magnon condensation at a certain momenta, and the order structure depends on the structure of the magnon condensates. We found that for all S, the ferromagnet becomes unstable towards the V phase when $J_2 < 1/8$, and towards stripe phase at $J_2 > 1/8$. To determine the nature of the phase transition between the V and the stripe phases, we studied the spin wave spectrum of the two states and obtained the phase boundaries at arbitrary S. We found that the phase transition is *first order* when $S \gg 1$, but for $S = 1/2$ and, possibly, $S = 1$, the spin-wave stability regions

of the V phase and the stripe phase do not overlap. In this situation, right below $h_{\rm sat}$ there exists a state in which a spontaneous long range magnetic order likely does not develop. We note that there is apparently no such state near a saturation field in $J_1 - J_2$ model on a square lattice [115, 116].

2.2.1 High field phase diagram at large S

We first study the phase diagram at large S right below the saturation field $h_{\rm sat}$. In the fully polarized state at $h > h_{\rm sat}$ an exact elementary excitation is a gapped magnon with spin quantum number $S_z = 1$. The magnon excitation gap decreases as the field reduces and vanishes at $h = h_{\rm sat}$. A magnon condensation below $h_{\rm sat}$ leads to transverse magnetic order, whose structure can be identified by analyzing condensate fields. Below we derive an effective Ginzburg-Landau functional to describe magnon condensates near $h_{\rm sat}$ and show that for $J_2 < 1/8$ quantum fluctuations, acting at order $1/S$, select the same V phase as when $J_2 = 0$, and for $J_2 > 1/8$, these fluctuations select the stripe phase.

The quadratic part of the spin wave Hamiltonian at $h > h_{\rm sat}$ is

$$\begin{aligned}
\mathcal{H}^{(2)} &= \sum_{\boldsymbol{k}\in B.Z.} (S\omega_{\boldsymbol{k}} - \mu) a^\dagger_{\boldsymbol{k}} a_{\boldsymbol{k}} \\
\omega_{\boldsymbol{k}} &= J_{\boldsymbol{k}} - J_{\boldsymbol{Q}_{\rm min}} \qquad \mu = S(J_0 - J_{\boldsymbol{Q}_{\rm min}}) - Sh = S(h_{\rm sat} - h) \\
J_{\boldsymbol{k}} &= \sum_{\pm\boldsymbol{\delta}_i} \mathrm{e}^{\pm i\boldsymbol{k}\cdot\boldsymbol{\delta}_i} + J_2 \sum_{\pm\boldsymbol{l}_i} \mathrm{e}^{\pm i\boldsymbol{k}\cdot\boldsymbol{l}_i} \\
&= 2(\cos k_x + 2\cos\frac{k_x}{2}\cos\frac{\sqrt{3}k_y}{2}) + 2J_2(\cos\sqrt{3}k_y + 2\cos\frac{\sqrt{3}k_y}{2}\cos\frac{3k_x}{2})
\end{aligned} \tag{2.2}$$

The interaction terms (the ones we will need below) are, keeping corrections from normal ordering at order $1/S$,

$$\mathcal{H}^{(4)} = \frac{1}{2N} \sum_{\boldsymbol{k}_1,\boldsymbol{k}_2,\boldsymbol{q}\in B.Z.} V_{\boldsymbol{q}}(\boldsymbol{k_1},\boldsymbol{k_2}) a^\dagger_{\boldsymbol{k_1}+\boldsymbol{q}} a^\dagger_{\boldsymbol{k_2}-\boldsymbol{q}} a_{\boldsymbol{k_2}} a_{\boldsymbol{k_1}} \tag{2.3}$$

$$\mathcal{H}^{(6)} = \frac{1}{16SN^2} \sum_{\boldsymbol{k}_1,\boldsymbol{k}_2,\boldsymbol{k}_3,\boldsymbol{q},\boldsymbol{q}'\in B.Z.} U_{\boldsymbol{q},\boldsymbol{q}'}(\boldsymbol{k_1},\boldsymbol{k_2},\boldsymbol{k}_3) a^\dagger_{\boldsymbol{k_1}+\boldsymbol{q}+\boldsymbol{q}'} a^\dagger_{\boldsymbol{k_2}-\boldsymbol{q}} a^\dagger_{\boldsymbol{k_3}-\boldsymbol{q}'} a_{\boldsymbol{k_3}} a_{\boldsymbol{k_2}} a_{\boldsymbol{k_1}} \tag{2.4}$$

where

$$V_{\boldsymbol{q}}(\boldsymbol{k_1},\boldsymbol{k_2}) = \frac{1}{2}[(J_{\boldsymbol{q}} + J_{\boldsymbol{k_2}-\boldsymbol{k_1}-\boldsymbol{q}}) - \frac{1}{2}(1+\frac{1}{8S})(J_{\boldsymbol{k_1}} + J_{\boldsymbol{k_1}+\boldsymbol{q}} + J_{\boldsymbol{k_2}} + J_{\boldsymbol{k_2}-\boldsymbol{q}})] \tag{2.5}$$

$$U_{\boldsymbol{q},\boldsymbol{q}'}(\boldsymbol{k_1},\boldsymbol{k_2},\boldsymbol{k}_3) = \frac{1}{9}(1+\frac{1}{4S})\big(J_{\boldsymbol{k}_1+\boldsymbol{q}} + J_{\boldsymbol{k}_3+\boldsymbol{q}} + J_{\boldsymbol{k}_1+\boldsymbol{k}_3-\boldsymbol{k}_2+\boldsymbol{q}} + J_{\boldsymbol{k}_1+\boldsymbol{q}'} + J_{\boldsymbol{k}_2+\boldsymbol{q}'} + J_{\boldsymbol{k}_1+\boldsymbol{k}_2-\boldsymbol{k}_3+\boldsymbol{q}'} + J_{\boldsymbol{k}_2+\boldsymbol{k}_3-\boldsymbol{k}_1-\boldsymbol{q}-\boldsymbol{q}'} + J_{\boldsymbol{k}_2-\boldsymbol{q}-\boldsymbol{q}'} + J_{\boldsymbol{k}_3-\boldsymbol{q}-\boldsymbol{q}'}\big) - \frac{1}{6}(1+\frac{3}{4S})(J_{\boldsymbol{k_1}} + J_{\boldsymbol{k_2}} + J_{\boldsymbol{k}_3} + J_{\boldsymbol{k}_1+\boldsymbol{q}+\boldsymbol{q}'} + J_{\boldsymbol{k}_2-\boldsymbol{q}} + J_{\boldsymbol{k}_3-\boldsymbol{q}'})] \quad (2.6)$$

Lowering the magnetic field below $h_{\rm sat}$ makes the quadratic spectrum negative in some momentum range and drives Bose-Einstein condensation of magnons at the minima of the dispersion. At $J_2 < 1/8$, the minima are at $\pm\boldsymbol{K} = \pm(4\pi/3,\, 0)$; at $J_2 > 1/8$, the minima are at $\boldsymbol{M}_1 = (0, 2\pi/\sqrt{3})$, $\boldsymbol{M}_2 = (\pi, \pi/\sqrt{3})$, $\boldsymbol{M}_3 = (-\pi, \pi/\sqrt{3})$; at $J_2 = 1/8$, the minima are at all the five momenta $\boldsymbol{K}$, $-\boldsymbol{K}$, $\boldsymbol{M}_1$, $\boldsymbol{M}_2$ and $\boldsymbol{M}_3$ (see Fig. 2.2). At even larger $J_2 > 1$, which we will not discuss here, the magnon condensates are at incommensurate momenta. The magnon operator in the condensate background can be written as

$$\begin{cases} a_{\boldsymbol{k}} = \sqrt{N}\Delta_1\delta_{\boldsymbol{k},\boldsymbol{K}} + \sqrt{N}\Delta_2\delta_{\boldsymbol{k},-\boldsymbol{K}} + \tilde{a}_{\boldsymbol{k}} & J_2 < 1/8 \\ a_{\boldsymbol{k}} = \sqrt{N}\Phi_1\delta_{\boldsymbol{k},\boldsymbol{M}_1} + \sqrt{N}\Phi_2\delta_{\boldsymbol{k},\boldsymbol{M}_2} + \sqrt{N}\Phi_3\delta_{\boldsymbol{k},\boldsymbol{M}_3} + \tilde{a}_{\boldsymbol{k}} & J_2 > 1/8 \end{cases} \quad (2.7)$$

When $J_2 < 1/8$, the ground state energy in terms of the uniform condensate fields Δ is:

$$E_\Delta/N = -\mu(|\Delta_1|^2 + |\Delta_2|^2) + \frac{1}{2}\Gamma_1(|\Delta_1|^4 + |\Delta_2|^4) + \Gamma_2\,|\Delta_1|^2|\Delta_2|^2 + \Gamma_{\rm u}(\bar{\Delta}_1^3\Delta_2^3 + h.c.) \quad (2.8)$$

When when $J_2 > 1/8$, the ground state energy in terms of the uniform condensate fields Φ is:

$$E_\Phi/N = -\bar{\mu}(|\Phi_1|^2 + |\Phi_2|^2 + |\Phi_3|^2) + \frac{1}{2}\bar{\Gamma}_1(|\Phi_1|^4 + |\Phi_2|^4 + |\Phi_3|^4) + \bar{\Gamma}_2(|\Phi_1|^2|\Phi_2|^2 + |\Phi_1|^2|\Phi_3|^2 + |\Phi_2|^2|\Phi_3|^2) + \bar{\Gamma}_{\rm u}(\bar{\Phi}_1^2\Phi_2^2 + \bar{\Phi}_2^2\Phi_3^2 + \bar{\Phi}_3^2\Phi_1^2 + h.c.) \quad (2.9)$$

where $\mu,\ \bar{\mu} \sim S(h_{\rm sat} - h)$. The selection of the condensates depends on the values of the quartic coefficients Γ_i and $\bar{\Gamma}_i$ $(i = 1, 2)$, which are determined from the analysis of the four-point vertex function. $\Gamma_{\rm u}$ and $\bar{\Gamma}_{\rm u}$ are from the Umklapp process. As we will see, $\Gamma_{\rm u}$ term determines the relative phase between Δ_1 and Δ_2. Similarly, $\bar{\Gamma}_{\rm u}$ term determines relative phases between Φ_i.

In the classical $S \to \infty$ limit, $\Gamma_1^{(0)} = \Gamma_2^{(0)} = 9$, and $\Gamma_{\rm u}^{(1)} = 0$ when $J_2 < 1/8$; $\bar{\Gamma}_1^{(0)} = \bar{\Gamma}_2^{(0)} = 8(1 + J_2)$, and $\bar{\Gamma}_{\rm u}^{(0)} = 0$ when $J_2 > 1/8$. The superscript (i) labels the order of perturbative expansion in power of $1/S$. The minimization of the energy

then yields $|\Delta|_1^2 + |\Delta|_2^2 \equiv \mu/\Gamma_1$ when $J_2 < 1/8$, and $|\Phi|_1^2 + |\Phi|_2^2 + |\Phi|_3^2 \equiv \mu/\bar{\Gamma}_1$ when $J_2 > 1/8$. Neither of these conditions specifies the ratio of $|\Delta_1|/|\Delta_2|$ or $|\Phi_2|/|\Phi_1|$ and $|\Phi_3|/|\Phi_1|$. In other words, in the $S \to \infty$ limit, the condensed phases retain the accidental degeneracy.

When quantum fluctuations of order $1/S$ are included, Γ_i and $\bar{\Gamma}_i$ acquire additional contributions, which are not necessarily equal for different Γ_i. We evaluated these contributions following the computation steps in Ref. [117], where a similar problem has been considered. Because our calculations parallel the ones in [117], we don't show the details of the derivations and just present the results. For $J_2 < 1/8$, $\Delta\Gamma = \Gamma_2 - \Gamma_1 = \Delta\Gamma^{(0)} + \Delta\Gamma^{(1)} = \Delta\Gamma^{(1)}$ is:

$$\Delta\Gamma = \frac{1}{SN}\sum_{\boldsymbol{k}}\Big(\frac{V_{\boldsymbol{k}}^2(\boldsymbol{K},\,\boldsymbol{K})}{\omega_{\boldsymbol{K}+\boldsymbol{k}}+\omega_{\boldsymbol{K}-\boldsymbol{k}}} - \frac{2\,V_{\boldsymbol{k}}^2(\boldsymbol{K},\,-\boldsymbol{K})}{\omega_{\boldsymbol{K}+\boldsymbol{k}}+\omega_{-\boldsymbol{K}-\boldsymbol{k}}}\Big) + \frac{3-2J_2}{8S} \tag{2.10}$$

In the thermodynamic limit, $\frac{1}{N}\sum_{\boldsymbol{k}} \to \frac{1}{\mathcal{A}_{B.Z.}}\int_{\boldsymbol{k}}$. The first term in $\Delta\Gamma$ is the second-order perturbation contribution from $\Delta_{1,2}^2\, a^\dagger a^\dagger + h.c.$ and $\Delta_1\Delta_2\, a^\dagger a^\dagger + h.c.$ terms in the Hamiltonian, the second term comes from the corrections to the quartic vertex associated with normal ordering of boson operators. Each of the two integrals in Eq. 2.10 is logarithmically divergent as the denominator in each integrand behaves as k^2 at small k. The difference between the two terms is, however, finite. We evaluated $\Delta\Gamma$ at different J_2 numerically and found that $\Delta\Gamma < 0$ for all $J_2 < 1/8$, i.e., $\Gamma_1 > \Gamma_2$. An elementary analysis then shows that it is energetically favorable for the system to develop both condensates Δ_1 and Δ_2 with equal amplitudes $\rho = \mu/(\Gamma_1 + \Gamma_2)$. To understand the structure of such an order in real space we set $\Delta_1 = \sqrt{\rho}e^{i\theta_1}$, $\Delta_2 = \sqrt{\rho}e^{i\theta_2}$, and define $\phi = (\theta_1 + \theta_2)/2$ and $\psi = (\theta_1 - \theta_2)/2$. The magnetic order $\langle \boldsymbol{S_r} \rangle$ is then

$$\langle \boldsymbol{S_r} \rangle = (S - 2\rho\cos^2[\boldsymbol{K}\cdot\boldsymbol{r} + \psi])\hat{z} + \sqrt{4S\rho}\cos[\boldsymbol{K}\cdot\boldsymbol{r} + \psi] \times (\cos\phi\,\hat{x} + \sin\phi\,\hat{y}) \tag{2.11}$$

This order parameter has only two components, one along $\hat{z}$ and the other along $\cos\phi\,\hat{x} + \sin\phi\,\hat{y}$ in XY plane, i.e., the order is co-planar. The ground state manifold has U(1)×U(1) symmetry. One of the U(1), associated with ϕ, is the freedom to select the direction of $\langle \boldsymbol{S_r} \rangle$ in the XY plane, another U(1), associated with ψ, is the freedom to select the origin of the coordinate. A choice of some ϕ and some ψ spontaneously breaks $U(1)\times U(1)$ symmetry. Beyond the order Δ^4, the $U(1)$ translational symmetry is explicitly broken if $\Gamma_{\rm u}$ is non-zero. Within $1/S$ expansion, a non-zero $\Gamma_{\rm u}$ emerges at order $1/S^2$. There are three contributions to $\Gamma_{\rm u}$ at this order. One, $\Gamma_{\rm u}^{(\rm n)}$, comes

J_2	0	0.1	1/8
$\Delta\Gamma$ $(1/S)$	-1.6	-6.9	-247.7
$\Gamma_{\rm u}$ $(1/S^2)$	-0.68	-0.81	-0.85

Table 2.1: (From [41]) The parameters of the Ginzburg-Landau functional of the V phase at different J_2, to leading order in $1/S$. $\Delta\Gamma = \Gamma_2 - \Gamma_1$ is the difference between the prefactors of the two quartic terms, and $\Gamma_{\rm u}$ is the prefactor for the sixth order term.

from normal ordering of the term of sixth order in bosons; another, $\Gamma_{\rm u}^{(\rm a)}$ comes from second order perturbation in cross-products of representatives $\Delta_{1,2}^2\, a^\dagger a^\dagger + h.c$ and $1/S(\Delta_1^3\overline{\Delta}_2 a^\dagger a^\dagger + h.c)$, $1/S(\Delta_2^3\overline{\Delta}_1 a^\dagger a^\dagger + h.c)$; and third contribution, $\Gamma_{\rm u}^{(\rm b)}$, comes from third order terms in $\Delta_{1,2}^2\, a^\dagger a^\dagger + h.c$ and $\Delta_1\overline{\Delta}_2\, a^\dagger a + h.c$. In explicit form we have

$$\Gamma_{\rm u}^{(\rm n)} = \frac{9(1-2J_2)}{32S^2} \tag{2.12}$$

$$\Gamma_{\rm u}^{(a)} = -\frac{1}{2S^2}\sum_{\boldsymbol{k}} \frac{V_{\boldsymbol{k}}(\boldsymbol{K},\,\boldsymbol{K})\big(3U_{\boldsymbol{k}+2\boldsymbol{K},\,2\boldsymbol{K}}(\boldsymbol{K},\,\boldsymbol{K},\,\boldsymbol{K})/4 + V_{-2\boldsymbol{K}+\boldsymbol{k}}(0,\,-\boldsymbol{K})\big)}{\omega_{\boldsymbol{K}+\boldsymbol{k}} + \omega_{\boldsymbol{K}-\boldsymbol{k}}} \tag{2.13}$$

$$\Gamma_{\rm u}^{(b)} = -\frac{2}{S^2}\sum_{\boldsymbol{k}} \frac{V_{\boldsymbol{k}}(-\boldsymbol{K},\,-\boldsymbol{K})V_{\boldsymbol{k}+\boldsymbol{Q}}(\boldsymbol{K},\,\boldsymbol{K})V_{-\boldsymbol{K}}(-\boldsymbol{k},\,\boldsymbol{K})}{(\omega_{-\boldsymbol{K}+\boldsymbol{k}} + \omega_{-\boldsymbol{K}-\boldsymbol{k}})(\omega_{-\boldsymbol{K}+\boldsymbol{k}} + \omega_{-\boldsymbol{k}})} \tag{2.14}$$

where $V_{\boldsymbol{q}}(\boldsymbol{k_1},\boldsymbol{k_2})$ and $U_{\boldsymbol{q}}(\boldsymbol{k_1},\boldsymbol{k_2},\boldsymbol{k}_3)$ are defined in Eqs. 2.5, and $J_{\boldsymbol{q}}$ is defined in Eq. 2.2. We verified that the total $\Gamma_{\rm u} = \Gamma_{\rm u}^{(\rm n)} + \Gamma_{\rm u}^{(a)} + \Gamma_{\rm u}^{(b)} + \mathcal{O}(\frac{1}{S^3})$ is non-singular (potential logarithmical terms cancel out), and computed $\Gamma_{\rm u}$ numerically for several $J_2 < 1/8$ and found that it is non-zero and negative (see Table 2.1). A negative $\Gamma_{\rm u}$ breaks the U(1) translational symmetry down to $\mathbb{Z}_3$ and reduces the continuum set of ψ to the discrete subset $\psi = \frac{l\pi}{3}$, $l = 0,\, 1,\, 2$. The order parameter in each of three possible spin states has a V-type shape with two spins in each triad pointing in one direction and the remaining spin in the other direction [93, 117].

We did similar analysis for $J_2 > 1/8$ and found that logarithmical singularities from individual contributions to $\Delta\bar{\Gamma} = \bar{\Gamma}_2 - \bar{\Gamma}_1$ do not cancel. To logarithmic accuracy,

$$\Delta\bar{\Gamma} = \frac{8(1+J_2)^2}{\pi}\left[\frac{1}{\sqrt{4J_2 - (1-3J_2)^2}} - \frac{1}{\sqrt{4J_2}}\right]\frac{|\log\bar{\mu}|}{S} \tag{2.15}$$

This formula is valid up to $J_2 = 1$, which, as we said, is the upper boundary (in J_2) of the stripe phase. We see that $\Delta\bar{\Gamma} = \bar{\Gamma}_2 - \bar{\Gamma}_1 > 0$ everywhere, except for $J_2 = 1/3$. A positive $\bar{\Gamma}_2 - \bar{\Gamma}_1$ implies that it is energetically favorable for the system to develop

just one condensate, either Φ_1, or Φ_2, or Φ_3 (i.e., to develop order parameter with one out of three possible momenta $\mathbf{M}_i$, $(i = 1 - 3)$). Setting $\Phi_1 = \sqrt{\rho}\mathrm{e}^{i\phi}, \Phi_2 = \Phi_3 = 0$, we obtain spin configuration in real space

$$\langle \boldsymbol{S}_{\boldsymbol{r}} \rangle = (S - \rho)\hat{z} + \sqrt{2S\rho}(\cos\left[\boldsymbol{M}_1 \cdot \boldsymbol{r} + \phi\right]\hat{x} + \sin\left[\boldsymbol{M}_1 \cdot \boldsymbol{r} + \phi\right]\hat{y}) \tag{2.16}$$

For a generic $\mathbf{M}$, such an order would be a non-coplanar cone phase. In our case, however, $\boldsymbol{M}_i$ are special points for which $\boldsymbol{M} \cdot \boldsymbol{\delta}_\alpha = 0$ or π. One can easily verify that in this situation the spins order in a stripe manner in XY plane – parallel in one direction and anti-parallel in the other. Such an order is co-planar and is termed as canted stripe.

Phase transition near $h_{\mathbf{sat}}$

To analyze the nature of the phase transition between the V and the stripe phase near h_{sat} we obtain the stability boundaries of the two phases by analyzing the spin wave spectrum. Near h_{sat} there are two small parameters – $1/S$ and the magnitude of a magnon condensate ρ in each of the two phases. In this section, we study the limit when $1/S$ is small enough such that $|\log\rho|/S \ll 1$. In the next section we explore another limit when $S = \mathcal{O}(1)$ and $|\log\rho|/S \gg 1$.

We first calculate the spin wave spectrum in the V phase near h_{sat}. Near the saturation field the angles between sublattice magnetizations and the direction of the magnetic field (the z axis) are small. In the classical limit, we obtain: $\theta_1 = (h_{\mathrm{sat}} - h)^{1/2}/3$, $\theta_2 = -2(h_{\mathrm{sat}} - h)^{1/2}/3$. The leading order quantum corrections to the tilt angles and to magnon self-energy are of order $(h_{\mathrm{sat}} - h)|\log(h_{\mathrm{sat}} - h)|/S$.

We expand the Hamiltonian up to the quartic order in terms of the magnons a, b, c defined in the local coordinates of $\boldsymbol{S}_a$, $\boldsymbol{S}_b$, $\boldsymbol{S}_c$ (see Appendix A for details) and keep terms of order $h_{\mathrm{sat}} - h$ (modulo logarithms). The quadratic term is

$$\mathcal{H}^{(2)} = \mathcal{H}_{2,0} + \delta\mathcal{H}_2 \tag{2.17}$$

where $\mathcal{H}_{2,0}$ is the same as in fully polarized state at $h = h_{\mathrm{sat}}$ and $\delta\mathcal{H}_2 \sim (h_{\mathrm{sat}} - h)$ is the perturbation to $\mathcal{H}_{2,0}$ due to the transverse magnetic order. We diagonalize $\mathcal{H}^{(2)}$ in two steps. First, we diagonalize $\mathcal{H}_{2,0}$ and find the eigenmodes $\phi_{\mu,\boldsymbol{k}} = \{A_{\boldsymbol{k}}, B_{\boldsymbol{k}}, C_{\boldsymbol{k}}\}$. Then we express the whole $\mathcal{H}^{(2)}$ with quantum corrections in the new basis $\Phi_{\mu,\boldsymbol{k}} = \{\phi_{\mu,\boldsymbol{k}}, \phi^\dagger_{\mu,-\boldsymbol{k}}\}$ and diagonalize $\mathcal{H}^{(2)}$ in this basis. The diagonalization of $\mathcal{H}_{2,0}$ is elementary and is achieved by simply rotating the original basis $(a_{\boldsymbol{k}}, b_{\boldsymbol{k}}, c_{\boldsymbol{k}})$ to $(A_{\boldsymbol{k}}, B_{\boldsymbol{k}}, C_{\boldsymbol{k}})$

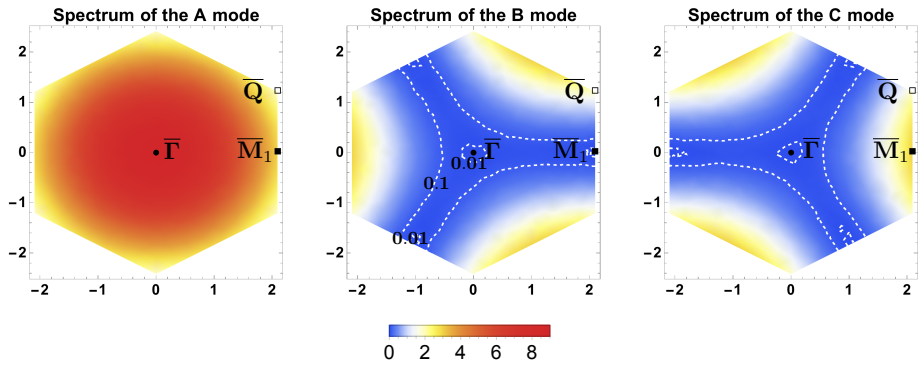

Figure 2.2: (From [41]) The magnon spectrum in three sublattice representation at $J_2 = 1/8$, and $h = h_{\rm sat}$. In the regions between the dashed lines the magnon energy is small and the dispersion is almost flat.

as

$$\begin{pmatrix} a_{\boldsymbol{k}} \\ b_{\boldsymbol{k}} \\ c_{\boldsymbol{k}} \end{pmatrix} = \begin{pmatrix} 1 & \jmath & \bar{\jmath} \\ 1 & \bar{\jmath} & \jmath \\ 1 & 1 & 1 \end{pmatrix} \begin{pmatrix} A_{\boldsymbol{k}} \\ B_{\boldsymbol{k}} \\ C_{\boldsymbol{k}} \end{pmatrix} \tag{2.18}$$

where $\jmath = e^{i2\pi/3}, \bar{\jmath} = e^{-i2\pi/3}$. A, B and C bands are

$$\begin{aligned} \omega_A^{(0)}(\boldsymbol{k}) &= 3 + 2J_2\,\mu_{\boldsymbol{k}} + 2\Re[\gamma_{\boldsymbol{k}}] \\ \omega_B^{(0)}(\boldsymbol{k}) &= 3 + 2J_2\,\mu_{\boldsymbol{k}} - \Re[\gamma_{\boldsymbol{k}}] + \sqrt{3}\Im[\gamma_{\boldsymbol{k}}] \\ \omega_C^{(0)}(\boldsymbol{k}) &= 3 + 2J_2\,\mu_{\boldsymbol{k}} - \Re[\gamma_{\boldsymbol{k}}] - \sqrt{3}\Im[\gamma_{\boldsymbol{k}}] \end{aligned} \tag{2.19}$$

where $\gamma_{\boldsymbol{k}}$, $\mu_{\boldsymbol{k}}$ are defined as

$$\gamma_{\boldsymbol{k}} = (\mathrm{e}^{i\,k_x} + 2\cos\frac{\sqrt{3}}{2}k_y\,\mathrm{e}^{-i\,k_x/2}), \quad \mu_{\boldsymbol{k}} = \cos\sqrt{3}k_y + 2\cos\frac{\sqrt{3}k_y}{2}\cos\frac{3}{2}k_x. \tag{2.20}$$

The Brillouin zone for three sublattice description is shown in Fig. 2.1 (b). At $J_2 < 1/8$, when we expect the V phase to be stable right below $h_{\rm sat}$, the dispersions of B and C modes have zeros at the $\overline{\Gamma}$ point. At $J_2 = 1/8$, $\omega_B^{(0)}$ has additional zero modes at the $\overline{\boldsymbol{M}}_1 = (2\pi/3, 0)$, $\overline{\boldsymbol{M}}_2 = (-\pi/3, \sqrt{3}\pi/3)$, $\overline{\boldsymbol{M}}_3 = (-\pi/3, -\sqrt{3}\pi/3)$ and $\omega_C^{(0)}$ has zero modes at $-\overline{\boldsymbol{M}}_1$, $-\overline{\boldsymbol{M}}_2$, $-\overline{\boldsymbol{M}}_3$. And when $J_2 > 1/8$, the spectrum near $\overline{\boldsymbol{M}}$ becomes complex and the V phase is unstable. We are interested in how the modes near the $\overline{\boldsymbol{M}}$ points become unstable right below $h_{\rm sat}$. Accordingly, we set J_2 to be near J_{cri}, expand in momentum near, say $\overline{\mathbf{M}}_1$ as $\boldsymbol{k} = \overline{\boldsymbol{M}}_1 + \boldsymbol{q}$, $|\boldsymbol{q}| << 1$, and keep only the soft B and C modes (It has been checked explicitly that the inclusion of

the gapped A mode does not change the conclusions below). With this, we computed the $1/S$ corrections to the relation between θ_1 and $(h_{\rm sat}-h)^{1/2}$ from cubic terms in the Hamiltonian, expressed in A, B and C bosons, and corrections to the classical dispersion from three-boson and four-boson terms. Collecting all $1/S$ contributions and combining them with classical result for $\mathcal{H}^{(2)}$ to order $(h_{\rm sat}-h)$ we obtain

$$\mathcal{H}^{(2)} = \frac{S}{2}\sum_{\boldsymbol{q}} \left(B^\dagger_{\boldsymbol{M}_1+\boldsymbol{q}}\ C_{-\boldsymbol{M}_1-\boldsymbol{q}}\right) \begin{pmatrix} \omega_{\boldsymbol{q}} + (\frac{1}{3}+\delta_1)(h_{\rm sat}-h) & (-\frac{1}{3}+\delta_2)(h_{\rm sat}-h) \\ (-\frac{1}{3}+\delta_2)(h_{\rm sat}-h) & \omega_{-\boldsymbol{q}} + (\frac{1}{3}+\delta_1)(h_{\rm sat}-h) \end{pmatrix} \begin{pmatrix} B_{\boldsymbol{M}_1+\boldsymbol{q}} \\ C^\dagger_{-\boldsymbol{M}_1-\boldsymbol{q}} \end{pmatrix} \tag{2.21}$$

where $\omega_{\boldsymbol{q}} = 1 - 8J_2 + \frac{1}{16}(q_x^2 + 21q_y^2)$, and δ_1 and δ_2 are $1/S$ quantum corrections to the normal and anomalous self-energy at $\boldsymbol{q}=0$, $\omega=0$, $J_2=1/8$. Note that other terms like $B^\dagger_{\boldsymbol{M}_1+\boldsymbol{q}}B^\dagger_{-\boldsymbol{M}_1-\boldsymbol{q}}$, $B^\dagger_{\boldsymbol{M}_1+\boldsymbol{q}}C_{\boldsymbol{M}_1+\boldsymbol{q}}$ do not contribute to the spectrum near $\boldsymbol{M}_1$ to first order in $1/S$. A simple algebra shows that the critical coupling of J_2, at which spin-wave excitations in the V phase becomes complex (and, as the consequence, the phase becomes unstable) is $J_{2\rm V} = 1/8 + \frac{(1/3+\delta_1)-|1/3-\delta_2|}{8}(h_{\rm sat}-h)$. In the limit $\frac{|\log(h_{\rm sat}-h)|}{S} \ll 1$, we found that to logarithmic accuracy, $\delta_1 = \frac{0.22}{S}|\log(h_{\rm sat}-h)|$ and $\delta_2 = \frac{1.58}{S}|\log(h_{\rm sat}-h)|$, thus $J_{2V} = 1/8 + \frac{0.22}{S}(h_{\rm sat}-h)|\log(h_{\rm sat}-h)|$.

Using a similar analysis for the stripe phase, we found $J_{2\rm stripe} = 1/8 - \frac{0.07}{S}(h_{\rm sat}-h)|\log(h_{\rm sat}-h)|$. We show more details of calculations in Appendix A.

By looking at the sign of the corrections to the critical J_2, we see that the phase boundary of the V phase shifts to the right of $1/8$ by $\mathcal{O}(1/S)$, while that of the stripe phase shift to the left of $1/8$, thus the stability regions of the two phases overlap near $J_2 = 1/8$. This implies that the transition between the V and stripe phase is *first order* with finite hysteresis in the large S limit near $h_{\rm sat}$.

2.2.2 High field region for a model with a generic spin

We now discuss the phase diagram of the model with an arbitrary spin $S=\mathcal{O}(1)$, with particular interest to $S=1/2$. In a generic field, there is no small parameter to justify perturbative calculations for $S=\mathcal{O}(1)$. However, right below $h_{\rm sat}$, the density of magnon condensates is small, as we pointed out in Sec. 2.2.1. In this situation, one can perturbatively expand in powers of magnon condensates (or, equivalently, in terms of the tilt angle between a sublattice magnetization and the z axis). The coefficients of this expansion can be obtained at arbitrary S, and this gives us an opportunity to

study the transition between V and stripe phases outside of semiclassical limit.

Below we first identify the orders at small and large J_2 near $h_{\rm sat}$, and find that the same V and stripe phases are selected for an arbitrary spin, as in the large S limit. Then we analyze the nature of the phase transition between the V phase and the stripe phase for a generic S.

In general, there are three options for the phase transition. It can be a first order transition with or without hysteresis, as in the classical and the large S cases. Or there can be an intermediate co-existence phase, in which both orders are present simultaneously. Or, one order looses it stability before the other becomes stable. In the latter case there is a intermediate region in which neither the V phase nor the canted phase are stable. This intermediate state may have some non-quasi-classical long-range order with or without a continuous symmetry breaking, or may have no spontaneous order. We illustrate these possibilities in Fig. 2.3. For the first two possibilities the prefactors μ and $\bar{\mu}$ for the quadratic terms in Δ and Φ in the Free energy of the V and the stripe phases respectively (see Eq. 2.27) are both positive over some range of J_2 at a given $h \lesssim h_{\rm sat}$. Whether the phase transition is first order or occurs via a co-existence phase is determined by the interplay between the prefactors of the fourth-order terms in the Ginzburg-Landau model, which includes both fields [118] (Fig. 2.3a and Fig. 2.3b). The third scenario occurs when both μ and $\bar{\mu}$ are negative in a finite range near $J_2 = 1/8$, i.e., neither of the two orders develop (Fig. 2.3c).

We present Ginzburg-Landau analysis in Sec. 2.2.2 below and present the analysis of spin-wave dispersion with quantum corrections in Sec. 2.2.2. We show that the fields Δ and Φ don't coexist for arbitrary S. For $S > 1$, the regions where $\mu > 0$ and $\bar{\mu} > 0$ overlap. Then the system remains ordered at all J_2, and the transition between the V and the stripe phases is first order. However, when $S = 1/2$ and, most likely, also $S = 1$, the two phases don't overlap near $J_2 = 1/8$. In this case, there exists an intermediate phase without a quasi-classical long-range magnetic order. We emphasize that *this happens near $h = h_{sat}$, where the density of magnons is small.* To identify the nature of this intermediate state one needs to go beyond the spin wave framework, and we leave this for future studies.

Ginzburg-Landau formalism

Like we discussed in Sec. 2.2.1 the transition at $h = h_{\rm sat}$ can be described as magnon condensation, and the condensation energy at $T = 0$ can be expandeded in powers of the condensate fields. For arbitrary S, the condensation energy in the V phase and

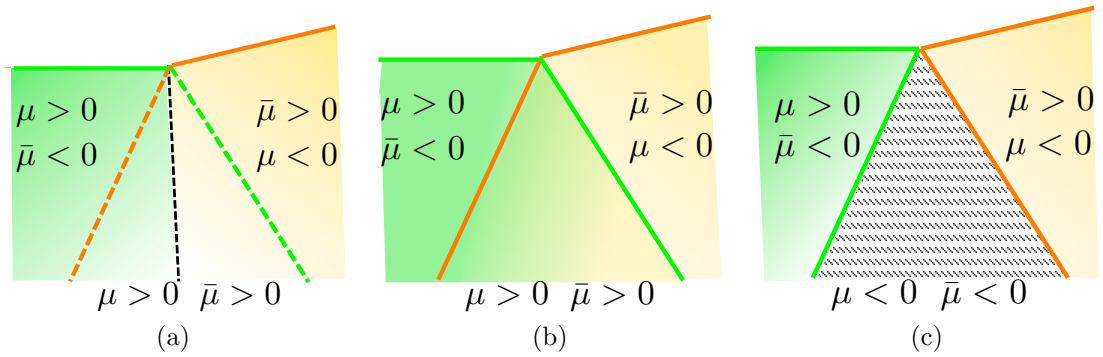

Figure 2.3: (From [41]) Three possibilities of the phase transition between the V phase and the canted stripe phase near h_{sat}. (a) and (b): Condensates associated with both the V and the stripe phase are stable over a range around $J_2 = 1/8$ (the region between the green and orange dashed lines). The phase transition can be either (a) first order or (b) involve an intermediate co-existence phase, depending on the interplay between quartic couplings Γ_i. (c) *Neither* of the two condensates are stable over a finite range around $J_2 = 1/8$ (shaded region). The transition between the V and the stripe phase then necessarily occurs via an intermediate state, which either has some non-quasi-classical long-range order with or without a continuous symmetry breaking, or has no spontaneous order.

in the stripe phase has the same form as in Eq. 2.8 and Eq. 2.33, but the quartic couplings $\Gamma_{1,2}$ and $\bar{\Gamma}_{1,2}$ are proportional to the fully renormalized four-point vertex function $\Gamma_{\boldsymbol{q}}(\boldsymbol{k_1}, \boldsymbol{k_2})$, taken at certain momenta. In our case

$$\begin{aligned}
\Gamma_1 &= \Gamma_{\boldsymbol{q}=0}(\boldsymbol{K}, \boldsymbol{K}) \\
\Gamma_2 &= \Gamma_{\boldsymbol{q}=0}(\boldsymbol{K}, -\boldsymbol{K}) + \Gamma_{-2\boldsymbol{K}}(\boldsymbol{K}, -\boldsymbol{K}) \\
\bar{\Gamma}_1 &= \Gamma_{\boldsymbol{q}=0}(\boldsymbol{M_1}, \boldsymbol{M_1}) \\
\bar{\Gamma}_2 &= \Gamma_{\boldsymbol{q}=0}(\boldsymbol{M_1}, \boldsymbol{M_2}) + \Gamma_{\boldsymbol{M_2}-\boldsymbol{M_1}}(\boldsymbol{M_1}, \boldsymbol{M_2})
\end{aligned} \tag{2.22}$$

To find $\Gamma_{\boldsymbol{q}}(\boldsymbol{k_1}, \boldsymbol{k_2})$, all orders of scattering of two excited magnons should be counted. We show this in the diagrammatic formalism in Fig. 2.4. The ladder series of diagrams is equivalent to the integral Bethe-Salpeter (BS) equation:

$$\Gamma_{\boldsymbol{q}}(\boldsymbol{k_1}, \boldsymbol{k_2}) = V_{\boldsymbol{q}}(\boldsymbol{k_1}, \boldsymbol{k_2}) - \frac{1}{N} \sum_{\boldsymbol{q'}} \frac{\Gamma_{\boldsymbol{q'}}(\boldsymbol{k_1}, \boldsymbol{k_2}) V_{\boldsymbol{q}-\boldsymbol{q'}}(\boldsymbol{k_1} + \boldsymbol{q'}, \boldsymbol{k_2} - \boldsymbol{q'})}{S(\omega_{\boldsymbol{k_1}+\boldsymbol{q'}} + \omega_{\boldsymbol{k_2}-\boldsymbol{q'}})} \tag{2.23}$$

where

$$V_{\boldsymbol{q}}(\boldsymbol{k_1}, \boldsymbol{k_2}) = \frac{1}{2}[(J_{\boldsymbol{q}} + J_{\boldsymbol{k_2}-\boldsymbol{k_1}-\boldsymbol{q}}) + 2S(K_s - 1)(J_{\boldsymbol{k_1}} + J_{\boldsymbol{k_1}+\boldsymbol{q}} + J_{\boldsymbol{k_2}} + J_{\boldsymbol{k_2}-\boldsymbol{q}})] \tag{2.24}$$

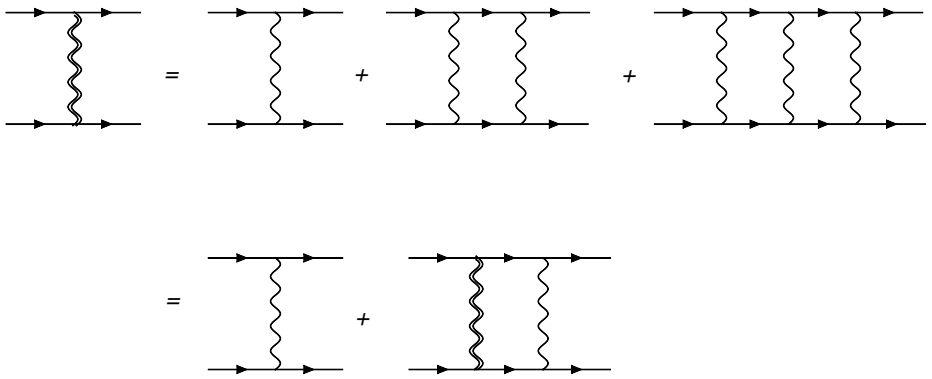

Figure 2.4: (From [41]) Self-consistency equation for the fully renormalized four-point vertex function $\Gamma_{\boldsymbol{q}}(\boldsymbol{k_1}, \boldsymbol{k_2})$, (double wavy line). A single wavy line is the four-boson interaction potential $V_{\boldsymbol{q}}(\boldsymbol{k_1}, \boldsymbol{k_2})$.

where $K_s = \sqrt{1 - 1/2S}$. K_s is obtained by re-expressing the H-P expansion of $\hat{S}^+/\hat{S}^-$, in terms of normally ordered bosons. This factor can can also be obtained by matching the matrix element of spin operators $\hat{S}^+/\hat{S}^-$ and their Bose representations [114]. We explicitly verified that for $S = 1/2$ this procedure yields the same result as the one in which spin operators are mapped to hard core bosons.

One can easily make sure that for q, $\boldsymbol{k_1}$ and $\boldsymbol{k_2}$, which we need in Eq. 2.22, the integrand scales as $1/(q')^2$ at small q', if we evaluate it right at $h = h_{\rm sat}$. The 2D integral over q' then diverges logarithmically. The log-divergence is cut at $h < h_{\rm sat}$ by $h_{\rm sat} - h$, which then appears under the logarithm. We already used this in the calculations at large S. In the latter case, we used the fact that, as a function of S, $V = \mathcal{O}(1)$ and $\epsilon_{\boldsymbol{k}} = S\omega_{\boldsymbol{k}} = \mathcal{O}(S)$, and $\Gamma_{\boldsymbol{q'}}(\boldsymbol{k_1}, \boldsymbol{k_2})$ is restricted with only one scattering process, i.e., replace $\Gamma_{\boldsymbol{q'}}(\boldsymbol{k_1}, \boldsymbol{k_2})$ in the r.h.s. of Eq. 2.23 by $V_{\boldsymbol{q}}(\boldsymbol{k_1}, \boldsymbol{k_2})$. This is how we obtained terms $(1/S)|\log(h_{\rm sat} - h)|$. Now $S = \mathcal{O}(1)$, but $|\log(h_{\rm sat} - h)|$ is still large, and all terms in the ladder series matter.

The ladder series for Γ contain higher powers of $(1/S)|\log(h_{\rm sat} - h)|$. We found that the series are geometrical, to logarithmic accuracy. Because $(1/S)|\log(h_{\rm sat} - h)| \gg 1$ for $S = \mathcal{O}(1)$ and $h \lesssim h_{\rm sat}$, the resulting Γ and $\bar{\Gamma}$ are actually small in $1/|\log(h_{\rm sat} - h)|$. For the V phase we found

$$\Gamma_1 = \Gamma_2 = (1 - 6J_2)4\pi\sqrt{3}\frac{S}{|\log(h_{\rm sat} - h)|} \tag{2.25}$$

We see that, to this accuracy, $\Gamma_1 = \Gamma_2$, like in the classical limit. However, the equivalence between Γ_1 and Γ_2 gets broken once we go beyond the leading term and compute contributions of order $1/|\log(h_{\rm sat} - h)|^2$. We did this numerically for

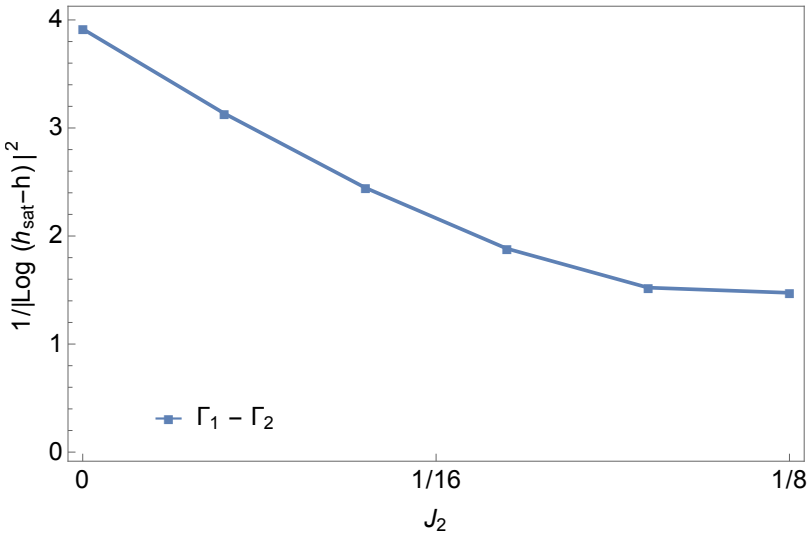

Figure 2.5: (From [41]) The difference between the two quartic coefficients, $\Gamma_1 - \Gamma_2$, in the Ginzburg-Landau expansion for the V phase, Eq. 2.8, for $S = 1/2$. The difference scales as $\frac{1}{|\log(h_{\rm sat}-h)|^2}$ with a J_2 dependent prefactor.

$S = 1/2$ and show the results in Fig. 2.5. We see that $\Delta\Gamma = \Gamma_1 - \Gamma_2$ is positive, like in the quasiclassical limit. A positive $\Delta\Gamma$ implies that it is energetically favorable for a system to develop both condensates, Δ_1 and Δ_2, with equal amplitude $\rho = \mu/(\Gamma_1+\Gamma_2)$ ($\mu \propto (h_{\rm sat} - h)$). This implies that the ordered state at small J_2 is coplanar. To determine the specific type of a coplanar order, i.e. to specify the angle Ψ in Eq. 2.11, one would, in principle, need to obtain Γ_{textu} – the prefactor for $(\Delta_1^3\overline{\Delta}_2^3 + h.c.)$ term in the condensation energy. This term selected the V phase in the quasiclassical limit. The calculation of Γ_{textu} at arbitrary S is rather involved and we didn't do it. Rather, we use the fact that the V state has been identified for $S = 1/2$ in the numerical analysis at $J_2 = 0$ [93], and assume that the same holds for finite J_2, i.e., that Γ_{textu} is negative at arbitrary S, as it is at $S \gg 1$.

As larger J_2, the condensation energy is expressed in terms of three Φ fields (see the second equation in Eq. 2.33). To leading order in $1/|\log(h_{\rm sat} - h)|$ we obtained

$$\begin{aligned}\overline{\Gamma}_1 &= 8\pi\sqrt{4J_2 - (1-3J_2)^2}\,\frac{S}{|\log(h_{\rm sat}-h)|}\\ \overline{\Gamma}_2 &= 8\pi\sqrt{4J_2}\,\frac{S}{|\log(h_{\rm sat}-h)|}\end{aligned} \tag{2.26}$$

We see that $\bar{\Gamma}_1 \leq \bar{\Gamma}_2$, the equality holds only when $J_2 = 1/3$. This matches the result that we obtained in the large S limit. For $\bar{\Gamma}_2 > \bar{\Gamma}_1$, only one out of three order parameters Φ_i develops a non-zero value, and the resulting state is the canted stripe

phase, same as at large S. Like we already said, the case $J_2 = 1/3$ requires a separate analysis.

We now use Ginzburg-Landau expansion to analyze the phase transition between the V and the stripe phases at arbitrary S. We introduce Δ field for the order parameter in the V phase ($\Delta_1 = \Delta_2 = \Delta/\sqrt{2}$) and Φ field for the order parameter in the stripe phase and derive the form of the condensation energy $E_{\rm cri}$ up to fourth order in the coupled Δ and Φ fields. The most generic form of $E_{\rm cri}$ is

$$E_{\rm cri}/N = -\mu|\Delta|^2 - \bar{\mu}|\Phi|^2 + \frac{1}{4}(\Gamma_1+\Gamma_2)|\Delta|^4 + \frac{1}{2}\bar{\Gamma}_1|\Phi|^4 + \Gamma_{\Delta,\Phi}|\Delta|^2|\Phi|^2 + \bar{\Gamma}_{\Delta,\Phi}|\Delta|^2|\Phi|^2\cos 2\phi \tag{2.27}$$

where ϕ is chosen such that $E_{\rm cri}$ is minimized. In the classical limit $\mu = \bar{\mu} = S(h_{\rm sat} - h)$. Quantum fluctuations renormalize the slope of $(h_{\rm sat} - h)$ dependence differently for μ and $\bar{\mu}$, and the two are generally different.

In the next Section we use spin-wave formalism to find out how μ and $\bar{\mu}$ behave near $J_2 = 1/8$. Here we analyze the prefactors of the quartic terms. The calculations are similar to the ones for the V and the stripe phases, and we just present the results. To leading order in $1/|\log(h_{\rm sat} - h)|$ we obtained

$$\Gamma_1 = \sqrt{3}\pi\frac{S}{|\log(h_{\rm sat}-h)|}, \quad \Gamma_2 = \sqrt{3}\pi\frac{S}{|\log(h_{\rm sat}-h)|}, \quad \bar{\Gamma}_1 = \sqrt{7}\pi\frac{S}{|\log(h_{\rm sat}-h)|}$$
$$\bar{\Gamma}_2 = 4\sqrt{2}\pi\frac{S}{|\log(h_{\rm sat}-h)|}, \quad \Gamma_{\Delta,\phi} = 2\sqrt{2}\pi\frac{S}{|\log(h_{\rm sat}-h)|}, \quad \bar{\Gamma}_{\Delta,\phi} = 0 \tag{2.28}$$

We see that $\frac{1}{2}(\Gamma_1+\Gamma_2)\bar{\Gamma}_1 < \Gamma^2_{\Delta,\phi}$. An elementary analysis of Eq. 2.27 shows that in this situation the V and the stripe orders repel each other and repulsion is strong enough so that mutual co-existence is excluded. This leaves two possibilities: if the regions around $J_2 = 1/8$ where $\mu > 0$ and $\bar{\mu} > 0$ overlap, the phase transition between the two phases is first order, like at large S (Fig. 2.3a). If upon increasing of J_2, μ changes sign from positive to negative before $\bar{\mu}$ changes from negative to positive, then there is a region near $J_2 = 1/8$ where neither V nor stripe order develops (Fig. 2.3c). In this situation, the transition between the V and the stripe phase occurs via an intermediate phase, which is either disordered or has some non-quasi-classical long-range order, different from both the V and the stripe orders. This last option is not realized at large S, but may develop at $S = \mathcal{O}(1)$. To check this we now analyze spin-wave excitations at an arbitrary S and find the stability regions of the two phases.

Spin wave calculations

We show the calculations for the V phase. The analysis of the stripe phase is performed in the same way. To study the instability of the V phase as J_2 increases from 0 to 1/8, we expand the Hamiltonian in powers of the Holstein-Primakoff bosons. For an arbitrary spin, the prefactors in the expansion of S^{+-} operators in powers of the density of Holstein-Primakoff bosons contain complex dependence of S due to the fact that one should perform normal ordering of the bosons after expanding $\sqrt{1-a^\dagger a/(2S)}$. The result of normal ordering is

$$\begin{aligned} S^+_{\boldsymbol{r}} &= \sqrt{2S}(1-\frac{1}{4S}(1+\frac{1}{8S}+\frac{1}{32S^2}+...)a^\dagger_{\boldsymbol{r}}a_{\boldsymbol{r}})a_{\boldsymbol{r}}+\mathcal{O}(a^5) \\ &= \sqrt{2S}(1+(\sqrt{1-\frac{1}{2S}}-1)a^\dagger_{\boldsymbol{r}}a_{\boldsymbol{r}})a_{\boldsymbol{r}}+\mathcal{O}(a^5) \end{aligned} \tag{2.29}$$

The computations of the spin-wave dispersions follows the same steps as for large S, but now we have to keep the explicit dependence on S in the prefactors of all terms. Like at large S, we analyze the dispersion around, say, $\overline{\mathbf{M}}_1$ point in the three-sublattice Brillouin zone, where the instability develops in the large S analysis. The low-energy Hamiltonian expressed in terms of soft B and C bosons has form similar to Eq. 2.32:

$$\begin{aligned} &\mathcal{H}^{(2)} = \frac{S}{2}\sum_{\boldsymbol{q}} \\ &\left(B^\dagger_{\boldsymbol{M}_1+\boldsymbol{q}}\ C_{-\boldsymbol{M}_1-\boldsymbol{q}}\right)\begin{pmatrix}\omega_{\boldsymbol{q}}+(3+9\delta_1)\theta^2 & (-3+9\delta_1)\theta^2\\ (-3+9\delta_1)\theta^2 & \omega_{-\boldsymbol{q}}+(3+9\delta_1)\theta^2\end{pmatrix}\begin{pmatrix}B_{\boldsymbol{M}_1+\boldsymbol{q}}\\ C^\dagger_{-\boldsymbol{M}_1-\boldsymbol{q}}\end{pmatrix} \end{aligned} \tag{2.30}$$

where θ is the angle between the spin order on A sublattice and the field, $\omega_{\boldsymbol{q}} = 1-8J_2+\frac{1}{16}(q_x^2+21q_y^2)$ is the spin wave dispersion at $h=h_{\rm sat}$, and δ_1 and δ_2 originate from magnon-magnon interactions. In distinction to large S, these two parameters are no longer simply $\mathcal{O}(1/S)$, but have complex dependence on S. The relation between θ^2 and $h_{\rm sat}-h$ is also affected by magnon-magnon interaction.

The computation of δ_1, δ_2 and θ at arbitrary S is somewhat involved. We show the computational steps in Appendix A and here present the results. With logarithmic accuracy, we found $\theta^2 = \alpha_1(h_{\rm sat}-h)|\log(h_{\rm sat}-h)|$, $\alpha_1>0$, $\delta_1 = -1/3+\mathcal{O}(1)$ and $\delta_2 = 1/3+\mathcal{O}(\frac{1}{|\log(h_{\rm sat}-h)|})$. Substituting these $\delta_{1,2}$ and θ^2 into Eq. 2.30, we found, to logarithmic accuracy, the dispersion near $\mathbf{M}_1$ in the form

$$\omega_{\mathbf{M}_1+\mathbf{q}} = \left(1-8J_2+(3+9\delta_1)\alpha_1(h_{\rm sat}-h)|\log(h_{\rm sat}-h)|\right)+\frac{1}{16}(q_x^2+21q_y^2) \tag{2.31}$$

	$S=1/2$	$S=1$	$1 \ll S \ll \lvert\log(h_{\rm sat}-h)\rvert$
$1/3+\delta_1$	-0.1	-0.02	$+0.03/S$
$J_{2V}-J_{2\rm stripe}$ $((h_{\rm sat}-h)\lvert\log(h_{\rm sat}-h)\rvert)$	$-$	$-$	$+$

Table 2.2: (From [41]) Quantum corrections to the mass of V phase spectrum at momentum $\boldsymbol{M}$ (first row), from which the width of overlap between the V phase and the stripe phase can be obtained. A negative width (sign) indicates that the two states don't overlap near $J_2 = 1/8$.

In the large-S limit we had $(1/3+\delta_1) > 0$ in Sec. 2.2.1. In this situation the instability develops at $\boldsymbol{q} = 0$, i.e., at $\mathbf{k} = \mathbf{M}_1 + \mathbf{q} \equiv \mathbf{M}_1$, and the critical $J_2 = J_{2\rm V} > 1/8$, i.e., the stability region of the V phase extends to the right of $J_2 = 1/8$. For arbitrary S we found that the sign of $(1/3+\delta_1)$ depends on S. For $S > 1$, it is positive, like at large S. For $S = 1/2$, however, we found that $1/3+\delta_1 = -0.1 < 0$. As the consequence, the V phase becomes unstable before J_2 reaches $J_2 = 1/8$. For $S = 1$, our numerical calculation yields a slightly negative $1/3+\delta_1$. We summarize our numerical results for $1/3+\delta_1$ in Table 2.2.

We analyzed the spin wave spectrum in the stripe phase, near momentum $\pm\boldsymbol{K}$. The low energy part of the quadratic Hamiltonian near $\pm\boldsymbol{K}$ can be expressed as:

$$\mathcal{H}^{(2)} = \frac{S}{2}\sum_{\boldsymbol{q}} \left(c^\dagger_{\boldsymbol{K}+\boldsymbol{q}}\, c_{-\boldsymbol{K}-\boldsymbol{q}}\right) \begin{pmatrix} \tilde{\omega}_{\boldsymbol{q}} + (3/2+9/2\,\tilde{\delta}_1)\tilde{\theta}^2 & (3/2+9/2\,\tilde{\delta}_2)\tilde{\theta}^2 \\ (3/2+9/2\,\tilde{\delta}_2)\tilde{\theta}^2 & \tilde{\omega}_{-\boldsymbol{q}} + (3/2+9/2\,\tilde{\delta}_1)\tilde{\theta}^2 \end{pmatrix} \begin{pmatrix} c_{\boldsymbol{K}+\boldsymbol{q}} \\ c^\dagger_{-\boldsymbol{K}-\boldsymbol{q}} \end{pmatrix} \tag{2.32}$$

where $\tilde{\theta}$ is the angle between the canted stripe order and the field, $\tilde{\omega}_{\boldsymbol{q}} = 8J_2 - 1 + \frac{3}{16}(q_x^2+q_y^2)$. Similar to the V phase case, $\tilde{\theta}^2 = \alpha_2(h_{\rm sat}-h)\lvert\log(h_{\rm sat}-h)\rvert$, $\alpha_2 > 0$. In the large S limit in Sec. 2.2.1, $(1/3+\tilde{\delta}_1) > 0$. In this situation, the instability develops at $\pm\boldsymbol{K}$, and at $J_{2\rm stripe} < 1/8$. At arbitrary S and $h \lesssim h_{\rm sat}$, we found that $3/2+9/2\,\tilde{\delta}_1$ and $3/2+9/2\,\tilde{\delta}_2$ both scale as $1/\lvert\log(h_{\rm sat}-h)\rvert$, and it is true as long as $S \ll \lvert\log(h_{\rm sat}-h)\rvert$. Hence, to logarithmic accuracy, the stripe phase becomes unstable right at $J_2 = J_{2\rm stripe} = 1/8$.

Comparing J_{2V} and $J_{2\rm stripe}$, we see that for $S > 1$, the stability regions of the two phases overlap. The Ginzburg-Landau analysis from the previous sub-section shows that the transition between the two stable phases is first order. For $S = 1/2$ and, possibly, $S = 1$, the situation is different because the V phase becomes unstable prior to the J_2 at which the stripe phase becomes stable. In this situation, there exists an

intermediate phase at which neither the V phase nor the stripe phase is stable. We illustrate this in the inset of Fig. 2.6.

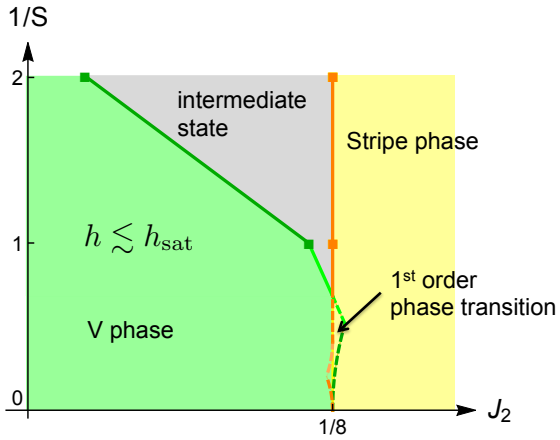

Figure 2.6: Phase diagram near $h_{\rm sat}$ for arbitrary spin S (Sec. 2.2.2) Phase boundaries of the V phase and the stripe phase right below $h_{\rm sat}$ are obtained without a simplifying assumption that S is large. Dashed lines in light color (light green and light orange) interpolate between finite S and large S data. At $S = 1/2$, the spin wave stability regions of the V and the stripe phase don't overlap, indicating an intermediate state (Gray) in between. The intermediate state has non-quasi-classical long-range magnetic order.

Whether the intermediate phase at high-field is disordered or has some non-quasi-classical long-range order is not clear at the moment. If we use Eq. 2.31 for the dispersion, we find that at $J_2 = J_{2V}$ the dispersion is quadratic at small q. For such dispersion, quantum corrections to sublattice magnetization logarithmically diverge in 2D and eliminate long-range order. We caution, however, that this spectrum was obtained to leading order in $1/|\log(h_{\rm sat} - h)|$. Subleading terms can potentially halt the divergence of the corrections to sublattice magnetization. Still, at $S = 1/2$, subleading terms are small near $h = h_{\rm sat}$, i.e., quantum corrections to sublattice magnetization are large and likely restore $U(1)$ symmetry, at least near $J_2 = J_{2V}$. A phase with a discrete, dimer-like order is another possibility. We verified that a columnar dimer phase is not an option, but this does not exclude some other dimer-like state. And yet another possibility is a disordered, spin-liquid type state, possibly the same as has been detected in numerical studies of zero-field phase diagram around $J_2 = 1/8$ [108, 109, 111].

2.3 A cascade of field induced magnetic transitions and half-magnetization plateau

In this section, we show our analysis of the large S phase diagram in the range $1/8 < J_2/J_1 < 1$. The set of classical ground states are in four sublattice configurations, in which four spins on two neighboring triads satisfy $\boldsymbol{S}_r + \boldsymbol{S}_{r+\boldsymbol{\delta}_1} + \boldsymbol{S}_{r+\boldsymbol{\delta}_2} + \boldsymbol{S}_{r+\boldsymbol{\delta}_3} = \boldsymbol{h}S/(2(J_1 + J_2))$ [See Fig. 2.1 (a)]. This condition does not uniquely specify spin order, even at zero field. The selection of the order by quantum fluctuations at $h = 0$ has been analyzed by various means [107–109, 119], and the consensus is that for $1/8 < J_2/J_1 < 1$ the winner is the stripe order with ferromagnetic alignment of spins along one of three principle axes on a triangular lattice and antiferromagnetic along the other two. The same order (the canted stripe state) is selected by quantum fluctuations near the saturation field, and semiclassical (large S) spin-wave analysis shows [41] that this state remains stable at all fields. It would seem natural to conjecture that this state, with monotonic magnetization $M(h)$, is the true quantum ground state for $1/8 < J_2/J_1 < 1$ in all fields.

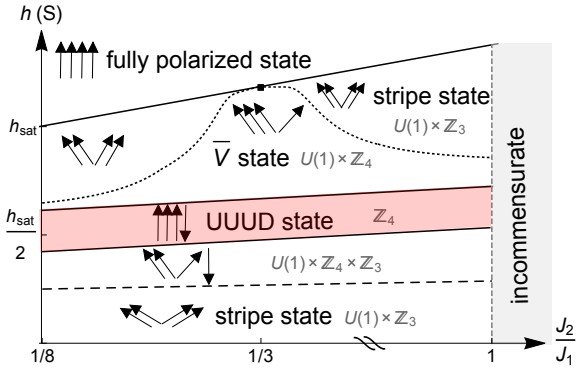

Figure 2.7: (From [38]) Schematic semiclassical phase diagram of a spin-S, $J_1 - J_2$ antiferromagnet on a triangular lattice, at $1/8 < J_2/J_1 < 1$. Solid (dotted) lines are second-order (first-order) phase transitions, which we identified and analyzed in this work. Dashed line is a first-order transition, which we expect to hold, but didn't analyze. Arrows indicate magnetic order in the four-sublattice representation, and symbols like $U(1) \times Z_3$ indicate the broken symmetry in each state. The physics in a narrow range (at order 1/S) of J_2/J_1 near $J_2/J_1 = 1/8$ and $J_2/J_1 = 1$ is not analyzed in this work.

We argue that the phase diagram of $J_1 - J_2$ model in a field is actually rather complex, with multiple phases [see Fig. 2.7], and the stripe order is the ground state configuration only in some range of fields and of J_2/J_1. For other values of h and J_2/J_1 the ground state configurations are the co-planar states, similar to those at

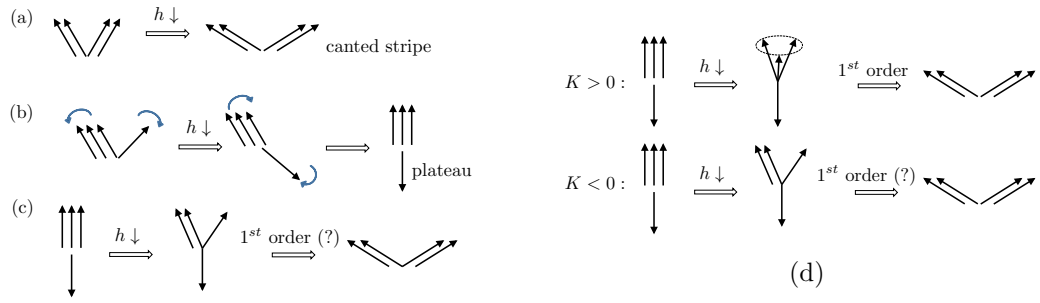

Figure 2.8: (From [38]) (a), (b) – two candidate quantum four-sublattice ground states upon decreasing of the magnetic field h towards a half of saturation value. (a) A Z_3 breaking canted stripe state. As field goes down, the angle between two pairs of parallel spins increases. (b) $\bar{\text{V}}$ and UUUD states. Both break Z_4 sublattice symmetry by selecting one sublattice with a different spin orientation compared to the other three. (c) Evolution from the UUUD state to the canted stripe state as h decreases below $h_{sat}/2$. (d) Evolution of the magnetic order below the UUUD state, depending on sign of the K term in Eq. 2.35.

small J_2. In particular, around $h = h_{sat}/2$, the ground state is the UUUD state, in which spins in three sublattices are aligned along the field and in the forth sublattice opposite to the field. This spin order breaks $\mathbb{Z}_4$ sublattice symmetry, but doesn't break any continuous symmetry. As a result, spin-wave excitations are gapped, and the magnetization has a plateau at exactly 1/2 of the saturation value. We argue that the UUUD state exists for all J_2 in the interval $1/8 < J_2/J_1 < 1$, i.e., the magnetization plateau exists for all $J_1 - J_2$ systems, either at 1/3 of the saturation value, at $J_2/J_1 < 1/8$, or at 1/2 of the saturation value, at $1/8 < J_2/J_1 < 1$. We also analyze the proximate states to the UUUD state. Above the upper critical field h_u, the UUUD state becomes unstable towards a state in which three up-spins rotate in one direction from the direction of $\boldsymbol{h}$, and the down-spin rotates in the opposite direction [see Fig. 2.8(b)]. Below the lower critical field h_l, we found, at large S, a particular coplanar state, in which down-spin does not move, while three up-spins again rotate, but now one of these three spins splits from the other two (see Fig. 2.8(c)). A non-coplanar, chiral umbrella state [106, 120] is close in energy and may be the ground state near h_l at smaller S [see Fig. 2.8 (d)].

A cascade of field-induced magnetic transitions at fields below $h_{sat}/2$ has been observed in $2H-\text{AgNiO}_2$ [121, 122]. It has been argued [123] that in this material Ni^{2+} ions are localized and form a $S = 1$ triangular lattice antiferromagnet with $J_2 = 0.15J_1$, single-ion easy axis anisotropy D, weak ferromagnetic exchange between layers. And Classical Monte-Carlo calculations for this model have found [124] the region of UUUD phase, whose width at $T = 0$ scales with D. We show that in a

quantum model the UUUD phase is stable in a finite range of h already at $D = 0$. We expect that future measurements of the magnetization in $2H{-}AgNiO_2$ at higher fields will be able to detect the UUUD phase and also the cascade of phases above $h_{sat}/2$. The analysis of the high-field phases will allow one to distinguish whether UUUD order is stabilized predominantly by quantum fluctuations or by single-ion anisotropy [1]

2.3.1 High field analysis

The first indication that the stripe phase is not the only ground state in a field comes from the Ginzburg-Landau analysis of the order immediately below the saturation field. We said in the Introduction that this analysis yields the stripe order. This is true for all J_2 in the interval of interest, however, with one exception – $J_2 = J_1/3$. To see why this J_2 is exceptional, we note that spin-wave excitations soften at $h = h_{sat}$ at three points in the Brillouin zone (M_1, M_2, M_3 in Fig. 2.1 (b). To understand the order below h_{sat} one then needs to introduce three condensates Φ_1, Φ_2, Φ_3. The ground state energy in terms of Φ is:

$$E_\Phi/N = -\mu \sum_{i=1,2,3} |\Phi_i|^2 + \frac{1}{2}\Gamma_1 \sum_{i=1,2,3} |\Phi_i|^4 + \Gamma_2(|\Phi_1|^2|\Phi_2|^2 + |\Phi_1|^2|\Phi_3|^2 + |\Phi_2|^2|\Phi_3|^2) + \Gamma_3(\Phi_1^2\Phi_2^2 + \Phi_2^2\Phi_3^2 + \Phi_3^2\Phi_1^2 + h.c.) \quad (2.33)$$

where $\mu \sim S(h_{\rm sat} - h)$. The type of spin order that minimizes E_Φ depends on the interplay between the quartic coefficients Γ_i. In the classical limit, $\Gamma_1 = \Gamma_2 = 8(J_1 + J_2)$, $\Gamma_3 = 0$, i.e., any state from the manifold $|\Phi|_1^2 + |\Phi|_2^2 + |\Phi|_3^2 \equiv \mu/\Gamma_1$ is the ground state. Quantum fluctuations lift the degeneracy. To leading order in $1/S$ we found [41], near $J_2 = J_1/3$,

$$\Gamma_2 - \Gamma_1 = \frac{24\sqrt{3}J_1}{\pi}\left(\frac{J_2}{J_1} - 1/3\right)^2 \frac{|\log(h_{\rm sat} - h)|}{S} - \beta_1/S$$
$$\Gamma_3 = -\beta_2/S \quad (2.34)$$

where $\beta_{1,2} > 0$ are numbers of order one. The logarithm $|\log(h_{\rm sat} - h)|$ is present because of quadratic dispersion near M-points in Fig. 2.1 (b): e.g., near $\mathbf{M}_1$, $\omega_{\boldsymbol{k}} = SJ_1((1 + \frac{9}{2}\alpha)k_x^2 + (1 - \frac{3}{2}\alpha)k_y^2) - \mu$, where $\boldsymbol{q} = \boldsymbol{k} + \boldsymbol{M}_1$ and $\alpha = J_2/J_1 - 1/3$. Because

[1] If the UUUD order is dominated by quantum fluctuations, one should expect to see both $\bar{V}$ phase and canted stripe phase at higher fields, like in Fig. 2.7. If UUUD order is mostly due to single-ion anisotropy, only $\bar{V}$ phase is present, see Ref. [125].

of the logarithm, $\Gamma_2 > \Gamma_1$, A straightforward analysis then shows that only one Φ_i is non-zero because it costs extra energy to develop simultaneously condensates from different valleys. The resulting order is the stripe state. A selection of Φ_i breaks $\mathbb{Z}_3$ symmetry, which for the stripe state can be understood as an orientational symmetry (spins align ferromagnetically along one of the three spatial directions). However, the prefactor for the logarithm in $\Gamma_2 - \Gamma_1$ in Eq. 2.34 is non-zero only when the dispersion is anisotropic, and it vanishes at $J_2 = J_1/3$, when $\omega_{\boldsymbol{k}}$ becomes isotropic ($\alpha = 0$). For this J_2/J_1, the sign of $\Gamma_2 - \Gamma_1$ is determined by regular $1/S$ terms, along with the sign of Γ_3. We computed these terms and found $\Gamma_2 - \Gamma_1 < 0$, $\Gamma_3 < 0$. As a result, at $J_2/J_1 = 1/3$, all three condensates emerge with equal amplitudes and relative phases 0 or π (because $\Gamma_3 < 0$). The four choices for (Φ_1, Φ_2, Φ_3) are (Φ, Φ, Φ), $(\Phi, -\Phi, -\Phi)$, $(-\Phi, \Phi, -\Phi)$, $(-\Phi, -\Phi, \Phi)$. In each of these states spins in three sublattices tilt to one direction from the field, and in one sublattice tilt to the opposite (see Fig. 2.8). We label such a state $\bar{\text{V}}$ by analogy with the corresponding V state [2] at $J_2 < J_1/8$ [93, 95, 126, 127]. The $\bar{\text{V}}$ state breaks $U(1)$ spin-rotational symmetry in the plane perpendicular to the field, and also breaks a $\mathbb{Z}_4$ sublattice symmetry by selecting a sublattice in which spin direction is different from that in other three sublattices.

Immediately below h_{sat}, the $\bar{\text{V}}$ state is stable in the infinitesimally small range around $J_2 = J_1/3$, at $(J_2/J_1 - 1/3)^2 < 1/|\log(h_{sat} - h)|$. As h decreases, the width grows and becomes $\mathcal{O}(1)$ at $h_{\text{sat}} - h = \mathcal{O}(1)$. The $\bar{\text{V}}$ and the stripe state break different discrete symmetries ($\mathbb{Z}_4$ and $\mathbb{Z}_3$, respectively), hence the transition between the two states is likely first order. The increase of the width of the $\bar{\text{V}}$ state with decreasing field can be understood as a generic consequence of the fact that this state is favored by regular $1/S$ terms, i.e., by quantum fluctuations at short length scales, while the stripe phase is favored by $|\log(h_{\text{sat}} - h)|$, which comes from long-wavelength fluctuations. As the magnitude of the transverse order increases with decreasing field, long wavelength fluctuations are suppressed, and $\bar{\text{V}}$ state becomes more favorable.

2.3.2 Half-magnetization plateau

As the field decreases towards $h_{sat}/2$, the $\bar{\text{V}}$ state evolves: the spin in one sublattice continuously rotates away from the field direction towards the direction antiparallel to $\boldsymbol{h}$. The spins in three other sublattices remain parallel to each other and first rotate away from the field, and then rotate back. Eventually, near $h = h_{sat}/2$, spins

[2] The three-sublattice V state has spins in two sublattices tilt in one direction from the field, and in another sublattice to the opposite direction.

in the three sublattices become parallel to $\boldsymbol{h}$ and spins in the fourth sublattice become antiparallel to $\boldsymbol{h}$ [see Fig. 2.8 (b)]. Once this happens, the system enters into the new, UUUD phase. In this phase, $U(1)$ symmetry is restored (there is no sublattice spin component transverse to the field), but Z_4 symmetry is still broken. To obtain the boundaries of the UUUD phase, we compute its excitation spectrum. For this, we introduce four sets of Holstein-Primakoff (H-P) bosons and do spin-wave calculations to order $1/S$. In the classical, $S \to \infty$ limit, the spin-wave excitations are stable only at $h = h_{sat}/2$, where the spectrum consists of one gapped spin wave branch (in-phase precession of all spins around the field), and three gapless branches, with zero modes at Γ point of the four-sublattice Brillouin zone [see Fig. 2.1 (b)]. Quantum $1/S$ correction to spectrum, however, make it stable in a finite range of h around $h_{sat}/2$. Namely, all spin-wave branches become gapped (and positive) in a range $h_l < h < h_u$, where $h_l = h_{sat}/2 - \delta_1$ and $h_u = h_{sat}/2 + \delta_2$. We show the details of the calculations in the Appendix A and present the results for δ_1 and δ_2 in Table 2.3. We found, somewhat unexpected, that the stability width of the UUUD phase is finite for *all* J_2 in the interval $1/8 < J_2/J_1 < 1$. We further computed the ground state energy of the UUUD phase to order $1/S$ (classical energy plus $1/S$ corrections from zero point fluctuations), and compared with that of the stripe phase. We found that for all J_2 the energy of the UUUD state is lower. Because of this and because the UUUD state naturally emerges from the $\bar{\text{V}}$ state, we argue that the UUUD state is the true ground state near $h = h_{sat}/2$ for all $1/8 < J_2/J_1 < 1$. As all excitations in the UUUD state are gapped, this state has magnetization fixed at exactly 1/2 of the saturation value.

We also verified that at the upper critical field of the UUUD state, it becomes unstable towards $\bar{\text{V}}$ state. Namely, at $h = h_u$ one of the spin-wave branches condenses, and the condensate leads to $\langle S_x \rangle = a$ for spins on three up-spin sublattices, and $-3a$ for the spins on the down-spin sublattice. This result in turn implies that the $\bar{\text{V}}$ state, which started at a point $J_2 = J_1/3$ at $h = h_{sat}$, extends over the whole range of J_2 near $h_{sat}/2$ (see Fig. 2.7).

J_2/J_1	1/8	1/4	1/3	1/2	1
$\delta_1(1/S)$	0.46	0.15	0.11	0.11	0.28
$\delta_2(1/S)$	1.2	0.80	0.75	0.75	1.09

Table 2.3: (From [38]) Results for the boundaries of UUUD state for different J_2/J_1 (see SM for details of calculations). The UUUD state is stable in the range $h_l < h < h_u$, where $h_l = h_{sat}/2 - \delta_1$ and $h_u = h_{sat}/2 + \delta_2$.

At the lower boundary of the UUUD phase, two other spin-wave modes become

unstable at the Γ point. To determine the the spin order below h_l, we again perform Landau Free energy analysis in terms of the corresponding two complex order parameters Δ_1 and Δ_2. We present the details in the SM. The Free energy has the form [128, 129]:

$$E_\Delta/N = -\mu(|\Delta_1|^2+|\Delta_2|^2)+\frac{1}{2}\Gamma(|\Delta_1|^2+|\Delta_2|^2)^2+\frac{1}{2}K|\Delta_1^2+\Delta_2^2|^2 \tag{2.35}$$

Classically, $\Gamma = h_{sat}/4$, $K=0$. Then $|\Delta_1|^2+|\Delta_2|^2 \equiv \mu/\Gamma$, i.e. different ordered states are degenerate. Quantum fluctuations lift the degeneracy, and the result depends on the sign of K. If $K>0$, $\Delta_1 = \pm i\Delta_2$. It can be checked that this gives rise to a non-coplanar umbrella state, in which the down-spin remains intact, and three up-spins split out and form a cone. Such a state breaks $U(1)\times\mathbb{Z}_4\times\mathbb{Z}_2$ symmetry. If $K<0$, the relative phase between Δ_1 and Δ_2 is either 0 or π, and the order is coplanar (see Fig. 2.8 (b)).

We computed K to accuracy $1/S$. The details of calculations are presented in SM, and here we quote the result: K is the sum of logarithmical, $|\log(h_l-h)|/S$, $\log S/S$, and non-logarithmical, $\mathcal{O}(1/S)$ terms, much like Eq. 2.34. The logarithmical term yields $K<0$, however the prefactor for the logarithm vanishes at $J_2 = J_1/3$, and at this value of J_2 non-logarithmical terms become relevant. Near $J_2 = J_1/3$, we have

$$K = -\frac{2\sqrt{3}J_1}{\pi}\left(\frac{J_2}{J_1}-1/3\right)^2\left(\frac{|\log(h_l-h)|}{S}+\beta_\phi\frac{\log S}{S}\right)-\frac{\beta_K}{S}. \tag{2.36}$$

Where the $|\log(h_l-h)|/S$ term is a contribution from spin wave modes which go as k^2 at $h=h_l$, and $\log S/S$ term comes from another spin wave mode that softens at $h=h_u=h_l+\mathcal{O}(1/S)$. In distinction to the situation near h_{sat}, here we found that K remains negative, even for $J_2/J_1 = 1/3$. This implies that the state below h_l is a co-planar state. An umbrella state is not ruled out, however, for smaller S as we computed β_K in Eq. 2.36 at $S\gg 1$.

To determine the structure of the coplanar state below h_l more work is actually required because for $K<0$, the Free energy to order Δ^4 is $E_\Delta/N = -\mu(|\Delta_1|^2+|\Delta_2|^2)+\frac{1}{2}(\Gamma-|K|)(|\Delta_1|^2+|\Delta_2|^2)^2$, i.e., the degeneracy is not fully lifted. To select the order, one has to compute $\mathcal{O}(\Delta^6)$ terms in the Free energy. We found (see SM for detail) that sixth-order terms select the order in which of the three up-spins two are tilting in one direction and another in the opposite direction, while the down spin remains intact (see Fig. 2.8 (b)). This state breaks $U(1)\times\mathbb{Z}_4\times\mathbb{Z}_3$ symmetry. It

can potentially transform gradually into the stripe state, which breaks $U(1) \times \mathbb{Z}_3$, if the down spin begins rotating at higher deviations from h_l and match the spin from up-triad, which is separated from the other two. Or, the transition can be first order. Either way, at small fields, the order becomes a stripe. A more complex phase diagram at low fields is expected in the presence of a single-ion anisotropy [121, 125].

2.4 Conclusion

In this Chapter, we studied the zero temperature phase diagram of a Heisenberg antiferromagnet on a frustrated triangular lattice with nearest neighbor (J_1) and next nearest neighbor (J_2) interactions, in a magnetic field. We analyzed the stabilization of the ordered phases at smaller and larger J_2/J_1 via order from disorder phenomenon and the phase transition between the ordered states at smaller and larger J_2/J_1. We first considered the limit of large but finite S and obtained the semiclassical phase diagram in all fields. We found that at $J_2/J_1 < 1/8 + \mathcal{O}(1/S)$, quantum fluctuations select the same set of co-planar states as at $J_2 = 0$: the Y state at fields $h < h_{\rm sat}/3$, the V phase at $h > h_{\rm sat}/3$, and the UUD phase at $h \approx h_{\rm sat}/3$. At $J_2 > 1/8 - \mathcal{O}(1/S)$, quantum fluctuations select the canted stripe phase. The stability regions of the two phases overlap around $J_2/J_1 = 1/8$, and semiclassical spin wave analysis shows that the transition between the two phases is first order, with a finite hysteresis width, of order $1/S$. We next analyzed the phase diagram near the saturation field at arbitrary S, by mapping the spin model to a dilute boson gas. We found the same V and stripe phase at smaller and larger J_2/J_1. For $S > 1$ we also found that the stability regions of the two states overlap, and the transition between them remains first order, like at large S. However, for $S = 1/2$ and, possibly, $S = 1$, we found that there exists an intermediate range near $J_2/J_1 = 1/8$, where neither of the two states is stable. We emphasize that this happens already arbitrary close to the saturation field, when the density of bosons is small. In the intermediate region the system either develops a non-quasi-classical long-range order (e.g., becomes dimerized), or remains quantum disordered. We note that the intermediate phase develops for the same $J_2/J_1 \approx 1/8$ where at $h = 0$ numerical calculations found evidence for a disordered, possibly spin-liquid state for $S = 1/2$ [108, 109, 111] (but, apparently, not $S = 1$ [99]). Whether the state we found at $h \approx h_{\rm sat}$ is the same one as found at $h = 0$ remains to be seen. We call for more numerical studies of $J_1 - J_2$ model in a finite field.

Chapter 3

Quantization of thermal Hall conductivity at small Hall angles

We consider the effect of coupling between phonons and a chiral Majorana edge in a gapped chiral spin liquid with Ising anyons (e.g., Kitaev's non-Abelian spin liquid on the honeycomb lattice). This is especially important in the regime in which the longitudinal bulk heat conductivity κ_{xx} due to phonons is much larger than the expected quantized thermal Hall conductance $\kappa_{xy}^{\mathrm{q}} = \frac{\pi T}{12}\frac{k_B^2}{\hbar}$ of the ideal isolated edge mode, so that the thermal Hall angle, i.e., the angle between the thermal current and the temperature gradient, is small. By modeling the interaction between a Majorana edge and bulk phonons, we show that the exchange of energy between the two subsystems leads to a transverse component of the bulk current and thereby an *effective* Hall conductivity. Remarkably, the latter is equal to the quantized value when the edge and bulk can thermalize, which occurs for a Hall bar of length $L \gg \ell$, where ℓ is a thermalization length. We obtain $\ell \sim T^{-5}$ for a model of the Majorana-phonon coupling. We also find that the quality of the quantization depends on the means of measuring the temperature and, surprisingly, a more robust quantization is obtained when the lattice, not the spin, temperature is measured. We present general hydrodynamic equations for the system, detailed results for the temperature and current profiles, and an estimate for the coupling strength and its temperature dependence based on a microscopic model Hamiltonian. Our results may explain recent experiments observing a quantized thermal Hall conductivity in the regime of small Hall angle, $\kappa_{xy}/\kappa_{xx} \sim 10^{-3}$, in α-$\mathrm{RuCl_3}$.

3.1 Introduction

Non-Abelian statistics is a deep generalization of quantum statistics in two dimensions, in which the final state depends upon the order in which exchanges of particles – non-Abelian anyons – are performed [130–132]. In addition to its fundamental interest, this provides a powerful paradigm for quantum computing, allowing for fault-tolerant processes [133, 134]. The main platforms in which non-Abelian topological phases have been sought are the $\nu = 5/2$ Fractional Quantum Hall Effect (FQHE) [130, 131], where non-Abelian anyons are suspected but have not been established, and hybrid semiconductor-superconductor structures, to which quantum computing groups are devoting massive efforts [135], but where confirmation is still awaited.

A third possible route to non-Abelian anyons is via a quantum spin liquid [6]. In his seminal work [40], Kitaev presented a spin-1/2 model on the honeycomb lattice with bond-dependent anisotropy which, in a magnetic field, realizes a non-Abelian topological phase. This phase hosts *Ising anyons*, topologically the same anyon type which is targeted by the hybrid efforts. A key and general characteristic of a topological phase is the *chiral central charge* c, which characterizes its gapless edge modes. It is directly measurable as a quantized thermal Hall conductivity, $\kappa_{xy}^{\mathrm{q}} = \pi c T/6$ ($\hbar = k_B = 1$). A non-integer value is an unambiguous indicator of a non-Abelian phase, and $c = 1/2$ for Ising anyons.

Stimulated by the recognition that Kitaev's anisotropic interactions arise naturally in certain strongly spin-orbit coupled Mott insulators [42, 43], mounting efforts have targeted such systems in the laboratory. There is now strong evidence that Kitaev interactions are substantial in several 2d honeycomb lattice materials [136]: α-Na_2IrO_3 [137], α-Li_2IrO_3 [138], and α-$RuCl_3$ [139]. While it is clear that none of these materials are exactly described by Kitaev's model, the beauty of a topological phase is its robustness: once obtained, it is stable to an arbitrary weak perturbation and its essential properties are completely independent of the details of the Hamiltonian. A very recent experiment [51] presents observations of an apparent plateau with a quantized thermal Hall conductivity with $c = 1/2$ in α-$RuCl_3$ in an applied field of 9-10T, at temperatures of 3-5K. If confirmed, it could be a revolutionary discovery not only in the non-Abelian context, but also as the first truly unambiguous signature of a quantum spin liquid phase in experiment. These results appear to complement recent experiments on quantum Hall systems which have observed half-integer thermal conductance, but through rather different means [140].

The α-$RuCl_3$ experiments do, however, present at least one major puzzle. The thermal *Hall angle* $\theta_H = \tan^{-1}(\kappa_{xy}/\kappa_{xx}) = 10^{-3}$ is small, i.e., $\kappa_{xx} \gg \kappa_{xy}$. This is incompatible with conduction solely through a Majorana edge mode. Indeed, in two dimensional electron gases, a quantized Hall effect is only observed when the Hall angle is large. This raises the fundamental question of whether the thermal Hall effect is different: is quantization even expected and possible at small Hall angles? We consider here a universal effective model for an Ising anyon phase, in which the chiral Majorana edge mode is augmented by acoustic bulk phonons, which can provide a diagonal bulk thermal conductivity. Remarkably, we find that not only does the quantized thermal Hall effect persist in the presence of the phonons, but it *relies* upon them. The ultimate view of the quantized transport is distinctly different from the usual isolated edge mode picture, and we predict notable experimental consequences of the mixing of edge and bulk heat propagation. Our considerations are quite general and we expect that similar physics applies to thermal transport in other systems with edge modes, such as topological superconductors and quantum Hall systems.

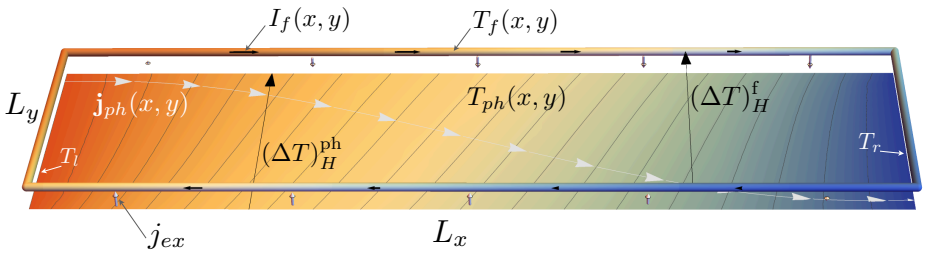

Figure 3.1: (From [49]) Temperature maps of our rectangular system with dimensions L_x and L_y consisting of a phonon bulk (lower box) and a Majorana fermion edge (upper edge). The phonon temperatures at the left and right edges are assumed to be fixed as $T_{l,r}$, respectively, due to the coupling of the lattice with the heater and thermal bath. The black arrows for I_f along the edge denote the direction and magnitude of the "clockwise" energy current associated with the chiral Majorana mode. The white arrows in the bulk show a stream line of $\mathbf{j}_{ph}$. The 3d white arrows for j_{ex} indicate the energy current between the Majorana edge and bulk phonons. $(\Delta T)_H^{ph}$ and $(\Delta T)_H^{f}$ are the measured "Hall" temperature differences when the contacts are coupled to the lattice or spins, respectively.

3.2 Hydrodynamic equations

We formulate the problem in terms of hydrodynamic equations describing the energy transport. We consider the following two subsystems: the phonons, or lattice, located in the bulk, and denoted with the index "*ph*", and the Majorana fermions, or spins,

confined to the edge and indexed by "f", as well as a coupling between them. For simplicity, we assume an isotropic bulk, with the relation

$$\mathbf{j}_{ph} = -\kappa \boldsymbol{\nabla} T_{ph}, \tag{3.1}$$

i.e., the energy current density in the bulk is parallel to the thermal gradient, with κ a characteristic of the lattice. The "clockwise" edge current is that of a chiral fermion with central charge $c = 1/2$, i.e.,

$$I_f = \frac{\pi c T_f^2}{12}. \tag{3.2}$$

The heat exchange between the phonons and Majoranas can be modeled phenomenologically through an energy current j_{ex} between the two subsystems (see the arrows in Fig. 3.1). Microscopically, it is due to the scattering events between edge Majorana fermions and bulk phonons, and is the rate of energy transfer at the edge per unit length, i.e., $j_{ex} \equiv \frac{1}{L}\left(\frac{\partial \mathcal{E}}{\partial t}\right)_{ph\to f} = -\frac{1}{L}\left(\frac{\partial \mathcal{E}}{\partial t}\right)_{f\to ph}$, where L is the length of the edge in evaluating $\left(\frac{\partial \mathcal{E}}{\partial t}\right)_{ph\to f}$ [1]. This in turn implies that the phonons and Majoranas have not fully thermalized with one another. Assuming, however, that thermalization is almost complete, i.e., $T_f \approx T_{ph}$, and that the fermions are strictly confined to the edge, j_{ex} can be linearized in the temperature difference $T_{ph} - T_f$ at the edge,

$$j_{ex} = \lambda(T)(T_{ph} - T_f), \tag{3.3}$$

where, crucially, $\lambda > 0$ is a function of the overall constant temperature $T \approx T_{ph,f}$, and can be parametrized as $\lambda(T) \sim T^\alpha$. We will determine α from a phase space analysis of the scattering events.

We assume our (two-dimensional) system to be a rectangular slab of width L_y and length $L_x \gtrsim L_y$ (see Fig. 3.1), and choose coordinates with $|x| < x_0 = L_x/2$ and $|y| < y_0 = L_y/2$.

The continuity equation in the bulk in a steady state is $\boldsymbol{\nabla} \cdot \mathbf{j}_{ph}(x, y) = 0$ which implies the Laplace equation

$$\nabla^2 T_{ph}(x, y) = 0. \tag{3.4}$$

Energy conservation at the edges gives rise to appropriate boundary conditions. At the left and right edges, we assume that only the *lattice* is coupled to thermal leads and the phonons have fixed constant temperatures, $T_{l,r}$, respectively. At the top and

[1] Note that $L = L_x$, resp. $L = L_y$, for j_{ex}(top/bottom), resp. j_{ex}(left/right)

bottom edges, the current out of the phonon subsystem must equal the exchange current, hence $\pm j^y_{ph}(x, \pm y_0) = j_{ex}(x, \pm y_0)$. Moreover, the continuity equations for the edges imply $\pm \partial_x I_f(x, \pm y_0) = j_{ex}(x, \pm y_0)$. Together these yield, given Eqs. (3.1) and (3.2),

$$\kappa \partial_y T_{ph}(x, \pm y_0) = -\kappa^{\mathrm{q}}_{xy} \partial_x T_f(x, \pm y_0). \tag{3.5}$$

Note the appearance of the ideal quantized Hall conductivity $\kappa^q_{xy} = \pi c T/6 = \pi T/12$ here, using $T_f \approx T$ (valid within our linearized treatment).

3.2.1 Quantization in the infinitely long limit

For simplicity, we first solve our hydrodynamic equations in the limit of an infinitely long system ($L_x \to \infty$). Note that, even for finite systems with $L_x \gg L_y$, this infinitely long limit is expected to be relevant far away from the left and right edges.

Since there is translation symmetry in the x direction, the boundary conditions $T_{ph}(\pm x_0, y) = T_{r,l}$ lead to a uniform temperature gradient $\overline{\frac{dT}{dx}} = \lim_{L_x \to \infty} \frac{T_r - T_l}{L_x}$, and the phonon and Majorana temperatures must take the forms

$$\begin{cases} T_{ph}(x, y) = \overline{\frac{dT}{dx}} x + \hat{T}(y) + \text{const.} \\ T_f(x, \pm y_0) = \overline{\frac{dT}{dx}} x + \text{const.}. \end{cases} \tag{3.6}$$

Laplace's equation, Eq. (3.4), immediately implies that $\hat{T}(y)$ must be a linear function of y which we write $\hat{T}(y) = \frac{(\Delta T)^{\mathrm{ph}}_H}{L_y} y$. Therefore, from Eq. (3.5), we get

$$\partial_y T_{ph}(x, y) = -\frac{\kappa^{\mathrm{q}}_{xy}}{\kappa} \overline{\frac{\mathrm{d}T}{\mathrm{d}x}}, \tag{3.7}$$

since $\partial_y T_{ph}(x, y) = \partial_y T_{ph}(x, \pm y_0) = \text{const.}$. From a phenomenological perspective, the *total* current in the Hall bar geometry must flow only along x, but Eq. (3.7) implies that the phonon thermal gradient is tilted from the current axis by a small Hall angle of $|\tan \theta_H| = \kappa^{\mathrm{q}}_{xy}/\kappa \ll 1$.

Next consider the view of Alice the experimentalist. She measures the temperature gradients via three contacts, and assumes for the moment that these measurements give the phonon temperature (the most reasonable assumption). To deduce the Hall conductivity, she posits a bulk heat current satisfying $\boldsymbol{j} = -\boldsymbol{\kappa}^{\mathrm{ph,expt}} \cdot \boldsymbol{\nabla} T$, and tries to deduce the tensor $\boldsymbol{\kappa}^{\mathrm{ph,expt}}$ [the ph (f) superscript means this quantity is obtained from a measurement of the phonon (Majorana fermion) temperature]. By measuring the longitudinal temperature gradient, she obtains $\kappa^{\mathrm{ph,expt}}_{xx} = \kappa$ as expected, and then,

imposing $j^y = 0$, she equates the experimental Hall angle $\tan\theta_H = \frac{(\Delta T)_H^{\rm ph}}{L_y}/\overline{\frac{dT}{dx}}$ to $\kappa_{xy}^{\rm ph,expt}/\kappa_{xx}^{\rm ph,expt}$. By comparing this equation to the theoretical result in Eq. (3.7), we immediately recognize that the magnitude of the effective Hall conductivity (denoted simply as $\kappa_{xy}^{\rm expt}$ in the rest of the text) is $|\kappa_{xy}^{\rm ph,expt}| = \kappa_{xy}^{\rm q}$, i.e., the experimentally measured thermal Hall conductivity takes the quantized value!

A few remarks are in order. First, a transverse temperature difference, $(\Delta T)_H^{\rm ph}$, leading to a "Hall thermal gradient" $(\Delta T)_H^{\rm ph}/L_y = -\frac{\kappa_{xy}^{\rm q}}{\kappa}\overline{\frac{dT}{dx}}$ develops which allows to compensate the transverse energy current j_{ex} at the edges and leads to a zero net transverse current. Second, the effective thermal Hall conductivity is only found to be quantized if the transverse temperature gradient is obtained from the *phonon* temperatures at the top and bottom edges. In contrast, if Bob somehow measures the Majorana temperatures, the transverse temperature gradient is identified as $(\Delta T)_H^{\rm f}/L_y$ and thus, from Eqs. (3.3) and (3.5), he finds a different effective thermal Hall conductivity [see also Fig. 3.2(a)]:

$$\kappa_{xy}^{\rm f,expt} = -\frac{\kappa(\Delta T)_H^{\rm f}}{L_y\overline{\frac{dT}{dx}}} = \kappa_{xy}^{q}\left(1+\frac{2\kappa}{\lambda(T)L_y}\right). \tag{3.8}$$

Note that $\kappa_{xy}^{\rm f,expt} \approx \kappa_{xy}^{\rm ph,expt}$ only for a large enough phonon-Majorana coupling $\lambda(T) \gg \kappa/L_y$.

3.2.2 General conditions for quantization

To understand how the quantization of the effective thermal Hall conductivity can break down and determine the range of its applicability, we now extend the solution of our hydrodynamic equations to a finite system with $L_x \gtrsim L_y$, where we must take into account all boundary conditions, i.e., include the right and left boundary conditions on top of those in Eq. (3.5). Again assuming that the leads are coupled to the phonons only, those are:

$$\begin{cases} T_{ph}(\pm x_0, y) = T_{r,l}, \\ j_{ex}(\pm x_0, y) = \lambda(T)(T_{ph} - T_f) = \mp\kappa_{xy}^{\rm q}\partial_y T_f. \end{cases} \tag{3.9}$$

Considering a small enough phonon-Majorana coupling λ, we aim to obtain a perturbative solution of the hydrodynamic equations. To this end, we write

$$T_{ph,f}(x,y) = T + \tilde{T}_{ph,f}(x,y), \tag{3.10}$$

with $\tilde{T}_{ph,f}(x,y) \ll T$. We express the temperature variations in series expansions as $\tilde{T}_{ph,f} = \sum_{n=0}^{\infty} \tilde{T}_{ph,f}^{(n)}$ and assume that terms of increasing order n are progressively less important. Note also that $\tilde{T}_{ph,f}(x,y) = -\tilde{T}_{ph,f}(-x,-y)$ generally follows from the symmetries of the hydrodynamic equations. Starting from the $\lambda = 0$ solution, $\tilde{T}_{ph}^{(0)}(x,y) = \frac{\overline{dT}}{dx} x$ and $\tilde{T}_{f}^{(0)}(x,y) = 0$, the temperature variations can then be found by an iterative procedure. At each iteration step $n > 0$, we first solve the ordinary differential equations [see Eqs. (3.5) and (3.9)]

$$\begin{aligned} \kappa_{xy}^{\mathrm{q}} \partial_x \tilde{T}_f^{(n)} &= \pm\lambda \left[\tilde{T}_{ph}^{(n-1)} - \tilde{T}_f^{(n)} \right] \qquad \text{for } y = \pm y_0, \\ \kappa_{xy}^{\mathrm{q}} \partial_y \tilde{T}_f^{(n)} &= \mp\lambda \left[\tilde{T}_{ph}^{(n-1)} - \tilde{T}_f^{(n)} \right] \qquad \text{for } x = \pm x_0, \end{aligned} \tag{3.11}$$

for the Majorana temperature $\tilde{T}_f^{(n)}$ along the edge. Then, using this solution, we obtain an appropriate Laplace equation $\nabla^2 \tilde{T}_{ph}^{(n)} = 0$ for the phonon temperature $\tilde{T}_{ph}^{(n)}$ in the bulk, along with Dirichlet boundary conditions $\tilde{T}_{ph}^{(n)}(\pm x_0, y) = 0$ at the left and right edges, and Neumann boundary conditions

$$\partial_y \tilde{T}_{ph}^{(n)} = \pm \frac{\lambda}{\kappa} \left[\tilde{T}_f^{(n)} - \tilde{T}_{ph}^{(n-1)} \right] \qquad \text{for } y = \pm y_0, \tag{3.12}$$

at the top and bottom edges. It is well known that such a Laplace equation with mixed Dirichlet and Neumann boundary conditions has a unique solution that can be obtained by standard methods. Our perturbative solution is convergent whenever $\lambda \ll \kappa / L_y$ (see [141] for the error analysis).

Assuming this condition, we perform the first iteration step (see [141]) to calculate the phonon temperature $\tilde{T}_{ph}^{(1)}$ and obtain the effective thermal Hall conductivity in terms of the transverse temperature difference $(\Delta T)_H^{\mathrm{ph}}(x)$ [see Fig. 3.2(a)]:

$$\kappa_{xy}^{\mathrm{ph,expt}}(x) = -\frac{\kappa}{\frac{\overline{dT}}{dx} L_y} \left[\tilde{T}_{ph}^{(1)}(x, y_0) - \tilde{T}_{ph}^{(1)}(x, -y_0) \right]. \tag{3.13}$$

Note that $\kappa_{xy}^{\mathrm{ph,expt}}(x)$ generally depends on the position x at which the temperatures are measured [see Fig. 3.2(b)]. Indeed, we find that $\kappa_{xy}^{\mathrm{ph,expt}}(x)$ only takes a quantized (or even constant) value if $L_x \gg L_y$ and $L_x \gg \ell \equiv \kappa_{xy}^{\mathrm{q}} / \lambda$. First, an accurate measurement of the thermal Hall conductivity generally requires an elongated system with $L_x \gg L_y$. Second, the system size L_x must be larger than the characteristic length ℓ associated with the thermalization of the Majorana edge mode (see Table 3.1 for a summary). Indeed, even for $L_x \gg L_y$, there are two regimes for the effective

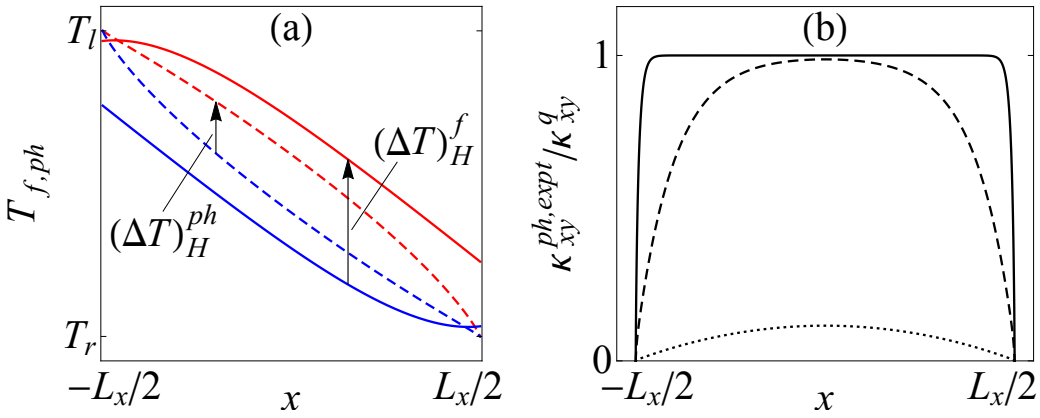

Figure 3.2: (From [49]) (a) Temperature profiles of the Majorana fermions (solid lines) and phonons (dashed lines) at the top (red lines) and bottom (blue lines) edges, $T_{f,ph}(x, \pm y_0)$. The measured "Hall" temperature differences $(\Delta T)_H^{ph,f}(x) \equiv T_{ph,f}(x, y_0) - T_{ph,f}(x, -y_0)$ are shown with the black arrows. (b) Measured thermal Hall conductivity $\kappa_{xy}^{\rm ph,expt}$ [Eq. (3.13)] as a function of the longitudinal position x at which $(\Delta T)_H^{ph}$ is measured for dimensionless thermal couplings $\lambda L_x/\kappa_{xy}^{\rm q} = 100$ (solid line), 10 (dashed line), and 1 (dotted line) at fixed $L_x/L_y = 100$.

thermal Hall conductivity (see [141]):

$$\kappa_{xy}^{\rm ph,expt}(x) \approx \begin{cases} \frac{\pi T}{12} & (L_x \gg \ell), \\ \frac{\pi T(L_x^2 - 4x^2)}{96\ell^2} & (L_x \ll \ell). \end{cases} \tag{3.14}$$

In the second regime we find that $\kappa_{xy}^{\rm ph,expt}(x)$ has a strong dependence on x and is smaller than $\kappa_{xy}^{\rm q} = (\pi/12)T$ by a factor $\sim (L_x/\ell)^2 \ll 1$.

3.3 Estimation of the spin-lattice thermal coupling

The phenomenological spin-lattice coupling $\lambda(T)$ defined in Eq. (3.3) can be obtained microscopically from, e.g., the Boltzmann equation. We calculate the rate of energy exchange per unit length $j_{ex} = \frac{1}{L}\left(\frac{\partial \mathcal{E}}{\partial t}\right)_{ph\to f}$ due to the scattering at the edge. Comparing to the form in Eq. (3.3), we extract $\lambda(T) = \lambda_0 T^\alpha$, i.e., the exponent α and the coefficient λ_0.

We consider a coupling at the top edge $y = y_0 = L_y/2$ of the form

$$H_{int} = \frac{-igv_f}{4} \int \mathrm{d}x\, \zeta(x) K_{ij} \partial_i u_j(x, y_0) \eta(x) \partial_x \eta(x), \tag{3.15}$$

where $\eta(x)$, $\vec{u}(x, y), \zeta(x)$ are the Majorana edge mode, the lattice displacement field,

and disorder potential, respectively, g parametrizes the spin-lattice coupling, and v_f is the fermion velocity. $K_{ij}\partial_i u_j$ with $i,j = x,y$ is some linear combination of the elastic tensor for u. Physically, Eq. (3.15) may be understood from the observation that the lattice displacement modifies the velocity of the Majorana edge mode by affecting the strength of the Kitaev coupling.

Using Eq. (3.15) and calculating the energy transfer rate using a Boltzmann equation, we obtain a large power $\alpha = 6$. The reason for the large exponent is twofold. First, the dispersions of both bulk phonons and edge Majoranas are linear which reduces the low energy phase space. Second, the vertex necessarily involves two gradients: one because $\eta(x)\eta(x) = \delta(0)$ is a c-number for Majorana fermions, and another because the strain tensor includes a gradient. We note that, without disorder, two-phonon processes are necessary to satisfy kinematic constraints in the physical regime, where the velocity of the acoustic phonon v_{ph} is larger than v_f. In that case one obtains an even larger $\alpha = 8$.

To estimate the coefficient λ_0, we further assume that the averaged disorder potential satisfies $\langle \zeta(x)\zeta(x')\rangle_{dis} = \zeta^2\,\delta(x-x')$, and consider an isotropic acoustic phonon mode only. From the Boltzmann equation solution (see [141]), we obtain

$$\lambda = \frac{g^2\zeta^2}{32(2\pi)^3 v_{ph}^4 v_f^2 \rho_0} f\, T^6, \tag{3.16}$$

where ρ_0 is the mass density of the lattice. In the model we consider, $f = 4.2\times 10^4$. Unfortunately, at this time an accurate quantitative estimate of λ for α-$RuCl_3$ is not possible due to the lack of knowledge of microscopic details of g, v_f and ζ. However, crudely applying Eq. (3.16), we estimate the characteristic length $\ell = \kappa_{xy}^{\mathrm{q}}/\lambda$ to be several orders of magnitude larger than the lattice spacing at temperatures of a few Kelvins. Importantly, due to the large exponent α, we expect that upon lowering the temperature of the sample, ℓ grows rapidly and that the system enters the regime where $L_x \ll \ell$ in Eq. (3.14) and thus the quantization of the thermal Hall conductivity breaks down.

3.4 Summary and discussion

By carefully analyzing the interplay between the chiral Majorana edge mode of an Ising anyon phase and the energy currents carried by bulk phonons, we have demonstrated that the thermal Hall conductivity of such a non-Abelian topological phase can be effectively quantized in the presence of a much larger longitudinal thermal

conductivity. This is in accordance with recent experiments on α-$RuCl_3$ [51]. However, this quantization only survives under certain conditions. The main results are summarized in Table 3.1.

Coupling regime	Weak	Intermediate	Strong
$\lambda \sim T^\alpha$	$\lambda \lesssim \lambda_f$	$\lambda_f \ll \lambda \ll \lambda_{ph}$	$\lambda_{ph} \ll \lambda$
L_x	$L_x \lesssim \ell$	$L_x \gg \ell$	
L_y	$L_y \ll \kappa/\lambda$		$L_y \gg \kappa/\lambda$
$\kappa_{xy}^{\mathrm{ph,expt}}$	$\kappa_{xy}^{\mathrm{ph,expt}} \ll \kappa_{xy}^{\mathrm{q}}$	κ_{xy}^{q}	κ_{xy}^{q}
$\kappa_{xy}^{\mathrm{f,expt}}$	–	$\kappa_{xy}^{\mathrm{f,expt}} \gg \kappa_{xy}^{\mathrm{q}}$	κ_{xy}^{q}

Table 3.1: (From [49]) Values of the effective thermal Hall conductivities extracted by measuring the temperatures of the phonon ($\kappa_{xy}^{\mathrm{ph,expt}}$) or Majorana ($\kappa_{xy}^{\mathrm{f,expt}}$) subsystems in three coupling regimes, defined by the value of λ relative to $\lambda_f = \kappa_{xy}^{\mathrm{q}}/L_x$ and $\lambda_{ph} = \kappa/L_y$. The three coupling regimes can also be identified by comparing the system dimensions L_x, L_y to the characteristic lengths $\ell = \kappa_{xy}^{\mathrm{q}}/\lambda$ and κ/λ. "–" in the last line means that the quantization $\kappa_{xy}^{\mathrm{f,expt}}$ relative to κ_{xy}^{q} is not generic ($\kappa_{xy}^{\mathrm{f,expt}} \gtrless \kappa_{xy}^{\mathrm{q}}$) in the weak coupling regime $\lambda \lesssim \lambda_f$, i.e., it depends on the strength of λ and the position x where the temperature is measured.

In words, those results are as follows. The quantization survives for a sufficiently strong spin-lattice coupling $\lambda \gg \lambda_f \equiv \kappa_{xy}^{\mathrm{q}}/L_x$, while it immediately disappears in the weak-coupling regime defined by $\lambda \lesssim \lambda_f$ [see Fig. 3.2(b)]. Importantly, since $\lambda \propto T^\alpha$ is strongly dependent on the temperature, with $\alpha \geq 6$ for the mechanisms considered in this work, we predict that the observed quantization of the thermal Hall conductivity should eventually break down as the temperature is lowered.

Even within the range of quantization ($\lambda \gg \lambda_f$), we can identify two separate regimes, depending on how λ compares to $\lambda_{ph} \equiv \kappa/L_y \gg \lambda_f$. In the strong-coupling regime, defined by $\lambda \gg \lambda_{ph}$, the spins and the lattice share the same temperature, and the quantization of the thermal Hall conductivity follows from effectively having a system with a diagonal conductivity $\kappa_{xx}^{\mathrm{expt}} = \kappa_{yy}^{\mathrm{expt}} = \kappa$ of the phonons and an off-diagonal $\kappa_{xy}^{\mathrm{expt}} = \kappa_{xy}^{q}$ of the Majoranas. Surprisingly, however, in the intermediate regime defined by $\lambda_f \ll \lambda \ll \lambda_{ph}$, the thermal Hall conductivity appears to be quantized *despite* a large temperature mismatch between the spins and the lattice. This is only true, however, if it is obtained by measuring the *lattice* temperatures along the edge. If one could directly measure the local temperature of the Majorana edge mode, it would appear to give a much larger thermal Hall conductivity.

Finally, we emphasize that our hydrodynamic equations are applicable far beyond the scope of the present work. Here, by solving them, we obtained a wide range of experimentally measurable quantities, such as detailed temperature profiles of various

degrees of freedom (e.g., spins and lattice) across the system. However, due to their phenomenological nature, the hydrodynamic equations we derived should readily extend to a rich variety of chiral topological phases and thus may find applications far away from the field of quantum spin liquids.

Chapter 4

Unconventional magnetism in the weak coupling theory

We consider a system of 2D fermions on a triangular lattice with well separated electron and hole pockets of similar sizes, centered at certain high-symmetry-points in the Brillouin zone. We first analyze Stoner-type spin-density-wave (SDW) magnetism. We show that SDW order is degenerate at the mean-field level. Beyond mean-field, the degeneracy is lifted and is either 120° "triangular" order (same as for localized spins), or a collinear order with antiferromagnetic spin arrangement on two-thirds of sites, and non-magnetic on the rest of sites. We also study a time-reversal symmetric directional spin bond order, which emerges when some interactions are repulsive and some are attractive. We show that this order is also degenerate at a mean-field level, but beyond mean-field the degeneracy is again lifted. We next consider the evolution of a magnetic order in a magnetic field starting from an SDW state in zero field. We show that a field gives rise to a canting of an SDW spin configuration. In addition, it necessarily triggers the directional bond order, which, we argue, is linearly coupled to the SDW order in a finite field. We derive the corresponding term in the Free energy. Finally, we consider the interplay between an SDW order and superconductivity and charge order. For this, we analyze the flow of the couplings within parquet renormalization group (pRG) scheme. We show that magnetism wins if all interactions are repulsive and there is little energy space for pRG to develop. However, if system parameters are such that pRG runs over a wide range of energies, the system may develop either superconductivity or an unconventional charge order, which breaks time-reversal symmetry.

4.1 Introduction

The nature of a magnetic order in itinerant electron systems and the interplay between magnetism, superconductivity, and charge order has attracted a substantial interest in the last decade [7–24], chiefly in the context of the analysis of cuprate and iron-based superconductors (FeSCs). Recently, studies of itinerant magnetism and its interplay with other orders have been extended to include itinerant systems on hexagonal lattices, like doped graphene [53,54,142–144] and transition metal dichalcogenides (TMDs) [56]. In localized spin system, a magnetic order on a hexagonal lattice (a triangular, honeycomb, or a Kagome lattice) is strongly influenced by geometrical frustration [3,5,145–147], and in certain cases a classical ground state magnetic configuration can be infinite degenerate, like in, e.g., an antiferromagnet on a Kagome lattice with nearest-neighbor Heisenberg interaction. However, such degeneracy is almost certainly lifted by interactions involving further neighbors [146,148].

In itinerant systems, relevant interactions are in general long-ranged in real space as they involve fermions near particular $k-$points in the Brillouin zone, where Fermi surfaces (FSs) are located. Yet, magnetism in itinerant systems also shows a strong frustration, this time because of competition between several symmetry-equivalent magnetic orderings between different FSs. This holds already in systems on non-frustrated lattices, e.g., in square lattice systems with a circular hole FS at $(0,0)$ and electron FSs at $(0,\pi)$ and $(\pi,0)$ (similar to parent compounds of Fe-pnictides). A dipole spin-density-wave (SDW) order parameter in such a system can be $\mathbf{M}_1$ with momenta $(\pi,0)$ or $\mathbf{M}_2$ with momentum $(0,\pi)$. At a mean-field level, the Free energy depends on $\mathbf{M}_1^2+\mathbf{M}_2^2$, i.e., the ground state is infinitely degenerate. The degeneracy is lifted either by changing the FS geometry, e.g., making the electron pockets non-circular, or by adding other interactions between fermions near hole and electron pockets [55,57,61,149], which do not contribute to SDW instability at the mean-field level, but distinguish between different ordered states from a degenerate manifold.

In this chapter we analyze the structure of an SDW order in a system of 2D itinerant fermions on a triangular lattice. We consider a band metal with a hole pocket at $\Gamma=(0,0)$ (c-band) and two electron pockets at $\pm\mathbf{K}$ (f-band), where $\mathbf{K}=(4\pi/3,0)$ (see Fig. 4.1a). We discuss the electronic structure and interactions in Sec. 4.2. In such a system an SDW order parameter can be either with momentum $\mathbf{K}$ or with $-\mathbf{K}$. The SDW order parameters with $\mathbf{K}$ and $-\mathbf{K}$ are $\mathbf{M}_{\pm K}=\frac{1}{2}(\mathbf{\Delta}_{\pm K}+\mathbf{\Delta}^*_{\mp K})$, where $\mathbf{\Delta}_K=\sum_{\boldsymbol{p}}\langle f^\dagger_{\mathbf{K}+\boldsymbol{p}}\vec{\sigma}c_{\boldsymbol{p}}\rangle$ and $\mathbf{\Delta}_{-K}=\sum_{\boldsymbol{p}}\langle f^\dagger_{-\mathbf{K}+\boldsymbol{p}}\vec{\sigma}c_{\boldsymbol{p}}\rangle$. The two underlying order parameters $\mathbf{\Delta}_K$ and $\mathbf{\Delta}_{-K}$ are coupled within a set self-consistent equations for a magnetic order,

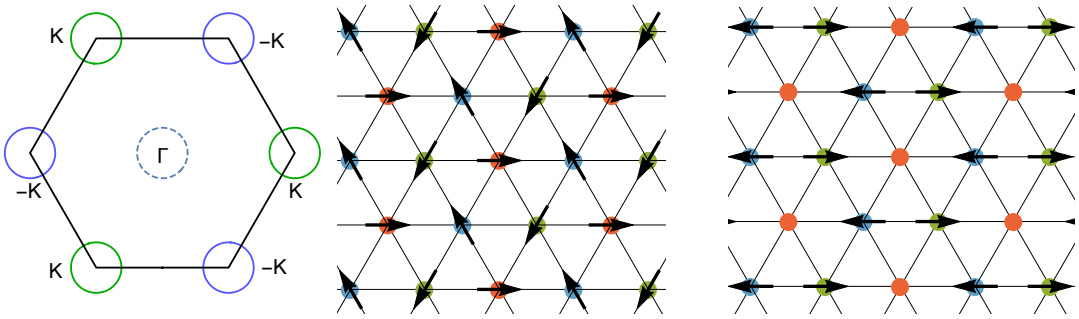

(a) (b) (c)

Figure 4.1: (From [59])(a) The Brillouin zone and the locations of the Fermi surfaces. There is one hole pocket, centered at Γ, (shown by the dashed line) and two electron pockets, centered at $\mathbf{K}$ (green solid line) and $-\mathbf{K}$ (blue solid line). (b), (c): Real space structure of on-site SDW order $\mathbf{M}_{\pm K} = \mathbf{M}_r \pm i\mathbf{M}_i$. At the mean-field level the ground state is infinitely degenerate for circular pockets (the ground state energy depends only on $\mathbf{M}_r^2 + \mathbf{M}_i^2$), but beyond mean-field and/or for non-circular (but C_3-symmetric) pockets, the degeneracy is lifted. Panels (b) and (c) – the two SDW configurations selected in the model – the 120° spiral order (the same as for localized spins) (b) and the collinear magnetic order with antiferromagnetic spin arrangement on two-thirds of sites, and no magnetization on the remaining one-third of the sites (a). The three colors indicate the three-sublattice structure of the SDW order.

and in zero magnetic field turn out to be complex conjugate to each other (Sec. 4.3). Then $\mathbf{M}_K = \mathbf{\Delta}_K$, $\mathbf{M}_{-K} = \mathbf{\Delta}_K^*$. However, because $\mathbf{K}$ and $-\mathbf{K}$ are in-equivalent points (a reciprocal lattice vector is $3\mathbf{K}$, not $2\mathbf{K}$ like in systems on a square lattice), $\mathbf{M}_K = \mathbf{\Delta}_K$ is a complex variable: $\mathbf{M}_K = \mathbf{M}_{-K}^* = \mathbf{M}_r + i\mathbf{M}_i$ (the magnetization at site $\mathbf{r}$ is $\mathbf{M}(\mathbf{r}) = \mathbf{M}_r \cos \mathbf{Kr} + \mathbf{M}_i \sin \mathbf{Kr}$). Keeping only the interactions in the SDW channel, we find in Sec. III that the ground state manifold is degenerate and the Free energy depends only on $\mathbf{M}_r^2 + \mathbf{M}_i^2$. A unique SDW order is selected by either interactions outside of SDW channel, or by the anisotropy of the pockets, or, potentially, by other perturbations. We show in Sec. 4.3 that these additional terms stabilize either a 120° spiral order with three-fold rotation symmetry ($\mathbf{M}_r \perp \mathbf{M}_i$, $|\mathbf{M}_r| = |\mathbf{M}_i|$), or a collinear SDW with non-equal magnitude of magnetization on different lattice sites ($\mathbf{M}_r \parallel \mathbf{M}_i$, or $\mathbf{M}_r = 0$, or $\mathbf{M}_i = 0$). In particular, when $|\mathbf{M}_r| = 0$, the SDW order is antiferromagnetic on two-third of sites and there is no magnetization on the remaining one-third of sites. We show SDW configurations in real space for these two types of order in Figs. 4.1b and Fig. 4.1c.

We also consider in Section 4.3 another type of magnetic order, with the order parameter $\mathbf{\Phi}_{\pm K} = \frac{1}{2}(\mathbf{\Delta}_{\pm K} - \mathbf{\Delta}_{\mp K}^*)$. At zero magnetic field, self-consistent equations for $\mathbf{\Phi}_{\pm K}$ and $\mathbf{M}_{\pm K}$ decouple. The one for $\mathbf{\Phi}_{\pm K}$ yields $\mathbf{\Delta}_{\pm K} = -\mathbf{\Delta}_{\mp K}^*$, i.e., $\mathbf{\Phi}_K = \mathbf{\Delta}_K$,

$\mathbf{\Phi}_{-K} = -\mathbf{\Delta}_K^*$. For repulsive interactions between low-energy fermions, the Free energy for $\mathbf{\Phi}$ order is higher than for $\mathbf{M}$ (SDW) order, i.e., the leading instability is SDW. However, $\mathbf{\Phi}$ order wins when some interactions are repulsive and some are attractive. Like for SDW, the $\mathbf{\Phi}$ order parameter is a complex vector, $\mathbf{\Phi}_K = \mathbf{\Phi}_r + i\mathbf{\Phi}_i$. At a mean-field level, the Free energy for the $\mathbf{\Phi}$ depends on $|\mathbf{\Phi}|^2$, i.e., the ground state manifold is degenerate. The degeneracy is lifted by other interactions, like for an SDW order, and the selected states are the analogs of 120° and collinear SDW states.

The order parameter $\mathbf{\Phi}_{\pm K}$ preserves the sign under time reversal and is similar to $iSDW$ order on a square lattice, discussed in the context of FeSCs [60, 150–152] (the direct analogy holds when $\mathbf{\Delta}_{\pm K}$ is purely imaginary and $\mathbf{\Phi}_{-K} = -\mathbf{\Phi}_K^*$). In real space, a non-zero $\mathbf{\Phi}_{\pm K}$ does not give rise to either site or bond real magnetic order, but it gives rise to a non-zero order parameter Φ, which is expressed via the imaginary part of the expectation value of a spin operator on a bond between $\mathbf{r} + \boldsymbol{\delta}/2$ and $\mathbf{r} - \boldsymbol{\delta}/2$:

$$\Phi^{\alpha}_{\mathbf{r},\boldsymbol{\delta}} = \frac{i}{\hbar}\hat{\boldsymbol{\delta}}\langle f^{\dagger}_{\mathbf{r}+\boldsymbol{\delta}/2}\sigma^{\alpha}c_{\mathbf{r}-\boldsymbol{\delta}/2} + c^{\dagger}_{\mathbf{r}+\boldsymbol{\delta}/2}\sigma^{\alpha}f_{\mathbf{r}-\boldsymbol{\delta}/2} - h.c.\rangle \tag{4.1}$$

We label the order with a non-zero Φ as "imaginary" spin bond (ISB) order. We show that one can associate $\Phi^{\alpha}_{\mathbf{r},\boldsymbol{\delta}}$ with a vector directed either along or opposite to $\boldsymbol{\delta}$, depending on the sign of $\Phi^{\alpha}_{\mathbf{r},\boldsymbol{\delta}}$. In Fig. 4.2 we display graphically ISB order parameter in real space for two Φ states – one is the analog of the 120° SDW order [$\mathbf{\Phi}_r \perp \mathbf{\Phi}_i$, $|\mathbf{\Phi}_r| = |\mathbf{\Phi}_i|$, panels (a) and (b) in Fig. 4.2]; the other is the analog of a partial collinear SDW order [the case $\mathbf{\Phi}_i = 0$, panels (c) and (d) in Fig. 4.2]. In a multi-band system an ISB order may give rise to circulating spin current [60] $J^{\alpha}_{\mathbf{r},\boldsymbol{\delta}} \sim \sum_{(a,b)} t^{(a,b)}_{\mathbf{r},\boldsymbol{\delta}}\Phi^{\alpha(a,b)}_{\mathbf{r},\boldsymbol{\delta}}$, if the hopping $t^{(a,b)}_{\mathbf{r},\boldsymbol{\delta}}$ has a proper form (a, b label orbitals of f- and c-fermions in Eq. 4.1). This does not hold in our model, where a potential multi-orbital composition of low-energy states are neglected. We show a potential circulating spin-current order in Fig. 4.3.

We next return to SDW order and analyze in Sec. 4.4 its evolution in a small magnetic field. We show that the 120° spiral order becomes cone-like, i.e. the order in the plane transverse to the field remains 120° spiral, and the order in the direction of the field is ferromagnetic, due to an imbalance of spin up and down electrons. In this respect, the field evolution of the 120° order in an itinerant system is different from the one in the Heisenberg model with nearest neighbor exchange, where spins remain in the same plane during the field evolution and pass through an intermediate up-up-down phase [38, 41, 112, 153]. We next argue that in a field, spin-polarization operators for spin components along and transverse to the field become different,

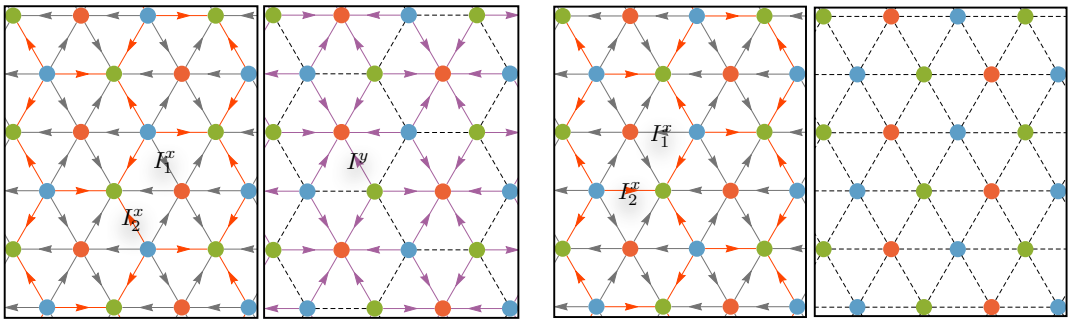

Figure 4.2: (From [59]) Real space structure of imaginary spin bond order $\mathbf{\Phi}_{\pm K} = \mathbf{\Phi}_r \pm i\mathbf{\Phi}_i$ (labeled as ISB order in the text). The order on the bonds between nearest neighbors is shown. At the mean-field level the ground state is infinitely degenerate for circular pockets (the ground state energy depends only on $\mathbf{\Phi}_r^2 + \mathbf{\Phi}_i^2$, but beyond mean-field and/or for non-circular (but C_3-symmetric) pockets, the degeneracy is lifted. In panels (**a**) - (**d**) we show two selected ISB configurations. Panels (**a**) and (**b**) show ISB order, analogous to the 120° spiral SDW order from Fig. 4.1b. This order corresponds to $\mathbf{\Phi}_r \perp \mathbf{\Phi}_i$, $|\mathbf{\Phi}_r| = |\mathbf{\Phi}_i|$ ($\varphi_x = 0, \varphi_y = \pi/2$ in Eq. 4.22. In units of $I_0 \sim \frac{h\Delta}{\hbar\mu}$, the magnitude of the ISB order is $I_1^x = \frac{\sqrt{3}}{4} I_0$ on a grey arrow and $I_2^x = \frac{\sqrt{3}}{2} I_0$ on an orange arrow in panel (**a**), and $I^y = \frac{3}{4} I_0$ on a purple arrow in (**a**). Panels (**c**) and (**d**) show ISB order analogous to the partial collinear SDW order from Fig. 4.1c. This ISB order configuration corresponds to $\mathbf{\Phi}_i = 0$. A dashed lines denote bonds with zero magnitude of ISB order. Notice that $\Phi^x_{\mathbf{r},\boldsymbol{\delta}}$ in (**c**) has the same pattern as in (**a**), but $\Phi^y_{\mathbf{r},\boldsymbol{\delta}}$ in (**b**) and (**d**) are very different.

and the bubbles made out of spin-up $c-$fermion and spin-down $f-$fermion and out of spin-down $c-$fermion and spin-up $f-$fermion also become different. The first discrepancy keeps $\mathbf{\Delta}_{\pm K}$ in the plane perpendicular to a field, the second breaks the equivalence between $\mathbf{\Delta}_K$ and $\mathbf{\Delta}^*_{-K}$. As the consequence, SDW and ISB orders get linearly coupled. We explicitly derive the bilinear coupling term $F_{cross}(\mathbf{M}, \mathbf{\Phi})$ in the Free energy. We found that a Zeeman field, which is odd under time reversal, serves as a glue that couples $\mathbf{M}$ and $\mathbf{\Phi}$, which are odd and even under time-reversal, respectively. Because of the linear coupling of $\mathbf{M}$ and $\mathbf{\Phi}$, *an itinerant system in a field necessarily possesses both SDW and ISB orders*, even if only SDW order was present in zero field (and vice versa).

Finally, in Sec. 4.5 we return to zero field and consider a model with purely repulsive interactions, when the magnetic order is SDW. We use parquet renormalization group (pRG) approach and analyze the competition between SDW magnetism and other orders bilinear in fermions, such as superconductivity and conventional and unconventional charge density-wave orders. Magnetism is an expected winner in an

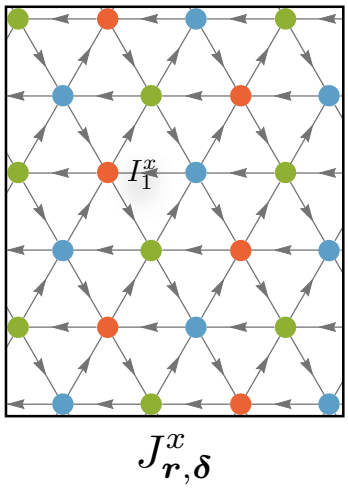

Figure 4.3: (From [59]) A potential circular spin current configuration generated from the ISB order for a proper symmetry of hopping integrals. Such behavior may hold in a multi-orbital 3 pocket model. The figure is obtained by changing the direction of all red bonds directed towards green sites of panel Fig. 4.2 (**a**) and by changing by half the magnitude of ISB order on these bonds.

itinerant system, if the corresponding instability temperature is high enough, because at relatively high energies the only attractive 4-fermion interaction is in the SDW channel. However, if an instability develops at a smaller energy/temperature, other channels compete with SDW because in the process of the flow from higher to lower energies, partial components of the interaction in some superconducting and charge-density-wave channels change sign and become attractive. As the consequence, the system may develop superconductivity or charge order instead of SDW magnetism. We show that this actually happens, at least in some range of input parameters, and the system develops either $s^{\pm}$-wave superconductivity, or an unconventional charge-order, which breaks time-reversal symmetry.

We present the summary of our results in Sec. 4.6.

4.2 Electronic structure and interactions

We consider a system of 2D itinerant fermions on a triangular lattice, with hole and electron FSs. The hole FS is centered at $\Gamma = (0, 0)$, and the two in-equivalent electron pockets are centered at $\pm\mathbf{K}$ (f-band), where $\mathbf{K} = (4\pi/3, 0)$. We show the Brillouin zone and the FSs in Fig. 4.1a. We label fermionic operators with momenta near Γ as $c_{\boldsymbol{p}}$ and the ones near $\pm\mathbf{K}$ as $f_{\pm\mathbf{K}+\boldsymbol{p}}$. The electronic dispersion is this three-pocket ($3p$) model can be approximated as $\epsilon_{\Gamma,\boldsymbol{k}} = -\frac{k^2}{2m_h} + \mu_h$ and $\epsilon_{\pm\mathbf{K}+\boldsymbol{k}} = \frac{k^2}{2m_e} - \mu_e$. The

quadratic Hamiltonian in zero field can be expressed via a 6-component electronic spinor $\Psi_{\boldsymbol{k}} = \{c_{\boldsymbol{k},\sigma}, f_{\mathbf{K}+\boldsymbol{k},\sigma}, f_{-\mathbf{K}+\boldsymbol{k},\sigma}\}^T$ as

$$\begin{aligned} \mathcal{H}_0 &= \Psi^\dagger_{\boldsymbol{k}} H_0 \Psi_{\boldsymbol{k}}, \\ H_0 &= \begin{pmatrix} \epsilon_{\Gamma,\boldsymbol{k}}\mathbb{I} & 0 & 0 \\ 0 & \epsilon_{\mathbf{K}+\boldsymbol{k}}\mathbb{I} & 0 \\ 0 & 0 & \epsilon_{-\mathbf{K}+\boldsymbol{k}}\mathbb{I} \end{pmatrix}. \end{aligned} \tag{4.2}$$

where each time $\boldsymbol{k}$ is shifted from the center of a FS and $\mathbb{I}$ is the 2×2 identity matrix in spin space.

There are 8 different four-fermion interactions between low-energy fermionic states near hole and electron pockets. We show the fermion propagators and four-fermion interactions graphically in Figs. 4.4 and 4.4. These 8 terms include inter-pocket and exchange interactions between fermions near a hole pocket and an electron pocket (g_1 and g_2 terms, respectively), a pair hopping from a hole pocket into electron pockets at $\mathbf{K}$ and $-\mathbf{K}$ (g_3 term), intra-pocket interactions between fermions near a hole pocket and one of electron pockets (g_4 and g_5 terms, respectively), inter-pocket density-density and exchange interactions between fermions near the two electron pockets (g_6 and g_7 terms, respectively), and umklapp interaction in which incoming fermions are near a hole pocket and one of electron pockets and outgoing fermions are near the other electron pocket. This last interaction is allowed because $3\mathbf{K}$ is a reciprocal lattice vector. We do not consider in this work potential multi-orbital composition of the excitations around hole and electron pockets, like in Fe-based superconductors. Accordingly, we treat g_i as some constants, independent on the angles along the FSs. For most of the paper we assume that all $g_i > 0$, i.e, all interactions are repulsive.

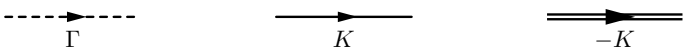

Figure 4.4: Fermion propagators.

4.3 Magnetic order and its selection by electronic correlations

At low enough temperature interactions may give rise to an instability of the normal state towards some form of electronic order. Like we said, the most natural candi-

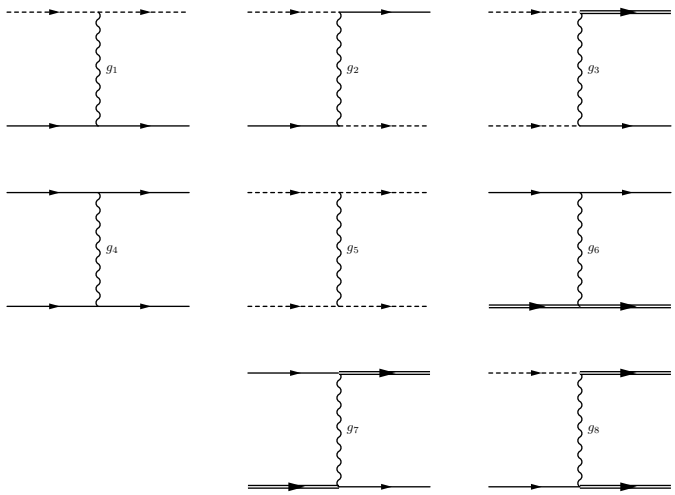

Figure 4.5: Four-fermion interactions.

date for the ordered state is SDW magnetism, because a magnetic order develops when electron-electron interaction is repulsive, while other instabilities, like superconductivity and charge order, require an attraction in some partial channel. This is particularly true if the instability develops at a relatively high energy, before interactions get modified in the RG flow. In this section we assume that itinerant SDW magnetism is the leading instability and study the structure of SDW order in zero magnetic field. We also consider the case when g_3 interaction is attractive, in which case the leading magnetic instability is towards ISB order.

4.3.1 The development of a magnetic order

We introduce two complex spin operators, bilinear in fermions, with transferred momentum near $\mathbf{K}$ and $-\mathbf{K}$:

$$\hat{\mathbf{\Delta}}_{\mathbf{K}+\boldsymbol{q}} = \sum_{\boldsymbol{p}} f^{\dagger}_{\mathbf{K}+\boldsymbol{p}+\boldsymbol{q}} \vec{\sigma} c_{\boldsymbol{p}}, \quad \hat{\mathbf{\Delta}}_{-\mathbf{K}+\boldsymbol{q}} = \sum_{\boldsymbol{p}} f^{\dagger}_{-\mathbf{K}+\boldsymbol{p}+\boldsymbol{q}} \vec{\sigma} c_{\boldsymbol{p}}. \tag{4.3}$$

Each order parameter is constructed out of a fermion near a hole pocket and near an electron pocket. The SDW order parameters with momenta $\pm\mathbf{K}$ are

$$\mathbf{M}_{\pm K} = \left\langle \frac{1}{2} \sum_{\mathbf{p},\alpha,\beta} \left(f^{\dagger}_{\pm\mathbf{K}+\mathbf{p},\alpha} \vec{\sigma}_{\alpha\beta} c_{\mathbf{p},\beta} + c^{\dagger}_{\mathbf{p}\alpha} \vec{\sigma}_{\alpha\beta} f_{\mp\mathbf{K}+\mathbf{p},\beta} \right) \right\rangle = \frac{1}{2} \left(\mathbf{\Delta}_{\pm K} + \mathbf{\Delta}^{*}_{\mp K} \right) \tag{4.4}$$

where $\mathbf{\Delta}_{\pm K} = \langle \hat{\mathbf{\Delta}}_{\pm K} \rangle$. In real space, $\mathbf{M}(\mathbf{r}) = \mathbf{M}_K e^{i\mathbf{Kr}} + \mathbf{M}_{-K} e^{-i\mathbf{Kr}}$. The ISB order parameters are

$$\mathbf{\Phi}_{\pm K} = \left\langle \frac{1}{2} \sum_{\mathbf{p},\alpha,\beta} \left(f^\dagger_{\pm\mathbf{K}+\mathbf{p},\alpha} \vec{\sigma}_{\alpha\beta} c_{\mathbf{p},\beta} - c^\dagger_{\mathbf{p}\alpha} \vec{\sigma}_{\alpha\beta} f_{\mp\mathbf{K}+\mathbf{p},\beta} \right) \right\rangle = \frac{1}{2} \left(\mathbf{\Delta}_{\pm K} - \mathbf{\Delta}^*_{\mp K} \right) \tag{4.5}$$

Out of eight interactions, the two, g_1 and g_3, can be re-expressed as the interactions between $\hat{\Delta}$s as

$$\begin{aligned} \mathcal{H}_4 = & \sum_{p,p',q,\sigma,\sigma'} g_3 \big(c^\dagger_{p+q,\sigma} c^\dagger_{p'-q,\sigma'} f_{K+p',\sigma'} f_{-K+p,\sigma} + h.c. \big) + \\ & g_1 \big(c^\dagger_{p+q,\sigma} f^\dagger_{K+p'-q,\sigma'} f_{K+p',\sigma'} c_{p,\sigma} + (K \to -K) \big) \\ = & -\frac{g_3}{2} \big(\hat{\mathbf{\Delta}}_{K-q} \hat{\mathbf{\Delta}}_{-K+q} + h.c. \big) \big) - \frac{g_1}{2} \big(\hat{\mathbf{\Delta}}^\dagger_{-K-q} \hat{\mathbf{\Delta}}_{K+q} + (K \to -K) \big) + ..., \end{aligned} \tag{4.6}$$

The self-consistent equations on infinitesimal $\mathbf{\Delta}_K$ and $\mathbf{\Delta}_{-K}$ are obtained by summing up series of ladder diagrams within the leading logarithmical approximation as shown in Fig. 4.6.

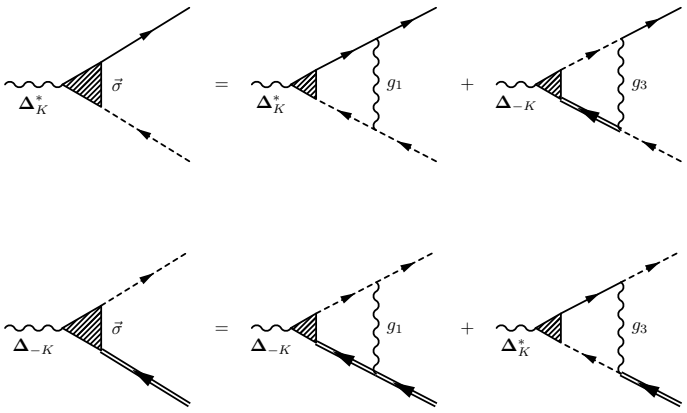

Figure 4.6: Linearized self-consistent equation for SDW order.

At zero magnetic field the equations for all three spin components of $\mathbf{\Delta}_{\pm K}$ are the same, and we have

$$\begin{aligned} \mathbf{\Delta}^*_K &= -(g_1 \Pi_{(+K)} \mathbf{\Delta}^*_K + g_3 \Pi_{(-K)} \mathbf{\Delta}_{-K}), \\ \mathbf{\Delta}_{-K} &= -(g_3 \Pi_{(+K)} \mathbf{\Delta}^*_K + g_1 \Pi_{(-K)} \mathbf{\Delta}_{-K}), \end{aligned} \tag{4.7}$$

where $\Pi_{(\pm K)} = T \sum_{\omega_n} \int \frac{\mathrm{d}^2 k}{\mathcal{A}_{B.Z.}} \mathcal{G}^f(\boldsymbol{k} \pm \mathbf{K}) \mathcal{G}^c(\boldsymbol{k})$, and $\mathcal{A}_{B.Z.}$ is the area of the Brillouin zone. Because the dispersions near $\mathbf{K}$ and $-\mathbf{K}$ are identical, $\Pi_{(+K)} = \Pi_{(-K)} = \Pi$.

Eq. 4.7 then decouples into

$$\begin{aligned}\boldsymbol{\Delta}_K^* + \boldsymbol{\Delta}_{-K} &= -(g_1+g_3)\Pi\,(\boldsymbol{\Delta}_K^* + \boldsymbol{\Delta}_{-K})\,,\\ \boldsymbol{\Delta}_K^* - \boldsymbol{\Delta}_{-K} &= -(g_1-g_3)\Pi\,(\boldsymbol{\Delta}_K^* - \boldsymbol{\Delta}_{-K})\end{aligned} \tag{4.8}$$

or

$$\begin{aligned}\mathbf{M}_{\pm K} &= -(g_1+g_3)\Pi\,\mathbf{M}_{\pm K},\\ \boldsymbol{\Phi}_{\pm K} &= -(g_1-g_3)\Pi\,\boldsymbol{\Phi}_{\pm K},\end{aligned} \tag{4.9}$$

We see that $\mathbf{M}$ and $\boldsymbol{\Phi}$ channels are decoupled.

One can easily verify that (i) $\Pi < 0$ and (ii) its magnitude grows logarithmically with decreasing T due to opposite signs of dispersions near Γ and near $\pm\mathbf{K}$, even if the masses and chemical potentials of the two dispersions are different (i.e., even if there is no true nesting). The mass difference only affects the prefactor for the logarithm. This, however, only holds when the running energy E is larger than the difference between μ_h and μ_e. When the two become comparable, the logarithm is cut. For example, we found numerically that the logarithmic enhancement holds down to $T \sim |\mu_h - \mu_e|/5$ The combination of (i) and (ii) implies that the magnetic instability develops already for small values of g_1, g_3, but still the interaction should be above the threshold.

4.3.2 The SDW order

When both g_1 and g_3 are positive, the leading instability occurs when $(g_1+g_3)|\Pi| = 1$, and the emerging order is SDW with $\boldsymbol{\Delta}_K = \boldsymbol{\Delta}_{-K}^*$, i.e., $\mathbf{M}_K = \boldsymbol{\Delta}_K = \mathbf{M}_{-K}^*$. We verified that the condition $\boldsymbol{\Delta}_K = \boldsymbol{\Delta}_{-K}^*$ holds also for the solution of the full non-linear self-consistent equation at a finite SDW order parameter.

Keeping $\mathbf{M}_K = \mathbf{M}_{-K}^*$ and adding to the quadratic Hamiltonian the SDW terms $\bar{\mathbf{M}}_{\pm K} = \frac{g_{sdw}}{2}\mathbf{M}_{\pm K}$, where $g_{sdw} = g_1 + g_3$, we found that H_0 modifies to

$$\begin{aligned}\mathcal{H}_{\mathbf{M}} &= \Psi_{\boldsymbol{k}}^\dagger H_{\mathbf{M}} \Psi_{\boldsymbol{k}}\\ H_{\mathbf{M}} &= \begin{pmatrix} \epsilon_{\Gamma\boldsymbol{k}}\mathbb{I} & -\bar{\mathbf{M}}_K\cdot\vec{\sigma} & -\bar{\mathbf{M}}_{-K}\cdot\vec{\sigma}\\ -\bar{\mathbf{M}}_K^*\cdot\vec{\sigma} & \epsilon_{\mathbf{K}+\boldsymbol{k}}\mathbb{I} & 0\\ -\bar{\mathbf{M}}_{-K}^*\cdot\vec{\sigma} & 0 & \epsilon_{-\mathbf{K}+\boldsymbol{k}}\mathbb{I}\end{pmatrix},\end{aligned} \tag{4.10}$$

Eq. 4.10 can be also obtained via Hubbard-Stratonovich transformation using the

interaction terms projected to the SDW channel. We show the derivation in Appendix B. We emphasize that each component of $\bar{\mathbf{M}}_K$ is a complex variable because in our case $\mathbf{K}$ and $-\mathbf{K}$ are not separated by a reciprocal lattice vector. In this respect, SDW on a hexagonal lattice differs from commensurate SDW with $\bar{\mathbf{M}}_Q$ on a square lattice as for the latter $\bar{\mathbf{M}}_Q$ is real because Q and -Q differ by a reciprocal lattice vector. For convenience, we separate $\bar{\mathbf{M}}_K$ and $\bar{\mathbf{M}}_{-K}$ into $\bar{\mathbf{M}}_K = \bar{\mathbf{M}}_r + i\bar{\mathbf{M}}_i$ and $\bar{\mathbf{M}}_{-K} = \bar{\mathbf{M}}_r - i\bar{\mathbf{M}}_i$.

The quadratic Hamiltonian $\mathcal{H}_{\mathbf{M}}$ can be diagonalized by two subsequent Bogolyubov transformations (see Appendix B for details). The result is

$$\mathcal{H}_{\mathbf{M}} = \sum_{\boldsymbol{k},\alpha} E^{+}_{\boldsymbol{k}} e^{\dagger}_{\boldsymbol{k},\alpha} e_{\boldsymbol{k},\alpha} + E^{-}_{\boldsymbol{k}} p^{\dagger}_{\boldsymbol{k},\alpha} p_{\boldsymbol{k},\alpha} + \epsilon_{K+\boldsymbol{k}} \bar{f}^{\dagger}_{\boldsymbol{k},\alpha} \bar{f}_{\boldsymbol{k},\alpha}) \tag{4.11}$$

where

$$E^{\pm}_{\boldsymbol{k}} = \frac{\epsilon_{\Gamma,\boldsymbol{k}} + \epsilon_{\mathbf{K}+\boldsymbol{k}}}{2} \pm \sqrt{\left(\frac{\epsilon_{\Gamma,\boldsymbol{k}} - \epsilon_{\mathbf{K}+\boldsymbol{k}}}{2}\right)^2 + 2\bar{M}^2}, \tag{4.12}$$

and $\bar{M} = \sqrt{|\bar{\mathbf{M}}_r|^2 + |\bar{\mathbf{M}}_i|^2}$. The operator $\bar{f}$ is the linear combination of f operators with momenta near $\mathbf{K}$ and $-\mathbf{K}$, which does not get coupled to c-operators in the presence of SDW order. Because of the last term in Eq. 4.11 the system remains a metal in the SDW phase, even in case of perfect nesting $\epsilon_{\Gamma,\boldsymbol{k}} = -\epsilon_{\mathbf{K}+\boldsymbol{k}}$, when excitations described by $E^{\pm}_{\boldsymbol{k}}$ are all gapped.

The self-consistent equation for the order parameter $\bar{M}$ reduces to

$$1 = \frac{g_{sdw}}{2N} \sum_{\boldsymbol{k}} \frac{1}{\sqrt{\left(\frac{\epsilon_{\Gamma,\boldsymbol{k}} - \epsilon_{\mathbf{K}+\boldsymbol{k}}}{2}\right)^2 + 2\bar{M}^2}} \tag{4.13}$$

As the dispersion depends on $\bar{M}$, but not separately on $\bar{\mathbf{M}}_r$ and $\bar{\mathbf{M}}_i$, the SDW ground state is degenerate for all configurations in the manifold of $|\bar{\mathbf{M}}_r|^2 + |\bar{\mathbf{M}}_i|^2 = \bar{M}^2$.

The Landau Free energy in terms of $\bar{M}$ is

$$F = a(\bar{\mathbf{M}}_r^2 + \bar{\mathbf{M}}_i^2) + b(\bar{\mathbf{M}}_r^2 + \bar{\mathbf{M}}_i^2)^2 + ... \tag{4.14}$$

Without loss of generality we can choose $\mathbf{M}_r$ and $\mathbf{M}_i$ to be in the $x-y$ plane and set $\mathbf{M}_r$ to be along x direction. We then have $\mathbf{M}_r = M_r \hat{e}_x = M\cos\tau \hat{e}_x$, $\mathbf{M}_i = M_{ix}\hat{e}_x + M_{iy}\hat{e}_y = M\sin\tau\cos\theta\hat{e}_x + M\sin\tau\sin\theta\hat{e}_y$. The SDW order parameter $\mathbf{M}(\mathbf{r})$

in real space is related to $\mathbf{M}_r, \mathbf{M}_i$ as (see Appendix B for derivation)

$$\begin{aligned} M^x(\mathbf{r}) &= 2(M_r \cos \mathbf{Kr} + M_{ix} \sin \mathbf{Kr}) \\ &= 2(M \cos\tau \cos \mathbf{Kr} + M \sin\tau \cos\theta \sin \mathbf{Kr}) \\ M^y(\mathbf{r}) &= 2M_{iy} \sin \mathbf{Kr} = 2M \sin\tau \sin\theta \sin \mathbf{Kr} \end{aligned} \tag{4.15}$$

For example, when $\theta = \pi/2$, $\tau = \pi/4$, i.e. $\mathbf{M}_r \perp \mathbf{M}_i$ and $|\mathbf{M}_r| = |\mathbf{M}_i|$, $M^x(\mathbf{r}) = \sqrt{2}\ M \cos \mathbf{Kr}$, $M^y(\mathbf{r}) = \sqrt{2}\ M \sin \mathbf{Kr}$, i.e. the SDW order configuration is 120° spiral (see Fig. 4.1b). When $\theta, \tau = \pi/2$, $M^x(\mathbf{r}) = 0$, $M^y(\mathbf{r}) = 2M \sin \mathbf{Kr}$, the SDW configuration is antiferromagnetic on two-thirds of sites, while the remaining one third of sites remains non-magnetic (see Fig. 4.1c). This kind of order is peculiar to itinerant systems. A similar partial order has been found in the studies of magnetism in in doped graphene [53, 54] and in doped FeSCs [55, 61].

The selection of the SDW order

Selection by the anisotropy of the spectrum – One way to lift the degeneracy is to include the anisotropy of the dispersion near the two electron pockets. The points **K** and -**K** are highly-symmetric points in the Brillouin zone, but still, the lattice symmetry only implies that the dispersion should remain invariant under the rotation by 120°. Then the most generic dispersion near $\pm\mathbf{K}$ is $\epsilon_{\pm\mathbf{K}+\boldsymbol{p}} = \frac{p^2}{2m_e} - \mu_2 \pm \delta \cos 3\theta_{\boldsymbol{p}}$, where $\theta_{\boldsymbol{p}}$ is the angle between $\mathbf{p}$ and $\mathbf{K}$. A conventional analysis, similar to the one in Ref. [154], shows that a non-zero δ gives rise to additional quartic term in Landau Free energy in the form $c(\mathbf{M}_r \times \mathbf{M}_i)^2$ with $c < 0$. The minimization of the Free energy then yields $\mathbf{M}_r \perp \mathbf{M}_i$ and $|\mathbf{M}_r| = |\mathbf{M}_i|$. This corresponds to the 120° SDW order.

Selection by the other couplings – Another way to lift the ground state degeneracy is to go beyond mean-field and include the corrections to the ground state energy from four-fermion couplings other than g_1 and g_3. These other couplings do not contribute to SDW order at the mean-field level, but affect the Free energy beyond mean-field. For simplicity of presentation, we analyze the effect of other couplings assuming that $\epsilon_{\Gamma,\boldsymbol{k}} = -\epsilon_{\pm\mathbf{K}+\boldsymbol{k}}$ (a perfect nesting).

In our case, there are two contributions from other interactions. First, the terms g_4, g_6, and g_7 have non-zero expectation values in the SDW state. This effect is similar to the one found in Fe-based systems [55, 57]. The contribution to the Free energy from an average value of these additional interactions is

$$\delta F_a = 2(g_6 - g_7 - 2g_4)\Big(\frac{\mathbf{M}_r \times \mathbf{M}_i}{M^2}\Big)^2 (N_F \bar{M})^2$$

$$= \frac{1}{2}(g_6 - g_7 - 2g_4)(N_F \bar{M})^2 \sin^2\theta \sin^2 2\tau, \tag{4.16}$$

where N_F is the density of states near the Fermi surface. The selection of SDW order depends on the relative strength of the couplings. When $g_6 - g_7 - 2g_4 < 0$, δF_a is minimized when $\theta = \pi/2 \pmod{\pi}$ and $\tau = \pi/4 \pmod{\pi/2}$, i.e. when $\mathbf{M}_r \perp \mathbf{M}_i$ and $|\mathbf{M}_r| = |\mathbf{M}_i|$. This gives 120° spiral SDW order. When $g_6 - g_7 - 2g_4 > 0$, $\theta = 0 \pmod{\pi}$ or $\tau = 0 \pmod{\pi/2}$. In the first case $\mathbf{M}_r \parallel \mathbf{M}_i$, in the second either $\mathbf{M}_r$ or $\mathbf{M}_i$ is equal to zero. In both cases, the SDW order is collinear and the ground state manifold remains infinitely degenerate because for $\mathbf{M}_r \parallel \mathbf{M}_i$, $\delta F_a = 0$, and the ratio $\mathbf{M}_i/\mathbf{M}_r$ is arbitrary ($\mathbf{M}_i = 0$ or $\mathbf{M}_r = 0$ are the two limits of the degenerate set).

The second effect comes from the g_8 term, which gives rise to SDW-mediated coupling between fermions near $\mathbf{K}$ and near $-\mathbf{K}$. Indeed, the g_8 term is

$$\begin{aligned} H_{g_8} =& g_8 \sum_{p_1,p_2,p_3,\sigma,\sigma'} \big(f^\dagger_{K+p_1,\sigma} f^\dagger_{K+p_2,\sigma'} f_{-K+p_3,\sigma'} c_{p_1+p_2-p_3\sigma} \\ &+ f^\dagger_{-K+p_1,\sigma} f^\dagger_{-K+p_2,\sigma'} f_{K+p_3,\sigma'} c_{p_1+p_2-p_3\sigma} + h.c. \big). \end{aligned} \tag{4.17}$$

In the SDW state, this term acquires a piece quadratic in fermions

$$H_{g_8} \to 2\gamma_8 \sum f^\dagger_{K,\sigma} (\bar{\mathbf{M}}_K \cdot \vec{\sigma})_{\sigma,\sigma'} f_{-K,\sigma'} + h.c., \tag{4.18}$$

where $\gamma_8 = g_8/g_{sdw}$. In the second order in perturbation, this term gives the correction to the Free energy, which also scales as $\bar{M}^2$:

$$\begin{aligned} \delta F_b =& -N_F(\gamma_8 \bar{M})^2 (3\cos^2\theta \sin^2 2\tau \big(\cos 2\tau + 1) \\ &+ \cos^2 2\tau (3 - \cos 2\tau) \big) \end{aligned} \tag{4.19}$$

The τ, θ that minimize δF_b are

$$\begin{aligned} \theta = -\pi,\ 0 \text{ and } \tau = \pm\pi/6,\ \ \pm 5\pi/6, \\ \text{or } \tau = \pm\pi/2 \ \text{ and } \theta \text{ arbitrary} \end{aligned} \tag{4.20}$$

One can verify that both choices for θ and τ describe a collinear spin configuration with antiferromagnetic spin ordering on two-thirds of sites, while the remaining one third of sites remain non-magnetic (see Fig. 4.1c), i.e. δF_b selects SDW configuration which corresponds to $\mathbf{M}_r = 0$. For example, when $\theta, \tau = \pi/2$, we obtain from Eq. 4.15 $M^x(\mathbf{r}) = 0$, $M^y(\mathbf{r}) = 2M \sin \mathbf{Kr}$. In other words, δF_b lifts the degeneracy of collinear

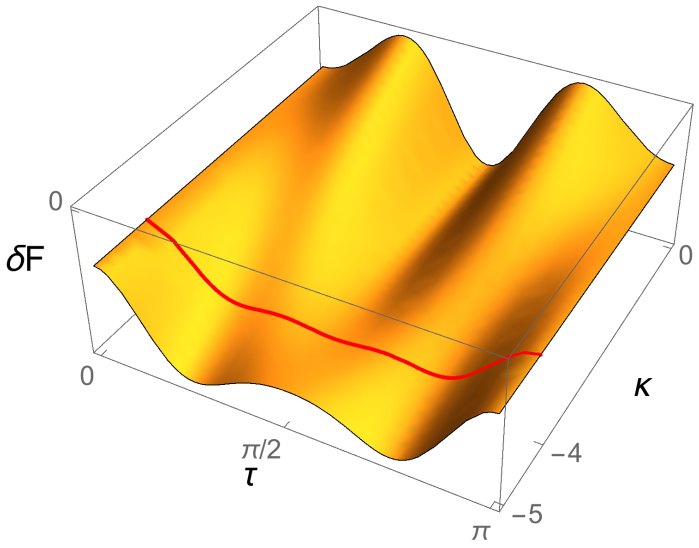

Figure 4.7: (From [59]) δF (correction to the Free energy from 4-fermion interactions) at $\theta = \frac{\pi}{2}$. At $\theta = \pi/2$, δF can minimized in both SDW order configurations at different τ: $\tau = \frac{\pi}{4}, \frac{3\pi}{4}$ for 120° spiral order (Fig. 4.1b) and $\tau = \frac{\pi}{2}$ for collinear order (Fig. 4.1c). At $\kappa = -4$ (thick red line), the ground state energy of the two SDW order configurations are the same, indicating a *first order* phase transition.

SDW states in favor of the state with antiferromagnetism on 2/3 of lattice cites.

The SDW ground state configuration is obtained by minimizing the total $\delta F = \delta F_a + \delta F_b$. We define the ratio of the prefactors for $\bar{M}^2$ terms in δF_a and δF_b as

$$\begin{aligned} \kappa &= \frac{1}{2} N_F \frac{(g_6 - g_7 - 2g_4)}{\gamma_8^2} \\ &= \frac{1}{2} N_F g_{sdw} \frac{(g_6 - g_7 - 2g_4) g_{sdw}}{g_8^2}. \end{aligned} \tag{4.21}$$

We find that for $\kappa < -4$ the system selects the 120° spiral state and for $\kappa > -4$ it selects the collinear antiferromagnetic state. At $\kappa = -4$ (highlighted in red in Fig. 4.7), both states correspond to local minima, i.e., the transition between the two is *first order*.

4.3.3 The ISB order

When g_3 is negative, the leading instability in the magnetic channel is towards ISB order $\mathbf{\Phi}_{\pm K}$. For this order we have $\mathbf{\Delta}_K = -\mathbf{\Delta}^*_{-K}$, i.e., $\mathbf{\Phi}_K = \mathbf{\Delta}_K$, $\mathbf{\Phi}_{-K} = \mathbf{\Delta}_{-K} = -\mathbf{\Phi}^*_K$. $\mathbf{\Phi_K}$ is also a complex vector $\mathbf{\Phi_K} = \mathbf{\Phi}_r + i\mathbf{\Phi}_i$ with $\mathbf{\Phi_{-K}} = -\mathbf{\Phi}_r + i\mathbf{\Phi}_i$. At the mean-field level the Free energy again depends on $\mathbf{\Phi}_r^2 + \mathbf{\Phi}_i^2$, i.e., the ground state is infinitely degenerate. The degeneracy is lifted by either the anisotropy of the electron

pockets or by other interactions.

In real space, a non-zero $\mathbf{\Phi}_K$ gives rise to a finite value of an imaginary part of an expectation value of a spin operator on a bond between $\mathbf{r}-\boldsymbol{\delta}/2$ and $\mathbf{r}+\boldsymbol{\delta}/2$. The corresponding real order parameter is

$$\begin{aligned}\Phi^{\alpha}_{\mathbf{r},\delta} &= \frac{i}{\hbar}\hat{\boldsymbol{\delta}}\langle f^{\dagger}_{\mathbf{r}+\boldsymbol{\delta}/2}\sigma^{\alpha}c_{\mathbf{r}-\boldsymbol{\delta}/2} + c^{\dagger}_{\mathbf{r}+\boldsymbol{\delta}/2}\sigma^{\alpha}f_{\mathbf{r}-\boldsymbol{\delta}/2} - h.c.\rangle \\ &= \frac{8}{\hbar}\hat{\boldsymbol{\delta}}|\Phi^{\alpha}_{K}|\sin\mathbf{K}\boldsymbol{\delta}\cos\left(\mathbf{K}\mathbf{r}-\phi^{\alpha}_{K}\right) \qquad (4.22)\end{aligned}$$

where $\Phi^{\alpha}{}_{K} = |\Phi^{\alpha}_{K}|e^{i\phi^{\alpha}_{K}}$ and $\phi^{\alpha}_{-K} = \pi - \phi^{\alpha}_{K}$. This last condition implies that $\Phi^{\alpha}_{\mathbf{r},\boldsymbol{\delta}}$ does not change under $\mathbf{K}\to-\mathbf{K}$.

Because $\Phi^{\alpha}_{\mathbf{r},\boldsymbol{\delta}}$ is an odd function of $\boldsymbol{\delta}$, the ISB order is "directional" in the sense that for a given $\mathbf{r}$, one can associate $\Phi^{\alpha}_{\mathbf{r},\boldsymbol{\delta}}$ with a vector directed either along or opposite to $\boldsymbol{\delta}$, depending on the sign of $\Phi^{\alpha}_{\mathbf{r},\boldsymbol{\delta}}$. In Fig. 4.2 we show $\Phi^{\alpha}_{\mathbf{r},\boldsymbol{\delta}}$ for the two ISB states selected by the lifting of the degeneracy. One is the analog of 120° SDW spiral state, another is the analog of a partially ordered collinear state. In the first case $\mathbf{\Phi}_r \perp \mathbf{\Phi}_i$, $|\mathbf{\Phi}_r| = |\mathbf{\Phi}_i|$, in the second $\mathbf{\Phi}_i = 0$. The direction of the arrow on each bond is determined by the sign of $\Phi^{\alpha}_{\mathbf{r},\boldsymbol{\delta}}$ (if it is positive, the arrow goes from $\mathbf{r}-\boldsymbol{\delta}/2$ to $\mathbf{r}+\boldsymbol{\delta}/2$). In the "120°" state (panels (a) and (b)), $\Phi^{x}_{\mathbf{r},\boldsymbol{\delta}}$ and $\Phi^{y}_{\mathbf{r},\boldsymbol{\delta}}$ are both non-zero. In the "collinear" state (panels (c) and (d)) only one component of $\mathbf{\Phi}_r$ is non-zero.

We emphasize that $\Phi^{\alpha}_{\mathbf{r},\boldsymbol{\delta}}$ is not a spin current operator ($\Phi^{\alpha}_{\mathbf{r},\boldsymbol{\delta}}$ at a given site is not conserved, as it would be required for a current due to local spin conservation). In a generic multi-orbital system a spin current is expressed in terms of ISB orders and hopping integrals as $J^{\alpha}_{\mathbf{r},\boldsymbol{\delta}} \sim \sum_{(a,b)} t^{(a,b)}_{\mathbf{r},\boldsymbol{\delta}}\Phi^{\alpha(a,b)}_{\mathbf{r},\boldsymbol{\delta}}$, where (a,b) label the orbital components of f- and c-fermions (see Ref. [60] for a discussion on the orbital currents). The hopping parameters $t^{(a,b)}_{\mathbf{r},\boldsymbol{\delta}}$ generally depend on $\mathbf{r}$ and, for a given $\mathbf{r}$, may change the sign between different $\boldsymbol{\delta}$. For a proper choice of $t^{(a,b)}_{\mathbf{r},\boldsymbol{\delta}}$ between orbitals, $J^{\alpha}_{\mathbf{r},\boldsymbol{\delta}}$ may become a spin current. For example, for the "collinear" $\Phi-$order (panels (c) and (d) in Fig. 4.2), a change of the direction and the magnitude on a half of the red bonds directed towards green sites in Fig. 4.2, will give rise to a circulating current, which obeys a local spin conservation. We show this in Fig. 4.3.

4.4 A finite magnetic field: a cone SDW state and a field-induced ISB order

In this section we consider the evolution of the SDW state in a Zeeman magnetic field. In a free electron system a Zeeman field shifts spin-up bands down and spin-down bands up, inducing a net magnetization along the field direction $\hat{z}$. For interacting fermions the effect of a magnetic field is more complex. Suppose we start with 120° spin ordering in zero field. For a system of localized spins on a 2D triangular lattice quantum fluctuations select field reorientation in which spins remain in the same plane in a finite field [38, 41, 112]. We show below that for itinerant fermions the evolution of the spin configuration with a field $\mathbf{h} = h\hat{z}$ proceeds differently – in a finite field the SDW becomes a non-coplanar cone state in which spins preserve a 120° order in the xy plane and simultaneously develop a net magnetization along the field. However, this is not the only effect of the field. We show that a magnetic field triggers the appearance of an ISB order $|\mathbf{\Phi}_{\pm K}| \propto (h/\mu)|\mathbf{M}_{\pm K}|$. We remind that $\mathbf{\Phi}_{\pm K}$ is even under time-reversal and may give rise to circulating spin currents.

4.4.1 Spin order in a magnetic field

When a Zeeman field is applied, say along $\hat{z}$, it splits the spin-up and spin-down bands, as shown in Fig. 4.8. It also breaks $SU(2)$ spin rotation symmetry down to $U(1)$, which means that SDW instabilities in $\sigma^{\pm}$ and σ^z channels now develop at different temperatures, which we label as $T_{c,tr}$ and $T_{c,z}$ respectively. Only the higher T_c is meaningful. We show that the SDW order develops in the $\sigma^{\pm}$ channel first, i.e. SDW is locked in the plane transverse to the field.

To see this we define the order parameters $\Delta_{\pm}$ and Δ_z as:

$$\begin{aligned} \Delta_{\pm K,\pm} &= \sum_{\boldsymbol{k},\alpha,\beta} \langle f^{\dagger}_{\boldsymbol{k}\pm K,\alpha} \sigma^{\pm}_{\alpha\beta} c_{\boldsymbol{k}\beta} \rangle \\ \Delta_{\pm K,z} &= \sum_{\boldsymbol{k},\alpha,\beta} \langle f^{\dagger}_{\boldsymbol{k}\pm K,\alpha} \sigma^{z}_{\alpha\beta} c_{\boldsymbol{k}\beta} \rangle \end{aligned} \tag{4.23}$$

where $\alpha,\ \beta = \{\uparrow, \downarrow\}$. The linearized equations on Δ in $\sigma^{\pm}$ channel are

$$\begin{aligned} \Delta_{K,+} &= -(g_1 \Pi_+ \Delta_{K,+} + g_3 \Pi_- \Delta^*_{-K,-}), \\ \Delta^*_{-K,-} &= -(g_3 \Pi_+ \Delta_{K,+} + g_1 \Pi_- \Delta^*_{-K,-}), \end{aligned} \tag{4.24}$$

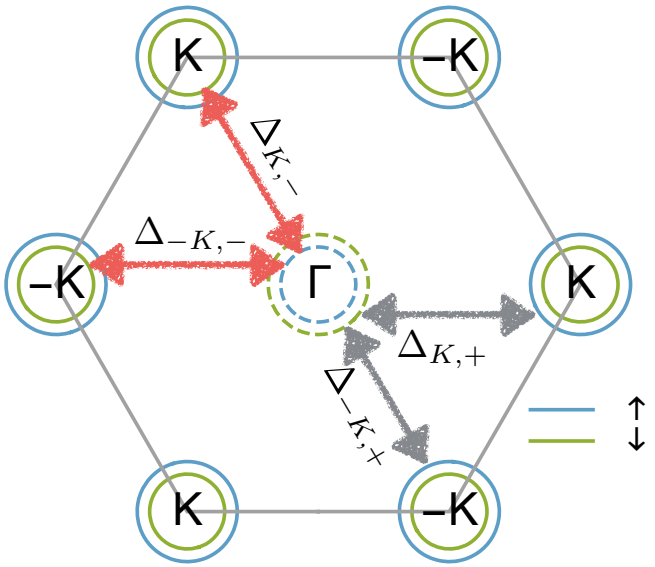

Figure 4.8: (From [59]) Fermi surface geometry in a magnetic field. Spin-up (blue) and spin-down (green) bands split by the Zeeman field. Double arrows connect electronic states that form SDW order in the σ^+ channel (grey arrow) and σ^- channel (red arrow). The quantity $\Delta_{\pm K,\pm}$ is defined in Eq. 4.23.

where

$$\Pi_\pm = T\sum_{\omega_n,\alpha,\beta}\int\frac{\mathrm{d}^2k}{\mathcal{A}_{B.Z.}}\mathcal{G}^{f,\alpha}(\boldsymbol{k}+\mathbf{K})\sigma^\pm_{\alpha,\beta}\mathcal{G}^{c,\beta}(\boldsymbol{k}).$$

It is essential that $\Pi_+ \neq \Pi_-$ (see below). In the σ^z channel we have

$$\begin{aligned}\Delta_{K,z} &= -g_1(\Pi_{z\uparrow}\Delta_{K,\uparrow} - \Pi_{z\downarrow}\Delta_{K,\downarrow}) - g_3(\Pi_{z\uparrow}\Delta^*_{-K,\uparrow} - \Pi_{z\downarrow}\Delta^*_{-K,\downarrow})\\ \Delta^*_{-K,z} &= -g_1(\Pi_{z\uparrow}\Delta^*_{-K,\uparrow} - \Pi_{z\downarrow}\Delta^*_{-K,\downarrow}) - g_3(\Pi_{z\uparrow}\Delta_{K,\uparrow} - \Pi_{z\downarrow}\Delta_{K,\downarrow})\end{aligned} \tag{4.25}$$

where $\Pi_{z,\alpha} = T\sum_{\omega_n}\int\frac{\mathrm{d}^2k}{\mathcal{A}_{B.Z.}}\mathcal{G}^{f,\alpha}(\boldsymbol{k}+\mathbf{K})\sigma^z_{\alpha,\alpha}\mathcal{G}^{c,\alpha}(\boldsymbol{k})$. Both $\Pi_{z,\alpha}$ and $\Pi_\pm$ do not change under $\mathbf{K}\to-\mathbf{K}$).

To get qualitative understanding, consider first the case of perfect nesting, i.e. set $m_h = m_e = m$ and $\mu_h = \mu_e = \mu$ such that $\epsilon_{\Gamma,\boldsymbol{k}} = -\epsilon_{\pm K+\boldsymbol{k}}$. Then the two larger FSs with Fermi momentum $k_F^+ = \sqrt{2m(\mu+h)}$ are the electron FS for up spins and the hole FS for down spins. The smaller FSs with $k_F^- = \sqrt{2m(\mu-h)}$ are the electron FS for down spins and the hole FS for up spins (see Fig. 4.8). One can easily verify that in this situation $\Pi_{z\downarrow} = \Pi_{z\uparrow}$. Eq. 4.25 is then simplified to

$$\Delta_{K,z} = -g_1\Pi_z\Delta_{K,z} - g_3\Pi_z\Delta^*_{-K,z}$$

$$\Delta^*_{-K,z} = -g_1\Pi_z\Delta^*_{-K,z} - g_3\Pi_z\Delta_{K,z} \tag{4.26}$$

Solving Eqs. 4.24 and 4.26 we obtain the SDW instability conditions in (i) $\sigma^{\pm}$ and (ii) σ^z channels as

$$\begin{aligned} &\text{(i)} \quad 1 + \frac{1}{2}\Big(g_1(\Pi_+ + \Pi_-) - \big((\Pi_+ - \Pi_-)^2 g_1^2 + 4\Pi_+\Pi_- g_3^2\big)^{1/2}\Big) = 0, \\ &\text{(ii)} \quad 1 + (g_1 + g_3)\Pi_z = 0. \end{aligned} \tag{4.27}$$

Evaluating the expectation value of polarization operators $\Pi_{\pm}$ and Π_z, we obtain at $h \ll T$ (see Appendix B for details),

$$\begin{aligned} \Pi_{ph,\pm} &= \Pi_{ph,0} \mp \frac{1}{2} N_F \frac{h}{\mu}, \\ \Pi_{ph,z} &= \Pi_{ph,0} + 0.43 N_F \frac{h^2}{T^2}, \end{aligned} \tag{4.28}$$

where $\Pi_{ph,0} \approx -(N_F/2)\log \mu/T$ is the polarization at zero field. Substituting into Eq. 4.27 we obtain the critical temperature of SDW order in the transverse and longitudinal channels as

$$\begin{aligned} &\text{(i)} \quad T_{c,tr}(h) = T_{c,0}\left[1 - \frac{g_3 - g_1}{2g_3}(g_3 + g_1) N_F \big(\frac{h}{\mu}\big)^2\right], \\ &\text{(ii)} \quad T_{c,z}(h) = T_{c,0}\left[1 - 0.86\big(\frac{h}{T}\big)^2\right] \end{aligned} \tag{4.29}$$

where $T_{c,0} = \mu e^{-2/(g_1+g_3)N_F}$. Because $T \ll \mu$, $T_{c,tr} > T_{c,z}$ independent on the sign of $g_3 - g_1$. For very low T, when in a finite field $h \gg T$, the expression for $T_{c,z}$ gets modified (see Appendix D), but still, $T_{c,tr} > T_{c,z}$. We also computed $T_{c,tr}$ and $T_{c,z}$ without assuming perfect nesting, by expanding in $\frac{\delta\mu}{\mu}$, and found that the condition instability temperature in the $\sigma_{\pm}$ channel is larger than that in the σ_z channel.

4.4.2 SDW order in a field

Because $T_{c,tr} > T_{c,z}$, the SDW instability develops in the $\sigma^{\pm}$ channel, i.e, the spontaneous order remains in xy plane. A finite field indeed also creates a magnetization component in z direction simply because the total densities of spin-up and spin-down fermions are now different. The ratio between $\Delta_{\pm K,\pm}$ and $\Delta^*_{\mp K,\mp}$, however, changes in the field. We remind that in zero field $\mathbf{\Delta}_{\pm K} = \mathbf{\Delta}^*_{\mp K}$, i.e. $\Delta_{\pm K,\pm} = \Delta^*_{\mp K,\mp}$, such that $\mathbf{M}_{\pm K} = \mathbf{\Delta}_{\pm K}$ and $\mathbf{\Phi}_{\pm K} = 0$. At a finite field the solution of self-consistent equations

on $\Delta_{\pm K,+}$ and $\Delta^*_{\mp K,-}$ yields

$$\gamma = \frac{\Delta^*_{\mp K,-}}{\Delta_{\pm K,+}} = 1 - \frac{(g_3 - g_1)N_F}{2g_3|\Pi_0|}\frac{h}{\mu} \tag{4.30}$$

The ground state still remains degenerate at the mean-field level, i.e., SDW order in xy plane can be either 120^0 spiral or a collinear state with 2/3 of lattice sites ordered. An arbitrary state from a degenerate manifold can be parametrized as

$$\begin{aligned} \Delta_{K,+} &= \cos\phi\,\Delta_+, & \Delta_{-K,+} &= e^{i\tilde{\theta}}\sin\phi\,\Delta_+, \\ \Delta_{K,-} &= e^{-i\tilde{\theta}}\sin\phi\,\Delta_-, & \Delta_{-K,-} &= \cos\phi\,\Delta_-, \end{aligned} \tag{4.31}$$

where $\phi, \tilde{\theta} \in (0, 2\pi)$, $\Delta_- = \gamma\Delta_+$ and without loss of generality we set Δ_+ to be real. We then have

$$\mathbf{M}_K = \frac{1}{2}(\mathbf{\Delta}_K + \mathbf{\Delta}^*_{-K}) = \frac{(1+\gamma)\Delta_+}{4}\{e^{-i\tilde{\theta}}(e^{i\tilde{\theta}}\cos\phi + \sin\phi), i\,e^{-i\tilde{\theta}}(e^{i\tilde{\theta}}\cos\phi - \sin\phi), 0\}, \tag{4.32}$$

and $\mathbf{M}_K = \mathbf{M}^*_{-K}$. The 120° spiral order corresponds to $\phi = 0, \pi$ and $\tilde{\theta}$ arbitrary (and its symmetry equivalents). The collinear state with two-thirds sites ordered corresponds to $\phi = -\frac{\pi}{4}$ and $\tilde{\theta} = 0$ (and symmetry equivalents). In the real space the SDW order is

$$\langle \hat{M}^\alpha_{\mathbf{r}} \rangle = 4|M^\alpha_K|\cos(\mathbf{Kr} - \phi_\alpha), \tag{4.33}$$

where $\alpha = x, y, z$, and ϕ_α is the phase of the α component of $\mathbf{M}_K$ in Eq. 4.32. In these notations, the 120° spiral order corresponds to $|\mathbf{M}^x_{\mathbf{K}}| = |\mathbf{M}^y_{\mathbf{K}}|, \phi_x = 0, \phi_y = \pi/2$ and the collinear order corresponds to $|\mathbf{M}^x_{\mathbf{K}}| = 0, \phi_y = \pi/2$.

To lift the degeneracy, one again has to include into consideration either the C_3 anisotropy of electron pockets, or four-fermion interactions other than g_1, g_3. We verified that if in zero field these terms select the 120° spiral SDW order, the same order remains at $h \neq 0$, i.e. at least in this case a Zeeman field doesn't change the type of the SDW order.

4.4.3 Field-induced ISB order

Eq. 4.30 has another, more prominent consequence. Because $\Delta_{\pm K,+} \neq \Delta^*_{\mp K,-}$, SDW and ISB channels no longer decouple, i.e., the emergence of a non-zero $\mathbf{M}_{\pm K} =$

$\frac{1}{2}(\mathbf{\Delta}_{\pm K}+\mathbf{\Delta}^*_{\mp K})$ triggers a non-zero ISB order parameter $\Phi_{\pm K}=\frac{1}{2}(\mathbf{\Delta}_{\pm K}-\mathbf{\Delta}^*_{\mp K})$. We remind that $\mathbf{M}_{\pm K}$ changes sign under time reversal, while $\mathbf{\Phi}_{\pm K}$ is symmetric under time-reversal. For a state from a degenerate manifold parametrized by Eq. 4.31

$$\mathbf{\Phi}_K=\frac{1}{2}(\mathbf{\Delta}_K-\mathbf{\Delta}^*_{-K})=\frac{(1-\gamma)\Delta_+}{4}\{e^{-i\tilde{\theta}}(e^{i\tilde{\theta}}\cos\phi-\sin\phi),i\,e^{-i\tilde{\theta}}(e^{i\tilde{\theta}}\cos\phi+\sin\phi),0\}, \tag{4.34}$$

and $\mathbf{\Phi}_K=-\mathbf{\Phi}^*_{-K}$. The ISB order triggered by the 120° spiral SDW order is $\mathbf{\Phi}_K=\frac{(1-\gamma)\Delta_+}{4}\{1,i,0\}$. Similarly, the ISB triggered by the partial collinear SDW order is $\mathbf{\Phi}_K=\frac{(1-\gamma)\Delta_+}{4}\{1,0,0\}$.

We emphasize that at small field, when $\gamma=1-\mathcal{O}(h/\mu)$, the magnitude of $\mathbf{\Phi}_K$ is linearly proportional to that of $\mathbf{M}_K$: $|\mathbf{\Phi}_K|\propto(h/\mu)|\mathbf{M}_K|$. This implies that a non-zero field mediates a *linear* coupling between SDW and ISB order parameters. This is different (and stronger) effect than a potential generation of $\mathbf{\Phi}_K$ in a field due to non-linear effects, considered in Ref [61].

We now derive explicitly the $F_{cross}(\mathbf{M}_{\pm K},\mathbf{\Phi}_{\pm K})$ term in the Free energy.

The Free energy

The Free energy in terms of $\bar{\mathbf{M}}_{\pm K}$ and $\bar{\mathbf{\Phi}}_{\pm K}$ can be obtained following the standard Hubbard-Stratonovich transformation. We present the details in Appendix B and here quote the result.

$$\begin{aligned}&F[\bar{\mathbf{M}}_{\pm\mathbf{K}},\bar{\mathbf{\Phi}}_{\pm\mathbf{K}}]=\\&\frac{2}{g_1+g_3}(|\bar{\mathbf{M}}_K|^2+|\bar{\mathbf{M}}_{-K}|^2)+\frac{2}{g_1-g_3}(|\bar{\mathbf{\Phi}}_K|^2+|\bar{\mathbf{\Phi}}_{-K}|^2)\\&+\frac{1}{2}\int_k\mathrm{Tr}(\mathcal{G}_{0,k}\mathcal{V})^2+\frac{1}{4}\int_k\mathrm{Tr}(\mathcal{G}_{0,k}\mathcal{V})^4+\mathcal{O}(\Delta^6)\end{aligned} \tag{4.35}$$

where $\int_k$ stands for integration over momentum and frequencies, $\mathcal{V}=\mathcal{V}^M+\mathcal{V}^\Phi$ and

$$\begin{aligned}\mathcal{V}^M&=-\begin{pmatrix}0&\bar{\mathbf{M}}_K\cdot\vec{\sigma}&\bar{\mathbf{M}}_{-K}\cdot\vec{\sigma}\\\bar{\mathbf{M}}_{-K}\cdot\vec{\sigma}&0&0\\\bar{\mathbf{M}}_K\cdot\vec{\sigma}&0&0\end{pmatrix},\\\mathcal{V}^\Phi&=-\begin{pmatrix}0&\bar{\mathbf{\Phi}}_K\cdot\vec{\sigma}&\bar{\mathbf{\Phi}}_{-K}\cdot\vec{\sigma}\\-\bar{\mathbf{\Phi}}_{-K}\cdot\vec{\sigma}&0&0\\-\bar{\mathbf{\Phi}}_K\cdot\vec{\sigma}&0&0\end{pmatrix}.\end{aligned} \tag{4.36}$$

The Green's function of free electrons in a field, $\mathcal{G}_{0,k}$, is:

$$\begin{aligned}\mathcal{G}_{0,\Gamma} &= \left((i\omega - \epsilon_{\Gamma,\boldsymbol{q}})\mathbb{I} + h\sigma_z\right)^{-1} \\ \mathcal{G}_{0,\pm K} &= \left((i\omega - \epsilon_{\pm K,\boldsymbol{q}})\mathbb{I} + h\sigma_z\right)^{-1}\end{aligned} \tag{4.37}$$

The bilinear coupling between $\mathbf{M}_{\pm\mathbf{K}}$, $\mathbf{\Phi}_{\pm\mathbf{K}}$ comes from the crossing terms of $\mathcal{V}^M$ and $\mathcal{V}^\Phi$ in $\frac{1}{2}\operatorname{Tr}(\mathcal{G}_{0,k}\mathcal{V})^2$,

$$\begin{aligned}F_{cross} =& \frac{1}{2}\int_k \operatorname{Tr}\left(\mathcal{G}_{0,k}\mathcal{V}^M\mathcal{G}_{0,k}\mathcal{V}^\Phi + \mathcal{G}_{0,k}\mathcal{V}^\Phi\mathcal{G}_{0,k}\mathcal{V}^M\right) \\ =& \frac{1}{2}\int_k \sum_{i=\pm K} \operatorname{Tr}\left(\mathcal{G}_{0,\Gamma}\mathbf{M}_i\cdot\vec{\sigma}\ \mathcal{G}_{0,i}\mathbf{\Phi}_i^*\cdot\vec{\sigma} + \mathcal{G}_{0,\Gamma}\mathbf{M}_i^*\cdot\vec{\sigma}\ \mathcal{G}_{0,i}\mathbf{\Phi}_i\cdot\vec{\sigma} + (\mathbf{M}_i \leftrightarrow \mathbf{\Phi}_i)\right) \\ =& 4\sum_{i=\pm K} \operatorname{Im}(\mathbf{M}_i\times\mathbf{\Phi}_i^*)\cdot\vec{h}\int_k (\mathcal{G}_{0,\Gamma}^{(0)2}\mathcal{G}_{0,i}^{(0)} - \mathcal{G}_{0,\Gamma}^{(0)}\mathcal{G}_{0,i}^{(0)2}) \\ =& -\frac{2N_F}{\mu}\sum_{i=\pm K}\operatorname{Im}(\mathbf{M}_i\times\mathbf{\Phi}_i^*)\cdot\vec{h}\end{aligned} \tag{4.38}$$

To obtain the last line in (4.38) we expanded $\mathcal{G}$ in powers of h as $\mathcal{G}_{0,\Gamma} = \mathcal{G}_{0,\Gamma}^{(0)} - \mathcal{G}_{0,\Gamma}^{(0)}h\sigma_z\mathcal{G}_{0,\Gamma}^{(0)} + \mathcal{O}(h^2)$ and $\mathcal{G}_{0,i} = \mathcal{G}_{0,i}^{(0)} - \mathcal{G}_{0,i}^{(0)}h\sigma_z\mathcal{G}_{0,i}^{(0)} + \mathcal{O}(h^2)$. In zero field, $F_{cross} = 0$ as the quantities under the trace in the upper line in Eq. 4.38 cancel each other. When a magnetic field is applied, $h\sigma_z$ doesn't commute with $\sigma^\pm$ components of SDW and ISB orders, and F_{cross} becomes finite.

4.5 Competition between magnetic and other orders

In this section we return back to the case of zero magnetic field and study the interplay between magnetism, superconductivity and charge density wave order. We remind that at the mean-field level, SDW magnetism is the leading instability because this channel is attractive and because for positive pair-hopping interaction g_3 the attraction is stronger than the one in ISB channel. The strength of the interactions in SC and CDW channels depends on the values of the bare couplings $g_1 - g_8$. If we set all bare couplings to be equal, the interactions in s^{++} SC channel and in CDW channel are repulsive, and the ones in ISB, "imaginary" charge bond, and s^{+-} SC channel vanish.

In a system with one type of FSs, a vanishing pairing interaction can be converted

into an attraction by going beyond mean-field and adding Kohn-Luttinger-type corrections to the pairing vertex from the particle-hole channel [155]. However, the corresponding SC T_c is smaller than the one for SDW, except for the case when all couplings are truly small. The situation is different in systems with hole and electron Fermi pockets. Here, a particle-hole bubble with the incoming momentum equal to the distance between the pockets ($\pm\mathbf{K}$ in our case) behaves as $\log W/E$ at energies E smaller than the bandwidth W but larger than, roughly, E_F. As the consequence, Kohn-Luttinger renormalization, as well as the renormalizations of the interaction in CDW channels, become logarithmic. The renormalizations in the particle-particle channel are also logarithmic in 2D at energies above E_F, as long as fermionic dispersion can be approximated as parabolic. The presence of the logarithms in the particle-hole and particle-particle channels implies that at energies between E_F and W the interactions $g_1 - g_8$ flow as one progressively integrates out fermions with higher energies, and split from each other even if at the bare level all g_i were set to be equal. This flow can be captured within pRG computational scheme [156–165]

Because g_i flow to different values, the interactions in some SC and CDW channels may flip the sign below a certain E and become attractive. These newly attractive interactions and the attractive interaction in SDW channel compete and mutually affect each other. SDW order still develops first if there is not enough "space" in energy domain for the flow of the couplings. However, if the system allows the couplings to flow over a sizable range of energies, the values of g_i at an energy/temperature, where the leading instability develops, are in general quite different from the bare ones. Then there is no guarantee that the leading instability will still be in the SDW channel, and not in one of SC or CDW channels. To find out which channel wins, one needs to (a) analyze the flow of the couplings, (b) use the running couplings to construct the effective interactions in different channels and compare their strength. This is what we will do below. For the full analysis one also has to compute the flow of the vertices in different channels and analyze the corresponding susceptibilities. This last analysis is important for the selection of subleading instabilities [164, 166, 167] and for computations in the channels where the bare susceptibility is non-logarithmic (e.g., for a particle-hole channel with zero momentum transfer [151, 152]). We will not consider such channels and will only be interested in the leading instability. For such an analysis it will be sufficient to compare the effective interactions constructed out of the running couplings.

4.5.1 the RG flow

As we said, there are 8 different 4-fermion interactions between fermions near hole and electron pockets, allowed by momentum conservation – the $g_1 - g_8$ terms. These couplings are shown graphically in Fig. 4.5. The flow of all 8 couplings can be obtained by applying pRG analysis similar to how this was done for Fe-based materials, which also have hole and electron pockets [151, 152, 160, 162, 163, 166, 167]. We perform one-loop pRG calculation keeping only logarithmically singular terms in the diagrams for the renormalizations of the couplings. In Fig. 4.9 we show diagrams for the renormalizations of the representative set of the couplings g_1, g_2, g_6 and g_7. The computation of the diagrams is time-consuming but straightforward, and we just present the result. The flow of the couplings is described by the set of differential equations:

$$\begin{aligned}
\dot{g}_1 &= g_1^2 + g_3^2 - g_8^2 \\
\dot{g}_2 &= 2g_2(g_1 - g_2) - g_8^2 \\
\dot{g}_3 &= g_3(4g_1 - 2g_2 - g_5 - g_6 - g_7) \\
\dot{g}_4 &= -g_4^2 \\
\dot{g}_5 &= -g_3^2 - g_5^2 \\
\dot{g}_6 &= -g_3^2 - g_6^2 - g_7^2 + 2g_8^2 \\
\dot{g}_7 &= -g_3^2 - 2g_6 g_7 \\
\dot{g}_8 &= g_8(3g_1 - 2g_2 + g_3 - g_4)
\end{aligned} \tag{4.39}$$

The derivatives are with respect to the RG "time" $t = \ln(W/E)$, where, we recall, W is the UV cutoff, of order bandwidth, and E is the running pRG scale. We define the critical temperature that certain instability develops as T_{ins}, the pRG flow terminates at $E \sim \max\{T_{ins}, E_F\}$, below which either an order develops in some channel at $E \sim T_{ins}$, when $T_{ins} > E_F$, or the flow equations become different, and the renormalizations of the interactions in particle-hole and particle-particle channels essentially decouple. The analysis of Eq. 4.39 shows that the equations for the intra-electron pocket coupling g_4 and for $g_{e-} = g_6 - g_7$ decouple from the equations for other couplings. As g_4 apparently flows to 0 and g_{e-} does not contribute to the instabilities which we consider here, and we neglect them. The remaining equations are

$$\begin{aligned}
\dot{g}_1 &= g_1^2 + g_3^2 - g_8^2 \\
\dot{g}_2 &= 2g_2(g_1 - g_2) - g_8^2
\end{aligned}$$

$$\dot{g}_3 = g_3(4g_1 - 2g_2 - g_5 - 2g_e)$$
$$\dot{g}_5 = -g_3^2 - g_5^2$$
$$\dot{g}_e = -g_3^2 - 2g_e^2 + g_8^2$$
$$\dot{g}_8 = g_8(3g_1 - 2g_2 + g_3 - g_4), \tag{4.40}$$

where $g_e = \frac{g_6+g_7}{2}$. Comparing this set with the corresponding pRG equations for the

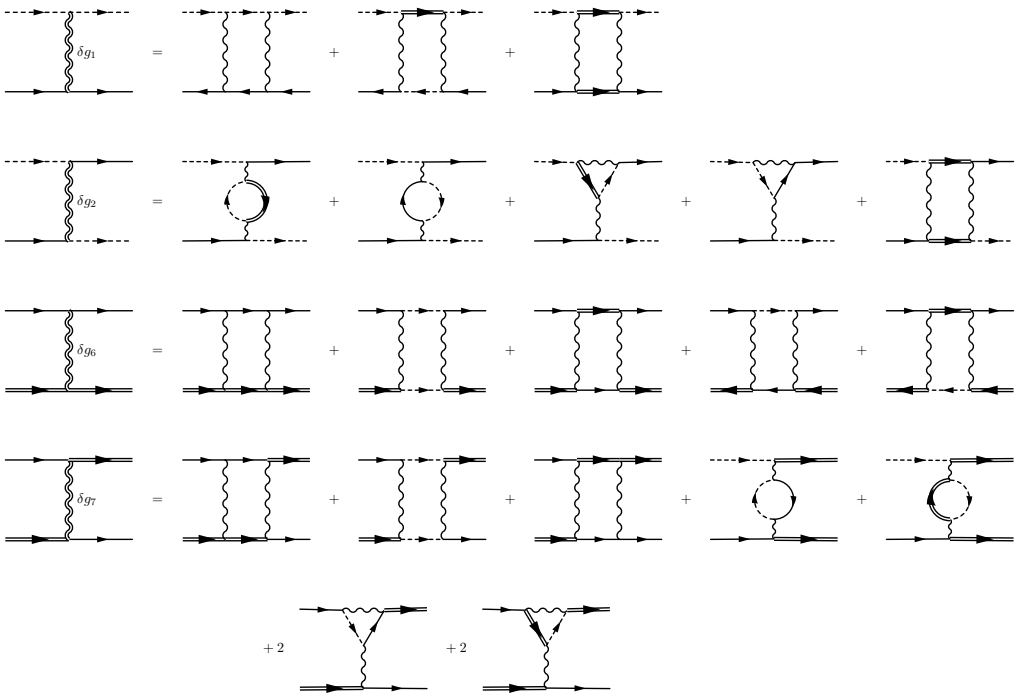

Figure 4.9: One loop diagrams for the renormalizations of the representative set of the couplings g_1, g_2, g_6 and g_7.

$3p$ model on a square lattice (one hole pocket at Γ and two electron pockets at $(0, \pi)$ and $(\pi, 0)$), we note that in our case the r.h.s of the flow equations contain additional terms due to the presence of the Umklapp g_8 term, which couples particle-particle and particle-hole channels [56].

To analyze the fixed trajectories of the pRG flow we rewrite interactions as $g_i = \gamma_i g$, where we choose g as one of the couplings, which increases under pRG and eventually diverges along the fixed trajectory (as we verify a'posteriori), and assume that γ_i tend to some constant values γ_i^* at the fixed trajectory [162]. We then search for the solutions

$$\beta_i = \dot{\gamma}_i = \frac{1}{g}(\dot{g}_i - \gamma_i \dot{g}) = 0 \tag{4.41}$$

The fixed trajectory is stable if small perturbations around it do not grow, i.e. the

real parts of the eigenvalues of the matrix $T_{ij} = \partial\beta_i/\partial\gamma_j|_{\gamma^*}$ are negative.

We focus on the effects of g_8 in the RG flow and study the fixed trajectories obtained by varying g_8 from weak to strong relative to other interactions $g_1 - g_7$. For definiteness we set the bare values of all other interactions to be equal and positive, i.e. set $g_i^{(0)} = g^{(0)}$, $i = 1, 2, 3, 5, e$. We find two stable fixed trajectories by varying $g_8^{(0)}$. The pRG flow is towards one fixed trajectory when $g_8^{(0)} < g_{8,c}^{(0)} = \frac{1}{2}g^{(0)}$ and towards the other when $g_8^{(0)} > g_{8,c}^{(0)}$. We show the pRG flow of the couplings for $g_8^{(0)} < g_{8,c}^{(0)}$ and $g_8^{(0)} > g_{8,c}^{(0)}$ in Fig. 4.10. We checked that these two fixed trajectories are stable. We didn't search for other possible fixed trajectories in the 6-dimensional space of the bare couplings.

The couplings along these two trajectories are:

(1) $g_8^{(0)} < g_{8,c}^{(0)}$. We choose $g_1 = g$, $g_i = \gamma_i g_1$. We find $g = (3/23)\frac{1}{(t_0-t)}$, $\gamma_2 = \gamma_8 = 0$, $\gamma_3 = 2\sqrt{5/3}$, $\gamma_5 = -1$, $\gamma_e = -4/3$. On a more careful look we find that g_8 still diverges, but with a smaller exponent, as $g_8 \sim \frac{1}{(t_0-t)^{0.56}}$.

(2) $g_8^{(0)} > g_{8,c}^{(0)}$. Now the system flows to another fixed point where g_2 remains the only leading divergent interaction and it changes sign in the process of pRG flow and becomes negative along the fixed trajectory. We choose $g_2 = g$, $g_i = \gamma_i g_2$, and obtain $g = (-1/2)\frac{1}{(t_0-t)}$, $\gamma_1 = \gamma_3 = \gamma_5 = \gamma_e = \gamma_8 = 0$. Again, on a more careful look we find that g_8 and g_1 actually also diverge and are only logarithmically smaller than g: $g_8 = \frac{1}{\sqrt{6}}\frac{1}{t_0-t}(\log\frac{1}{t_0-t})^{-0.5}$, $g_1 = \frac{-1}{6}\frac{1}{t_0-t}(\log\frac{1}{t_0-t})^{-1}$.

4.5.2 Interactions in different channels

We now need to relate pRG results to the competition between different ordering tendencies. To do this, we introduce infinitesimal vertices for various bilinear combinations of fermions and find which combination of g_i contributes to the renormalization of each of these vertices. We recall that we consider the model in which interactions are assumed to be independent on the angle along the pockets. In a more generic multi-orbital model the interactions generally have some symmetry-induced angular dependence. In this case the pRG analysis becomes more involved [151, 167], and other instability channels, e.g. d-wave superconductivity or d-wave orbital order, may become competitors to SDW, CDW, and s-wave SC. In the simple model considered here, we introduce SDW and CDW vertices with incoming momentum $\pm\mathbf{K}$ and SC vertices for fermions near hole or electron pockets, with zero total momentum. These

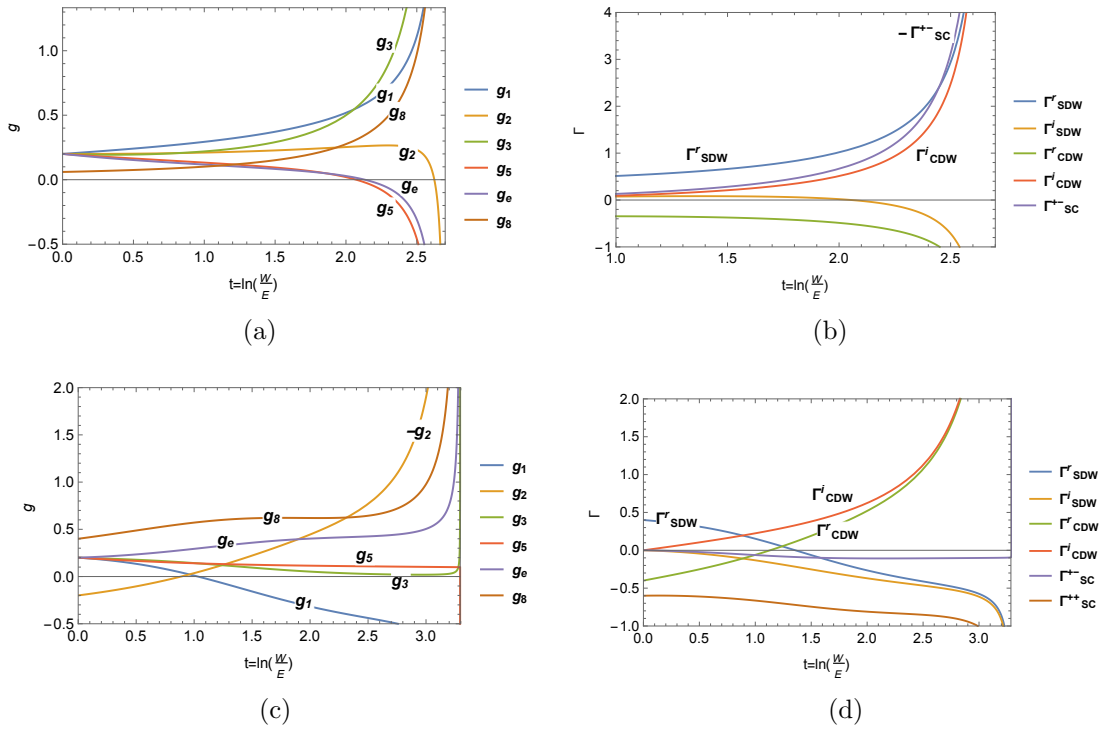

Figure 4.10: (From [59]) The renormalization group (RG) flow of the interactions and the effective vertices. We assume that system parameters are such that parquet RG flow runs over a wide range of energies. Panels (**a**) and (**b**) – the flow when the initial values of the couplings are $g_1^{(0)} = g_2^{(0)} = g_3^{(0)} = g_5^{(0)} = g_e^{(0)} = g^{(0)} = 0.2,\ g_8^{(0)} = 0.3g^{(0)}$. At the beginning of the flow SDW vertex Γ^r_{SDW} is the largest, but near the fixed trajectory the vertex Γ^{+-}_{sc} in superconducting s^{+-} channel diverges stronger than other vertices. Panels **(c) and (d)**: the flow when the initial values of the couplings are $g_1^{(0)} = g_2^{(0)} = g_3^{(0)} = g_5^{(0)} = g_e^{(0)} = g^{(0)} = 0.2, g_8^{(0)} = 2g^{(0)}$. The SDW vertex Γ^r_{SDW} is again the largest one at the beginning of the flow, but near the fixed trajectory the vertex Γ^i_{CDW} in "imaginary" charge density wave channel becomes the largest. The divergence of Γ^i_{CDW} signals an instability into a state with non-zero magnitude of the imaginary part of the expectation value of a charge operator on a bond.

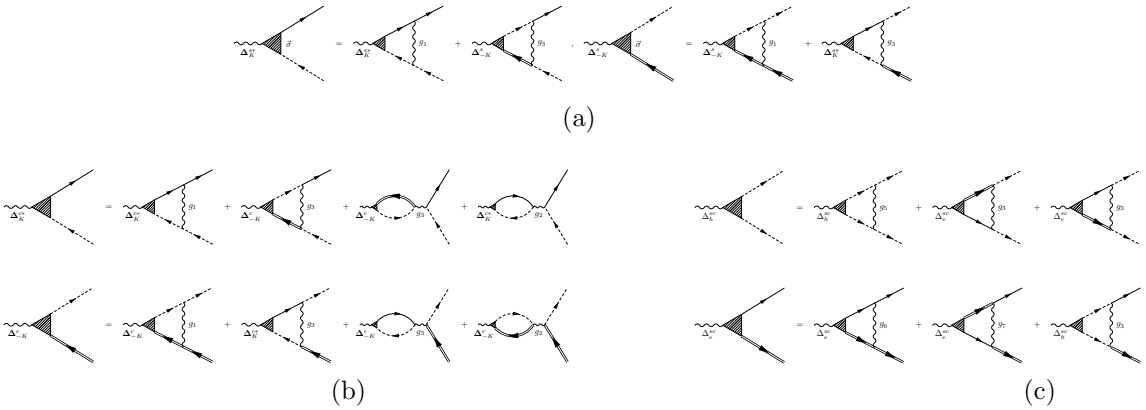

Figure 4.11: (a)-(c): Linearized self-consistent equations for SDW, CDW, s-wave superconductivity order, respectively.

vertices are

$$\begin{aligned}
&\text{SDW} \quad \boldsymbol{\Delta}^{s}_{\pm K} \cdot \sum_{\boldsymbol{k}} c^{\dagger}_{\boldsymbol{k}} \vec{\sigma} f_{\boldsymbol{k}\pm K}, \\
&\text{CDW} \quad \Delta^{c}_{\pm K} \sum_{\boldsymbol{k}} c^{\dagger}_{\boldsymbol{k}} \sigma^{0} f_{\boldsymbol{k}\pm K}, \\
&\text{SC} \qquad \Delta^{sc}_{h} \sum_{\boldsymbol{k}} c^{\dagger}_{\boldsymbol{k}} i\sigma^{y} c^{\dagger}_{-\boldsymbol{k}}, \ \Delta^{sc}_{e} \sum_{\boldsymbol{k}} f^{\dagger}_{\boldsymbol{k}+K} i\sigma^{y} f^{\dagger}_{-\boldsymbol{k}-K}
\end{aligned} \tag{4.42}$$

where σ^0, $\vec{\sigma}$ are the identity and the Pauli matrices in spin space, respectively. The equations for different vertices are presented diagrammatically in Fig. 4.11a-4.11c.

We defined the couplings in the magnetic, charge, and SC channels as Γ_s, Γ_c, and Γ_{sc}. The sign convention is such that the corresponding interaction is attractive if $\Gamma_c, \Gamma_s > 0$ and $\Gamma_{sc} < 0$.

In the magnetic channel, the result is the same as in our earlier consideration – the two order parameters are SDW and ISB, and the corresponding couplings are

$$\Gamma_s^{r,i} = g_1 \pm g_3, \tag{4.43}$$

where the superscript r stands for SDW and i stands for ISB (symmetric and anti-symmetric combinations of $\Delta^s_{\pm K}$ and $(\Delta^s_{\pm K})^*$, respectively).

In the charge channel we have

$$\Gamma_c^{r,i} = g_1 \mp g_3 - 2g_2, \tag{4.44}$$

where r and i again stand for *symmetric* and *antisymmetric* combinations of $\Delta^c_{\pm K}$

and $(\Delta^c_{\pm K})^*$. The symmetric solution describes a conventional CDW order and the antisymmetric solution describes imaginary charge bond (ICB) order [160, 168]. The latter may give rise to circulating charge currents, if the hopping integrals have proper symmetry properties.

In the SC channel we have

$$\begin{aligned}\Gamma^+_{sc} =& \frac{(g_5+2g_e)+\sqrt{8g_3^2+(g_5-2g_e)^2}}{2},\\ \Gamma^-_{sc} =& \frac{(g_5+2g_e)-\sqrt{8g_3^2+(g_5-2g_e)^2}}{2}\end{aligned} \tag{4.45}$$

The solution with Γ^+_{sc} is a conventional s^{++} pairing with $\Delta^{sc}_h, \Delta^{sc}_e$ having the same sign. The solution with Γ^-_{sc} is a s^{+-} pairing for which Δ^{sc}_h and Δ^{sc}_e having opposite signs.

The transition temperatures of potential density-wave and pairing instabilities are

$$\begin{aligned}&1 = -T^{r,i}_s \Gamma^{r,i}_s \Pi_{ph}(\pm K), \quad 1 = -T^{r,i}_c \Gamma^{r,i}_c \Pi_{ph}(\pm K),\\ &1 = -T^{+,-}_{sc} \Gamma^{+,-}_{sc} \Pi_{pp}(0)\end{aligned} \tag{4.46}$$

where

$$\begin{aligned}\Pi_{ph}(\pm\mathbf{K}) &= \sum_{\omega_m} \int \mathrm{d}\epsilon_{\boldsymbol{k}} \mathcal{G}^c(\boldsymbol{k},\omega_m)\mathcal{G}^f(\boldsymbol{k}\pm K,\omega_m),\\ \Pi_{pp}(0) &= \sum_{\omega_m} \int \mathrm{d}\epsilon_{\boldsymbol{k}} \mathcal{G}^c(\boldsymbol{k},\omega_m)\mathcal{G}^c(-\boldsymbol{k},-\omega_m).\end{aligned} \tag{4.47}$$

At a perfect nesting, $\Pi_{ph}(\pm\mathbf{K}) = -\Pi_{pp}(0)$. Then the leading instability will be in the channel for which Γ is of proper sign and the largest by magnitude. Away from perfect nesting, $\Pi_{ph}(\pm\mathbf{K})$ and $-\Pi_{pp}(0)$ differ by the ratio of the masses m_h/m_e, but still are logarithmic. For simplicity, below we assume $m_h = m_e$.

If we set the bare values of the couplings to be the same, the interactions in s^{++} SC channel and in CDW channel are repulsive, the ones in ISB, ICB, and s^{+-} SC channel vanish, and the interaction in SDW channel is attractive. At this level, the SDW is the leading instability.

If, however, we allow RG to run and compare Γ's for the couplings along the fixed trajectory, we obtain different results. For the first fixed trajectory (smaller $g_8^{(0)}$) we have

$$\Gamma^r_s = \Gamma^i_c = 3.58 g_1, \quad \Gamma^i_s = \Gamma^r_c = -1.58 g_1,$$

$$\Gamma^{+}_{sc} = 1.91 g_1, \quad \Gamma^{-}_{sc} = -5.58 g_1, \quad g_1 = \frac{3}{23}\frac{1}{t_0 - t} \tag{4.48}$$

We see that the largest coupling is in s^{+-} superconducting channel. For the second fixed trajectory (larger $g_8^{(0)}$) we have

$$\begin{aligned} &\Gamma^r_s = \Gamma^i_s = 0, \quad \Gamma^r_c = \Gamma^r_c = 2|g_2| = \frac{1}{t_0 - t}, \\ &\Gamma^{+}_{sc} = \Gamma^{-}_{sc} = 0 \end{aligned} \tag{4.49}$$

Now the largest vertex is in CDW and ICB channels. To lift the degeneracy between the two we notice that the condition $\gamma_1 = \gamma_3 = 0$ along this fixed trajectory does not imply that g_1 and g_3 vanish but rather that they are parametrically smaller than $|g_2|$. For our purpose, it is sufficient to note that $\Gamma^{r,i}_c = g_1 \pm g_3 - 2g_2$, and $g_3 > 0$ remains positive in the pRG flow. As the consequence, $\Gamma^i_c > \Gamma^r_c$, i.e., the leading instability is towards an unconventional ICB order. A similar instability has been previously found in $4p$ model on a hexagonal lattice [56].

4.6 Summary

In this work we studied the three-pocket itinerant fermion system on a 2D triangular lattice. We assumed that there is a small hole pocket centered at $\Gamma = (0, 0)$ and two electron pockets centered at $\pm\mathbf{K} = \pm(4\pi/3, 0)$. Our goals were to study in detail the magnetic order in such a system in zero and a finite magnetic field, and the interplay between magnetism and another potential orders like superconductivity and charge order. We first analyzed Stoner type magnetism in zero field. We found that for purely repulsive interaction the leading instability is towards a conventional SDW order with momentum $\pm\mathbf{K}$. The SDW order parameter $\mathbf{M}_K$ satisfies $\mathbf{M}_{-K} = \mathbf{M}^*_K$, but $\mathbf{M}_K$ is a complex order parameter $\mathbf{M}_K = \mathbf{M}_r + i\mathbf{M}_i$. In mean-field approximation the Free energy depends on $\mathbf{M}^2_r + \mathbf{M}^2_i$, i.e., the ground state is infinitely divergent. Different choices of $\mathbf{M}_r$ and $\mathbf{M}_i$, subject to $\mathbf{M}^2_r + \mathbf{M}^2_i = const$, yield different spin configurations from a degenerate manifold. Beyond mean-field, we found that the ground state degeneracy is lifted. Depending on parameters, the ground state configuration is either 120° "triangular" structure (same as for localized spins), or a collinear state with antiferromagnetic spin order on 2/3 of sites and no magnetic order on the remaining 1/3 sites. Such partial order with non-equal magnitude of magnetization on different sites cannot be realized in a localized spin system.

When some interactions are repulsive and some attractive, the system develops another type of order, which we labeled as ISB order. The corresponding order parameter is the imaginary part of the (complex) expectation value of a spin operator on a bond. This order parameter is even under time reversal. We argued that an ISB state can possess circulating spin currents if the hopping integrals have a certain symmetry.

We then returned to a system with purely repulsive interactions and considered a magnetic order in a non-zero field. We found that 120° "triangular" spin configuration becomes a non-coplanar cone state with 120° spin order in the plane perpendicular to the field and ferromagnetic order along the field. We also found that a field generates a bilinear coupling between SDW and ISB order parameters, i.e., a SDW order in a field immediately triggers an ISB order. This is one of the central results of our work.

We next considered the interplay between magnetism and superconductivity and charge order. For this, we analyzed the flow of the couplings within pRG and used the running couplings to analyze the flow of the effective interactions in magnetic, SC, and charge channels. We argued that magnetic order develops if there is little space for pRG, however if the system parameters are such that pRG runs over a wide window of energies, the couplings flow towards one of the two fixed trajectories (depending on the values of the bare couplings), and for both fixed trajectories magnetism is not the leading instability. For one fixed trajectory we found that the leading instability is towards $s^{\pm}$ superconductivity, for the other the leading instability is towards ICB order, which may support circulating charge currents. This highly unconventional charge order is induced by the Umklapp scattering process (g_8 term), which couples particle-hole and particle-particle channels.

We call for the extension of our work to multi-orbital models of fermions on a triangular lattice. Among other things, these studies should settle the issue whether the ISB/ICB orders, which we found, support circulating spin/charge currents.

Chapter 5

Pseudogap due to spin-density-wave fluctuations

We calculate the fermionic spectral function $A_k(\omega)$ in the spiral spin-density-wave (SDW) state of the Hubbard model on a quasi-2D triangular lattice at small but finite temperature T. The spiral SDW order $\Delta(T)$ develops below $T = T_N$ and has momentum $\mathbf{K} = (4\pi/3, 0)$. We pay special attention to fermions with momenta $\mathbf{k}$, for which $\mathbf{k}$ and $\mathbf{k}+\mathbf{K}$ are close to Fermi surface in the absence of SDW. At the mean field level, $A_k(\omega)$ for such fermions has peaks at $\omega = \pm\Delta(T)$ at $T < T_N$ and displays a conventional Fermi liquid behavior at $T > T_N$. We show that this behavior changes qualitatively beyond mean-field due to singular self-energy contributions from thermal fluctuations in a quasi-2D system. We use a non-perturbative eikonal approach and sum up infinite series of thermal self-energy terms. We show that $A_k(\omega)$ shows peak/dip/hump features at $T < T_N$, with the peak position at $\Delta(T)$ and hump position at $\Delta(T = 0)$. Above T_N, the hump survives up to $T = T_p > T_N$, and in between T_N and T_p the spectral function displays the pseudogap behavior. We show that the difference between T_p and T_N is controlled by the ratio of in-plane and out-of-plane static spin susceptibilities, which determines the combinatoric factors in the diagrammatic series for the self-energy. For certain values of this ratio, $T_p = T_N$, i.e., the pseudogap region collapses. In this last case, thermal fluctuations are logarithmically singular, yet they do not give rise to pseudogap behavior. Our computational method can be used to study pseudogap physics due to thermal fluctuations in other systems.

5.1 Introduction

The pseudogap behavior, observed in several classes of materials, most notably high T_c cuprates, remains one of the mostly debated phenomenon in correlated electron systems. There are two key scenarios of the pseudogap, each supported by a set of experiments. One is that the pseudogap is a distinct state of matter with an order parameter, which is either bilinear in fermions (e.g., loop current order [65, 66]), or a four-fermion composite order (e.g., a spin nematic [57, 67, 68]), or a topological order that cannot be easily expressed via fermionic operators [69]. Within this scenario, the experimentally detected onset temperature of a pseudogap, T_p, is a phase transition temperature. The other scenario is that the pseudogap is a precursor to an ordered state – SDW magnetism [29, 70–73], superconductivity [74–77], or both, with the relative strength of the two precursors set by doping (a precursor to SDW is the dominant one at smaller dopings, and a precursor to superconductivity is the dominant one at larger dopings). Within this scenario, the system retains a dynamical memory about the underlying order in some temperature range where the order is already destroyed, and this memory gradually fades and disappears at around T_p. At around this temperature the behavior of the spectral function crosses-over to that in a (bad) metal. A similar but not equivalent scenario, is for pseudogap as a precursor to Mott physics [78]. The precursor scenario is not strictly orthogonal to the competing order scenario as, e.g., the depletion of the spectral weight at low energies in the antinodal region due to pseudogap formation does enhance the system's tendency to develop a CDW order with axial momenta, consistent with the one observed in the cuprates [30, 169–171]. The same holds for pair density-wave order [172–174]. Whether a pre-existing pseudogap helps the system to develop a topological order is less clear.

In this Chapter we analyze several aspects of the precursor scenario. There is no clear path to get a precursor behavior at $T = 0$, but earlier works [70–73, 76, 175] have found that thermal (static) SDW and/or superconducting fluctuations do give rise to precursors and associated pseudogap behavior. In particular, previous studies of quasi-2D systems on a square lattice have found that the pseudogap does develop in some T range above the critical T_N towards a commensurate (π, π) SDW order due to magnetic thermal fluctuations [70, 71, 73]. There have also been extensive numerical efforts in understanding the underlining mechanism of pseudogap in the 2D Hubbard model on a square lattice (see e.g. [78, 81, 82]). The fluctuation diagnostics method have identified the static antiferromangetic fluctuation as the dominant contribution

that gives rise to pseudogap behavior at $T > 0$ [81]. *The question we address is whether pseudogap is a generic property of a system near a magnetic ordered state, or there are situations (e.g. for different lattice geometries) when magnetic thermal fluctuations are logarithmically singular, but do not give rise to pseudogap behavior.* To analyze this, lowest-order perturbation theory is not sufficient, and one has to sum up infinite series of singular self-energy corrections due to thermal SDW fluctuations. There is a well established computational procedure for this, similar to eikonal approximation in the scattering theory [176]. Here we consider, within the same computational scheme, the effects of thermal SDW fluctuations for the Hubbard model on a triangular lattice. Importantly, the SDW order on a triangular lattice is coplanar but non-collinear in the large U limit near half-filling (with ordering wave vector $\mathbf{K} = (4\pi/3, 0)$), and the in-plane and out-of-plane magnetic susceptibilities are generally different.

We argue that the prefactors in the diagrammatic series for the thermal self-energy depend on the ratio of the two susceptibilities, and by changing this ratio one can control the outcome of the summation of the series. This introduces a *control parameter*, by which one can vary the strength of the pseudogap behavior. We show that, for a certain value of the control parameter, the system does not develop the pseudogap, despite that self-energy corrections are singular. We note in passing that there is a similarity between this last case in our model and the "supermetal" scenario for 2D fermions near a single Van-Hove point [177]. In both cases, corrections to fermionic propagator are logarithmically singular, yet the system retains a conventional Fermi liquid behavior.

As we said, we consider the Hubbard model on a triangular lattice, in the large U limit. At $T = 0$, this model displays a co-planar, 120^0 SDW order with ordering momentum $\mathbf{K} = (4\pi/3, 0)$. Within mean-field [178], the magnitude of the SDW order is $\Delta(0) = U|\langle\vec{S}\rangle| = U/2$ at half-filling. Quantum fluctuations reduce $|\langle\vec{S}\rangle|$ by about 50% [102, 104], but do not destroy the order, nor change that $\Delta(0) \sim U$. The order gaps fermions at hot spots, and the distance between the conduction and the valence band is $2U|\langle\vec{S}\rangle|$ (which in the mean-field approximation is the Hubbard U).

At a finite T, the order is strongly affected by thermal fluctuations. In a 2D system, they destroy long-range order at any finite T. In a quasi-2D system, which we consider, the corrections to $|\langle\vec{S}\rangle|$ scale as $(T/J)|\log\epsilon|$, where $J = O(t^2/U)$ is the exchange interaction (t is the hopping), and ϵ measures the deviations from pure two dimensionality. Long-range order get destroyed at $T_N \sim J/|\log\epsilon|$.

In our analysis we primarily focus on the "hot spots" in momentum space, i.e., on

the $\mathbf{k}$ points, for which $\mathbf{k}$ and $\mathbf{k}+\mathbf{K}$ are both on the Fermi surface without SDW. An SDW order $\Delta(T)$ opens up a spectral gap at these $\mathbf{k}$. In the mean-field approximation, the spectral function $A_k(\omega)$ at hot spots then has two peaks at $\omega = \pm\Delta(T)$ (see Fig. 5.1(a)). Within mean-field, the peak position scales with the magnitude of a SDW order and vanishes right at T_N, where the order disappears. At higher T, the spectral function of a hot fermion is peaked at $\omega = 0$, as is expected for a fermion on the Fermi surface in an ordinary paramagnetic metal (see Fig. 5.1(b)). Thermal fluctuations can change this behavior. In general case, the spectral function at $T \ll T_N$ and at $T \gg T_N$ are similar to that in the mean field approximation, and Fig. 5.2(a) (Fig. 5.2 (e)) is equivalent to Fig. 5.1(a) (Fig. 5.1 (b)). However, in the mean field approximation, there is no intermediate behavior, i.e., the spectral function changes between Fig. 5.1(a) and Fig. 5.1(b) at $T = T_N$. In the presence of fluctuations, there is intermediate behavior, as shown in Fig. 5.2 (b, c, d). For a generic value of our control parameter, $A_k(\omega)$ in a SDW state displays a peak, a dip, and a hump. A peak is at $\Delta(T)$, a hump is near $\Delta(T = 0)$, and a dip is in between these two scales (see the dashed line in Fig. 5.2(b)). The spectral function almost vanishes below the peak, i.e., a true gap is $\Delta(T)$, like in a mean-field approximation. However, the spectral weight in the peak is reduced compared to a mean-field $A_k(\omega)$, and the difference is transferred into a hump. At T_N, the peak disappears, but the hump survives (see Fig. 5.2 (c)). In between T_N and T_p, the spectral function at a hot spot is non-zero at $\omega = 0$, like at $\mathbf{k}_F$ in a ordinary metal, but the maximum in $A_k(\omega)$ remains at a finite frequency, i.e., the system displays a pseudogap behavior (see Fig. 5.2(d)). As T increases towards T_p, the value of $A_k(0)$ increases, and above T_p, the maximum of $A_k(\omega)$ moves to $\omega = 0$ (see Fig. 5.2(e)). Fig. 5.2 is the *key result* of our analysis. We show later how it was obtained.

We also note that at a special value of the control parameter, the spectral function below T_N has only a peak at $\omega = \pm\Delta(T)$, but no hump. Above T_N, the peak disappears, and the spectral function has a single maximum at $\omega = 0$, like in ordinary paramagnetic metal. In this situation, precursor behavior does not develop. Still, even in this case, the spectral function dressed by thermal SDW fluctuations is quite different from the mean-field $A_k(\omega)$ (see Eq. (5.31)).

We will use three simplifications in our analysis. First, we neglect thermal variation of the chemical potential μ. In principle, $\mu(T)$ has to be computed simultaneously with the fermionic self-energy, from the condition on the total number of fermions. In the SDW state, and in the pseudogap state above T_N, $\mu(T)$ by itself evolves with temperature, and this evolution keeps the position of the hump at distance $O(J)$ from

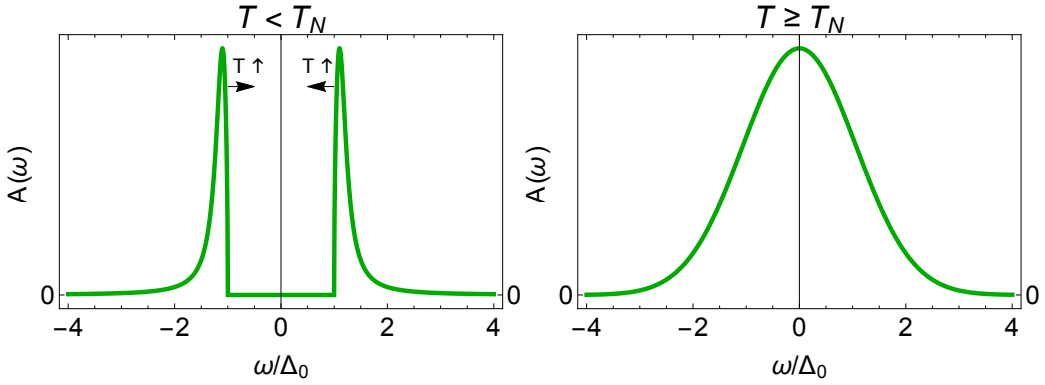

Figure 5.1: (From [86]) The evolution of the spectral function in mean-field approximation, at a hot spot on the Fermi surface. (a) In the SDW state, the spectral function has two peaks at energies $\pm\Delta(T)$, where $\Delta(T)$ is proportional to the magnitude of SDW order parameter. (b) At $T = T_N$, the two peaks merge, and at $T > T_N$, the spectral function has a single maximum at $\omega = 0$, like in an ordinary metal. The peaks are $\delta-$functional in "pure" mean-field approximation, but get broadened by regular (i.e., non-logarithmical) thermal and quantum fluctuations. We added a finite broadening phenomenologically to model these effects.

the Fermi energy. As we said, our key goal is to analyze how the pseudogap behavior varies as we change the control parameter. Because the distance between the two humps at positive and negative ω in Fig. 5.2 does not depend on μ, we will not include the thermal evolution of μ into our analysis and just use the non-pseudogap normal state value for μ. As the consequence of keeping μ fixed, the spectral function $A_k(\omega)$ at a hot spot is a symmetric function of frequency, and the positions of the peak and the hump in the SDW state and the hump in the pseudogap state are all set by U. Second, we compute the spectral function only at $T < T_N$. This is enough for our purpose. Indeed, it is clear from Fig. 5.2 that when the spectral function retains a hump at $T = T_N - 0$, it necessary displays a pseudogap behavior at $T > T_N$. And, likewise, when the spectral function does not have a hump at $T = T_N - 0$, it does not display a pseudogap behavior at $T > T_N$. Third, in this work we only consider the renormalization of the fermionic propagator due to an exchange of transverse spin fluctuations. The self-energy due to an exchange of longitudinal spin fluctuations is non-singular and we neglect it. We caution that this last approximation works well at T substantially smaller than T_N, when the transverse fluctuations are gapless, but the longitudinal fluctuations are gapped. At $T \approx T_N$, the gap for longitudinal fluctuations gets smaller, and these fluctuations may enhance the tendency towards pseudogap behavior [70, 71].

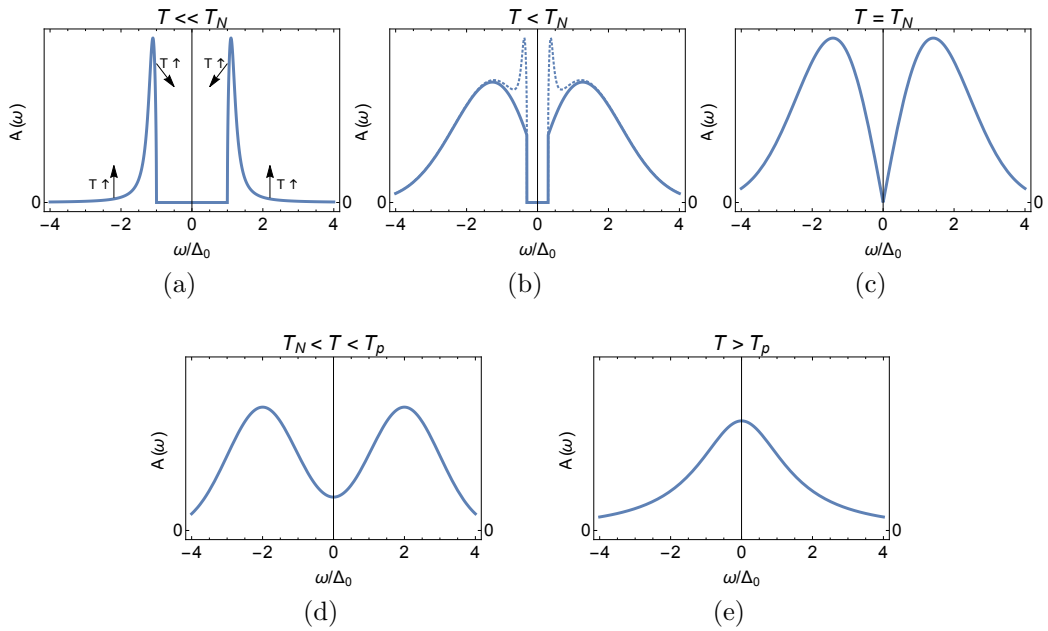

Figure 5.2: (From [86]) The sketch of the evolution of the spectral function at a hot spot, when series of logarithmical corrections from thermal fluctuations are included. (a) Deep inside the SDW phase, the spectral function is the same as in mean-field approximation - there are peaks at $\omega = \pm\Delta(0) \sim U$. (b) At $T \leq T_N$, the spectral weight vanishes at $|\omega| < \Delta(T)$, like in mean-field, but the spectral function also develops a hump at $|\omega| \sim \Delta(0)$. (c) At $T = T_N$, the true gap vanishes, but the hump remains. (d) At $T \geq T_N$, the spectral function is non-zero at all frequencies, but has a minimum at $\omega = 0$ rather than a peak. This has been termed as pseudogap behavior. (e) The conventional metallic behavior is restored only at $T > T_p$ ($T \gg T_N$). The temperature around which the hump vanishes is defined as T_p. The solid lines in panel (b) show the result for the spectral function, when only singular thermal self-energy corrections are included. The dashed lines show the full result, including non-singular self-energy corrections (see the discussion in Sec. 5.4.3).

Before we proceed, we briefly outline the computational procedure. As we said, it is similar to the eikonal approximation in the scattering theory [176]. To our knowledge, its was first applied in the solid state context in the study of one-dimensional (1D) systems with charge density wave (CDW) fluctuations [179–182] (see also Refs. [183]). The eikonal approximation been applied to cuprates to analyze the precursors of a collinear (π, π) SDW state, in the paramagnetic phase [70, 71] and in the SDW state [73]. It has also been used in the calculations of non-analytical corrections to Fermi liquid behavior in a 2D metal [184]. In our analysis, we follow Ref. [73], introduce valence and conduction bands in the SDW state, and derive the vertex for the interaction between fermions and magnons (Goldstone modes of the transverse

fluctuations of the order parameter). The 120° SDW order is co-planar, but not collinear, which implies that it fully breaks the $SU(2)$ spin rotation symmetry. As the consequence, there are three Goldstone modes. The first two are associated with transformations that rotate the plane, where the order sets in. The third one rotates the SDW order parameter within the plane. Accordingly, there are two different spin susceptibilities, $\chi_\perp$ and $\chi_\parallel$ [185, 186], for out-of-plane and in-plane rotations, respectively.

At a finite temperature, the leading contributions to the renormalization of the Green's function come from scattering of thermal bosons (in Matsubara formalism, this corresponds to scattering processes with zero transferred bosonic frequency). These thermal self-energy contributions are logarithmically singular, and scale as powers of $T/J|\log\epsilon|$, where, we remind, ϵ measures the deviations from pure two dimensionality (see Eq. (5.19) below). We use $|\log\epsilon| \gg 1$ as a parameter, which allows us to separate singular contributions due to thermal fluctuations from regular contributions of these fluctuations (the terms of order T/J, without $|\log\epsilon|$), and perturbative contributions of quantum fluctuations. The latter are of order one, but are not relevant from physics perspective and can be safely neglected in our analysis of the pseudogap due to precursors to SDW [29] (non-perturbative quantum corrections may be quite relevant [69], but this goes beyond the scope of our work). We assume that T_N/J is small and for n-loop self-energy keep only the terms of order $(T/J|\log\epsilon|)^n$. These terms contain both self-energy and vertex corrections, which we put on equal footings.

We show that the combinatoric factor at n-loop order, (which we define as $\mathcal{C}_n$ in the text) scales factorially with n, and its magnitude depends on the ratio $\chi_\parallel/\chi_\perp$. We sum the contributions from all orders and obtain the full self-energy. We then convert from Matsubara to real axis and obtain the spectral function $A_k(\omega)$.

The rest of the Chapter is organized as follows. In Sec. 5.2 we introduce the Hamiltonian, discuss mean-field solution, and obtain the dynamical magnetic susceptibility associated with the Goldstone modes, the effective 4-fermion interaction mediated by magnons, and the magnon-fermion vertex function. In Sec. 5.3, we obtain and sum up the series of leading logarithmical diagrams for the fermionic Green's function. In Sec. 5.4 we obtain the spectral function for different ratios of $\chi_\parallel/\chi_\perp$. This is the main result of this Chapter. In Sec. 5.5 we discuss the results and summarize our findings.

5.2 The model

5.2.1 The Hamiltonian and the mean field solution

The point of departure for our analysis is the one band Hubbard model for spin 1/2 fermions on a triangular lattice

$$\mathcal{H} = -\sum_{\langle i,j\rangle,\sigma} t_{i,j}(c^\dagger_{i,\sigma}c_{j,\sigma} + c^\dagger_{j,\sigma}c_{i,\sigma}) - \mu\sum_i c^\dagger_i c_i + U\sum_i n_{i\uparrow}n_{i\downarrow} \tag{5.1}$$

Without loss of generality, we restrict the hopping to nearest neighbors.

We take as an input the fact that the ground state of the model for large U is the 120° co-planar SDW order. Without loss the generality, we set the global coordinate such that the coplanar order is in the x-z plane, and $\langle S^z_i\rangle + i\langle S^x_i\rangle = \bar{S}\exp(\pm i\mathbf{K}\cdot\mathbf{R}_i)$, where $\mathbf{K} = (4\pi/3, 0)$ and $\bar{S}$ is the magnitude of average magnetization ($\bar{S} \approx 1/2$ at mean field level near half-filling and in the large U limit). The $\pm$ sign in the exponent determines whether the "direction" of the spiral, i.e., whether the order is $+120°$ or $-120°$. Without loss of generality we consider the $+$ case in the rest of the Chapter. We introduce the rotating reference frame [178], in which all spins are along the same direction $\tilde{z}_i$. The transformation of fermionic operators c_i to the new basis is given by $c_i = T_i\tilde{c}_i$, where $T_i = \exp(-i\mathbf{K}\cdot\mathbf{R}_i\sigma_y/2)$. One can straightforwardly verify that in the new coordinate frame $\langle\tilde{\mathbf{S}}_i\rangle = (1/2)\langle\tilde{c}^\dagger_{i,\alpha}\sigma_{\alpha\beta}\tilde{c}_{i,\beta}\rangle = \{0, 0, \bar{S}\}$, i.e. the original 120° SDW order becomes ferromagnetic. The Hubbard Hamiltonian in the rotating reference frame takes the form

$$\mathcal{H} = -\sum_{\langle i,j\rangle} t_{i,j}(\tilde{c}^\dagger_i T_{i,j}\tilde{c}_j + \tilde{c}^\dagger_j T_{j,i}\tilde{c}_i) - \mu\sum_i \tilde{c}^\dagger_i\tilde{c}_i + U\sum_i \tilde{c}^\dagger_{i,+}\tilde{c}_{i,+}\tilde{c}^\dagger_{i,-}\tilde{c}_{i,-}, \tag{5.2}$$

where $T_{i,j} = T^\dagger_i T_j$. In explicit form, we have

$$T_{i,j} = \begin{pmatrix} \cos(\mathbf{K}\cdot\mathbf{R}_{ij}/2) & \sin(\mathbf{K}\cdot\mathbf{R}_{ij}/2) \\ -\sin(\mathbf{K}\cdot\mathbf{R}_{ij}/2) & \cos(\mathbf{K}\cdot\mathbf{R}_{ij}/2) \end{pmatrix}, \tag{5.3}$$

where $\mathbf{R}_{ij} = \mathbf{R}_i - \mathbf{R}_j$.

The quadratic Hamiltonian Eq. (5.2) in momentum space is:

$$\mathcal{H}_{quad} = \sum_k \begin{pmatrix} \tilde{c}^\dagger_{k,+} & \tilde{c}^\dagger_{k,-} \end{pmatrix} \begin{pmatrix} (\epsilon_{k+}+\epsilon_{k-})/2 - \mu & i(\epsilon_{k+}-\epsilon_{k-})/2 \\ -i(\epsilon_{k+}-\epsilon_{k-})/2 & (\epsilon_{k+}+\epsilon_{k-})/2 - \mu \end{pmatrix} \begin{pmatrix} \tilde{c}_{k,+} \\ \tilde{c}_{k,-} \end{pmatrix}, \tag{5.4}$$

where $\epsilon_{k+} = \epsilon_{k+K/2}$, $\epsilon_{k-} = \epsilon_{k-K/2}$ and $\epsilon_k = -t\sum_{\langle i,j\rangle}\exp(ik\cdot r_{ij}) = -2t(\cos k_x + 4\cos k_x/2\cos\sqrt{3}k_y/2)$. To simplify notations, we define $\omega_k = \frac{1}{2}(\epsilon_{k+}+\epsilon_{k-})$, $\eta_k = \frac{1}{2}(\epsilon_{k+}-\epsilon_{k-})$. In these notations,

$$\mathcal{H}_{quad} = \sum_k \begin{pmatrix}\tilde{c}^\dagger_{k,+} & \tilde{c}^\dagger_{k,-}\end{pmatrix}\begin{pmatrix}\omega_k-\mu & i\eta_k \\ -i\eta_k & \omega_k-\mu\end{pmatrix}\begin{pmatrix}\tilde{c}_{k,+}\\ \tilde{c}_{k,-}\end{pmatrix}. \tag{5.5}$$

The mean-field approximation

In the SDW state, $\langle\tilde{c}^\dagger_{i,+}\tilde{c}_{i,+}\rangle = -\langle\tilde{c}^\dagger_{i,-}\tilde{c}_{i,-}\rangle = \bar{S}$. The interaction term in mean field approximation reduces to

$$\begin{aligned}\mathcal{H}_{int} &= U\sum_i \tilde{c}^\dagger_{i,+}\tilde{c}_{i,+}\tilde{c}^\dagger_{i,-}\tilde{c}_{i,-}\\ &\to \Delta c^\dagger_{i,-}\tilde{c}_{i,-} - \Delta c^\dagger_{i,+}\tilde{c}_{i,+},\end{aligned} \tag{5.6}$$

where $\Delta = U\bar{S}$. The mean field Hamiltonian becomes

$$\mathcal{H}_{MF} = \begin{pmatrix}\tilde{c}^\dagger_{k,+} & \tilde{c}^\dagger_{k,-}\end{pmatrix}\begin{pmatrix}\omega_k-\mu-\Delta & i\,\eta_k \\ -i\,\eta_k & \omega_k-\mu+\Delta\end{pmatrix}\begin{pmatrix}\tilde{c}_{k,+}\\ \tilde{c}_{k,-}\end{pmatrix}. \tag{5.7}$$

This Hamiltonian can be diagonalized by introducing the operators of canonical modes $\Gamma_k = \{\gamma^c_k, \gamma^v_k\}^T$ via $\Gamma_k = V^\dagger_k\tilde{c}_k$, where the unitary matrix V_k is

$$V_k = \begin{pmatrix}\cos\phi_k & i\sin\phi_k \\ i\sin\phi_k & \cos\phi_k\end{pmatrix}, \tag{5.8}$$

and $\cos\phi_k = \sqrt{\frac{1}{2}\big(1-\frac{\Delta}{\sqrt{\Delta^2+\eta_k^2}}\big)}$, $\sin\phi_k = -\sqrt{\frac{1}{2}\big(1+\frac{\Delta}{\sqrt{\Delta^2+\eta_k^2}}\big)}$. The mean-field Hamiltonian in terms of canonical modes is $\mathcal{H}_{MF} = \Gamma^\dagger_k\Lambda_k\Gamma_k$. where $\Lambda_k = V^\dagger_k H_{MF}V_k$ is diagonal. In explicit form

$$\mathcal{H}_{MF} = \sum_k (E^c_k\gamma^{c\dagger}_k\gamma^c_k + E^v_k\gamma^{v\dagger}_k\gamma^v_k), \tag{5.9}$$

and $E^c_k = \omega_k + \sqrt{\Delta^2+\eta^2_k}$, $E^v_k = \omega_k - \sqrt{\Delta^2+\eta^2_k}$.

A comment is in order here. The expressions for E^c_k and E^v_k are in the rotated coordinate frame. At $\Delta = 0$, $E^{c,v}_k = \epsilon_\pm = \epsilon_{\mathbf{k}\pm\mathbf{K}/2}$. A hot spot location $\mathbf{k}_{hs}$ in the rotated coordinate frame is defined as a point for which $\epsilon_{\mathbf{k}_{hs}+\mathbf{K}/2} = \epsilon_{\mathbf{k}_{hs}-\mathbf{K}/2} = 0$, hence $E^c_{k_{hs}} = E^v_{k_{hs}} = 0$. However, once we shift $\mathbf{k}_{hs}$ by $\mathbf{K}$, we find that $E^{c,v}_{k_{hs}+\mathbf{K}}$ is

either zero or $\epsilon_{\mathbf{k}_{hs}+3\mathbf{K}/2}$. The latter is numerically small at half-filling but strictly vanishes only for a certain hole doping. In the SDW state we then have $|E^{c,v}_{k_{hs}}| = \Delta$, but $|E^{c,v}_{k_{hs}+\mathbf{K}}|$ is not exactly Δ, with some small correction at order t. Below we neglect this complication and approximate $|E^{c,v}_{k_{hs}+\mathbf{K}}|$ by Δ.

The chemical potential μ and the SDW order parameter Δ should be obtained self-consistently as a function of the interaction strength U. At small U/t, self-consistent analysis yields $\Delta = 0$, i.e., a paramagnetic Fermi liquid state with large Fermi surface remains stable down to $T = 0$. This is similar to the case of the Hubbard model on a square lattice with both nearest and next nearest neighbor hopping. Once the interaction exceeds a threshold, $U > U_c$, the SDW order develops. This changes the Fermi surface topology to a set of small electron and hole pockets. The sizes of electron and hole pockets shrinks as U increases. At half-filling, both electron and hole pockets vanish the large U limit, i.e., all excitations are gapped: there is a filled valence band with energy $E^v_k = \omega_k - \sqrt{\Delta^2 + \eta_k^2}$ and an empty conduction band with energy $E^c_k = \omega_k + \sqrt{\Delta^2 + \eta_k^2}$. Such a state can be adiabatically connected to a Mott insulator, which, strictly speaking, does not require magnetic order. Away from the half-filling, the size of the remaining electron and hole pockets is determined by the Luttinger theorem for a SDW state [187]. We show the evolution of Fermi surface geometry with increasing U in Fig. 5.3.

Across the transition at U_c, the spectral function at the "hot spot" $A_{c,v}(k_{hs}, \omega) = -\frac{1}{\pi}\mathrm{Im}\, G_{c,v}(k_{hs}, \omega)$ changes qualitatively (see Fig. 5.1). At $\Delta = 0$, $A_c(k_{hs}, \omega) = A_v(k_{hs}, \omega) = 1/(\omega + i\delta)$, i.e., the spectral function is strongly peaked at $\omega = 0$. At a finite Δ, $G^{(0)}_{c,v}(k_{hs}, \omega) = \frac{1}{\omega + i\delta \mp \Delta}$, and the maximum shifts to $\omega = \pm\Delta$. In the large U limit, $\Delta = U\bar{S}$, i.e., the distance between the two peaks is Hubbard U, like in a Mott insulator.

5.2.2 Magnon-fermion interaction

To obtain the Green's function renormalized by thermal fluctuations in the SDW state, one should first find the effective magnon-fermion interaction vertex.

The magnon propagator can be obtained by either the linear spin wave analysis [186] or by evaluating the spin susceptibility within the generalized RPA framework in the large U limit [178]. We present the details of the spin wave analysis in Appendix C and here list the results and use physical arguments to rationalize them.

We set the 120° coplanar order to be in the $x - z$ plane and move to rotating coordinate frame, where the order becomes ferromagnetic.

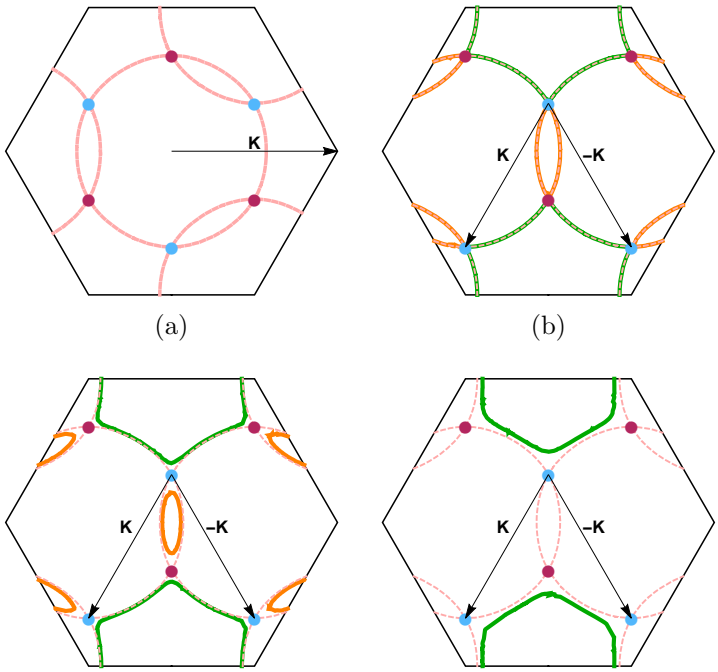

Figure 5.3: (From [86]) The evolution of Fermi surface at $T + 0$ as the SDW order Δ develops upon increasing of the Hubbard U. For definiteness, we consider the case of weak hole doping. (a): The Fermi surface at $U = U_c$, $\Delta = 0^+$ in the original (not rotated) coordinate frame. The Fermi surface for one spin component is shifted by $\mathbf{K}$ compared to the Fermi surface for the other spin component. (b)-(d): The evolution of the Fermi surface in the rotated (spin-dependent) coordinate frame. The Fermi surfaces are shifted by $\mathbf{K}/2$ compared to those in panel (a) (see Eq. (5.3)). The blue and red dots mark the hot spots – the points where the two Fermi surfaces cross at $\Delta = 0^+$. The three hot spots in blue (red) are connected by the wave vector $\pm K$. Panel (b) – Fermi surfaces at $U = U_c$, $\Delta = 0^+$, panels (c) and (d) – Fermi surfaces at $U > U_c$, $\Delta > 0$. Both electron (orange line) and hole (green line) pockets shrink as Δ increases.

The local coordinates for the A, B, C sublattices are shown in Fig. 5.4(a). A straightforward symmetry analysis shows that in the SDW state there should be three gapless Goldstone modes, one associated with in-plane fluctuations, and two associated with out-of-plane fluctuations [185, 186]. From Fig. 5.4(b) we see that the in-plane transverse spin wave is along $\tilde{x}$ for all sub-lattices, which means that this Goldstone mode comes from fluctuations of $S^{\tilde{x}}$ at the Γ point. The corresponding dynamical susceptibility is

$$\chi^{\tilde{x}\tilde{x}}(q, \Omega) = \frac{\rho_\parallel}{\Omega^2 - v_\parallel^2 q^2}. \tag{5.10}$$

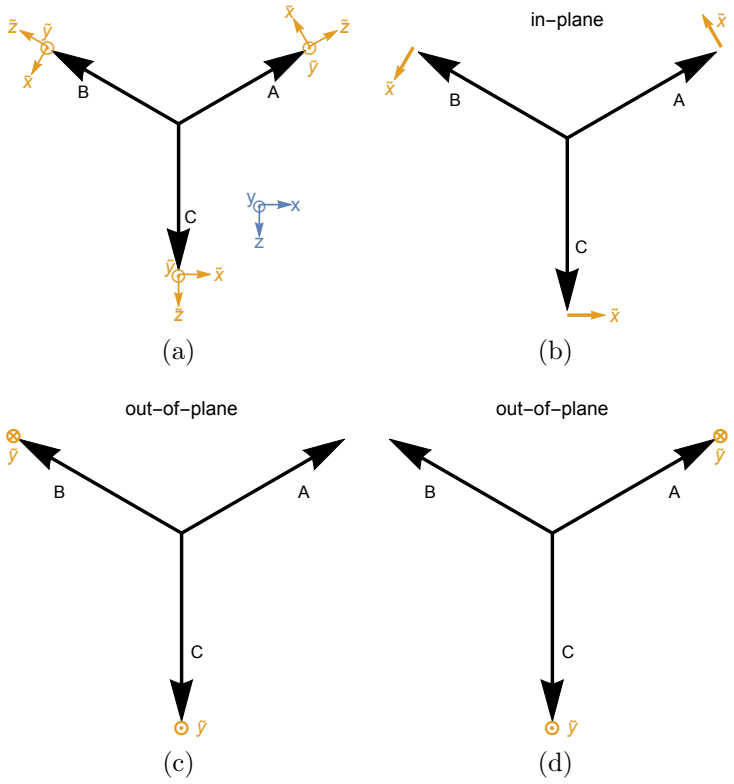

Figure 5.4: (From [86]) (a) Magnetic order (black arrow) on three sublattices A, B, C. Blue and orange arrows indicate, respectively, global and local coordinates in spin space. (b-d) Momentum and spin components for the three Goldstone modes [see Eq. (5.13)]. The in-plane Goldstone mode in (b) is described by the pole in $\chi^{\tilde{x}\tilde{x}}(\Gamma)$, and the linear combinations of the out-of-plane modes in (c) and (d) are described by the poles in $\chi^{\tilde{y}\tilde{y}}(\pm K)$.

The other two Goldstone modes correspond to out-of-plane spin wave fluctuations. Figs. 5.4(c,d) show two independent modes. In one of them spins on the A sublattice are fixed, and spins on the B and C sublattices rotate along $y(\tilde{y})$ in the opposite direction. In the other mode, spins on the B sublattice are fixed, and spins on the A and C sublattices rotate along y in the opposite direction. The linear combinations of the two fluctuations yield two Goldstone modes with equal velocities around $\pm\mathbf{K} = (\pm 4\pi/3, 0)$ in momentum space. The corresponding dynamical spin susceptibility is

$$\chi^{\tilde{y}\tilde{y}}(q \pm K, \Omega) = \frac{\rho_\perp}{\Omega^2 - v_\perp^2 q^2}. \tag{5.11}$$

In the rest of the Chapter, we drop the $\sim$ label for local coordinates unless there is ambiguity.

In Hamiltonian approach, static $\chi^{xx}(q,0) = \chi^{xx}(q)$ and $\chi^{yy}(q,0) = \chi^{yy}(q)$ de-

termine the effective static interaction between fermions, mediated by magnons. To get this interaction, we take the Hubbard interaction $\mathcal{H}_{int} = U\sum_i c^\dagger_{i,+}c_{i,+}c^\dagger_{i,-}c_{i,-} = \sum_i \frac{U}{2}(\hat{n}_{i,+}+\hat{n}_{i,-}) - \frac{U}{2}\hat{S}^2_i$, dress it by RPA renormalization, and keep the spin part of the dressed interaction [188] in the $\sigma^x\sigma^x$ and $\sigma^y\sigma^y$ channels. This yields

$$\begin{aligned}\mathcal{H}_{xx} &= -\frac{U^2}{N}\sum_{k,k',q}\chi^{xx}(q)c^\dagger_{k+q}\sigma^x c_k\, c^\dagger_{k'-q}\sigma^x c_{k'}\\ \mathcal{H}_{yy} &= -\frac{U^2}{N}\sum_{k,k',q}\chi^{yy}(q)c^\dagger_{k+q\pm K}\sigma^y c_k\, c^\dagger_{k'-q\mp K}\sigma^y c_{k'}\end{aligned} \tag{5.12}$$

We now introduce the magnon operators $(e^x_q,\, e^y_{q\pm K})$ via

$$\begin{aligned} i\int \mathrm{d}t e^{i\Omega t}\langle Te^{\tilde{x}}_{-q}(t)e^{\tilde{x}}_q(0)\rangle &= \chi^{\tilde{x}\tilde{x}}(q,\Omega) = \frac{\rho_\parallel}{\Omega^2 - v^2_\parallel q^2}\\ i\int \mathrm{d}t e^{i\Omega t}\langle Te^{\tilde{y}}_{-q\mp K}(t)e^{\tilde{y}}_{q\pm K}(0)\rangle &= \chi^{\tilde{y}\tilde{y}}(q\pm K,\Omega) = \frac{\rho_\perp}{\Omega^2 - v^2_\perp q^2}\end{aligned} \tag{5.13}$$

A little experimentation shows that Eq. (5.12) are reproduced if we set magnon-fermion interaction to be

$$\mathcal{H}_{m-f} = -U\sqrt{\frac{2}{N}}\sum_{k,q}\left(c^\dagger_{k+q}\sigma^x c_k\,\hat{e}^x_q + c^\dagger_{k+q\pm K}\sigma^y c_k\,\hat{e}^y_{q\pm K}\right) \tag{5.14}$$

In terms of the conduction and valence fermions, the interaction near the hot spot can be approximated as

$$\begin{aligned}\mathcal{H}_{m-f} &= -U\sqrt{\frac{2}{N}}\sum_{k,q}\hat{e}^x_q(\gamma^{c\,\dagger}_{k+q}\gamma^v_k + \gamma^{v\,\dagger}_{k+q}\gamma^c_k)\\ &- iU\sqrt{\frac{2}{N}}\sum_{k,q}\hat{e}^y_{q\pm K}(\gamma^{c\,\dagger}_{k+q\pm K}\gamma^v_k - \gamma^{v\,\dagger}_{k+q\pm K}\gamma^c_k).\end{aligned} \tag{5.15}$$

We present this interaction graphically in Fig. 5.5. We use a double wavy line ($\approx\!\!\approx$) for magnon propagator and use a filled circle ($\bullet$) for magnon-fermion vertex with outgoing valence fermion ($\gamma^{v\dagger}$) and incoming conduction fermion (γ^c), and an empty circle ($\circ$) for the vertex with outgoing conduction fermion ($\gamma^{c\dagger}$) and incoming valence fermion (γ^v). From Eq. (5.15), the magnon-fermion vertex for $\hat{e}^y$ is purely imaginary, and is of opposite sign for $\bullet$ and $\circ$ vertices. This turns out important when we calculate the full Green's function at the two-loop and higher orders. The interaction terms involving only conduction or only valence fermions are small in q and will not be

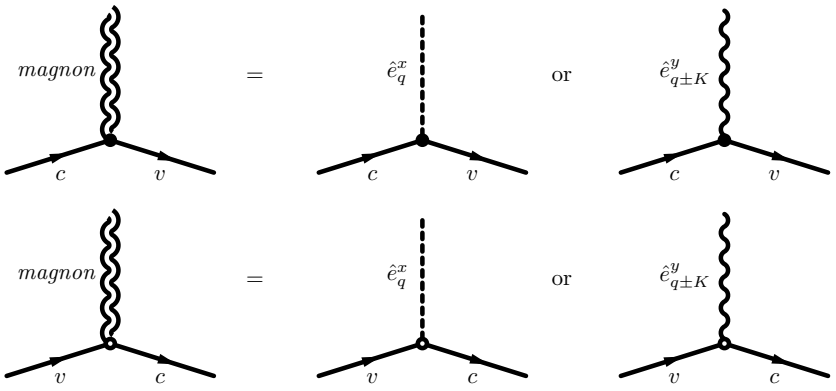

Figure 5.5: (From [86]) Magnon-fermion vertex. Double wavy line describes a magnon propagator with a generic momentum and spin component. Dashed and single wavy lines describe magnon propagators $\hat{e}^x_q$ near the Γ point and for magnon propagator $\hat{e}^y_{q\pm K}$ near the $\pm K$ points, respectively. We use filled $\bullet$ (hollow $\circ$) circles to label vertices with incoming (outgoing) conduction fermion and outgoing (incoming) valence fermion.

relevant to our analysis. The presence of q in these terms is consistent with the Adler principle, which states that the interaction between Goldstone bosons and fermions from the same branch should be of gradient type, to preserve the Goldstone theorem (see Ref. [189] for more discussions). Note that the strength of magnon-fermion interaction is of order Hubbard U.

5.3 The full fermionic Green's function in the SDW state

We now use the expressions for the quadratic SDW Hamiltonian, Eq. (5.7), and the magnon-fermion interaction, Eq. (5.15), and obtain the expression for the full fermionic propagator $G^{c,v}(k_{hs}, \omega)$ at a finite temperature T. We show explicitly that the leading corrections come from the exchange of thermal transverse spin wave fluctuations. These corrections are logarithmically singular in quasi-2D systems, and n-loop correction scales as $|\log \epsilon|^n$, where, we remind, ϵ measures the deviation from pure two-dimensionality and serves as the infrared cutoff to regularize the divergence.

The fully renormalized Green's function at one of the hot spots is expressed as

$$G^{c,v}(k_{hs}, i\omega_n, z) = G^{c,v\,(0)}(k_{hs}, i\omega_n) \sum_{n=0}^{\infty} \mathcal{C}_n(z)(\beta U^2)^n \left[G^{v,c\,(0)}(k_{hs}, i\omega_n) G^{c,v\,(0)}(k_{hs}, i\omega_n)\right]^n, \tag{5.16}$$

where the combinatoric factor $\mathcal{C}_n(z)$ increases factorially with n and depends on the ratio of in-plane and out-of-plane spin-wave susceptibilities. The factor $\beta = \frac{\pi T}{\mathcal{A}_{BZ}} |(\chi_{\parallel} - 2\chi_{\perp})| |\log \epsilon|$ measures the strength of thermal fluctuations (see below).

To simplify the presentation below, we express the fully renormalized Green's function as

$$G^{c,v}(k_{hs}, i\omega_n, z) = G^{c,v\,(0)}(k_{hs}, i\omega_n) + [G^{c,v\,(0)}(k_{hs}, i\omega_n)]^2 \tilde{\Sigma}(k_{hs}, i\omega_n), \tag{5.17}$$

where $\tilde{\Sigma}(k_{hs}, i\omega_n)$ can be evaluated order by order in terms of β. We will use $\tilde{\Sigma}^{(m)}(k_{hs}, i\omega_n)$ to label the m^{th}-loop correction. Note that $\tilde{\Sigma}^{(m)}(k_{hs}, i\omega_n)$ is not equivalent to the m^{th}-loop self-energy as it includes both irreducible and reducible diagrams, which we will count on equal footings. Below we will use the term "reducible self-energy" in reference to $\tilde{\Sigma}$.

5.3.1 Perturbation theory at one-loop order

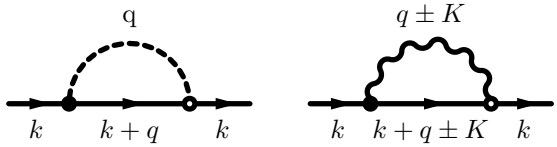

Figure 5.6: One-loop self-energy diagrams from the exchange of thermal transverse spin fluctuations.

The fermion (reducible) self-energy in Matsubara frequency at one-loop order is

$$\begin{aligned} &\tilde{\Sigma}^{c,v\,(1)}(k, i\omega_n) = \\ &- U^2 \frac{T}{N} \sum_{q,m,j} \chi^{jj}(q, i\Omega_m) G^{v,c\,(0)}(k+q, i\Omega_m + i\omega_n) \end{aligned} \tag{5.18}$$

The two singular contributions to $\Sigma^{c,v\,(1)}(k, i\omega_n)$ come from xx and yy components of the susceptibility. The contribution from $\chi^{xx}(q, i\Omega)$ to the leading logarithmical

order is

$$\begin{aligned}
&\tilde{\Sigma}^{c,v\,(1a)}(k,i\omega_n) \\
&= -U^2\frac{T}{N}\sum_{q,m}\frac{\rho_\parallel}{(i\Omega_m)^2-v_\parallel^2q^2}\frac{1}{i\Omega_m+i\omega_n-E^{v,c}_{k+q}} \\
&\approx -U^2\frac{T}{N}\sum_{q,m=0}\frac{\rho_\parallel}{-v_\parallel^2q^2}\frac{1}{i\omega_n-E^{v,c}_{k+q}} \\
&= U^2\frac{\rho_\parallel T}{v_\parallel^2}\int\frac{\mathrm{d}^2q}{\mathcal{A}_{BZ}}\frac{1}{q^2}\frac{1}{i\omega_n-E^{v,c}_{k+q}} \\
&\approx U^2\frac{\pi\rho_\parallel T}{v_\parallel^2\mathcal{A}_{BZ}}|\log\epsilon|\frac{1}{i\omega_n-E^{v,c}_{k}} = \frac{\beta_1U^2}{i\omega_n-E^{v,c}_{k}},
\end{aligned} \tag{5.19}$$

where we define $\beta_1 = \frac{\pi\rho_\parallel T}{v_\parallel^2\mathcal{A}_{BZ}}|\log\epsilon| = \frac{\pi\chi_\parallel T}{\mathcal{A}_{BZ}}|\log\epsilon|$. The contributions from non-zero bosonic Matsubara frequencies are finite, and we neglect them. The contribution from $\chi^{yy}(q\pm K,i\Omega)$ is, similarly,

$$\begin{aligned}
\tilde{\Sigma}^{c,v\,(1b)}(k,i\omega_n) &\approx U^2\frac{\pi\rho_\perp T}{v_\perp^2\mathcal{A}_{BZ}}|\log\epsilon|\frac{1}{i\omega_n-E^{v,c}_{k\pm K}} \\
&= \frac{\beta_2U^2}{i\omega_n-E^{v,c}_{k\pm K}},
\end{aligned} \tag{5.20}$$

where $\beta_2 = \frac{\pi\rho_\perp T}{v_\perp^2\mathcal{A}_{BZ}}|\log\epsilon| = \frac{\pi\chi_\perp T}{\mathcal{A}_{BZ}}|\log\epsilon|$. At a hot spot, $\mathbf{k}=\mathbf{k}_{hs}$, $E^{v,c}_{\mathbf{k}_{hs}} = E^{v,c}_{\mathbf{k}_{hs}+\mathbf{K}} = \Delta$. The sum of the two singular contributions then gives $\tilde{\Sigma}^{c,v\,(1)}(k,i\omega_n) = \frac{(\beta_1+2\beta_2)U^2}{i\omega_n-E^{v,c}_{k_{hs}}}$. We will see later that it is convenient to define $\beta = |\beta_1-2\beta_2|$ and re-express $\tilde{\Sigma}^{c,v\,(1)}(k,i\omega_n)$ as $\tilde{\Sigma}^{c,v\,(1)}(k,i\omega_n) = \left(\frac{\beta_1+2\beta_2}{\beta}\right)\beta U^2G^{v,c\,(0)}(k_{hs},i\omega_n)$.

5.3.2 Perturbation theory at two-loop order

The reducible self-energy at the two-loop order is obtained by summing over $27 = 3^2\,3!!$ diagrams, where $(2n-1)!!\to 3!!$ counts the number of diagrams with different topology [see Fig. 5.7(a)]. As there are three Goldstone modes, there are $3^n\to 3^2$ diagrams in each topology. The overall factor for each diagram is β_1 or β_2, like for one-loop diagrams, but the sign is either plus or minus. To explain the origin of sign alternation, consider the crossing diagram in Fig. 5.7(b) as an example. Because the magnon-fermion vertex for $\hat{e}^y$ is imaginary [see Eq. (5.15)], one can show that the two-loop Green's function from magnon propagator of $\hat{e}^y$ (wavy line) has prefactor $1 = (\pm i)(\mp i)$ when ending with vertices of the opposite type ($\circ\approx\!\!\approx\bullet$ or $\bullet\approx\!\!\approx\circ$) as the

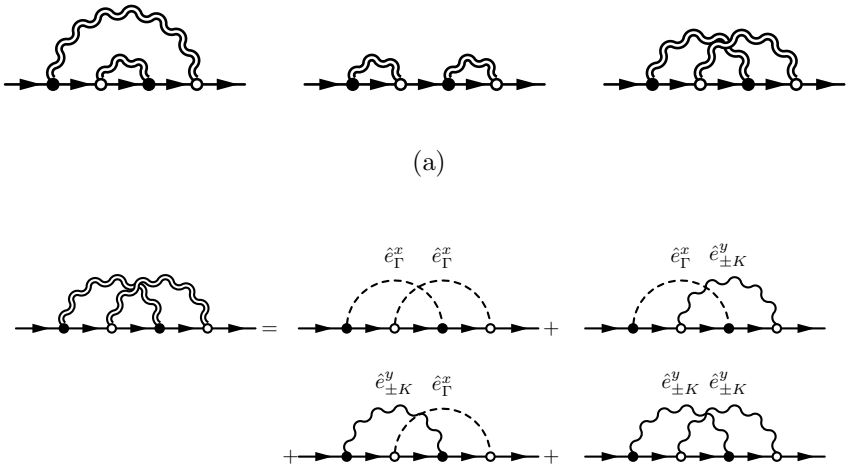

Figure 5.7: (a) The generic structure of two-loop diagrams. (b) The two-loop crossing diagrams from three magnon Goldstone modes. The overall factors in these diagrams are, from left to right and top to bottom, β_1^2, $-2\beta_1\beta_2$, $-2\beta_1\beta_2$, $(-2\beta_2)^2$.

magnon-fermion vertices associated with $\hat{e}^y$ contribute to a term $(i\gamma^{c\dagger}\gamma^v)(-i\gamma^{v\dagger}\gamma^c)$ in the expansion. Whereas it has prefactor $-1 = (\pm i)(\pm i)$ when ending with vertices of the same type ($\bullet\approx\bullet$ or $\circ\approx\circ$) as the term takes a form $(i\gamma^{c\dagger}\gamma^v)(i\gamma^{c\dagger}\gamma^v)$ or $(-i\gamma^{v\dagger}\gamma^c)(-i\gamma^{v\dagger}\gamma^c)$. On the other hand, magnon propagator of $\hat{e}^x$ (dashed line) has the same prefactor U^2 for both the two ways that vertices are connected. Following these rules, we find that the two-loop reducible self-energy from crossing diagrams is

$$\tilde{\Sigma}^{c,v\,(2,crossing)}(k, i\omega_n) = (\beta_1 - 2\beta_2)^2 \times (U^2)^2 G^{v,c\,(0)}(k_{hs}, i\omega_n)^2 G^{c,v\,(0)}(k_{hs}, i\omega_n). \tag{5.21}$$

Similarly, we find that the reducible self-energy from non-crossing diagrams [the last two diagrams in Fig. 5.7(a)] is

$$\tilde{\Sigma}^{c,v\,(2,non-crossing)}(k, i\omega_n) = 2(\beta_1 + 2\beta_2)^2 \times (U^2)^2 G^{v,c\,(0)}(k_{hs}, i\omega_n)^2 G^{c,v\,(0)}(k_{hs}, i\omega_n). \tag{5.22}$$

The total reducible self-energy at the two-loop order is

$$\tilde{\Sigma}^{c,v\,(2)}(k, i\omega_n) = \mathcal{C}_2(\beta U^2)^2 G^{v,c\,(0)}(k_{hs}, i\omega_n)^2 G^{c,v\,(0)}(k_{hs}, i\omega_n), \tag{5.23}$$

where $\beta = |\beta_1 - 2\beta_2|$ and $\mathcal{C}_2 = 1 + 2\left(\frac{\beta_1+2\beta_2}{\beta}\right)^2$.

5.3.3 perturbation theory at n^{th}-loop

Following the same procedure of computing the prefactors for the diagrams in which magnon propagators are connected by vertices of the same type or of opposite types, we find the reducible self-energy at order n to be

$$\tilde{\Sigma}^{c,v\,(n)}(k, i\omega_n) = \mathcal{C}_n(z)(\beta U^2)^n G^{v,c\,(0)}(k_{hs}, i\omega_n)^n G^{c,v\,(0)}(k_{hs}, i\omega_n)^{n-1}, \tag{5.24}$$

where

$$z = \frac{\beta_1 + 2\beta_2}{\beta} = \frac{\chi_\parallel + 2\chi_\perp}{|\chi_\parallel - 2\chi_\perp|}, \tag{5.25}$$

and the coefficient $\mathcal{C}_n(z)$ for $n = 2m$ even and $n = 2m+1$ odd is expressed as (see Appendix C for details):

$$\begin{aligned} \mathcal{C}_{2m}(z) &= \sum_{l=0}^{m} \Big[\frac{(2m)\,!}{(2m-2l)\,!!}\Big]^2 \frac{z^{2l}}{(2l)\,!}, \\ \mathcal{C}_{2m+1}(z) &= \sum_{l=0}^{m} \Big[\frac{(2m+1)\,!}{(2m-2l)\,!!}\Big]^2 \frac{z^{2l+1}}{(2l+1)\,!}, \end{aligned} \tag{5.26}$$

where l counts the number of magnon propagators ($2l$ for n even, $2l+1$ for n odd) which connect vertices of opposite type $\circ\approx\!\!\approx\bullet$ or $\bullet\approx\!\!\approx\circ$.

Summing up contributions from all loop orders, we find that the full fermionic Green's function can be expressed as

$$G^{c,v}(k_{hs}, i\omega_n, z) = G^{c,v\,(0)}(k_{hs}, i\omega_n) \sum_{n=0}^{\infty} \mathcal{C}_n(z)(\beta U^2)^n \left[G^{v,c\,(0)}(k_{hs}, i\omega_n) G^{c,v\,(0)}(k_{hs}, i\omega_n)\right]^n. \tag{5.27}$$

where $\mathcal{C}_0 = 1$ (this also follows from Eq. (5.26), if we set $m = 0$).

We see from Eq. (5.25) that the value of z depends on microscopic details, which

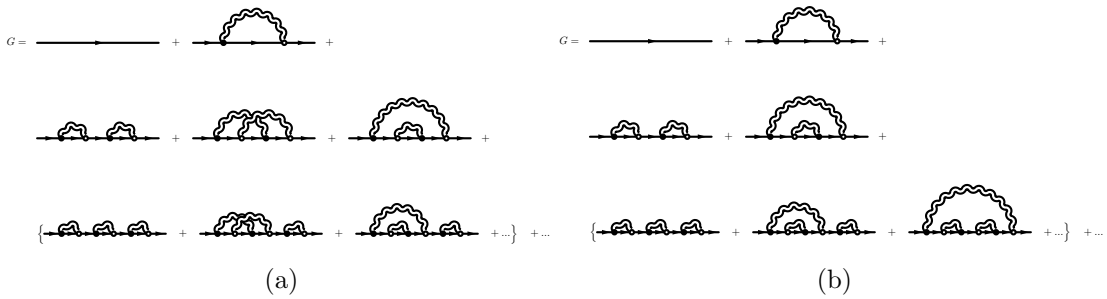

Figure 5.8: The structure of the diagrammatic series for the cases of (a) $z = 1$ and (b) $z = \infty$.

set the ratio of the susceptibilities. In the large U limit, the Hubbard model is well approximated by the nearest-neighbor Heisenberg model [190, 191]. For the latter, spin-wave calculations done at large S (the case reproduced by taking $2S$ flavors of fermions) yield $\chi_\parallel = \frac{2}{9\sqrt{3}Ja^2}(1 - \frac{0.449}{2S})$, $\chi_\perp = \frac{2}{9\sqrt{3}Ja^2}(1 - \frac{0.285}{2S})$ [186]. Using these expressions we find $z = 3 - \frac{0.32}{S} + \mathcal{O}(1/S^2)$. At smaller U, the value of z changes, because there appear additional terms in the effective spin Hamiltonian, and, in principle, can be any number. In particular, $z = 1$ when $\chi_\parallel = 0$ or $\chi_\perp = 0$; $z = \infty$ when $\chi_\perp = \chi_\parallel/2$.

For these two limiting cases, the combinatoric factor $\mathcal{C}_n(z)$ can be obtained in a closed form, as a function of n (as opposed to the sum for a generic z, as in Eq. (5.26)). For $z = 1$, there is no distinction between magnon propagators which connect vertices of opposite types, $\circ\!\approx\!\bullet$, $\bullet\!\approx\!\circ$ or of the same type, $\circ\!\approx\!\circ$, $\bullet\!\approx\!\bullet$. For n-loop diagrams, there are $2n$ vertices, thus there are $(2n-1)!!$ topologically distinct diagrams [see Fig. 5.8(a)]. In this situation, $\mathcal{C}_n(z = 1) = (2n-1)!!$. In the opposite limit $z \to \infty$, we need to introduce β' via $\beta = \frac{\beta'}{z} \to 0$, and keep β' as a constant. The most relevant term in Eq. (5.26) at $z \to \infty$ is the one with $l = m$. The corresponding diagrams contain only magnon propagators connecting vertices of the opposite type ($\circ\!\approx\!\bullet$ and $\bullet\!\approx\!\circ$). At n^{th}-loop order, there are $n!$ topologically distinct diagrams [see Fig. 5.8(b)], so $\beta^n \mathcal{C}_n(z = \infty) = n!\beta'^n$, i.e., $\mathcal{C}_n(z = \infty) \to n!$.

We note in passing that the structure of multi-loop corrections to a fermionic propagator for $z = 1$ and for $z = \infty$ is the same as quasi-1D models with CDW order/fluctuations. The case $z = 1$ is realized at half-filling, when the ordering wave vector is $Q = \pi$). The case $z = \infty$ is realized in generic filling [179–182]. To our knowledge, there have been no prior analysis of a generic z, only specific cases have been considered. In our case, the value of z is determined by ratio of $\chi_\parallel/\chi_\perp$ and can be arbitrary in the interval $[1, \infty)$. In the next section we analyze how the spectral

function behaves for different z.

5.4 The spectral function

5.4.1 Evaluation

The spectral function is defined as $A^{c,v}(k_{hs},\omega) = -\frac{1}{\pi}\,\mathrm{Im}\,G^{c,v}(k_{hs},\omega+i\delta)$, where ω is a real frequency. Our goal is to evaluate $A^{c,v}(k_{hs},\omega)$ analytically, starting from Eqs. (5.26) and (5.27). The key technical challenge is to perform the summation over n in Eq. (5.27) in a situation when $\mathcal{C}_n(z)$ is not expressed in a closed form. We note that because $\mathcal{C}_n(z) \sim \mathcal{O}(n!)$, a numerical computation of $A^{c,v}(k_{hs},\omega)$ is quite challenging on its own.

Our strategy is to first sum over l in Eq. (5.26), and express $\mathcal{C}_n(z)$ in an integral form as

$$\mathcal{C}_n(z) = \frac{n!}{2^n 2\pi i}\oint^{(0+)} \mathrm{d}v\,\big(\frac{1}{v}\big)^{n+1}\frac{(1+2zv)^n}{\sqrt{1-4v^2}} \tag{5.28}$$

for $n \in \mathbb{Z}$ ($\oint^{(0+)}$ means the contour integral goes around the pole at $v=0$ counter-clockwisely). Eq. (5.28) makes the analytic summation over n in Eq. (5.27) possible, as n only appears as an overall factor $n!$ and as an exponent in the integrand. Summing over n and converting from Matsubara to real frequency ($i\omega_m \to \omega + i\delta$), we find the spectral function in the form of a single integral (see Appendix C for details).

$$A^{c,v}(k_{hs},\omega) = \frac{1}{\pi}\Big|\frac{1}{\omega \mp \Delta}\Big| \int_{\frac{1}{(z+1)\,u_\omega}}^{\frac{1}{(z-1)\,u_\omega}} \mathrm{d}t\, e^{-t}\,\frac{1}{\sqrt{(u_\omega\, t)^2 - (1-u_\omega\, t\, z)^2}}\Theta(u_\omega), \tag{5.29}$$

where $u_\omega = \frac{\beta U^2}{\omega^2-\Delta^2}$ and $\Theta(u_\omega)$ is the Heaviside step function. Eq. (5.29) is the main result of this Chapter. In the next section we analyze qualitative features of the spectral function for different z.

5.4.2 Results

We can extract from Eq. (5.29) a few generic properties of the spectral function.

- The presence of the Heaviside step function $\Theta(\frac{\beta U^2}{\omega^2-\Delta^2})$ on the r.h.s. of Eq. (5.29) means that $A^{c,v}(k_{hs},\omega)$ vanishes for $\omega \in (-\Delta,\Delta)$, i.e., the SDW order parameter defines the real gap at a hot spot.

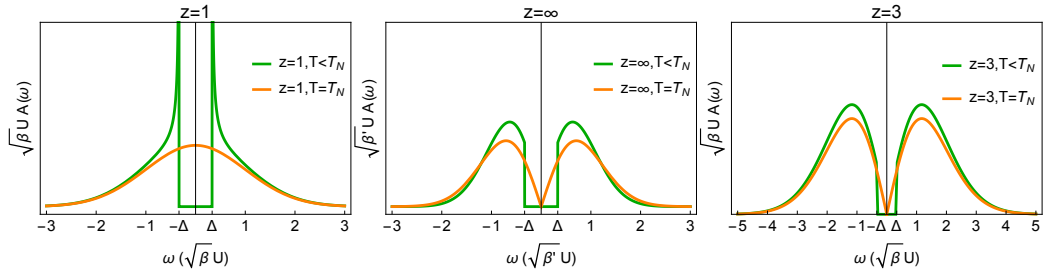

Figure 5.9: (From [86]) The spectral function at a hot spot for different $z = |\frac{\chi_{\parallel} - 2\chi_{\perp}}{\chi_{\parallel} + 2\chi_{\perp}}|$. This spectral function includes the effects of series of scattering by transverse thermal fluctuations. Green lines – deep in the ordered state, $T \ll T_N$; orange lines – at $T = T_N$, when $\Delta = 0^+$. Panels (a)-(c) are for $z = 1$, $z = \infty$, and $z = 3$.

- At the point where SDW order disappears, $\Delta = 0$ and $u_\omega = \frac{\beta U^2}{\omega^2}$. One can understand whether at this point the system displays a pseudogap behavior or a conventional Fermi liquid behavior by analyzing how the spectral function behaves at $\omega \sim 0$. When $z > 1$, the integral is bounded in the ultra-violet, and a straightforward analysis shows that $A^{c,v}(k_{hs}, \omega) \sim \omega$, i.e., the maximum of $A^{c,v}(k_{hs}, \omega)$ is at a finite frequency. This implies that the system displays a pseudogap behavior. At $z = 1$, the upper bound of the integral becomes infinite ($\frac{1}{(z-1)u_\omega} \to \infty$). Then $A^{c,v}(k_{hs}, \omega = 0)$ doesn't vanish. One can expand in ω and check that $A^{c,v}(k_{hs}, \omega)$ has a maximum at $\omega = 0$. This is the expected behavior in an ordinary Fermi liquid. We verified the dichotomy between the cases $z > 1$ and $z = 1$ by analytical calculations for $z = 1$ and $z = \infty$ and numerical calculations for an arbitrary $z \in (1, \infty)$, as we show below.

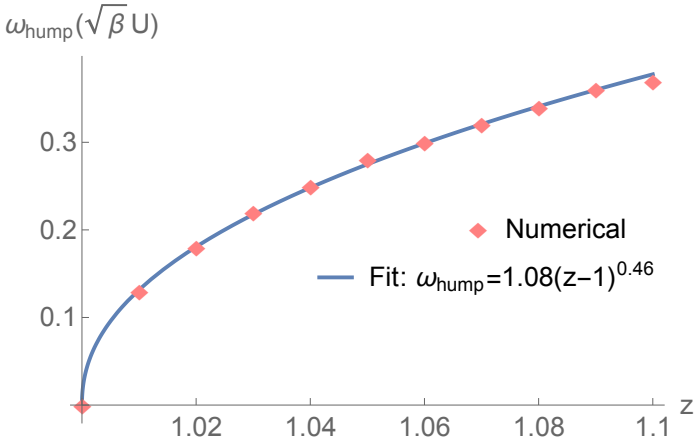

Figure 5.10: (From [86]) The position of the hump, ω_{hump}, as a function of z.

Analytical result at $z = 1$. At $z = 1$, the upper bound of the integral goes to ∞ and the integral in Eq. (5.29) can be evaluated analytically. The result is

$$\begin{aligned} & A^{c,v}(k_{hs}, \omega) \\ & = \frac{1}{\pi}\Big|\frac{1}{\omega \mp \Delta}\Big| \int_{\frac{1}{2u_\omega}}^{\infty} \mathrm{d}t\, e^{-t} \frac{1}{\sqrt{2u_\omega t - 1}} \Theta(u_\omega) \\ & = \frac{1}{\pi}\Big|\frac{1}{\omega \mp \Delta}\Big| \int_{0}^{\infty} \mathrm{d}\eta\, \frac{1}{2u_\omega} e^{-\frac{\eta+1}{2u_\omega}} \frac{1}{\sqrt{\eta}} \Theta(u_\omega) \\ & = \frac{1}{\pi}\Big|\frac{1}{\omega \mp \Delta}\Big| \sqrt{\frac{\pi}{2u_\omega}} e^{-\frac{1}{2u_\omega}} \Theta(u_\omega) \\ & = \Theta(|\omega| - \Delta) \sqrt{\frac{1}{2\pi\beta U^2}} \sqrt{\Big|\frac{\omega \pm \Delta}{\omega \mp \Delta}\Big|} e^{-\frac{\omega^2 - \Delta^2}{2\beta U^2}}, \end{aligned} \tag{5.30}$$

The same result was obtained in Ref. [73]. We plot $A^{c,v}(k_{hs}, \omega)$ in Fig. 5.9(a). Taking the limit $\Delta \to 0$, we obtain

$$A^{c,v}(k_{hs}, \omega) = \sqrt{\frac{1}{2\pi\beta U^2}} e^{-\frac{\omega^2}{2\beta U^2}}. \tag{5.31}$$

We see that at $\Delta \to 0$ (i.e., at $T \to T_N$) the spectral function is peaked at $\omega = 0$. This implies, as we anticipated, that for $z = 1$ thermal fluctuations do not give rise to SDW precursors. We emphasize that this could not be anticipated from the few first terms in loop expansion of the reducible self-energy as these terms show little difference between $z = 1$ and larger values of z. In the SDW phase, the spectral weight is zero at $\omega \in (-\Delta, \Delta)$, has a peak at $\omega = \pm(\Delta + 0)$, and gradually decays at higher frequencies, i.e., it does not show peak/dip/hump structure. This is indeed consistent with the absence of a pseudogap at $T = T_N$.

Analytical result at $z = \infty$. The integral in Eq. (5.29) can be evaluated analytically also at $z \to \infty$. As we discussed before, in this limit one should introduce β' via $\beta = \frac{\beta'}{z}$ and keep β' finite. Expanding the upper and lower bounds of the integral in Eq. (5.29) as $\frac{1}{(z \mp 1)u_\omega} = \frac{\omega^2 - \Delta^2}{\beta' U^2}(1 \mp \frac{1}{z})$, and substituting into Eq. (5.29), we obtain after some algebra

$$A^{c,v}(k_{hs}, \omega) = \Theta(|\omega| - \Delta) \frac{|\omega \pm \Delta|}{\beta' U^2} e^{-\frac{\omega^2 - \Delta^2}{\beta' U^2}}. \tag{5.32}$$

This result is also obtained if we replace $\beta^n \mathcal{C}_n(z = \infty)$ by $n!\beta'^n$ and directly sum up over n. We show $A^{c,v}(k_{hs}, \omega)$ in Fig. 5.9 (b).

At $T = T_N$, we have

$$A^{c,v}(k_{hs}, \omega) = \frac{\omega}{\beta' U^2} e^{-\frac{\omega^2}{\beta' U^2}}. \tag{5.33}$$

We see that now the spectral function scales as $\sim \omega$ at small frequencies and has a maximum (a hump) at a frequency $\omega \sim \sqrt{\beta' U}$. This implies that at $T = T_N$ the system retains memory about an SDW state. As T increases above T_N, the maximum in the spectral function remains at a finite frequency over some range of T. This is a canonical pseudogap (precursor to magnetism) behavior.

Numerical results at $z \in (1, \infty)$. We found numerically that for any $z > 1$ the spectral function behaves qualitatively the same as at $z = \infty$. Fig. 5.9 (c) shows the spectral function for $z = 3$ (the value of z for our system at large U and large spin S, i.e., large number of fermionic flavors). As we said above, this "universality" is expected because the upper bound of the integral in Eq. (5.29) is finite, as long as $z > 1$. Then Eq. (5.29) can be simplified as

$$\begin{aligned} A^{c,v}(k_{hs}, \omega) &= \frac{1}{\pi} \Big| \frac{\Theta(u)}{\omega \mp \Delta} \Big| \int_{\frac{1}{(z+1)u}}^{\frac{1}{(z-1)u}} \mathrm{d}t \, e^{-t} \frac{1}{\sqrt{\left(\frac{1}{(z-1)u} - t\right)\left(t - \frac{1}{(z+1)u}\right)(z-1)u(1+z)u}} \\ &= \Theta(|\omega| - \Delta) \frac{|\omega \pm \Delta|}{\pi \beta U^2 \sqrt{(z-1)(z+1)}} \int_{\frac{1}{(z+1)u}}^{\frac{1}{(z-1)u}} \mathrm{d}t \, \frac{e^{-t}}{\sqrt{\left(\frac{1}{(z-1)u} - t\right)\left(t - \frac{1}{(z+1)u}\right)}}. \end{aligned} \tag{5.34}$$

At $T = T_N$, $A^{c,v}(k_{hs}, \omega)$ scales linearly with ω at small frequencies. This necessarily implies pseudogap behavior in some range of temperatures above T_N. We found numerically that a maximum (a hump) is located at $\omega \sim \sqrt{\beta} U$.

To understand the behavior near $z = 1$ we calculated numerically the position of the hump (ω_{hump}) at $T = T_N$, as a function of z. We show the result in Fig. 5.10. Observe that ω_{hump} increases quite rapidly, as $(z-1)^{0.46}$. This indicates that the pseudogap feature at $T = T_N$ is quite robust, as long as $z > 1$, while $z = 1$ should be viewed as a special case. However, we should note that varying the value of z changes the temperature where the hump starts to show up in the spectral function. In this Chapter, though an accurate analysis that maps the temperature $T \sim \beta$ with the order parameter Δ was not done, we can see the trend from a qualitative argument. On the one hand, $\omega_{hump} \sim (z-1)^{0.46} \sqrt{\beta} U$ increases with temperature. On the other hand, Δ decreases with temperature. As the hump shows up when $\omega_{hump} \gtrsim \Delta$, a higher temperature is needed to compensate for the smallness of $(z-1)^{0.46}$ as $z \to 1$.

5.4.3 Additional considerations

First, we note that the spectral function, which we obtained, doesn't have the coherent peak at $\omega = \pm\Delta$. This is an artifact of the approximation, in which we only include logarithmically singular contributions to the reducible self-energy from thermal spin fluctuations. A coherent peak at $\omega = \pm\Delta$ is recovered once we add contributions to the self-energy from quantum fluctuations and non-singular self-energy piece from thermal fluctuations. This issue has been addressed in Ref. [73]. We show the result of including these additional terms into the self-energy (and the spectral function) by dashed line in Fig. 5.2 (b).

Second, in this Chapter we considered the reducible self-energy due to exchange of transverse spin-wave fluctuations. As we said, such an exchange gives rise to series of logarithmically singular reducible self-energy terms. Deep inside the SDW phase, longitudinal spin fluctuations are gapped and contribute only little to the reducible self-energy. However, as the temperature increases towards T_N, the gap in the longitudinal fluctuations gets reduced. A more careful study at $T \lesssim T_N$ should take into account the contribution from longitudinal channel. Such analysis has been performed for a system on a square lattice [70, 71, 73], and the conclusion was that longitudinal fluctuations enhance the tendency towards precursor behavior. In mathematical terms, this happens because the combinatoric factor changes from $n!$ (only transverse fluctuations, $z \to \infty$), to $(2n+1)!!$ (transverse and longitudinal fluctuations). We note in this regard that our $\mathcal{C}_n(z)$ does not become $(2n+1)!!$ for any z. As a result, the behavior of spectral function near $\omega = 0$ changes from $\sim \omega$ to $\sim \omega^2$, and the energy of the hump increases. In our case (fermions on a triangular lattice) the analysis of the reducible self-energy from longitudinal fluctuations is more involved than in the case of square lattice, and we refrain from making a definite prediction. Still, it is possible that longitudinal fluctuations induce some precursor behavior near T_N even for $z = 1$.

Third, it is interesting to compare our non-perturbative solution for the spectral function with a conventional perturbative solution in which one restricts with the one-loop self-energy. In our computational approach, this implies that one includes irreducible diagrams for the Green's function at one-loop order and only reducible diagrams at higher orders. The perturbative result for the spectral function is then

$$A_k^{pert}(\omega) = \mathrm{Re}\, G^{(0)} \times \mathrm{Im} \sum_{n=0}^{\infty} u_\omega^n = \mathrm{Re}\, G^{(0)}\, \mathrm{Im}\, \frac{1}{1-u_\omega} = \pi\delta(1-u_\omega)\, \mathrm{Re}\, G^{(0)} \qquad (5.35)$$

where, we remind, $u_\omega = \frac{\beta U^2}{\omega^2 - \Delta^2}$. This result holds for any value of z. We see that $A_k^{pert}(\omega)$ has two δ-functional peaks at $\omega = \pm\sqrt{\Delta^2 + \beta U^2}$. The peak frequency remains finite at $\Delta = 0$, which implies that some evidence for a precursor to magnetism appears already within the perturbation theory. However, the full expression (Eqs. (C.18) and (C.21) in Appendix C), is more involved:

$$A_k(\omega) = \mathrm{Re}\, G^{(0)} \times \mathrm{Im} \sum_{n=0}^{\infty} \mathcal{C}_n(z) u_\omega^n$$
$$= \mathrm{Re}\, G^{(0)}\, \mathrm{Im} \int_{\frac{1}{(z+1)u_\omega}}^{\frac{1}{(z-1)u_\omega}} \mathrm{d}t\, e^{-t}\, \frac{1}{\sqrt{1-4v_0^2}} \frac{1}{1 - u_\omega\, t\, z}. \tag{5.36}$$

The most essential difference is that the full $A_k(\omega)$ has contributions not only from the pole but also from the branch cut (the $\frac{1}{\sqrt{1-4v_0^2}}$ term). The branch cut contribution gives rise to the incoherent part of the spectral function. Combining the pole and the branch cut contributions, we obtain both the gap below $\Delta(T)$ and the hump at an energy $\Delta(0) \approx U/2$ (and we recall that with respect to the renormalized $\mu(T)$, the hump is at energy of order J).

Fourth, there are certain visible similarities between the peak-dip-hump behavior in our theory (see dashed line in Fig. 5.2(b)) and in Eliashberg theory of superconductivity, induced by soft bosonic fluctuations. However, the underlining physics is different. In our case, the peak-dip-hump behavior emerges due to thermal (static) bosonic fluctuations. While in Eliashberg theory, this behavior is a feedback from the pairing by a dynamical boson (see e.g. Refs. [192–194]).

5.5 Summary

In this Chapter, we studied the effects of thermal fluctuations on the spectral function of hot fermions on a triangular lattice, in the 120° SDW state (the ordering momentum is $\mathbf{K} = (4\pi/3, 0)$).

We argued that the exchange of static Goldstone bosons between fermions in the valence and the conduction band gives rise to logarithmically singular self-energy corrections. We obtained fully renormalized Green's function by summing up infinite series of thermal reducible self-energy diagrams. In this sense, we went beyond a conventional perturbation theory, which in practice includes only a few leading terms in the series.

The key goal of our study was to understand whether the exchange of static ther-

mal bosonic fluctuations necessarily gives rise to pseudogap behavior, or the system may display a conventional Fermi liquid behavior despite that self-energy corrections are logarithmically singular. We argued that one can address this issue by studying fermions on a triangular lattice. Specifically, we showed that the contributions from in-plane and out-of-plane spin-wave fluctuations are not equivalent, and the strength of the self-energy renormalization depends on the ratio of in-plane and out-of-plane spin-wave susceptibilities $\chi_\parallel/\chi_\perp$. This ratio is an input parameter for low-energy theory, and by varying it one can study the changes in the structure of diagrammatic series for the reducible self-energy. When $\chi_\parallel/\chi_\perp \sim 1$, our calculations show that the behavior of the spectral function for a fermion at a hot spot ($\mathbf{k}_{hs}$ and $\mathbf{k}_{hs}+\mathbf{K}$ are both on the Fermi surface) is similar to that for the case of a square lattice and collinear (π,π) SDW order: there is a real gap below $\Delta(T)$ and a maximum (hump) at an energy of order Hubbard U (see Fig. 5.2). The hump persists at $T=T_N$, where Δ vanishes, and survives in some range of T above T_N. In this range the system displays a pseudogap behavior. On the other hand, when $\chi_\parallel/\chi_\perp \ll 1$ or $\chi_\parallel/\chi_\perp \gg 1$, the pseudogap behavior exists only near T_N. In the limiting case when $\chi_\parallel/\chi_\perp = 0$ or $\chi_\parallel/\chi_\perp = \infty$, there is no pseudogap behavior at any $T > T_N$, despite that perturbative self-energy corrections are logarithmically singular.

The calculations we presented in this Chapter can be readily extended to other microscopic models. The only requirement is to obtain the value of the *control parameter* for a specific model. Our results show that by looking at the structure of perturbation series one would be able to immediately conclude whether singular self-energy corrections lead to a pseudogap behavior, or to an ordinary Fermi liquid behavior. We emphasize in this regard that, unless special conditions ($z=1$) are satisfied, a magnetic pseudogap is present independent on the lattice geometry. This is consistent with the fact that pseudogap behavior near a magnetic transition has been seen in many different systems.

As a final remark, the key assumption in our computation is that thermal (static) fluctuations are dominant near a magnetic transition at a finite temperature. This assumption has been supported by 2D numerics for the Hubbard model on a square lattice [81]. We call for numerical studies of systems with different lattice geometries, that in each case will identify the dominant fluctuation contribution. We hope that, combined with our analytical results, this will push forward the understanding of the underlining mechanism of pseudogap physics in correlated electron systems.

Chapter 6

Summary and Outlook

The rapid progress in understanding the origins and consequences of emergent quantum phenomena in correlated electron systems is pushed by the advances in theoretical development, quantum material realization and experiment probes. Magnetism has been found to be a driving force in many examples.

In this dissertation, I discussed several aspects of magnetism in correlated electron systems.

In the strong coupling limit at half electron filling, the Mott insulating state can exhibit exotic magnetic phases, such as unconventional ordered state due to the "order from disorder" mechanism and quantum spin liquid with high entanglement. In Chapter 2, I present our study of the phase diagram of triangular lattice Heisenberg J_1-J_2 model in a magnetic field, which in different regimes of couplings and magnetic field, can exhibit a half-magnetization plateau described by the "order from disorder" mechanism or a disordered phase that may be smoothly connected to the quantum spin liquid state observed numerically at zero field. The smoking gun experimental evidence of a quantum spin liquid is still awaiting, and a combination of multiple indirect probes is valuable to understand the physical properties of its elementary excitations from multiple facets. In Chapter 3, I presented our study that showed that the quantized thermal Hall measurement performed in Kitaev materials requires a critical analysis due to the mixing of energy propagation between unconventional chiral edge modes and conventional bulk phonon modes.

Magnetism can also play an important role in a metal, which may develop competing orders as Fermi surface instabilities due to the interplay between magnetic fluctuation and other fluctuation channels such as superconductivity and charge fluctuation. In Chapter 4, I presented our study of a compensated metal on a hexagonal lattice in the spin-density-wave state. The response of the magnetic order to a mag-

netic field is fundamentally different from that in a Mott insulator, and the magnetic field triggers a time-reversal-invariant bond ordered state.

The transition between a Mott insulator with magnetic order and a normal metal by varying certain external parameter, such as temperature or the doping level away from half-filling, exhibits anomalies of the electronic properties. In Chapter 5, I presented our study of the pseudogap physics that shows maximum of spectral weight at finite energy away from the Fermi level due to magnetic fluctuations at finite temperature. In this study, we introduced a knob that controls the strength of the pseudogap behavior, and showed that the pseudogap feature is quite generic in a quasi-2D system with magnetic order. This study also finds a unique exception that the system doesn't exhibit any pseudogap physics.

Through the combined efforts in the theoretical, numerical and experimental communities, the studies of magnetism in correlated electron systems are progressing rapidly. I am particularly interested in the following few directions.

In the search for quantum spin liquid states, the relatively well developed theoretical models that can realize quantum spin liquid phase and lack of smoking gun experiment requires more efforts that bridge the two. By means of indirect measurement that couples the elementary excitations of a spin liquid to certain conventional mode, the data may reveal the unique symmetry and dynamical properties of the quantum spin liquid. For example, in an ongoing work, we examined the possibility of sound attenuation experiment in search for the low energy Majorana fermions with Dirac spectrum in Kitaev materials. It will be more revolutionary if new probe that serves to directly measure single excitation of a quantum spin liquid is made possible.

In the understanding of pseudogap physics, a clear path that leads to the pseudogap feature at zero temperature that explains well both the spectral and transport data remains missing. In another ongoing work, we examined the condition when a Fermi liquid coupled to the short range magnetic fluctuation can lead to the spectral weight which resembles the pseudogap data in experiments. On the other hand, a careful and critical analysis of the Hall measurement that goes beyond single particle picture will be highly desirable.

Appendix A

Appendix to Chapter 2

A.1 Holstein-Primakoff transformation

In this Appendix we review the basics of Holstein-Primakoff transformation and spin wave formalism. In the formulas below, N is defined as the number of sites in one sublattice, i.e. $N = \frac{N_{\text{tot}}}{n_{\text{bands}}}$. For example, for the three sublattice states, $n_{\text{bands}} = 3$, and $N = \frac{1}{3}N_{\text{tot}}$.

Spins polarized in the positive z direction are expressed in terms of Holstein-Primakoff (H-P) bosons as:

$$\begin{aligned} S^z_{\boldsymbol{r}}(\boldsymbol{z}) &= S - a^\dagger_{\boldsymbol{r}} a_{\boldsymbol{r}} \\ S^+_{\boldsymbol{r}}(\boldsymbol{z}) &= \sqrt{2S}\sqrt{1 - \frac{a^\dagger_{\boldsymbol{r}} a_{\boldsymbol{r}}}{2S}}\, a_{\boldsymbol{r}} \\ S^-_{\boldsymbol{r}}(\boldsymbol{z}) &= \sqrt{2S}\, a^\dagger_{\boldsymbol{r}} \sqrt{1 - \frac{a^\dagger_{\boldsymbol{r}} a_{\boldsymbol{r}}}{2S}} \end{aligned} \tag{A.1}$$

The spin operators $S^\alpha(\boldsymbol{l})$ in a local coordinate with the local z-axis along a vector $\boldsymbol{l} = \boldsymbol{z}\cos\theta - \boldsymbol{x}\sin\theta$ are related with $S^\alpha(\boldsymbol{z})$ defined in the global coordinate as [104]:

$$\begin{aligned} S^x(\boldsymbol{z}) &= \cos\theta S^x(\boldsymbol{l}) - \sin\theta S^z(\boldsymbol{l}) \\ S^y(\boldsymbol{z}) &= S^y(\boldsymbol{l}) \\ S^z(\boldsymbol{z}) &= \sin\theta S^x(\boldsymbol{l}) + \cos\theta S^z(\boldsymbol{l}) \end{aligned} \tag{A.2}$$

To express the Hamiltonian in terms of the H-P bosons, we expand $\sqrt{1 - a^\dagger_{\boldsymbol{r}} a_{\boldsymbol{r}}/2S}$ in powers of the bosons. For generic spin, due to the normal ordering of the bosons

in the expansion, e.g. $(a_r^\dagger a_r)^2 = a_r^\dagger a_r^\dagger a_r a_r + a_r^\dagger a_r$, $S_{\boldsymbol{r}}^+$ can be written as:

$$\begin{aligned} S_{\boldsymbol{r}}^+ &= \sqrt{2S}(1 - \frac{1}{4S}(1 + \frac{1}{8S} + \frac{1}{32S^2} + ...)a_{\boldsymbol{r}}^\dagger a_{\boldsymbol{r}})a_{\boldsymbol{r}} + \mathcal{O}(a^5) \\ &= \sqrt{2S}(1 + (\sqrt{1 - \frac{1}{2S}} - 1)a_{\boldsymbol{r}}^\dagger a_{\boldsymbol{r}})a_{\boldsymbol{r}} + \mathcal{O}(a^5) \end{aligned} \tag{A.3}$$

In the limit $S \gg 1$, keeping the leading order in $1/S$:

$$S_{\boldsymbol{r}}^+ \approx \sqrt{2S}(1 - \frac{1}{4S}a_{\boldsymbol{r}}^\dagger a_{\boldsymbol{r}})a_{\boldsymbol{r}} + \mathcal{O}(a^5) \tag{A.4}$$

The Hamiltonian in powers of the H-P bosons can be expanded as:

$$\mathcal{H} = \mathcal{H}^{(0)} + \mathcal{H}^{(1)} + \mathcal{H}^{(2)} + ... + \mathcal{H}^{(n)} + ... \tag{A.5}$$

$\mathcal{H}^{(0)}$ is the ground state energy. $\mathcal{H}^{(n)}$ is the normal ordered n-bosons term.

The quadratic term $\mathcal{H}^{(2)}$ can be written in the matrix form as:

$$\mathcal{H}^{(2)} = \frac{S}{2}\sum_{\boldsymbol{k}} \Psi_{\boldsymbol{k}}^\dagger H_{\boldsymbol{k}} \Psi_{\boldsymbol{k}} \tag{A.6}$$

where $\Psi_{\boldsymbol{k}} = \left(a_{\alpha,\boldsymbol{k}},\, a_{\alpha,-\boldsymbol{k}}^\dagger\right)^T$. To obtain the spin wave spectrum and the canonical eigenmodes, one can solve the eigenvalue problem of a matrix defined as $\mathcal{M}_{\boldsymbol{k}} = \tau_3 H_{\boldsymbol{k}}$. $\tau_3 \equiv \sigma_3 \otimes I_n$, σ_3 is the z-component of Pauli matrix that acts on the particle-hole conjugate space and I_n is the identity matrix of size n that acts on the n-sublattice space. To prove, define the $\Psi'_{\boldsymbol{k}}$ as the vector formed by eigenmodes. There must exist a matrix T such that $\Psi_{\boldsymbol{k}} = T\Psi'_{\boldsymbol{k}}$, the quadratic term in the Hamiltonian:

$$\mathcal{H}^{(2)} = \frac{1}{2}\sum_{\boldsymbol{k}} \Psi_{\boldsymbol{k}}^\dagger H_{\boldsymbol{k}} \Psi_{\boldsymbol{k}} = \frac{1}{2}\sum_{\boldsymbol{k}} \Psi_{\boldsymbol{k}}'^\dagger T^\dagger H_{\boldsymbol{k}} T \Psi'_{\boldsymbol{k}} \tag{A.7}$$

$K_{\boldsymbol{k}} = T^\dagger H_{\boldsymbol{k}} T$ is diagonal matrix. On the other hand, from the commutation relation of boson operator which reads as $[a_i^\dagger, a_j] = \delta_{i,j}$, we have $T\tau_3 T^\dagger = \tau_3$. Combing the two equations, we have:

$$\begin{aligned} \tau_3 K_{\boldsymbol{k}} = \tau_3 T^\dagger H_{\boldsymbol{k}} T &= \tau_3(\tau_3 T^{-1}\tau_3) H_{\boldsymbol{k}} T \\ &= T^{-1}\tau_3 H_{\boldsymbol{k}} T \end{aligned} \tag{A.8}$$

Thus solving for T and the eigenenergy of $H_{\boldsymbol{k}}$ is equivalent to the eigenvalue problem of matrix $\mathcal{M}_{\boldsymbol{k}} = \tau_3 H_{\boldsymbol{k}}$. *Q.E.D.*

Different branches of the magnon modes can decouple for certain types of ordered states, such as the stripe phase and 120° Neel phase discussed in the text. $\mathcal{H}^{(2)}$ can be written as:

$$\begin{aligned}\mathcal{H}^{(2)} &= \frac{S}{2}\sum_{\alpha}\phi^{\dagger}_{\alpha,\boldsymbol{k}}H_{\alpha,\boldsymbol{k}}\phi_{\alpha,\boldsymbol{k}}\\ H_{\alpha,\boldsymbol{k}} &= \begin{pmatrix} A_{\alpha,\boldsymbol{k}} & B_{\alpha,\boldsymbol{k}} \\ B_{\alpha,\boldsymbol{k}} & A_{\alpha,-\boldsymbol{k}}\end{pmatrix}\\ \phi_{\alpha,\boldsymbol{k}} &= (a_{\alpha,\boldsymbol{k}}, a^{\dagger}_{\alpha,-\boldsymbol{k}})^{T}\end{aligned} \tag{A.9}$$

The eigenmodes of the quadratic Hamiltonian $\mathcal{H}$ are:

$$\begin{aligned}\mathcal{H}^{(2)} &= \frac{S}{2}\sum_{\alpha}\omega_{\alpha,\boldsymbol{k}}\eta^{\dagger}_{\alpha,\boldsymbol{k}}\eta_{\alpha,\boldsymbol{k}}\\ \omega_{\alpha,\boldsymbol{k}} &= \sqrt{A^{2}_{\alpha,\boldsymbol{k}} - B^{2}_{\alpha,\boldsymbol{k}}}\\ a_{\alpha,\boldsymbol{k}} &= u_{\alpha,\boldsymbol{k}}\tilde{a}_{\alpha,\boldsymbol{k}} + v_{\alpha,\boldsymbol{k}}\tilde{a}^{\dagger}_{\alpha,-\boldsymbol{k}}\\ \eta_{\alpha,\boldsymbol{k}} &= (\tilde{a}_{\alpha,\boldsymbol{k}}, \tilde{a^{\dagger}}_{\alpha,-\boldsymbol{k}})^{T}\end{aligned} \tag{A.10}$$

$u_{\alpha,\boldsymbol{k}}$ and $v_{\alpha,\boldsymbol{k}}$ are defined as:

$$u_{\alpha,\boldsymbol{k}} = \sqrt{\frac{A_{\alpha,\boldsymbol{k}} + \omega_{\alpha,\boldsymbol{k}}}{2\omega_{\alpha,\boldsymbol{k}}}} \qquad v_{\alpha,\boldsymbol{k}} = -\mathrm{sign}(B_{\alpha,\boldsymbol{k}})\sqrt{\frac{A_{\alpha,\boldsymbol{k}} - \omega_{\alpha,\boldsymbol{k}}}{2\omega_{\alpha,\boldsymbol{k}}}} \tag{A.11}$$

As $\phi_{\alpha,\boldsymbol{k}}$ is a linear combination of creation and annihilation canonical modes, the vacuum expectation value of $\phi^{\dagger}_{\boldsymbol{k}}\phi_{\boldsymbol{k}}$ is non-zero:

$$\langle a^{\dagger}_{\alpha,\boldsymbol{k}}a_{\alpha,\boldsymbol{k}}\rangle = \Big\langle\frac{A_{\alpha,\boldsymbol{k}} - \omega_{\alpha,\boldsymbol{k}}}{2\omega_{\alpha,\boldsymbol{k}}}\Big\rangle \qquad \langle a^{\dagger}_{\alpha,\boldsymbol{k}}a^{\dagger}_{\alpha,-\boldsymbol{k}}\rangle = -\Big\langle\frac{B_{\alpha,\boldsymbol{k}}}{2\omega_{\alpha,\boldsymbol{k}}}\Big\rangle \tag{A.12}$$

$\langle ...\rangle$ is defined as the average over the Brillouin zone, $\langle ...\rangle = \frac{1}{N}\sum_{\boldsymbol{k}} ....$ To obtain the quantum corrections to the spectrum at the leading order in $1/S$, one can work in the basis of $\phi_{\boldsymbol{k}}$ and calculate $\delta A_{\boldsymbol{k}}$ and $\delta B_{\boldsymbol{k}}$ at the order of $1/S$. We replace $A_{\boldsymbol{k}} \to A_{\boldsymbol{k}} + \delta A_{\boldsymbol{k}}$ and $B_{\boldsymbol{k}} \to B_{\boldsymbol{k}} + \delta B_{\boldsymbol{k}}$. The normal and anomalous self-energy of the canonical modes are:

$$\begin{aligned}\delta\omega_{\boldsymbol{k}} &= \delta A_{\boldsymbol{k}}(u^{2}_{\boldsymbol{k}} + v^{2}_{\boldsymbol{k}}) + 2\delta B_{\boldsymbol{k}}u_{\boldsymbol{k}}v_{\boldsymbol{k}}\\ &= \frac{A_{\boldsymbol{k}}\delta A_{\boldsymbol{k}} - B_{\boldsymbol{k}}\delta B_{\boldsymbol{k}}}{\omega_{\boldsymbol{k}}}\end{aligned}$$

$$\begin{aligned}\delta\omega_{\boldsymbol{k}}^{\text{off}} &= 2\delta A_{\boldsymbol{k}} u_{\boldsymbol{k}} v_{\boldsymbol{k}} + \delta B_{\boldsymbol{k}}(u_{\boldsymbol{k}}^2 + v_{\boldsymbol{k}}^2) \\ &= \frac{A_{\boldsymbol{k}}\delta B_{\boldsymbol{k}} - B_{\boldsymbol{k}}\delta A_{\boldsymbol{k}}}{\omega_{\boldsymbol{k}}}\end{aligned} \tag{A.13}$$

Thus the spectrum with quantum corrections is:

$$\omega_{\boldsymbol{k}}^{(1)} = \sqrt{(\omega_{\boldsymbol{k}} + \delta\omega_{\boldsymbol{k}})^2 - (\delta\omega_{\boldsymbol{k}}^{\text{off}})^2} = \sqrt{(A^2 - B^2) + 2(A\delta A - B\delta B) + (\delta A^2 - \delta B^2)}\Big|_{\boldsymbol{k}} \tag{A.14}$$

When $\omega_{\boldsymbol{k}} \sim \mathcal{O}(1)$, the quantum corrections to $\omega_{\alpha,\boldsymbol{k}}^{(1)}$ is at the order of $1/S$ and they won't change the spectrum qualitatively as long as there is no singularity in $\delta\omega_{\boldsymbol{k}}$. We have:

$$\omega_{\boldsymbol{k}}^{(1)} \simeq \omega_{\boldsymbol{k}} + \delta\omega_{\boldsymbol{k}} \tag{A.15}$$

When $\omega_{\boldsymbol{k}} \sim 0$, one needs to distinguish between two situations. Suppose it is a classical zero mode at $\boldsymbol{k} = 0$. It can be $A_{\boldsymbol{k}=0} = B_{\boldsymbol{k}=0} = 0$, which is generally the case of accidental degeneracy. Thus the dispersion around $\boldsymbol{k} = 0$ can be written as $\omega_{\boldsymbol{k}} \sim \boldsymbol{k}^2$. It can also be $|A_{\boldsymbol{k}=0}| = |B_{\boldsymbol{k}=0}| \neq 0$, which is the case of linearly dispersing zero mode, such as the Goldstone mode. Thus the dispersion around $\boldsymbol{k} = 0$ can be written as $\omega_{\boldsymbol{k}} \sim v\boldsymbol{k}$. We define the quantum corrections to the spectrum as δm such that $\omega_{\boldsymbol{k}}^{(1)} \simeq \sqrt{\omega_{\boldsymbol{k}}^2 + \delta m}$. δm to the leading order in $1/S$ is expressed in the two cases as:

$$\delta m = \begin{cases} (\delta A^2 - \delta B^2)\big|_{\boldsymbol{k}=0} = \delta\omega^2 - (\delta\omega^{\text{off}})^2\big|_{\boldsymbol{k}=0} & \text{if } A,\ B|_{\boldsymbol{k}=0} = 0 \\ 2(A\delta A - B\delta B)\big|_{\boldsymbol{k}=0} = 2\omega\delta\omega\big|_{\boldsymbol{k}=0} & \text{if } A,\ B|_{\boldsymbol{k}=0} \sim \mathcal{O}(1) \end{cases} \tag{A.16}$$

We calculate δm at certain momentum following Eq. A.16. One can calculate either δA, δB or $\delta\omega$, $\delta\omega^{\text{off}}$, whichever way is the easiest. For the second case, as δm is linear in δA, δB, it is most straight forward to obtain the quantum corrections from the cubic terms by calculating $\delta\omega$, $\delta\omega^{\text{off}}$, and corrections from the quartic terms by δA, δB, and sum the two contributions.

A.2 Dilue bose gas approximation in high field

In this section, we show details of determining the quartic couplings Γ in the expressions of the condensate energy, i.e. Eq. 2.8, Eq. 2.33 and Eq. 2.27. The quartic couplings Γ are at leading order in $1/S$ in Sec. **??**, and are summed up to all orders in $1/S$ in Sec. 2.2.2. In the following, we show how Γ is obtained for a generic spin. The calculation of Γ at leading order in $1/S$ follows the same idea and is simpler, and

it will not discussed further here. One can refer [117] for more details.

As shown in the main text, to determine the magnetic order structure, compared with calculating the exact numerical values of Γ, the sign of the differences of Γs (e.g. Γ_1 v.s. Γ_2, $\frac{1}{2}(\Gamma_1+\Gamma_2)\bar{\Gamma}_1$ v.s. $\Gamma^2_{\Delta,\phi}$) are more relevant. As the sign of the differences of relevant Γs shouldn't change across the 2nd order phase transition from right above h_{sat} to right below h_{sat}, the criterion introduced above to know the order structure slightly *below* h_{sat} can be determined by the fully renormalized four-point vertex function slightly *above* h_{sat}.

The fully renormalized 2n-point vertex functions of ferromagnet can be determined exactly above h_{sat} for all spins, as the single-magnon excitations of the ferromagnet are exact and the quantum corrections to the 2n-point vertex only come from magnon-magnon scattering.

The four-point and six-point bare vertex functions are defined in Eq. 2.2 as $V_{\boldsymbol{q}}(\boldsymbol{k_1},\boldsymbol{k_2})$ and $U_{\boldsymbol{q},\boldsymbol{q'}}(\boldsymbol{k_1},\boldsymbol{k_2},\boldsymbol{k}_3)$:

$$V_{\boldsymbol{q}}(\boldsymbol{k_1},\boldsymbol{k_2})=\frac{1}{2}[(J_{\boldsymbol{q}}+J_{\boldsymbol{k_2}-\boldsymbol{k_1}-\boldsymbol{q}})+2S(K_s-1)(J_{\boldsymbol{k_1}}+J_{\boldsymbol{k_1}+\boldsymbol{q}}+J_{\boldsymbol{k_2}}+J_{\boldsymbol{k_2}-\boldsymbol{q}})] \quad \text{(A.17)}$$

$J_{\boldsymbol{q}}$ is defined in Eq. 2.2. The expression includes normal ordering of the magnon to all orders in $1/S$ by $K_s=\sqrt{1-\frac{1}{2S}}$. To the leading order in $1/S$, $K_s=1-1/4S$. $U_{\boldsymbol{q},\boldsymbol{q'}}(\boldsymbol{k_1},\boldsymbol{k_2},\boldsymbol{k}_3)$ keeping the $1/S$ correction from the normal ordering is:

$$\begin{aligned}U_{\boldsymbol{q},\boldsymbol{q'}}(\boldsymbol{k_1},\boldsymbol{k_2},\boldsymbol{k}_3)=&\frac{1}{9}(1+1/4S)\big(J_{\boldsymbol{k}_1+\boldsymbol{q}}+J_{\boldsymbol{k}_3+\boldsymbol{q}}+J_{\boldsymbol{k}_1+\boldsymbol{k}_3-\boldsymbol{k}_2+\boldsymbol{q}}+J_{\boldsymbol{k}_1+\boldsymbol{q'}}+J_{\boldsymbol{k}_2+\boldsymbol{q'}}\\&+J_{\boldsymbol{k}_1+\boldsymbol{k}_2-\boldsymbol{k}_3+\boldsymbol{q'}}+J_{\boldsymbol{k}_2+\boldsymbol{k}_3-\boldsymbol{k}_1-\boldsymbol{q}-\boldsymbol{q'}}+J_{\boldsymbol{k}_2-\boldsymbol{q}-\boldsymbol{q'}}+J_{\boldsymbol{k}_3-\boldsymbol{q}-\boldsymbol{q'}}\big)\\&-\frac{1}{6}(1+3/4S)(J_{\boldsymbol{k_1}}+J_{\boldsymbol{k_2}}+J_{\boldsymbol{k}_3}+J_{\boldsymbol{k}_1+\boldsymbol{q}+\boldsymbol{q'}}+J_{\boldsymbol{k}_2-\boldsymbol{q}}+J_{\boldsymbol{k}_3-\boldsymbol{q'}})]\end{aligned} \quad \text{(A.18)}$$

We define the fully renormalized four-point vertex function as $\Gamma_{\boldsymbol{q}}(\boldsymbol{k_1},\boldsymbol{k_2})$. The quartic coefficients Γ in the action are determined by $\Gamma_{\boldsymbol{q}}(\boldsymbol{k_1},\boldsymbol{k_2})$ at particular momenta as:

$$\begin{aligned}\Gamma_1&=\Gamma_{\boldsymbol{0}}(\boldsymbol{K},\boldsymbol{K})\\\Gamma_2&=\Gamma_{\boldsymbol{0}}(\boldsymbol{K},-\boldsymbol{K})+\Gamma_{-2\boldsymbol{K}}(\boldsymbol{K},-\boldsymbol{K})\\\bar{\Gamma}_1&=\Gamma_{\boldsymbol{0}}(\boldsymbol{M_1},\boldsymbol{M_1})\\\bar{\Gamma}_2&=\Gamma_{\boldsymbol{0}}(\boldsymbol{M_1},\boldsymbol{M_2})+\Gamma_{\boldsymbol{M_2}-\boldsymbol{M_1}}(\boldsymbol{M_1},\boldsymbol{M_2})\\\Gamma_{\Delta,\phi}&=\Gamma_{\boldsymbol{0}}(\boldsymbol{M_1},\boldsymbol{K})+\Gamma_{\boldsymbol{K}-\boldsymbol{M_1}}(\boldsymbol{M_1},\boldsymbol{K})\\\bar{\Gamma}_{\Delta,\phi}&=\Gamma_{\boldsymbol{K}-\boldsymbol{M_1}}(\boldsymbol{M_1},\boldsymbol{M_1})+\Gamma_{-\boldsymbol{K}-\boldsymbol{M_1}}(\boldsymbol{M_1},\boldsymbol{M_1})\end{aligned} \quad \text{(A.19)}$$

To find $\Gamma_{\boldsymbol{q}}(\boldsymbol{k_1}, \boldsymbol{k_2})$, all orders of magnon-magnon scattering process should be counted (see Fig. 2.4), which is equivalent to solving a consistency equation, also known as Bethe-Salpeter (BS) equation:

$$\Gamma_{\boldsymbol{q}}(\boldsymbol{k_1}, \boldsymbol{k_2}) = V_{\boldsymbol{q}}(\boldsymbol{k_1}, \boldsymbol{k_2}) - \frac{1}{N}\sum_{\boldsymbol{q'}} \frac{\Gamma_{\boldsymbol{q'}}(\boldsymbol{k_1}, \boldsymbol{k_2}) V_{\boldsymbol{q}-\boldsymbol{q'}}(\boldsymbol{k_1}+\boldsymbol{q'}, \boldsymbol{k_2}-\boldsymbol{q'})}{S(\omega_{\boldsymbol{k_1}+\boldsymbol{q'}} + \omega_{\boldsymbol{k_2}-\boldsymbol{q'}})} \tag{A.20}$$

To solve for $\Gamma_{\boldsymbol{q}}(\boldsymbol{k_1}, \boldsymbol{k_2})$, we follow the method introduced in [93], which converts the problem of solving an integral equation to that of solving a matrix equation. As $V_{\boldsymbol{q}}(\boldsymbol{k_1}, \boldsymbol{k_2})$, $V_{\boldsymbol{q}-\boldsymbol{q'}}(\boldsymbol{k_1}+\boldsymbol{q'}, \boldsymbol{k_2}-\boldsymbol{q'})$ can be expanded by lattice Harmonics, $\Gamma_{\boldsymbol{q}}(\boldsymbol{k_1}, \boldsymbol{k_2})$ can also be expressed by the lattice Harmonics. We write the ansatz for $\Gamma_{\boldsymbol{q}}(\boldsymbol{k_1}, \boldsymbol{k_2})$ as:

$$\begin{aligned} \Gamma_{\boldsymbol{q}}(\boldsymbol{k_1}, \boldsymbol{k_2}) &= A_0 + A_\alpha \cos q_\alpha + B_\alpha \sin q_\alpha + \tilde{A}_\alpha \cos \tilde{q}_\alpha + \tilde{B}_\alpha \sin \tilde{q}_\alpha \equiv \mathcal{A}^T \Gamma_{\mathrm{b}\boldsymbol{q}} \\ \Gamma_{\mathrm{b}\boldsymbol{q}} &= \{1, \cos q_\alpha, \sin q_\alpha, \cos \tilde{q}_\alpha, \sin \tilde{q}_\alpha\} \end{aligned} \tag{A.21}$$

$\alpha = 1, 2, 3$ and q_α , $\tilde{q}_\alpha$ are defined as $q_\alpha = \boldsymbol{q} \cdot \boldsymbol{\delta}_\alpha$, $\tilde{q}_\alpha = \boldsymbol{q} \cdot \boldsymbol{l}_\alpha$. $\boldsymbol{\delta}_\alpha$, $\boldsymbol{l}_\alpha$ are defined in Fig. 2.1 (a). Express $V_{\boldsymbol{q}}(\boldsymbol{k_1}, \boldsymbol{k_2})$, $V_{\boldsymbol{q}-\boldsymbol{q'}}(\boldsymbol{k_1}+\boldsymbol{q'}, \boldsymbol{k_2}-\boldsymbol{q'})$ in the basis of $\Gamma_{\mathrm{b}\boldsymbol{q}}$ as:

$$\begin{aligned} V_{\boldsymbol{q}}(\boldsymbol{k_1}, \boldsymbol{k_2}) &= \mathcal{A}_0^T \Gamma_{\mathrm{b}\boldsymbol{q}} \\ V_{\boldsymbol{q}-\boldsymbol{q'}}(\boldsymbol{k_1}+\boldsymbol{q'}, \boldsymbol{k_2}-\boldsymbol{q'}) &= \Gamma_{\mathrm{b}\boldsymbol{q'}}^T \mathcal{V}_0 \Gamma_{\mathrm{b}\boldsymbol{q}} \end{aligned} \tag{A.22}$$

Eq. A.20 in the matrix form is:

$$\mathcal{A}^T \Gamma_{\mathrm{b}\boldsymbol{q}} = \mathcal{A}_0^T \Gamma_{\mathrm{b}\boldsymbol{q}} - \mathcal{A}^T \Big(\frac{1}{N} \sum_{\boldsymbol{q'}} \frac{\Gamma_{\mathrm{b}\boldsymbol{q'}} \Gamma_{\mathrm{b}\boldsymbol{q'}}^T}{S(\omega_{\boldsymbol{k_1}+\boldsymbol{q'}} + \omega_{\boldsymbol{k_2}-\boldsymbol{q'}})} \Big) \mathcal{V}_0 \Gamma_{\mathrm{b}\boldsymbol{q}} \tag{A.23}$$

$\Gamma_{\boldsymbol{q}}(\boldsymbol{k}_1, \boldsymbol{k}_2)$ relevant to find the quartic coupling Γ satisfies $\omega_{\boldsymbol{k}_1} = \omega_{\boldsymbol{k}_2} = 0$. So the sum over $\boldsymbol{q'}$, $\frac{1}{N}\sum_{\boldsymbol{q'}} \frac{\Gamma_{\mathrm{b}\boldsymbol{q'}} \Gamma_{\mathrm{b}\boldsymbol{q'}}^T}{\omega_{\boldsymbol{k_1}+\boldsymbol{q'}} + \omega_{\boldsymbol{k_2}-\boldsymbol{q'}}}$ is logarithmically divergent. The solution to Eq. A.23 can be expanded order by order in $\frac{1}{|\log \mu|}$, where μ is the low energy cutoff with $\mu \to 0^+$ as $h \to h_{\mathrm{sat}}^+$.

Solving for $\mathcal{A}$ in Eq. A.23 is however not efficient numerically. In the following, we show the simplification of Eq. A.23 to Eq. A.36. The label of incoming momenta $(\boldsymbol{k_1}, \boldsymbol{k_2})$ is omitted to keep the expressions compact. First take the average of Eq. A.20 with respect to $\boldsymbol{q}$:

$$\langle \Gamma_{\boldsymbol{q}} \rangle_{\boldsymbol{q}} = \langle V_{\boldsymbol{q}} \rangle_{\boldsymbol{q}} - \frac{1}{N} \sum_{\boldsymbol{q'}} \frac{\Gamma_{\boldsymbol{q'}} \langle V_{\boldsymbol{q}-\boldsymbol{q'}}(\boldsymbol{k_1}+\boldsymbol{q'}, \boldsymbol{k_2}-\boldsymbol{q'}) \rangle_{\boldsymbol{q}}}{S(\omega_{\boldsymbol{k_1}+\boldsymbol{q'}} + \omega_{\boldsymbol{k_2}-\boldsymbol{q'}})} \tag{A.24}$$

As $\langle \cos q_\alpha \rangle = 0$, $\langle \sin q_\alpha \rangle = 0$, $\langle \cos \tilde{q}_\alpha \rangle = 0$, $\langle \sin \tilde{q}_\alpha \rangle = 0$, we have $\langle J_{\boldsymbol{q}+\boldsymbol{k}} \rangle_{\boldsymbol{q}} = 0$. Thus Eq. A.24 gives:

$$\begin{aligned} A_0 &= S(K_s-1)(J_{\boldsymbol{k}_1}+J_{\boldsymbol{k}_2}) - S(K_s-1)\frac{1}{N}\sum_{\boldsymbol{q}'}\frac{\Gamma_{\boldsymbol{q}'}(J_{\boldsymbol{k}_1+\boldsymbol{q}'}+J_{\boldsymbol{k}_2-\boldsymbol{q}'})}{S(\omega_{\boldsymbol{k}_1+\boldsymbol{q}'}+\omega_{\boldsymbol{k}_2-\boldsymbol{q}'})} \\ &= S(K_s-1)\Big((J_{\boldsymbol{k}_1}+J_{\boldsymbol{k}_2}) - \Big\langle \frac{\Gamma_{\boldsymbol{q}'}(J_{\boldsymbol{k}_1+\boldsymbol{q}'}+J_{\boldsymbol{k}_2-\boldsymbol{q}'}-J_{\boldsymbol{k}_1}-J_{\boldsymbol{k}_2}+J_{\boldsymbol{k}_1}+J_{\boldsymbol{k}_2})}{S(\omega_{\boldsymbol{k}_1+\boldsymbol{q}'}+\omega_{\boldsymbol{k}_2-\boldsymbol{q}'})}\Big\rangle_{\boldsymbol{q}'}\Big) \\ &= S(K_s-1)\Big((J_{\boldsymbol{k}_1}+J_{\boldsymbol{k}_2})(1-\Big\langle \frac{\Gamma_{\boldsymbol{q}'}}{S(\omega_{\boldsymbol{k}_1+\boldsymbol{q}'}+\omega_{\boldsymbol{k}_2-\boldsymbol{q}'})}\Big\rangle_{\boldsymbol{q}'}) - A_0/S\Big) \end{aligned} \tag{A.25}$$

The first consistency equation gives:

$$\frac{K_s}{K_s-1}A_0 = S(J_{\boldsymbol{k}_1}+J_{\boldsymbol{k}_2})\Big(1-\Big\langle \frac{\Gamma_{\boldsymbol{q}'}}{S(\omega_{\boldsymbol{k}_1+\boldsymbol{q}'}+\omega_{\boldsymbol{k}_2-\boldsymbol{q}'})}\Big\rangle_{\boldsymbol{q}'}\Big) \tag{A.26}$$

Secondly, plug the expression of $V_{\boldsymbol{q}}(\boldsymbol{k_1},\boldsymbol{k_2})$ into Eq. A.20

$$\begin{aligned} &\Gamma_{\boldsymbol{q}}(\boldsymbol{k_1},\boldsymbol{k_2}) = \\ &\frac{1}{2}(J_{\boldsymbol{q}}+J_{\boldsymbol{k}_2-\boldsymbol{k}_1-\boldsymbol{q}}) + S(K_s-1)(J_{\boldsymbol{k}_1}+J_{\boldsymbol{k}_1+\boldsymbol{q}}+J_{\boldsymbol{k}_2}+J_{\boldsymbol{k}_2-\boldsymbol{q}}) - \frac{1}{N}\times \\ &\sum_{\boldsymbol{q}'}\frac{\Gamma_{\boldsymbol{q}'}\big(\frac{1}{2}(J_{\boldsymbol{q}-\boldsymbol{q}'}+J_{\boldsymbol{k}_2-\boldsymbol{k}_1-\boldsymbol{q}-\boldsymbol{q}'}) + S(K_s-1)(J_{\boldsymbol{k}_1+\boldsymbol{q}'}+J_{\boldsymbol{k}_1+\boldsymbol{q}}+J_{\boldsymbol{k}_2-\boldsymbol{q}'}+J_{\boldsymbol{k}_2-\boldsymbol{q}})\big)}{S(\omega_{\boldsymbol{k}_1+\boldsymbol{q}'}+\omega_{\boldsymbol{k}_2-\boldsymbol{q}'})} \\ &= \frac{1}{2}(J_{\boldsymbol{q}}+J_{\boldsymbol{k}_2-\boldsymbol{k}_1-\boldsymbol{q}}) - \frac{1}{N}\sum_{\boldsymbol{q}'}\frac{\Gamma_{\boldsymbol{q}'}\frac{1}{2}(J_{\boldsymbol{q}-\boldsymbol{q}'}+J_{\boldsymbol{k}_2-\boldsymbol{k}_1-\boldsymbol{q}-\boldsymbol{q}'})}{S(\omega_{\boldsymbol{k}_1+\boldsymbol{q}'}+\omega_{\boldsymbol{k}_2-\boldsymbol{q}'})} \\ &+ S(K_s-1)\big((J_{\boldsymbol{k}_1}+J_{\boldsymbol{k}_2}) - \frac{1}{N}\sum_{\boldsymbol{q}'}\frac{\Gamma_{\boldsymbol{q}'}(J_{\boldsymbol{k}_1+\boldsymbol{q}'}+J_{\boldsymbol{k}_2-\boldsymbol{q}'})}{S(\omega_{\boldsymbol{k}_1+\boldsymbol{q}'}+\omega_{\boldsymbol{k}_2-\boldsymbol{q}'})}) \\ &+ S(K_s-1)(J_{\boldsymbol{k}_1+\boldsymbol{q}}+J_{\boldsymbol{k}_2-\boldsymbol{q}})(1-\frac{1}{N}\sum_{\boldsymbol{q}'}\frac{\Gamma_{\boldsymbol{q}'}}{S(\omega_{\boldsymbol{k}_1+\boldsymbol{q}'}+\omega_{\boldsymbol{k}_2-\boldsymbol{q}'})}) \end{aligned} \tag{A.27}$$

The second to last line is exactly A_0 from the first line of Eq. A.25; the last line is $K_s\frac{(J_{\boldsymbol{k}_1+\boldsymbol{q}}+J_{\boldsymbol{k}_2-\boldsymbol{q}})}{(J_{\boldsymbol{k}_1}+J_{\boldsymbol{k}_2})}A_0$ according to Eq. A.26, so we have:

$$\Gamma_{\boldsymbol{q}} = \tag{A.28}$$

$$\frac{1}{2}(J_{\boldsymbol{q}}+J_{\boldsymbol{k}_2-\boldsymbol{k}_1-\boldsymbol{q}}) - \frac{1}{N}\sum_{\boldsymbol{q}'}\frac{\Gamma_{\boldsymbol{q}'}\frac{1}{2}(J_{\boldsymbol{q}-\boldsymbol{q}'}+J_{\boldsymbol{k}_2-\boldsymbol{k}_1-\boldsymbol{q}-\boldsymbol{q}'})}{S(\omega_{\boldsymbol{k}_1+\boldsymbol{q}'}+\omega_{\boldsymbol{k}_2-\boldsymbol{q}'})} + A_0\big(1+K_s\frac{(J_{\boldsymbol{k}_1+\boldsymbol{q}}+J_{\boldsymbol{k}_2-\boldsymbol{q}})}{(J_{\boldsymbol{k}_1}+J_{\boldsymbol{k}_2})}\big) \tag{A.29}$$

Define a integral matrix τ as:

$$\tau_{\boldsymbol{k}_1,\boldsymbol{k}_2} = \frac{1}{N}\sum_{\boldsymbol{q}'} \frac{\Gamma_{\mathrm{b}\boldsymbol{q}'}\Gamma_{\mathrm{b}\boldsymbol{q}'}^T}{S(\omega_{\boldsymbol{k_1}+\boldsymbol{q}'} + \omega_{\boldsymbol{k_2}-\boldsymbol{q}'}) + 2\mu} \tag{A.30}$$

The consistency equations Eq. A.26, Eq. A.29 in the matrix form are:

$$\mathrm{id}^T\Gamma_{\mathrm{b}\boldsymbol{q}} = \mathcal{A}^T\left(\frac{K_s}{K_s-1}\frac{1}{S(J_{\boldsymbol{k_1}}+J_{\boldsymbol{k_2}})} + \tau_{\boldsymbol{k}_1,\boldsymbol{k}_2}\right)\mathrm{id}\cdot\mathrm{id}^T\Gamma_{\mathrm{b}\boldsymbol{q}} \quad \mathrm{id} = (1,0,0,0,0)^T \tag{A.31}$$

$$\mathcal{J}^T\Gamma_{\mathrm{b}\boldsymbol{q}} = \mathcal{A}^T(\mathcal{I} + \tau_{\boldsymbol{k}_1,\boldsymbol{k}_2}\mathcal{M} - \mathcal{K})\Gamma_{\mathrm{b}\boldsymbol{q}} \tag{A.32}$$

$\mathcal{I}$ is the identity matrix. $\mathcal{J}$, $\mathcal{M}$ and $\mathcal{K}$ depend on the two incoming momenta $(\boldsymbol{k}_1, \boldsymbol{k}_2)$, and they are defined as:

$$\frac{1}{2}(J_{\boldsymbol{q}} + J_{\boldsymbol{k}_2-\boldsymbol{k}_1-\boldsymbol{q}}) = \mathcal{J}^T\Gamma_{\mathrm{b}\boldsymbol{q}} \tag{A.33}$$

$$\mathcal{J} = \{0, 1+\cos(k_{2\alpha}-k_{1\alpha}), \sin(k_{2\alpha}-k_{1\alpha}), J_2(1+\cos(\tilde{k}_{2\alpha}-\tilde{k}_{1\alpha})), J_2\sin(\tilde{k}_{2\alpha}-\tilde{k}_{1\alpha})\}^T$$

$$\frac{1}{2}(J_{\boldsymbol{q}-\boldsymbol{q}'} + J_{\boldsymbol{k}_2-\boldsymbol{k}_1-\boldsymbol{q}-\boldsymbol{q}'}) = \Gamma_{\mathrm{b}\boldsymbol{q}'}^T\mathcal{M}\Gamma_{\mathrm{b}\boldsymbol{q}} \tag{A.34}$$

$$\mathcal{M} = \begin{pmatrix} 0 & 0 & 0 & 0 & 0 \\ 0 & 1+\cos k_\alpha & \sin k_\alpha & 0 & 0 \\ 0 & \sin k_\alpha & 1-\cos k_\alpha & 0 & 0 \\ 0 & 0 & 0 & J_2(1+\cos\tilde{k}_\alpha) & J_2\sin\tilde{k}_\alpha \\ 0 & 0 & 0 & J_2\sin\tilde{k}_\alpha & J_2(1-\cos\tilde{k}_\alpha) \end{pmatrix}$$

k_α, $\tilde{k}_\alpha$ are defined as $\boldsymbol{k}\cdot\boldsymbol{\delta}_\alpha$, $\boldsymbol{k}\cdot\boldsymbol{l}_\alpha$ respectively, $\boldsymbol{k} = \boldsymbol{k}_2 - \boldsymbol{k}_1$.

$$A_0\big(1 + K_s\frac{(J_{\boldsymbol{k_1}+\boldsymbol{q}} + J_{\boldsymbol{k_2}-\boldsymbol{q}})}{(J_{\boldsymbol{k_1}} + J_{\boldsymbol{k_2}})}\big) = \mathcal{A}^T\mathcal{K}\Gamma_{\mathrm{b}\boldsymbol{q}} \tag{A.35}$$

The first row of $\mathcal{K}$ is:

$$\mathcal{K}_1 = \big\{1, \frac{2K_s}{J_{\boldsymbol{k_1}}+J_{\boldsymbol{k_2}}}(\cos k_{1\alpha} + \cos k_{2\alpha}), \frac{2K_s}{J_{\boldsymbol{k_1}}+J_{\boldsymbol{k_2}}}(-\sin k_{1\alpha} + \sin k_{2\alpha}),$$
$$\frac{2J_2K_s}{J_{\boldsymbol{k_1}}+J_{\boldsymbol{k_2}}}(\cos\tilde{k}_{1\alpha} + \cos\tilde{k}_{2\alpha}), \frac{2J_2K_s}{J_{\boldsymbol{k_1}}+J_{\boldsymbol{k_2}}}(-\sin\tilde{k}_{1\alpha} + \sin\tilde{k}_{2\alpha})\big\}$$

Other rows of $\mathcal{K}$ are zero.

Note that the matrix on the RHS of Eq. A.31 is nonzero only in the first column, and the matrix on the RHS of Eq. A.32 is zero in the first column, i.e. combing the

two equations by adding them doesn't lose any information, and we have:

$$\mathcal{A}^T \mathcal{O}_{\boldsymbol{k_1},\boldsymbol{k_2}} \Gamma_{\mathrm{b}\boldsymbol{q}} = \bar{\mathcal{J}}^T \Gamma_{\mathrm{b}\boldsymbol{q}} \tag{A.36}$$

$$\text{where} \quad \mathcal{O}_{\boldsymbol{k_1},\boldsymbol{k_2}} = \mathcal{I} + \tau_{\boldsymbol{k}_1,\boldsymbol{k}_2}(\mathcal{M} + \mathrm{id}\cdot\mathrm{id}^T) - (\mathcal{K}_{\boldsymbol{k}_1,\boldsymbol{k}_2} - \frac{K_s}{K_s - 1}\frac{1}{S(J_{\boldsymbol{k_1}} + J_{\boldsymbol{k}_2})}\mathrm{id}\cdot\mathrm{id}^T)$$

$$\bar{\mathcal{J}} = \mathcal{J} + \mathrm{id}$$

As matrix $\mathcal{M}$ doesn't depend on K_s, $\tau_{\boldsymbol{k}_1,\boldsymbol{k}_2}$ in $\mathcal{O}_{\boldsymbol{k}_1,\boldsymbol{k}_2}$ couple to K_s. To solve for $\mathcal{A}^T$

$$\mathcal{A}^T = \bar{\mathcal{J}}^T \mathcal{O}^{-1}_{\boldsymbol{k_1},\boldsymbol{k_2}} \tag{A.37}$$

Near h_{sat}, at $h = \mu + h_{\mathrm{sat}}$ when $\mu \to 0^+$, the matrix elements of $\tau_{\boldsymbol{k_1},\boldsymbol{k_2}}$ is log divergent. $\tau_{\boldsymbol{k}_1,\boldsymbol{k}_2}$ is expressed as the sum of the log divergent part and the finite part.

$$\tau_{\boldsymbol{k}_1,\boldsymbol{k}_2} = \frac{|\log\mu|}{S}\tau^{(0)}_{\boldsymbol{k}_1,\boldsymbol{k}_2} + \frac{1}{S}\tau^{(1)}_{\boldsymbol{k}_1,\boldsymbol{k}_2} \tag{A.38}$$

We keep the spin S explicit, and $\tau^{(0)}$, $\tau^{(1)}$ are independent of S. So we can solve for $\mathcal{A}$ order by order in $\frac{1}{|\log\mu|}$. It is straight forward to find $\tau^{(0)}_{\boldsymbol{k}_1,\boldsymbol{k}_2}$ using:

$$\frac{1}{N}\sum_{\boldsymbol{q}'} \to \frac{1}{\mathcal{A}_{B.Z.}}\int_{B.Z.} \mathrm{d}\boldsymbol{q}'$$

$$\frac{1}{\mathcal{A}_{B.Z.}}\int_{\Lambda} \mathrm{d}\boldsymbol{q}' \frac{q_x^\alpha q_y^\beta}{aq_x^2 + bq_y^2 + \mu} = \frac{\pi}{\mathcal{A}_{B.Z.}}\frac{1}{\sqrt{a}^{\alpha+1}}\frac{1}{\sqrt{b}^{\beta+1}}|\log\frac{\mu}{\Lambda}|\delta_{\alpha,0}\delta_{\beta,0} \tag{A.39}$$

We find that the leading order of $\Gamma_{\boldsymbol{q}} = \mathcal{A}^T\Gamma_{\mathrm{b}\boldsymbol{q}}$ only depend on the log divergent part of $\mathcal{O}_{\boldsymbol{k}_1,\boldsymbol{k}_2}$, so it doesn't depend on $K_s = \sqrt{1 - \frac{1}{2S}}$. The leading order of $\Gamma_{\boldsymbol{q}}$ should be $\sim \frac{S}{|\log\mu|}$, we get it by

$$\Gamma^{(0)}_{\boldsymbol{q}} = (\mathcal{A}^{(0)})^T\Gamma_{\mathrm{b}\boldsymbol{q}} = \frac{S}{|\log\mu|}\lim_{\mu\to 0}\frac{|\log\mu|}{S}\bar{\mathcal{J}}^T\big(\mathcal{I} + \frac{|\log\mu|}{S}\tau^{(0)}_{\boldsymbol{k}_1,\boldsymbol{k}_2}(\mathcal{M} + \mathrm{id}\cdot\mathrm{id}^T)\big)^{-1}\Gamma_{\mathrm{b}\boldsymbol{q}} \tag{A.40}$$

To solve $\Gamma_{\boldsymbol{q}}$ at higher orders, we solve Eq. A.37 exactly. The quartic couplings can be obtained following Eq. A.19.

Appendix B

Appendix to Chapter 4

B.1 Effective action for the spin order

In this section, we follow the standard Hubbard-Stratonovich transformation and derive the effective action for the spin order. We show that the symmetric and antisymmetric component of $\{\bar{\mathbf{M}}_K, \bar{\mathbf{M}}^*_{-K}\}$ naturally decouple in zero field, and are coupled by the magnetic field.

Consider interactions restricted to the spin channel, Eq. 4.6 in the main text,

$$\mathcal{H}_4 = \sum_{\boldsymbol{q}} -\frac{g_3}{2}\big(\hat{\boldsymbol{\Delta}}_{K-q}\hat{\boldsymbol{\Delta}}_{-K+q} + h.c.\big) - \frac{g_1}{2}\big(\hat{\boldsymbol{\Delta}}^\dagger_{K-q}\hat{\boldsymbol{\Delta}}_{K+q} + (K \to -K)\big) + ..., \quad \text{(B.1)}$$

We apply the identity $e^{w^\dagger A w} = \int \mathcal{D}v\ e^{-v^\dagger A^{-1} v + w^\dagger v + v^\dagger w}$ (A should be positive definite for convergence), and obtain the partition function in terms of 6-component fermionic field Ψ and bosonic field v:

$$Z = \int \mathcal{D}\bar{\Psi}\mathcal{D}\Psi\mathcal{D}v\ e^{-S[\Psi, v]}. \quad \text{(B.2)}$$

From Eq. B.1, $w = \{\hat{\boldsymbol{\Delta}}_K, \hat{\boldsymbol{\Delta}}_{-K}, \hat{\boldsymbol{\Delta}}^\dagger_K, \hat{\boldsymbol{\Delta}}^\dagger_{-K}\}^T$ and

$$A = \frac{1}{4}\begin{pmatrix} g_1 & 0 & 0 & g_3 \\ 0 & g_1 & g_3 & 0 \\ 0 & g_3 & g_1 & 0 \\ g_3 & 0 & 0 & g_1 \end{pmatrix} \quad \text{(B.3)}$$

The action written in compact form as :

$$S[\Psi, v] = \int_k -\Psi_k^\dagger \mathcal{G}_{0,k}^{-1} \Psi_k + v^\dagger A^{-1} v - w^\dagger v - v^\dagger w \tag{B.4}$$

We express the bosonic field v as $v = \frac{1}{2}\{\bar{\mathbf{\Delta}}_K, \bar{\mathbf{\Delta}}_{-K}, \bar{\mathbf{\Delta}}_K^*, \bar{\mathbf{\Delta}}_{-K}^*\}^T$ to relate it with the order parameter field at mean field level. Eq. B.4 becomes:

$$S[\Psi, v] = \int_k -\Psi_k^\dagger \mathcal{G}_k^{-1} \Psi_k + v^\dagger A^{-1} v \tag{B.5}$$

where $\mathcal{G}_k^{-1} = \mathcal{G}_{0,k}^{-1} - \mathcal{V}$, with

$$\mathcal{V} = -\begin{pmatrix} 0 & \bar{\mathbf{\Delta}}_K \cdot \vec{\sigma} & \bar{\mathbf{\Delta}}_{-K} \cdot \vec{\sigma} \\ \bar{\mathbf{\Delta}}_K^* \cdot \vec{\sigma} & 0 & 0 \\ \bar{\mathbf{\Delta}}_{-K}^* \cdot \vec{\sigma} & 0 & 0 \end{pmatrix}, \quad A^{-1} = \frac{4}{g_1^2 - g_3^2} \begin{pmatrix} g_1 & 0 & 0 & -g_3 \\ 0 & g_1 & -g_3 & 0 \\ 0 & -g_3 & g_1 & 0 \\ -g_3 & 0 & 0 & g_1 \end{pmatrix} \tag{B.6}$$

The canonical bosonic fields can be obtained by diagonalizing A^{-1}, and are

$$\begin{aligned} \bar{\mathbf{M}}_{\pm K} &= \frac{1}{2}(\bar{\mathbf{\Delta}}_{\pm K} + \bar{\mathbf{\Delta}}_{\mp K}^*), \\ \bar{\mathbf{\Phi}}_{\pm K} &= \frac{1}{2}(\bar{\mathbf{\Delta}}_{\pm K} - \bar{\mathbf{\Delta}}_{\mp K}^*). \end{aligned} \tag{B.7}$$

We note that under time-reversal, $\bar{\mathbf{\Delta}}_{\pm K} \to -\bar{\mathbf{\Delta}}_{\mp K}^*$. As a result, $\bar{\mathbf{M}}_{\pm K}$ is odd under time-reversal and $\bar{\mathbf{\Phi}}_{\pm K}$ is time-reversal symmetric. $\mathbf{M}_{\pm K}$ and $\mathbf{\Phi}_{\pm K}$, defined in momentum space, contributes to SDW and ISB order in real space, respectively. $v^\dagger A^{-1} v$ becomes:

$$v^\dagger A^{-1} v = \frac{2}{g_1 + g_3}(|\bar{\mathbf{M}}_K|^2 + |\bar{\mathbf{M}}_{-K}|^2) + \frac{2}{g_1 - g_3}(|\bar{\mathbf{\Phi}}_K|^2 + |\bar{\mathbf{\Phi}}_{-K}|^2) \tag{B.8}$$

The quadratic coupling of fermions $\mathcal{V}$ can be written as $\mathcal{V} = \mathcal{V}^M + \mathcal{V}^\Phi$, with

$$\mathcal{V}^M = -\begin{pmatrix} 0 & \bar{\mathbf{M}}_K \cdot \vec{\sigma} & \bar{\mathbf{M}}_{-K} \cdot \vec{\sigma} \\ \bar{\mathbf{M}}_{-K} \cdot \vec{\sigma} & 0 & 0 \\ \bar{\mathbf{M}}_K \cdot \vec{\sigma} & 0 & 0 \end{pmatrix}, \quad \mathcal{V}^\Phi = -\begin{pmatrix} 0 & \bar{\mathbf{\Phi}}_K \cdot \vec{\sigma} & \bar{\mathbf{\Phi}}_{-K} \cdot \vec{\sigma} \\ -\bar{\mathbf{\Phi}}_{-K} \cdot \vec{\sigma} & 0 & 0 \\ -\bar{\mathbf{\Phi}}_{-K} \cdot \vec{\sigma} & 0 & 0 \end{pmatrix}. \tag{B.9}$$

Since the action is quadratic in fermion operators, it is straight forward to integrate

out the fermion fields and obtain the effective action in terms of bosonic fields as

$$S_{eff}[\bar{\mathbf{M}}_K, \bar{\mathbf{M}}_{-K}] = -\operatorname{Tr}\ln\left(1-\mathcal{G}_{0,k}\mathcal{V}\right) + \int_{\boldsymbol{q}} \frac{2}{g_1+g_3}(|\bar{\mathbf{M}}_K|^2+|\bar{\mathbf{M}}_{-K}|^2) + \frac{2}{g_1-g_3}(|\bar{\mathbf{\Phi}}_K|^2+|\bar{\mathbf{\Phi}}_{-K}|^2) \tag{B.10}$$

Right below the transition temperature that the ordering instability starts developing, $\operatorname{Tr}\ln\left(1-\mathcal{G}_{0,k}\mathcal{V}\right)$ can be expanded in powers of $\mathcal{V}$ as

$$S_{eff}[\bar{\mathbf{M}}_K, \bar{\mathbf{M}}_{-K}] = \sum_n \frac{1}{n}\operatorname{Tr}(\mathcal{G}_{0,k}\mathcal{V})^n + \int_{\boldsymbol{q}} \frac{2}{g_1+g_3}(|\bar{\mathbf{M}}_K|^2+|\bar{\mathbf{M}}_{-K}|^2) + \frac{2}{g_1-g_3}(|\bar{\mathbf{\Phi}}_K|^2+|\bar{\mathbf{\Phi}}_{-K}|^2), \tag{B.11}$$

where Tr(...) sums over momentum, frequency and spin indices. By solving self-consistency equations, we verified that $\bar{\mathbf{\Delta}}_{\pm\mathbf{K}} = \frac{g_{sdw}}{2}\mathbf{\Delta}_{\pm\mathbf{K}}$, $\bar{\mathbf{\Phi}}_{\pm\mathbf{K}} = \frac{g_{sdw}}{2}\mathbf{\Phi}_{\pm\mathbf{K}}$, $\bar{\mathbf{M}}_{\pm\mathbf{K}} = \frac{g_{sdw}}{2}\mathbf{M}_{\pm\mathbf{K}}$, where $\mathbf{\Delta}_{\pm\mathbf{K}}, \mathbf{M}_{\pm\mathbf{K}}, \mathbf{\Phi}_{\pm\mathbf{K}}$ are defined in the main text, e.g. Eq. 4.3.

B.1.1 Effective action in zero field

In zero field, evaluation of the trace $\frac{1}{2}\operatorname{Tr}(\mathcal{G}_{0,k}\mathcal{V})^2$ yields identical quadratic coefficients for both $|\bar{\mathbf{M}}|^2$ and $|\bar{\mathbf{\Phi}}|^2$, i.e.

$$S_{eff,2} = \int_{\boldsymbol{q}} (\frac{2}{g_1+g_3}+\xi_0)(|\bar{\mathbf{M}}_K|^2+|\bar{\mathbf{M}}_{-K}|^2) + (\frac{2}{g_1-g_3}+\xi_0)(|\bar{\mathbf{\Phi}}_K|^2+|\bar{\mathbf{\Phi}}_{-K}|^2) \tag{B.12}$$

where $\xi_0 = T\sum_{\omega_m}\int \mathrm{d}\epsilon_{\boldsymbol{k}}\mathcal{G}^c(\boldsymbol{k},\omega_m)\mathcal{G}^f(\boldsymbol{k}\pm K,\omega_m) < 0$.

At mean field level, due to the repulsive Coulomb interaction, $g_1+g_3 > g_1-g_3$. As a result, the quadratic coefficient for $\mathbf{M}_{\pm K}$ becomes negative first, i.e. the leading instability should be SDW order. Beyond mean field, the four-fermion interactions are strongly renormalized by the logarithmically singular fluctuations in particle-particle and particle-hole channel. From the pRG analysis shown in Sec. 4.5, in the interaction range that stabilize spin ordering, $g_1+g_3 > g_1-g_3$, again SDW order wins over ISB order.

To be precise, if $g_1-g_3 < 0$, i.e. the effective interaction in the antisymmetric spin ordering channel is repulsive, $\mathbf{\Phi}_{\pm K}$ condensates are impossible to develop in any

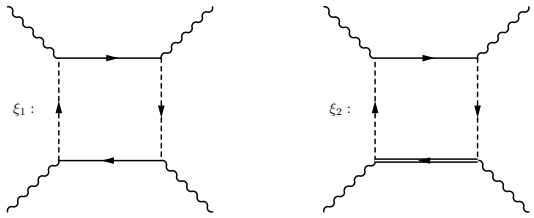

Figure B.1: Feynman diagrams for the quartic terms in the Landau Free energy in Eq. B.13.

case. In this case, the formulation should be modified as the Hubbard-Stratonovich for the channel with repulsion should be $e^{-w^\dagger A w} = \int \mathcal{D}v\, e^{-v^\dagger A^{-1} v + i w^\dagger v - i v^\dagger w}$, A positive definite. As there is no essential change of physics, we don't consider this possibility further.

As terms linear in $\mathbf{\Phi}_{\pm K}$ should vanish in the expansion due to time-reversal symmetry, the ISB instability cannot be triggered by the SDW order in zero field. We restrict to the SDW channel, and calculate the quartic term by evaluating $\frac{1}{4}\,\mathrm{Tr}(\mathcal{G}_k^{(0)}\mathcal{V})^4$. It is convenient to express the $\bar{\mathbf{M}}_{\pm K}$ in terms of real and imaginary component of SDW order, and $\bar{\mathbf{M}}_K = \frac{1}{\sqrt{2}}(\bar{\mathbf{M}}_r + i\bar{\mathbf{M}}_i)$, $\bar{\mathbf{M}}_{-K} = \frac{1}{\sqrt{2}}(\bar{\mathbf{M}}_r - i\bar{\mathbf{M}}_i)$. $\frac{1}{4}\,\mathrm{Tr}(\mathcal{G}_k^{(0)}\mathcal{V})^4$ in terms of $\{\bar{\mathbf{M}}_r, \bar{\mathbf{M}}_i\}$ is:

$$S_{eff,4} = 2(\xi_1 + \xi_2)(\bar{\mathbf{M}}_r^2 + \bar{\mathbf{M}}_i^2)^2 + 8(\xi_1 - \xi_2)(\bar{\mathbf{M}}_r \times \bar{\mathbf{M}}_i)^2 \tag{B.13}$$

where $\xi_1 = \int_k (\mathcal{G}_k^c)^2 (\mathcal{G}_{K+k}^f)^2$, $\xi_2 = \int_k (\mathcal{G}_k^c)^2 \mathcal{G}_{K+k}^f \mathcal{G}_{-K+k}^f$ and are shown diagrammatically in Fig. B.1.

For circular Fermi surface, $\mathcal{G}_{K+k}^f = \mathcal{G}_{-K+k}^f$, the second term in Eq. B.13 vanishes and the degeneracy of SDW order cannot be lifted by the quartic term, consistent with the analysis of Eq. 4.12.

Anisotropy in the Fermi surface breaks the degeneracy similar to the analysis of the iron-based materials on a square lattice. Consider the quadratic spectrum $\epsilon_{\Gamma,\boldsymbol{k}} = \frac{k^2}{2m} - \mu$, $\epsilon_{\pm K,\boldsymbol{k}} = \frac{k^2}{2m} - \mu + \delta_\mu \pm \delta_m \cos 3\theta_{\boldsymbol{k}}$, we find $\xi_2 - \xi_1 > 0$. Thus to lower the free energy in Eq. B.13, $\mathbf{M}_r \perp \mathbf{M}_i$ and $|\mathbf{M}_r| = |\mathbf{M}_i|$, i.e. the SDW in real space is the 120° spiral order due to anisotropy of the electron Fermi surface.

B.1.2 Effective action in a Zeeman field

We now derive the effective action in a Zeeman field, and show that the Zeeman field introduces bilinear coupling between $\bar{\mathbf{M}}$ and $\bar{\mathbf{\Phi}}$ as $F_{cross} = -\frac{2N_F}{\mu}\sum_{i=\pm K} \mathrm{Im}(\bar{\mathbf{M}}_i \times$

$\bar{\mathbf{\Phi}}_i^*) \cdot \vec{h}$.

The Green's function of free electrons in the normal state is:

$$\begin{aligned}\mathcal{G}_{0,\Gamma} &= \left((i\omega - \epsilon_{\Gamma,\boldsymbol{q}})\mathbb{I} + h\sigma_z\right)^{-1} \\ \mathcal{G}_{0,\pm K} &= \left((i\omega - \epsilon_{\pm K,\boldsymbol{q}})\mathbb{I} + h\sigma_z\right)^{-1}\end{aligned} \tag{B.14}$$

The bilinear coupling comes from the crossing terms of $\mathcal{V}^M$ and $\mathcal{V}^\Phi$ in $\frac{1}{2}\operatorname{Tr}(\mathcal{G}_{0,k}\mathcal{V})^2$.

$$\begin{aligned}F_{cross} =& \frac{1}{2\beta}\operatorname{Tr}\left(\mathcal{G}_{0,k}\mathcal{V}^M\mathcal{G}_{0,k}\mathcal{V}^\Phi + \mathcal{G}_{0,k}\mathcal{V}^\Phi\mathcal{G}_{0,k}\mathcal{V}^M\right) \\ =& \frac{1}{2\beta}\sum_{i=\pm K}\operatorname{Tr}\left(\mathcal{G}_{0,\Gamma}\bar{\mathbf{M}}_i\cdot\vec{\sigma}\ \mathcal{G}_{0,i}\bar{\mathbf{\Phi}}_i^*\cdot\vec{\sigma} + \mathcal{G}_{0,\Gamma}\bar{\mathbf{M}}_i^*\cdot\vec{\sigma}\ \mathcal{G}_{0,i}\bar{\mathbf{\Phi}}_i\cdot\vec{\sigma} + (\bar{\mathbf{M}}_i \leftrightarrow \bar{\mathbf{\Phi}}_i)\right) \\ =& 4\sum_{i=\pm K}\operatorname{Im}(\bar{\mathbf{M}}_i\times\bar{\mathbf{\Phi}}_i^*)\cdot\vec{h}\int(\mathcal{G}_{0,\Gamma}^{(0)2}\mathcal{G}_{0,i}^{(0)} - \mathcal{G}_{0,\Gamma}^{(0)}\mathcal{G}_{0,i}^{(0)2})\end{aligned} \tag{B.15}$$

From the second to the third line, we expand $\mathcal{G}$ in powers of h as $\mathcal{G}_{0,\Gamma} = \mathcal{G}_{0,\Gamma}^{(0)} - \mathcal{G}_{0,\Gamma}^{(0)}h\sigma_z\mathcal{G}_{0,\Gamma}^{(0)} + \mathcal{O}(h^2)$ and $\mathcal{G}_{0,i} = \mathcal{G}_{0,i}^{(0)} - \mathcal{G}_{0,i}^{(0)}h\sigma_z\mathcal{G}_{0,i}^{(0)} + \mathcal{O}(h^2)$, and use the identities for tracing spin index

$$\operatorname{Tr}[(\sigma_z\vec{a}\cdot\vec{\sigma})(\vec{b}\cdot\vec{\sigma})] = 2i(\vec{a}\times\vec{b})\cdot\hat{z}, \quad \operatorname{Tr}[(\vec{a}\cdot\vec{\sigma})(\sigma_z\vec{b}\cdot\vec{\sigma})] = -2i(\vec{a}\times\vec{b})\cdot\hat{z}. \tag{B.16}$$

The integral $\mathcal{I}^{(3)} = \int_k(\mathcal{G}_\Gamma^{(0)2}\mathcal{G}_i^{(0)} - \mathcal{G}_\Gamma^{(0)}\mathcal{G}_i^{(0)2})$ is:

$$\begin{aligned}\mathcal{I}^{(3)} &= \int\frac{\mathrm{d}\omega}{2\pi}\frac{\mathrm{d}^2k}{\mathcal{B}}(\mathcal{G}_\Gamma^{(0)2}\mathcal{G}_i^{(0)} - \mathcal{G}_\Gamma^{(0)}\mathcal{G}_i^{(0)2}) = N_F\int\frac{\mathrm{d}\omega}{2\pi}\,\mathrm{d}\epsilon\frac{1}{i\omega+\epsilon}\frac{1}{i\omega-\epsilon}(\frac{1}{i\omega+\epsilon} - \frac{1}{i\omega-\epsilon}) \\ &= -\frac{N_F}{2\mu}\end{aligned} \tag{B.17}$$

B.2 Spin ordering instability in a magnetic field

In this section, we show details of solving the linearized spin ordering equations in (i) $\sigma^\pm$ and (ii) σ^z channel assuming perfect nesting between electron and hole pockets (Eq. 4.27 in the main text),

$$\begin{aligned}&\text{(i)} \quad 1 + \frac{1}{2}\Big(g_1(\Pi_+ + \Pi_-) - \left((\Pi_+ - \Pi_-)^2g_1^2 + 4\Pi_+\Pi_-g_3^2\right)^{1/2}\Big) = 0, \\ &\text{(ii)} \quad 1 + (g_1 + g_3)\Pi_z = 0.\end{aligned} \tag{B.18}$$

To solve for Eq. B.18 requires calculating the particle-hole polarization Π_{ph} for different spin channels, where

$$\Pi_{ph} = T\sum_{\omega_n}\int \frac{\mathrm{d}^2k}{\mathcal{A}_{B.Z.}}\mathcal{G}^f(\boldsymbol{k}\pm K)\mathcal{G}^c(\boldsymbol{k}) = \int \frac{\mathrm{d}^2k}{\mathcal{A}_{B.Z.}}\frac{n_F(\epsilon_{\boldsymbol{k}})-n_F(\epsilon_{\boldsymbol{k}\pm K})}{\epsilon_{\boldsymbol{k}}-\epsilon_{\boldsymbol{k}\pm K}}$$
$$= N_F\int \mathrm{d}\epsilon_{\boldsymbol{k}}\frac{n_F(\epsilon_{\boldsymbol{k}})-n_F(\epsilon_{\boldsymbol{k}\pm K})}{\epsilon_{\boldsymbol{k}}-\epsilon_{\boldsymbol{k}\pm K}}. \tag{B.19}$$

In the following, we discuss the result of the integral for different band structure configurations.

In zero field, Π_{ph} is

$$\Pi_{ph,0} = N_F\int_{-\mu}^{\Lambda}\mathrm{d}\epsilon\frac{n_F(\epsilon)-n_F(-\epsilon)}{2\epsilon} = -\frac{1}{2}N_F\int_{-\mu}^{\Lambda}\mathrm{d}\epsilon\frac{\tanh\frac{\beta\epsilon}{2}}{\epsilon}\sim -\frac{1}{2}N_F\ln\frac{\mu}{T}+const. \tag{B.20}$$

In a Zeeman field, with $\mathcal{H}_Z = -\boldsymbol{h}\cdot\sum_{\boldsymbol{k}}(c^\dagger_{\boldsymbol{k}}\boldsymbol{\sigma}c_{\boldsymbol{k}}+f^\dagger_{\boldsymbol{k}}\boldsymbol{\sigma}f_{\boldsymbol{k}})$, the particle and hole pockets involved in the spin ordering in the $\sigma^\pm$ channel remain perfectly nested, and $\epsilon_{\boldsymbol{k}\pm K,\uparrow} = -\epsilon_{\boldsymbol{k},\downarrow} = \frac{k^2}{2m}-\mu-h$, $\epsilon_{\boldsymbol{k}\pm K,\downarrow} = -\epsilon_{\boldsymbol{k},\uparrow} = \frac{k^2}{2m}-\mu+h$. As a result, the band splitting only modifies the energy at the bottom of the band, i.e. the high energy cutoff in the integral from $\mu\to\mu\pm h$.

$$\Pi_{ph,\pm} = -\frac{1}{2}N_F\int_{-(\mu\pm h)}^{\Lambda\mp h}\mathrm{d}\epsilon\frac{\tanh\frac{\beta\epsilon}{2}}{\epsilon}\sim -\frac{1}{2}N_F\big(\ln\frac{\mu\pm h}{T}+const.\big) = -(|\Pi_{ph,0}|\pm\frac{1}{2}N_F\frac{h}{\mu}) \tag{B.21}$$

Plug it into Eq. B.18, to the leading order in h/μ, the solution to the linearized ordering equation in $\sigma^\pm$ channel becomes

$$1+(g_1+g_3)\Pi_0(T)\Big(1-\frac{g_3-g_1}{4g_3}\big(\frac{N_F}{\Pi_0}\big)^2\big(\frac{h}{\mu}\big)^2\Big) = 0. \tag{B.22}$$

In the σ_z channel, the particle-hole symmetry between the involved bands is broken. For example, in the evaluation of $\Pi_{ph,\uparrow}$, as $\epsilon_{\boldsymbol{k}\pm K,\uparrow} = \frac{k^2}{2m}-\mu-h$, $\epsilon_{\boldsymbol{k},\uparrow} = -(\frac{k^2}{2m}-\mu+h) = -\epsilon_{\boldsymbol{k}\pm K,\uparrow}-2h$,

$$\Pi_{ph,\uparrow} = \int\frac{\mathrm{d}^2k}{\mathcal{A}_{B.Z.}}\frac{n_F(\epsilon_{\boldsymbol{k},\uparrow})-n_F(\epsilon_{\boldsymbol{k}\pm K,\uparrow})}{\epsilon_{\boldsymbol{k},\uparrow}-\epsilon_{\boldsymbol{k}\pm K,\uparrow}} = N_F\int_{-(\mu+h)}^{\Lambda}\mathrm{d}\epsilon\frac{n_F(-\epsilon-2h)-n_F(\epsilon)}{-2\epsilon-2h}$$
$$= -\frac{N_F}{2}\int_{-(\mu+h)}^{\Lambda}\mathrm{d}\epsilon\frac{1}{\epsilon+h}\big(\frac{1}{e^{\beta(-\epsilon-2h)}+1}-\frac{1}{e^{\beta\epsilon}+1}\big)$$

$$= -\frac{N_F}{2}\int_{-\mu}^{\Lambda} \mathrm{d}\epsilon \frac{1}{\epsilon}\Big(\frac{1}{e^{-\beta\epsilon-\beta h}+1} - \frac{1}{e^{\beta\epsilon-\beta h}+1}\Big)$$
$$= -\frac{N_F}{2}\int_{-\mu\beta}^{\Lambda\beta} \mathrm{d}x \frac{1}{x}\Big(\frac{1}{e^{-x-\beta h}+1} - \frac{1}{e^{x-\beta h}+1}\Big) \tag{B.23}$$

Similarly, $\Pi_{ph,\downarrow} = -\frac{N_F}{2}\int_{-\mu}^{\Lambda} \mathrm{d}\epsilon \frac{1}{\epsilon}\Big(\frac{1}{e^{-\beta\epsilon+\beta h}+1} - \frac{1}{e^{\beta\epsilon+\beta h}+1}\Big) = \Pi_{ph,\uparrow}$. To evaluate the integral in Eq. B.23, we note that the integrand is a function of βh, and it behaves differently in the cases of $\beta h \ll 1$ and $\beta h \gg 1$.

The limit $h \ll T$ – The integral is suppressed only near $\epsilon = 0$, to the leading order in βh, we have

$$\begin{aligned}
\Pi_{ph,\uparrow} &= -\frac{N_F}{2}\int_{-\mu}^{\Lambda} \mathrm{d}\epsilon \frac{1}{\epsilon}\Big(\frac{1}{e^{-\beta\epsilon-\beta h}+1} - \frac{1}{e^{\beta\epsilon-\beta h}+1}\Big) \\
&= -\frac{N_F}{2}\int_{-\mu}^{\Lambda} \mathrm{d}\epsilon \frac{1}{\epsilon}\tanh\frac{\beta\epsilon}{2}\Big(1 - \frac{(\beta h)^2}{4}\frac{1}{\cosh^2\frac{\beta\epsilon}{2}}\Big) + \mathcal{O}(\beta h)^3 \\
&= -\frac{N_F}{2}\Big(\int_{-\mu}^{\Lambda} \mathrm{d}\epsilon \frac{1}{\epsilon}\tanh\frac{\beta\epsilon}{2} - \beta^2 h^2 \int_{-\mu}^{\Lambda} \mathrm{d}\epsilon \frac{1}{4\epsilon}\tanh\frac{\beta\epsilon}{2}\frac{1}{\cosh^2\frac{\beta\epsilon}{2}}\Big) \\
&= -(|\Pi_{ph,0}| - \frac{0.85}{2}N_F\frac{h^2}{T^2})
\end{aligned} \tag{B.24}$$

where $\int_{-\mu}^{\Lambda} \mathrm{d}\epsilon \frac{1}{4\epsilon}\tanh\frac{\beta\epsilon}{2}\frac{1}{\cosh^2\frac{\beta\epsilon}{2}} = 0.85$ is evaluated numerically in the limit $\beta\mu, \beta\Lambda \gg 1$. Plug $\Pi_{ph,\uparrow}, \Pi_{ph,\downarrow}$ into Eq. B.18, to the leading order in h/T, the solution to the linearized ordering equation in σ^z channel becomes

$$1 + (g_1 + g_3)\Pi_0(T)\Big(1 - 0.43\frac{N_F}{|\Pi_0|}\frac{h^2}{T^2}\Big) = 0 \tag{B.25}$$

Comparing Eq. B.22 and Eq. B.25, as $\frac{N_F}{|\Pi_0|} \ll 1$, $\frac{h}{\mu} \ll \frac{h}{T}$, we conclude that the ordering instability in the $\sigma^{\pm}$ channel develops first.

The limit $h \gg T$ – βh modifies the integrand non perturbatively and sets the cutoff in the integral as βh. As a result, $\Pi_{ph,\uparrow}$ simply changes to $\Pi_{ph,\uparrow} = -\frac{1}{2}N_F(\ln\frac{\mu}{h} + const.)$. Because $h \gg T$, $\Pi_{ph,\uparrow} \ll \Pi_{ph,0}$ in this limit. The correction to $\Pi_{ph,\pm}$ remains the same dependance on h/μ as in the limit $h \ll T$. Due to the further non-perturbative suppression of Π_{ph} in σ^z channel, the ordering instability must also first develop in the $\sigma^{\pm}$ channel in the $h \gg T$ limit.

We also did a similar analysis when the particle-hole symmetry of the band structure in zero field is slightly broken, i.e. $\epsilon_{\boldsymbol{k}} = -\epsilon_{\boldsymbol{k}\pm K} + \delta\mu$, and $\delta\mu \ll \mu$. The conclusion remains unchanged.

Appendix C

Appendix to Chapter 5

C.1 Goldstone modes

In this appendix, we give more mathematical details of how the momentum and spin structure of the low energy bosonic collective modes in the SDW state, i.e., the magnon Goldstone modes, can be obtained by studying the eigenstates of its corresponding linear spin wave Hamiltonian. As we show in the main text, these universal properties of the Goldstone modes are enough to obtain the effective magnon-fermion interaction.

To be precise, as our starting point is the SDW state out of itinerant fermions, the collective modes in the interacting fermion system, magnons in this case, should be obtained in principle by calculating the spin correlation function. On the other hand, as the low energy magnons are essentially the Goldstone modes which are uniquely determined by the pattern of the spontaneous spin rotation symmetry breaking, the universal properties of the Goldstone modes can be obtained from other models that are adiabatically connected to the Hubbard model in the large U limit, e.g. the isotropic Heisenberg model. For the square lattice Hubbard model, it has been checked that the spectrum calculated from the two methods match over the whole Brillouin [28, 195]. For the triangular lattice Hubbard model, though it turns more tricky at higher energy [178], the matching should work in principle for the low energy Goldstone modes for the reason we explained above. We also checked that it is indeed the case. In the following, we work with the nearest neighbor isotropic Heisenberg antiferromagnetic model using linear spin wave analysis. The large S spin wave expansion can be reproduced by taking $2S$ fermion flavors in the Hubbard model.

The global and local coordinates are set up as shown in Fig. 5.4(a). To obtain the linear spin wave Hamiltonian, we express the spin operators in terms of Holstein-

Primakoff bosons a, $a^\dagger$. In the local coordinate where the magnetic order is along $\tilde{z}$, the spin operator is:

$$S_r^+(\tilde{z}) = \sqrt{2S}\sqrt{1-\frac{a_r^\dagger a_r}{2S}}a_r, \quad S_r^-(\tilde{z}) = \sqrt{2S}a_r^\dagger\sqrt{1-\frac{a_r^\dagger a_r}{2S}}, \quad S_r^z(\tilde{z}) = S - a_r^\dagger a_r \tag{C.1}$$

The spin operators in the global coordinate can be expressed as:

$$S_i^x = S^x(\tilde{z})\cos\theta_i + S^z(\tilde{z})\sin\theta_i, \quad S_i^y = S_i^y(\tilde{z}) \quad S_i^z = -S^x(\tilde{z})\sin\theta_i + S^z(\tilde{z})\cos\theta_i, \tag{C.2}$$

where i is the sublattice index $i = a, b, c$, and $\theta_i = 0, 2\pi/3, 4\pi/3$. The linear spin wave Hamiltonian can be expressed as []

$$\mathcal{H}^{(2)} = \frac{S}{2}\sum_k \Psi_k^\dagger H_k \Psi_k, \tag{C.3}$$

where $\Psi_k = \{a_k, a_{-k}^\dagger\}^T$,

$$H_k = \begin{pmatrix} A_k & B_k \\ B_k & A_{-k} \end{pmatrix}, \tag{C.4}$$

$A_k = J(3 + \frac{1}{2}\gamma_k)$, $B_k = -\frac{3}{2}J\gamma_k$, $\gamma_k = \cos k_x + 2\cos k_x/2 \cos\sqrt{3}k_y/2$. The spin wave Hamiltonian can be diagonalized by the transformation $\Psi_k = T\Psi_k'$, where $\Psi_k' = \{e_k, e_{-k}^\dagger\}^T$, such that $T^{-1}\sigma_z H_k T = \omega_k \sigma_z$. We found $\omega_k = \sqrt{A_k^2 - B_k^2}$, and

$$T_k = \begin{pmatrix} \sqrt{\frac{A_k+\omega_k}{2\omega_k}} & -\mathrm{sgn}B_k\sqrt{\frac{A_k-\omega_k}{2\omega_k}} \\ -\mathrm{sgn}B_k\sqrt{\frac{A_k-\omega_k}{2\omega_k}} & \sqrt{\frac{A_k+\omega_k}{2\omega_k}} \end{pmatrix}. \tag{C.5}$$

As the $SU(2)$ spin rotation symmetry of the Hamiltonian is fully broken by the magnetic order, there are three Goldstone modes, associated with the three broken symmetry generators. It is straight forward to show that there are three zero modes at momentum $\Gamma = (0, 0)$ and $\pm K = \pm(\frac{4\pi}{3}, 0)$, respectively. To check if they are the Goldstone modes and learn the spin structure, let us analyze the eigenmodes near $\Gamma, \pm K$.

Near Γ – The spin wave spectrum is $\omega_{q+\Gamma} = \frac{3\sqrt{3}JS}{4}q$. The transformation matrix

T_k is

$$T_{q+\Gamma} = \frac{\sqrt[4]{3}}{\sqrt{2q}} \times \begin{pmatrix} 1 & 1 \\ 1 & 1 \end{pmatrix} + \frac{\sqrt{q}}{2\sqrt{2}\sqrt[4]{3}} \times \begin{pmatrix} 1 & -1 \\ -1 & 1 \end{pmatrix} + \mathcal{O}(q) \tag{C.6}$$

The part singular in $\sqrt{q}$ at order $1/\sqrt{q}$ corresponds to the Goldstone mode excitation, which contributes to the divergent static susceptibility as $q \to 0$, while the subleading term at order $\sqrt{q}$ corresponds to the soft modes, whose static susceptibility is finite at $q = 0$. From the singular part, we obtain the leading order dynamical spin susceptibility (labeled by superscript "(0)") at $S = 1/2$

$$\begin{aligned} -i\langle TS^{\tilde{x}}_{-q}(t)S^{\tilde{x}}_{q}(0)\rangle^{(0)}_{\omega} &= -\frac{i}{4}\langle T(a_{-q}(t) + a^{\dagger}_{q}(t))(a_q(0) + a^{\dagger}_{-q}(0))\rangle_{\omega} \\ &= -i\langle T(e_{-q}(t) + e^{\dagger}_{q}(t))(e_q(0) + e^{\dagger}_{-q}(0))\rangle_{\omega} \times \big(\frac{\sqrt[4]{3}}{\sqrt{2q}}\big)^2 \\ &= \frac{9JS}{2}\frac{1}{\omega^2 - \omega_q^2} = \frac{9J}{4}\frac{1}{\omega^2 - \omega_q^2} \\ -i\langle TS^{\tilde{y}}_{-q}(t)S^{\tilde{y}}_{q}(0)\rangle^{(0)}_{\omega} &= 0. \end{aligned} \tag{C.7}$$

Similarly, we obtain from the $\sqrt{q}$ order terms in Eq. (C.6) the next order dynamical spin susceptibility (labeled by superscript "(1)") at $S = 1/2$

$$-i\langle TS^{\tilde{x}}_{-q}(t)S^{\tilde{x}}_{q}(0)\rangle^{(1)}_{\omega} = 0, \qquad -i\langle TS^{\tilde{y}}_{-q}(t)S^{\tilde{y}}_{q}(0)\rangle^{(1)}_{\omega} = \frac{3Jq^2}{16}\frac{1}{\omega^2 - \omega_q^2}. \tag{C.8}$$

Note that by $\tilde{x}, \tilde{y}$, we mean the spin component in the local coordinates. For our interest of obtaining the logarithmical divergent contribution to the thermal self-energy, only non-zero terms in Eq. (C.7) is needed, which physically means spin fluctuations along the local $\tilde{x}$ direction at the Γ point (see Fig. 5.4(b)).

Near $\pm K$ – By doing the same analysis near $\pm K$, we found the spin wave spectrum is $\omega_{q\pm K} = \frac{3\sqrt{3}JS}{2\sqrt{2}}q$, and to the leading order in q,

$$T_{q\pm K} = \frac{\sqrt[4]{3}}{2^{3/4}\sqrt{q}} \times \begin{pmatrix} 1 & -1 \\ -1 & 1 \end{pmatrix} + \mathcal{O}(\sqrt{q}). \tag{C.9}$$

The leading order dynamical spin susceptibility at $S = 1/2$ is

$$-i\langle TS^{\tilde{y}}_{-q\pm K}(t)S^{\tilde{y}}_{q\mp K}(0)\rangle^{(0)}_{\omega} = \frac{9J}{8}\frac{1}{\omega^2 - \omega^2_{q\pm K}}. \tag{C.10}$$

Eqs. (C.7) and (C.10) are essentially what we have in Eq. (5.13) in the main text. The two Goldstone modes are shown graphically in Fig. 5.4(c),(d).

C.2 Calculation of $\mathcal{C}_n(z)$

To obtain $\mathcal{C}_n(z)$ for a generic n, we review the rules found in Sec. 5.3.1. These are

- We use $\circ$ and $\bullet$ for magnon-fermion vertex $\hat{e}\,\gamma^{v\dagger}\gamma^{c}$ and $\hat{e}\,\gamma^{c\dagger}\gamma^{v}$, respectively. As vertices like $\hat{e}\,\gamma^{v\dagger}\gamma^{v}$ are not considered to the leading logarithmical order, the renormalized Green's function at n-loop order should have n pairs of alternating $\circ$ and $\bullet$ vertices;
- Adding contributions from χ^{xx} and χ^{yy}, each $\circ\!\approx\!\circ$ or $\bullet\!\approx\!\bullet$ magnon propagator contribute a factor $(\beta_1 - 2\beta_2)U^2$;
- Similarly, each $\circ\!\approx\!\bullet$ or $\bullet\!\approx\!\circ$ magnon propagator contribute a factor $(\beta_1 + 2\beta_2)U^2$.

All diagrammatic configurations at n-loop order can be grouped by the total number of $\bullet\!\approx\!\bullet$, $\circ\!\approx\!\circ$, $\circ\!\approx\!\bullet$ and $\bullet\!\approx\!\circ$ propagators, and the contribution from each diagram is the same within a given group. In the following, we discuss $n = 2m$ even and $n = 2m+1$ odd seperately.

C.2.1 n=2m

Each diagram is in a group (labeled by l) that has $m-l$ of $\bullet\!\approx\!\bullet$, $m-l$ of $\circ\!\approx\!\circ$ propagators, and a total $2l$ of $\bullet\!\approx\!\circ$ or $\circ\!\approx\!\bullet$ propagators, where $l = 0, 1, ..., m$. For a given group labeled as l, the combinatoric factor contributing to the renormalized Green's function is

$$\begin{aligned}&\Big\{\Big[\frac{C_{2m}^2 C_{2m-2}^2..C_{2l+2}^2}{(m-l)!}\Big]^2[(\beta_1-2\beta_2)U^2]^{2(m-l)}\Big\}\Big\{(2l)![(\beta_1+2\beta_2)U^2]^{2l}\Big\}\\ =&(\beta U^2)^{2m}\Big\{\Big[\frac{(2m)!}{(2m-2l)!!}\Big]^2\frac{z^{2l}}{(2l)!}\Big\},\end{aligned} \tag{C.11}$$

where the first $\{...\}$ in the first line above comes from contributions of $\bullet\!\approx\!\bullet$ and $\circ\!\approx\!\circ$ propagators, and the second $\{...\}$ comes from contributions of $\bullet\!\approx\!\circ$ and $\circ\!\approx\!\bullet$ propagators. Summing up all factors, we find $\mathcal{C}_{2m}(z) = \sum_{l=0}^{m}\big[\frac{(2m)!}{(2m-2l)!!}\big]^2\frac{z^{2l}}{(2l)!}$.

C.2.2 n=2m+1

For n odd, as the total number of $\circ$ or $\bullet$ vertices used up for $\circ\!\approx\!\circ$ or $\bullet\!\approx\!\bullet$ propagators must be even, there must be a total odd number of $\bullet\!\approx\!\circ$ and $\circ\!\approx\!\bullet$ propagators. As a result, each group labeled by l has $m-l$ of $\bullet\!\approx\!\bullet$, $m-l$ of $\circ\!\approx\!\circ$ propagators, and a total $2l+1$ of $\bullet\!\approx\!\circ$ and $\circ\!\approx\!\bullet$ propagators, where $l=0,1,...,m$. The combinatoric factor is

$$\begin{aligned}&\Big\{\Big[\frac{C_{2m+1}^2 C_{2m-1}^2..C_{2l+3}^2}{(m-l)!}\Big]^2[(\beta_1-2\beta_2)U^2]^{2(m-l)}\Big\}\Big\{(2l+1)![(\beta_1+2\beta_2)U^2]^{2l+1}\Big\}\\ =&(\beta U^2)^{2m+1}\Big\{\Big[\frac{(2m+1)!}{(2m-2l)!!}\Big]^2\frac{z^{2l+1}}{(2l+1)!}\Big\}.\end{aligned}\tag{C.12}$$

Summing up all factors, we find $\mathcal{C}_{2m+1}(z)=\sum_{l=0}^{m}\big[\frac{(2m+1)\,!}{(2m-2l)\,!!}\big]^2\frac{z^{2l+1}}{(2l+1)\,!}$.

C.3 Evaluate the spectral function

We now evaluate the spectral function defined as $A^{c,v}(k_{hs},\omega)=-\frac{1}{\pi}\,\mathrm{Im}\,G^{c,v}(k_{hs},\omega+i\delta)$ analytically starting from Eqs. (5.26) and (5.27). The key challenge is to perform the summation over n in Eq. (5.27) where $\mathcal{C}_n(z)$ doesn't have a simple closed form. Moreover, as $\mathcal{C}_n(z)\sim\mathcal{O}(n!)$, a numerical calculation of $A^{c,v}(k_{hs},\omega)$ is quite challenging on its own. Our point of departure is to sum over l in Eq. (5.26) by noting that from $\frac{(p+q)\,!}{p\,!q\,!}=\frac{1}{2\pi i}\oint^{(0+)}\mathrm{d}t\,t^{-p-1}(1-t)^{-q-1}$ [$p,q\in$ Integers $(\mathbb{Z})$ and $p+q\geq-2$] [196],

$$\frac{1}{[(2m-2l)\,!!]^2}=\frac{1}{2^{2m-2l}}\frac{1}{(2m-2l)\,!}\frac{1}{2\pi i}\oint^{(0+)}\mathrm{d}t\,t^{-m+l-1}(1-t)^{-m+l-1},\tag{C.13}$$

where $\oint^{(0+)}$ means the contour integral goes around the pole at $t=0$ counter-clockwisely [see Fig. C.1(a)]. For concreteness, we take $n=2m$ as an example. Plug Eq. (C.13) into Eq. (5.26), we have

$$\mathcal{C}_{2m}(z)=\frac{(2m)\,!}{2^{2m}}\frac{1}{2\pi i}\oint^{(0+)}\mathrm{d}t\,\Big[\frac{1}{t(1-t)}\Big]^{m+1}\sum_{l=0}^{m}\frac{(2m)\,!}{(2m-2l)\,!(2l)\,!}(2z)^{2l}[t(1-t)]^l.\tag{C.14}$$

To sum over l in Eq. (C.14), we note that from $(1+x)^m=\sum_{p=0}^{m}\frac{m!}{(m-p)!\,p!}x^p$,

$$\sum_{l=0}^{m}\frac{(2m)\,!}{(2m-2l)\,!(2l)\,!}(2z)^{2l}[t(1-t)]^l=\sum_{l=0}^{m}\frac{(2m)\,!}{(2m-2l)\,!(2l)\,!}(2z)^{2l}v^{2l}$$

$$
\begin{aligned}
&= \frac{1}{2}\{\sum_{p=0}^{2m} \frac{(2m)!}{(2m-p)!\,p!}(2zv)^p + \sum_{p=0}^{2m} \frac{(2m)!}{(2m-p)!\,p!}(-2zv)^p\} \\
&= \frac{1}{2}\big[(1+2zv)^{2m} + (1-2zv)^{2m}\big], \qquad \text{(C.15)}
\end{aligned}
$$

where we define $v = \sqrt{t(1-t)}$. Note that by summing over l, non-analytic branch-cuts must be introduced, which turns important to get the imaginary part of the spectral function later. Changing variable from t to v, the integration contour changes from a circle around $t = 0$ to a semi-circle around $v = 0$ on the right-half-plane, and $\mathrm{d}t = \frac{2v}{\sqrt{1-4v^2}}\,\mathrm{d}v$. By adding the two terms in Eq. (C.15) and changing variable $v \to -v$ for the second term, Eq. (C.14) becomes [see Fig. C.1(b)]

$$
\mathcal{C}_{2m}(z) = \frac{(2m)\,!}{2^{2m}} \frac{1}{2\pi i} \oint^{(0+)} \mathrm{d}v \left(\frac{1}{v}\right)^{2m+2} \frac{v}{\sqrt{1-4v^2}} (1+2zv)^{2m}. \qquad \text{(C.16)}
$$

Similarly, we found that $\mathcal{C}_{2m+1}(z)$ has the same form but changes $2m$ in the expression to $2m+1$, thus

$$
\mathcal{C}_{n}(z) = \frac{n!}{2^{n}} \frac{1}{2\pi i} \oint^{(0+)} \mathrm{d}v \left(\frac{1}{v}\right)^{n+2} \frac{v}{\sqrt{1-4v^2}} (1+2zv)^{n} \text{ for } n \in \mathbb{Z}. \qquad \text{(C.17)}
$$

From Eq. (C.14) to Eq. (C.17), we are essentially transforming the summation over l in Eq. (C.14) into evaluating the residue of the integrand at $v = 0$ in Eq. (C.17). The gain we have is that the number n now only appears as a simple coefficient $n!$ and as exponents in the integrand, which simplifies the summation over n in Eq. (5.27).

To find $A^{c,v}(k_{hs}, \omega)$, we analytically continue $G^{c,v}(k_{hs}, \omega)$ from Eq. (5.27) to real frequencies by replacing $i\omega \to \omega + i\delta$. As long as the series over n converge, doing the analytical continuation before or after the summation over n should give the same result. For convenience, we perform the analytical continuation before the summation, and have

$$
\begin{aligned}
A^{c,v}(k_{hs}, \omega) &= -\frac{1}{\pi} \operatorname{Im} G^{c,v}(k_{hs}, \omega + i\delta) \\
&= -\frac{1}{\pi} \operatorname{Im}\{G^{c,v\,(0)}(k_{hs}, \omega + i\delta) \sum_{n=0}^{\infty} \mathcal{C}_n(z)[u(\omega + i\delta)]^n\}, \qquad \text{(C.18)}
\end{aligned}
$$

where $u(\omega + i\delta) = \beta U^2 G^{v,c\,(0)}(k_{hs}, \omega + i\delta) G^{c,v\,(0)}(k_{hs}, \omega + i\delta)$. The imaginary part inside $\{...\}$ comes from two places – from $\operatorname{Im} G^{c,v\,(0)}(k_{hs}, \omega + i\delta) \times \operatorname{Re} \sum_{n=0}^{\infty} ...$ and from $\operatorname{Re} G^{c,v\,(0)}(k_{hs}, \omega + i\delta) \times \operatorname{Im} \sum_{n=0}^{\infty} ....$ As $\operatorname{Im} G^{c,v\,(0)}(k_{hs}, \omega + i\delta) = -i\pi\delta(\omega \mp \Delta)$,

the first contribution should be a delta-function peak at $\omega = \pm\Delta$ if $\int_{\Delta-0}^{\Delta+0} \mathrm{d}\omega A(\omega)$ is finite. We checked that this integral actually vanishes. This implies that thermal fluctuations destroy the delta-function peak. To evaluate the second contribution, we use Eq. (C.17) and $n! = \int_0^{+\infty} \mathrm{d}t\, e^{-t} t^n$, express $\sum_{n=0}^{\infty} \mathcal{C}_n(z)[u(\omega+i\delta)]^n$ in Eq. (C.18) as

$$\begin{aligned}
\sum_{n=0}^{\infty} \mathcal{C}_n(z) u_\omega^n &= \frac{1}{2\pi i} \sum_{n=0}^{\infty} n! \oint^{(0+)} \mathrm{d}v\, \frac{1}{v} \frac{1}{\sqrt{1-4v^2}} \Big[\frac{u_\omega(1+2zv)}{2v}\Big]^n \\
&= \frac{1}{2\pi i} \int_0^{+\infty} \mathrm{d}t\, e^{-t} \oint^{(0+)} \mathrm{d}v\, \frac{1}{v} \frac{1}{\sqrt{1-4v^2}} \sum_{n=0}^{\infty} \Big[\frac{u_\omega\, t\,(1+2zv)}{2v}\Big]^n \\
&= \frac{1}{2\pi i} \int_0^{+\infty} \mathrm{d}t\, e^{-t} \oint \mathrm{d}v\, \frac{1}{v} \frac{1}{\sqrt{1-4v^2}} \frac{1}{1-\frac{u_\omega\, t\,(1+2zv)}{2v}} \\
&= \frac{1}{2\pi i} \int_0^{+\infty} \mathrm{d}t\, e^{-t} \oint^{(0-v_0,+)} \mathrm{d}v\, \frac{2}{\sqrt{1-4v^2}} \frac{1}{2v - u_\omega\, t\,(1+2zv)} \\
&= \frac{1}{2\pi i} \int_0^{+\infty} \mathrm{d}t\, e^{-t} \oint^{(0-v_0,+)} \mathrm{d}v\, \frac{2}{\sqrt{1-4v^2}} \frac{1}{2(1-u_\omega\, t\, z)(v - \frac{u_\omega\, t}{2(1-u_\omega\, t\, z)})},
\end{aligned} \tag{C.19}$$

where $u(\omega+i\delta)$ is replaced by u_ω for brevity. Importantly, by summing over n, the multi-pole at $v = 0$ vanishes, while a single pole at $v = v_0 = \frac{u_\omega\, t}{2(1-u_\omega\, t\, z)}$ emerges due to the non-analyticity at $v = 0$. Then the contour $\oint^{(0+)}$ changes to $\oint^{(0-v_0,+)}$, where $\oint^{(0-v_0,+)}$ indicates a counter-clockwise contour enclosing $v = 0$ and $v = v_0$ [see Fig. C.1(c)]. Enforcing $\omega \to \omega + i\delta$, we find $u_\omega \to u_\omega - i\delta\mathrm{sgn}(\omega)$ and $v_0 \to v_0 - i\delta\mathrm{sgn}(\omega)$. As v_0 remains on the lower or upper half-plane [depending on $\mathrm{sgn}(\omega)$] as t varies, the integrals from 0 to v_0 and from v_0 to 0 cancel, and Eq. (C.19) becomes

$$\sum_{n=0}^{\infty} \mathcal{C}_n(z) u_\omega^n = \frac{1}{2\pi i} \int_0^{+\infty} \mathrm{d}t\, e^{-t} \oint^{(v_0+)} \mathrm{d}v\, \frac{1}{\sqrt{1-4v^2}} \frac{1}{(1-u_\omega\, t\, z)(v-v_0)}. \tag{C.20}$$

To obtain the imaginary part of Eq. (C.20), one can show that the only contribution comes from the residue of the integrand of $\oint^{(v_0+)}$ when v_0 sits at the branch cut, i.e., $|v_0| \geq 1/2$. By examining $v_0 = \frac{u_\omega\, t}{2(1-u_\omega\, t\, z)}$ for $t \in (0, \infty)$, we find $|v_0| \geq 1/2$ only when $u_\omega > 0$ and $t \in (\frac{1}{(z+1)u_\omega}, \frac{1}{(z-1)u_\omega})$ [see Fig. C.1(d)]. In particular, if $z = 1$, the upper bound for t is $+\infty$. Thus the imaginary part of Eq. (C.20) when $u_\omega > 0$ is

$$i\,\mathrm{Im} \sum_{n=0}^{\infty} \mathcal{C}_n(z) u_\omega^n = \int_{\frac{1}{(z+1)u_\omega}}^{\frac{1}{(z-1)u_\omega}} \mathrm{d}t\, e^{-t} \frac{1}{2\pi i} \oint^{(v_0+)} \mathrm{d}v\, \frac{1}{\sqrt{1-4v^2}} \frac{1}{(1-u_\omega\, t\, z)(v-v_0)}$$

$$= \int_{\frac{1}{(z+1)u_\omega}}^{\frac{1}{(z-1)u_\omega}} \mathrm{d}t\, e^{-t} \frac{1}{\sqrt{1-4v_0^2}} \frac{1}{1-u_\omega\, t\, z} \tag{C.21}$$

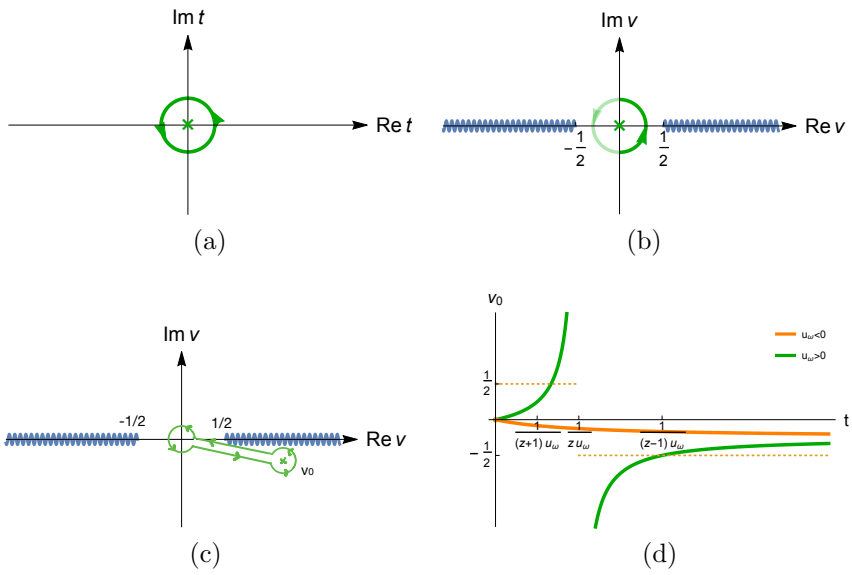

Figure C.1: (a)-(c): The integration contours for the computation of the combinatoric factors. (a) The integration contour for Eqs. (C.13) and (C.14). There is only one multi-pole at $t = 0$ for each given n and l. (b) The contour for Eqs. (C.16) and (C.17). The contour contains the multi-pole and the branch cuts (blue wavy lines). The parts of the contour on the right (darker green line) and on the left (lighter green line) come from the first and second terms in Eq. (C.15). (c) The integration contour for Eq. (C.19). The multi-pole at $v = 0$ moves and becomes a single pole at v_0. (d) v_0 as a function of $t \in (0, \infty)$ for $u_\omega > 0$ and $u_\omega < 0$.

In the following, let us consider $\omega > 0$ for concreteness, so $v_0 \to v_0 - i\delta$. Note that $\frac{1}{\sqrt{1-4v_0^2}}$ is pure imaginary when $t \in (\frac{1}{(z+1)u_\omega}, \frac{1}{(z-1)u_\omega})$. As we explain below, it needs some care to determine the sign at different t. From Fig. C.1(d), we see that when $t \in (\frac{1}{(z+1)u_\omega}, \frac{1}{zu_\omega})$, $\mathrm{Re}\, v_0 > 1/2$, so $\mathrm{Im}\, \frac{1}{\sqrt{1-4v_0^2}} = \frac{1}{\sqrt{1+2v_0}\sqrt{1-2v_0}} = \frac{-i}{\sqrt{1+2v_0}\sqrt{2v_0-1}} = \frac{-i}{\sqrt{4v_0^2-1}}$, $1 - u_\omega\, t\, z > 0$; when $t \in (\frac{1}{z\,u_\omega}, \frac{1}{(z-1)u_\omega})$, $\mathrm{Re}\, v_0 < -1/2$, so $\mathrm{Im}\, \frac{1}{\sqrt{1-4v_0^2}} = \frac{1}{\sqrt{1+2v_0}\sqrt{1-2v_0}} = \frac{i}{\sqrt{4v_0^2-1}}$, $1 - u_\omega\, t\, z < 0$. So Eq. (C.21) becomes

$$i\,\mathrm{Im} \sum_{n=0}^{\infty} \mathcal{C}_n(z) u_\omega^n = \int_{\frac{1}{(z+1)u_\omega}}^{\frac{1}{z\,u_\omega}} \mathrm{d}t\, e^{-t} \frac{-i}{\sqrt{4v_0^2-1}} \frac{1}{1-u_\omega\, t\, z} + \int_{\frac{1}{z\,u_\omega}}^{\frac{1}{(z-1)\,u_\omega}} \mathrm{d}t\, e^{-t} \frac{i}{\sqrt{4v_0^2-1}} \frac{1}{1-u_\omega\, t\, z}$$

$$= \int_{\frac{1}{(z+1)u_\omega}}^{\frac{1}{(z-1)u_\omega}} \mathrm{d}t\, e^{-t} \frac{-i}{\sqrt{(4v_0^2-1)(1-u_\omega\, t\, z)^2}}$$
$$= -i \int_{\frac{1}{(z+1)u_\omega}}^{\frac{1}{(z-1)u_\omega}} \mathrm{d}t\, e^{-t} \frac{1}{\sqrt{(u_\omega\, t)^2-(1-u_\omega\, t\, z)^2}}, \tag{C.22}$$

where the integral over t is convergent and positive definite. Similarly, we find when $\omega < 0$, $i\,\mathrm{Im}\sum_{n=0}^{\infty}\mathcal{C}_n(z)u_\omega^n = i\int_{\frac{1}{(z+1)u_\omega}}^{\frac{1}{(z-1)u_\omega}} \mathrm{d}t\, e^{-t}\frac{1}{\sqrt{(u_\omega\, t)^2-(1-u_\omega\, t\, z)^2}}$. Plug them back to Eq. (C.18), the spectral function is

$$A^{c,v}(k_{hs},\omega) = \frac{1}{\pi}\Big|\frac{1}{\omega \mp \Delta}\Big| \int_{\frac{1}{(z+1)u_\omega}}^{\frac{1}{(z-1)u_\omega}} \mathrm{d}t\, e^{-t} \frac{1}{\sqrt{(u_\omega\, t)^2-(1-u_\omega\, t\, z)^2}} \Theta(u_\omega), \tag{C.23}$$

where we remind $u_\omega = \frac{\beta U^2}{\omega^2-\Delta^2}$.

Bibliography

[1] Assa Auerbach. *Interacting Electrons and Quantum Magnetism*. Springer-Verlag, 1994.

[2] Naoto Nagaosa. *Quantum field theory in strongly correlated electronic systems*. Berlin, Germany: Springer (1999), 1999.

[3] Claudine Lacroix, Philippe Mendels, and Frédéric Mila, editors. *Introduction to Frustrated Magnetism*. Springer Berlin Heidelberg, 2011.

[4] Leon Balents. Spin liquids in frustrated magnets. *Nature*, 464(7286):199–208, 03 2010.

[5] O. A. Starykh. Unusual ordered phases of highly frustrated magnets: a review. *Reports on Progress in Physics*, 78(5):052502, May 2015.

[6] Lucile Savary and Leon Balents. Quantum spin liquids: a review. *Reports on Progress in Physics*, 80(1):016502, 2017.

[7] Kenji Ishida, Yusuke Nakai, and Hideo Hosono. To what extent iron-pnictide new superconductors have been clarified: a progress report. *Journal of the Physical Society of Japan*, 78(6):062001, 2009.

[8] S. Graser, T. A. Maier, P. J. Hirschfeld, and D. J. Scalapino. Near-degeneracy of several pairing channels in multiorbital models for the Fe pnictides. *New Journal of Physics*, 11(2):025016, 2009.

[9] D. C. Johnston. The puzzle of high temperature superconductivity in layered iron pnictides and chalcogenides. *Advances in Physics*, 59(6):803–1061, 2010.

[10] Johnpierre Paglione and Richard L Greene. High-temperature superconductivity in iron-based materials. *Nature Physics*, 6(9):645–658, 2010.

[11] G. R. Stewart. Superconductivity in iron compounds. *Rev. Mod. Phys.*, 83:1589–1652, Dec 2011.

[12] Paul C Canfield and Sergey L Bud´ko. FeAs-Based Superconductivity: A Case Study of the Effects of Transition Metal Doping on BaFe2As2. *Annu. Rev. Condens. Matter Phys.*, 1(1):27–50, 2010.

[13] A. B. Vorontsov, M. G. Vavilov, and A. V. Chubukov. Superconductivity and spin-density waves in multiband metals. *Phys. Rev. B*, 81:174538, May 2010.

[14] R. M. Fernandes, A. V. Chubukov, and J. Schmalian. What drives nematic order in iron-based superconductors? *Nature Physics*, 10(2):97–104, 2014.

[15] Andrey Chubukov. Pairing Mechanism in Fe-Based Superconductors. *Annual Review of Condensed Matter Physics*, 3(1):57–92, 2012.

[16] Andrey Chubukov. *Itinerant Electron Scenario*, pages 255–329. Springer International Publishing, Cham, 2015.

[17] H.-H. Wen and S. Li. Materials and novel superconductivity in iron pnictide superconductors. *Annual Review of Condensed Matter Physics*, 2(1):121–140, 2011.

[18] Fa Wang and Dung-Hai Lee. The electron-pairing mechanism of iron-based superconductors. *Science*, 332(6026):200–204, 2011.

[19] C. Platt, W. Hanke, and R. Thomale. Functional renormalization group for multi-orbital fermi surface instabilities. *Advances in Physics*, 62(4-6):453–562, 2013.

[20] D. J. Scalapino. A common thread: The pairing interaction for unconventional superconductors. *Rev. Mod. Phys.*, 84:1383–1417, Oct 2012.

[21] Amalia I. Coldea and Matthew D. Watson. The Key Ingredients of the Electronic Structure of FeSe. *Annual Review of Condensed Matter Physics*, 9(1):null, 2018.

[22] B. Keimer, S. A. Kivelson, M. R. Norman, S. Uchida, and J. Zaanen. From quantum matter to high-temperature superconductivity in copper oxides. *Nature*, 518:179 EP –, 02 2015.

[23] Eduardo Fradkin, Steven A. Kivelson, Michael J. Lawler, James P. Eisenstein, and Andrew P. Mackenzie. Nematic fermi fluids in condensed matter physics. *Annual Review of Condensed Matter Physics*, 1(1):153–178, 2010.

[24] Claudine Lacroix. Frustrated metallic systems: A review of some peculiar behavior. *Journal of the Physical Society of Japan*, 79(1):011008, 2010.

[25] Fradkin, Eduardo. *Field Theories of Condensed Matter Physics*. Cambridge University Press, Cambridge, 2013.

[26] Subir Sachdev. Quantum criticality: Competing ground states in low dimensions. *Science*, 288(5465):475–480, 2000.

[27] Matthias Vojta and Subir Sachdev. Charge order, superconductivity, and a global phase diagram of doped antiferromagnets. *Phys. Rev. Lett.*, 83:3916–3919, Nov 1999.

[28] J. R. Schrieffer, X. G. Wen, and S. C. Zhang. Dynamic spin fluctuations and the bag mechanism of high-T_c superconductivity. *Phys. Rev. B*, 39:11663–11679, Jun 1989.

[29] Ar. Abanov, Andrey V. Chubukov, and J. Schmalian. Quantum-critical theory of the spin-fermion model and its application to cuprates: Normal state analysis. *Advances in Physics*, 52(3):119–218, 2003.

[30] Max A. Metlitski and Subir Sachdev. Quantum phase transitions of metals in two spatial dimensions. ii. spin density wave order. *Phys. Rev. B*, 82:075128, Aug 2010.

[31] William Witczak-Krempa, Gang Chen, Yong Baek Kim, and Leon Balents. Correlated quantum phenomena in the strong spin-orbit regime. *Annual Review of Condensed Matter Physics*, 5(1):57–82, 2014.

[32] Villain, J., Bidaux, R., Carton, J.-P., and Conte, R. Order as an effect of disorder. *J. Phys. France*, 41(11):1263–1272, 1980.

[33] Christopher L. Henley. Ordering due to disorder in a frustrated vector antiferromagnet. *Phys. Rev. Lett.*, 62:2056–2059, Apr 1989.

[34] Andrey V. Chubukov and Th. Jolicoeur. Order-from-disorder phenomena in heisenberg antiferromagnets on a triangular lattice. *Phys. Rev. B*, 46:11137–11140, Nov 1992.

[35] R. Moessner and J. T. Chalker. Low-temperature properties of classical geometrically frustrated antiferromagnets. *Phys. Rev. B*, 58:12049–12062, Nov 1998.

[36] Subir Sachdev. Kagome and triangular-lattice Heisenberg antiferromagnets: Ordering from quantum fluctuations and quantum-disordered ground states with unconfined bosonic spinons. *Phys. Rev. B*, 45:12377–12396, Jun 1992.

[37] I. Rousochatzakis, S. Kourtis, J. Knolle, R. Moessner, and N. B. Perkins. Quantum spin liquid at finite temperature: Proximate dynamics and persistent typicality. *Phys. Rev. B*, 100:045117, Jul 2019.

[38] Mengxing Ye and Andrey V. Chubukov. Half-magnetization plateau in a heisenberg antiferromagnet on a triangular lattice. *Phys. Rev. B*, 96:140406, Oct 2017.

[39] Claire Lhuillier. Frustrated Quantum Magnets. *arXiv e-prints*, pages cond–mat/0502464, Feb 2005.

[40] Alexei Kitaev. Anyons in an exactly solved model and beyond. *Annals of Physics*, 321(1):2–111, 2006.

[41] Mengxing Ye and Andrey V. Chubukov. Quantum phase transitions in the Heisenberg $J_1 - J_2$ triangular antiferromagnet in a magnetic field. *Phys. Rev. B*, 95:014425, Jan 2017.

[42] Simon Trebst. Kitaev materials. *arXiv preprint arXiv:1701.07056*, 2017.

[43] G Jackeli and G Khaliullin. Mott insulators in the strong spin-orbit coupling limit: from heisenberg to a quantum compass and kitaev models. *Physical review letters*, 102(1):017205, 2009.

[44] Yi Zhou and Patrick A. Lee. Spinon phonon interaction and ultrasonic attenuation in quantum spin liquids. *Phys. Rev. Lett.*, 106:056402, Feb 2011.

[45] Maksym Serbyn and Patrick A. Lee. Spinon-phonon interaction in algebraic spin liquids. *Phys. Rev. B*, 87:174424, May 2013.

[46] Gábor B. Halász, Natalia B. Perkins, and Jeroen van den Brink. Resonant inelastic x-ray scattering response of the kitaev honeycomb model. *Phys. Rev. Lett.*, 117:127203, Sep 2016.

[47] Leon Balents and Oleg A. Starykh. Spinon waves in magnetized spin liquids. *arXiv e-prints*, page arXiv:1904.02117, Apr 2019.

[48] Yuan Wan and N. P. Armitage. Resolving continua of fractional excitations by spinon echo in thz 2d coherent spectroscopy. *Phys. Rev. Lett.*, 122:257401, Jun 2019.

[49] Mengxing Ye, Gábor B. Halász, Lucile Savary, and Leon Balents. Quantization of the thermal hall conductivity at small hall angles. *Phys. Rev. Lett.*, 121:147201, Oct 2018.

[50] Yuval Vinkler-Aviv and Achim Rosch. Approximately quantized thermal hall effect of chiral liquids coupled to phonons. *Phys. Rev. X*, 8:031032, Aug 2018.

[51] Y. Kasahara, T. Ohnishi, Y. Mizukami, O. Tanaka, Sixiao Ma, K. Sugii, N. Kurita, H. Tanaka, J. Nasu, Y. Motome, T. Shibauchi, and Y. Matsuda. Majorana quantization and half-integer thermal quantum hall effect in a kitaev spin liquid. *Nature*, 559(7713):227–231, 2018.

[52] W. Kohn and J. M. Luttinger. New mechanism for superconductivity. *Phys. Rev. Lett.*, 15:524–526, Sep 1965.

[53] Gia-Wei Chern and C. D. Batista. Spontaneous quantum hall effect via a thermally induced quadratic fermi point. *Phys. Rev. Lett.*, 109:156801, Oct 2012.

[54] Rahul Nandkishore, Gia-Wei Chern, and Andrey V. Chubukov. Itinerant half-metal spin-density-wave state on the hexagonal lattice. *Phys. Rev. Lett.*, 108:227204, May 2012.

[55] I. Eremin and A. V. Chubukov. Magnetic degeneracy and hidden metallicity of the spin-density-wave state in ferropnictides. *Phys. Rev. B*, 81:024511, Jan 2010.

[56] R. Ganesh, G. Baskaran, Jeroen van den Brink, and Dmitry V. Efremov. Theoretical Prediction of a Time-Reversal Broken Chiral Superconducting Phase Driven by Electronic Correlations in a Single $TiSe_2$ Layer. *Phys. Rev. Lett.*, 113:177001, Oct 2014.

[57] R. M. Fernandes, A. V. Chubukov, J. Knolle, I. Eremin, and J. Schmalian. Preemptive nematic order, pseudogap, and orbital order in the iron pnictides. *Phys. Rev. B*, 85:024534, Jan 2012.

[58] Gia-Wei Chern, Rafael M. Fernandes, Rahul Nandkishore, and Andrey V. Chubukov. Broken translational symmetry in an emergent paramagnetic phase of graphene. *Phys. Rev. B*, 86:115443, Sep 2012.

[59] Mengxing Ye and Andrey V. Chubukov. Itinerant fermions on a triangular lattice: Unconventional magnetism and other ordered states. *Phys. Rev. B*, 97:245112, Jun 2018.

[60] M. Klug, J. Kang, R. M. Fernandes, and J. Schmalian. Orbital loop currents in iron-based superconductors. *ArXiv e-prints*, September 2017.

[61] R. M. Fernandes, S. A. Kivelson, and E. Berg. Vestigial chiral and charge orders from bidirectional spin-density waves: Application to the iron-based superconductors. *Phys. Rev. B*, 93:014511, Jan 2016.

[62] Akash V. Maharaj, Ronny Thomale, and S. Raghu. Particle-hole condensates of higher angular momentum in hexagonal systems. *Phys. Rev. B*, 88:205121, Nov 2013.

[63] N. F. MOTT. Metal-insulator transition. *Rev. Mod. Phys.*, 40:677–683, Oct 1968.

[64] A. A. Kordyuk. Pseudogap from arpes experiment: Three gaps in cuprates and topological superconductivity (review article). *Low Temperature Physics*, 41(5):319–341, 2015.

[65] C. M. Varma. Non-fermi-liquid states and pairing instability of a general model of copper oxide metals. *Phys. Rev. B*, 55:14554–14580, Jun 1997.

[66] C. M. Varma. Pseudogap phase and the quantum-critical point in copper-oxide metals. *Phys. Rev. Lett.*, 83:3538–3541, Oct 1999.

[67] S. A. Kivelson, E. Fradkin, and V. J. Emery. Electronic liquid-crystal phases of a doped mott insulator. *Nature*, 393(6685):550–553, 1998.

[68] Eduardo Fradkin, Steven A. Kivelson, and John M. Tranquada. Colloquium: Theory of intertwined orders in high temperature superconductors. *Rev. Mod. Phys.*, 87:457–482, May 2015.

[69] Subir Sachdev. Topological order, emergent gauge fields, and fermi surface reconstruction. *Reports on Progress in Physics*, 82(1):014001, nov 2018.

[70] Jörg Schmalian, David Pines, and Branko Stojković. Weak pseudogap behavior in the underdoped cuprate superconductors. *Phys. Rev. Lett.*, 80:3839–3842, Apr 1998.

[71] Jörg Schmalian, David Pines, and Branko Stojković. Microscopic theory of weak pseudogap behavior in the underdoped cuprate superconductors: General theory and quasiparticle properties. *Phys. Rev. B*, 60:667–686, Jul 1999.

[72] É. Z. Kuchinskii and M. V. Sadovskii. Models of the pseudogap state of two-dimensional systems. *Journal of Experimental and Theoretical Physics*, 88(5):968–979, May 1999.

[73] Tigran A. Sedrakyan and Andrey V. Chubukov. Pseudogap in underdoped cuprates and spin-density-wave fluctuations. *Phys. Rev. B*, 81:174536, May 2010.

[74] M. R. Norman, M. Randeria, H. Ding, and J. C. Campuzano. Phenomenology of the low-energy spectral function in high-T_c superconductors. *Phys. Rev. B*, 57:R11093–R11096, May 1998.

[75] M. Franz and A. J. Millis. Phase fluctuations and spectral properties of underdoped cuprates. *Phys. Rev. B*, 58:14572–14580, Dec 1998.

[76] Erez Berg and Ehud Altman. Evolution of the fermi surface of d-wave superconductors in the presence of thermal phase fluctuations. *Phys. Rev. Lett.*, 99:247001, Dec 2007.

[77] Yi-Ming Wu, Artem Abanov, Yuxuan Wang, and Andrey V. Chubukov. Special role of the first matsubara frequency for superconductivity near a quantum critical point: Nonlinear gap equation below T_c and spectral properties in real frequencies. *Phys. Rev. B*, 99:144512, Apr 2019.

[78] J. P. F. LeBlanc, Andrey E. Antipov, Federico Becca, Ireneusz W. Bulik, Garnet Kin-Lic Chan, Chia-Min Chung, Youjin Deng, Michel Ferrero, Thomas M. Henderson, Carlos A. Jiménez-Hoyos, E. Kozik, Xuan-Wen Liu, Andrew J. Millis, N. V. Prokof'ev, Mingpu Qin, Gustavo E. Scuseria, Hao Shi, B. V. Svistunov, Luca F. Tocchio, I. S. Tupitsyn, Steven R. White, Shiwei Zhang, Bo-Xiao Zheng, Zhenyue Zhu, and Emanuel Gull. Solutions of the two-dimensional hubbard model: Benchmarks and results from a wide range of numerical algorithms. *Phys. Rev. X*, 5:041041, Dec 2015.

[79] G. Aeppli, T. E. Mason, S. M. Hayden, H. A. Mook, and J. Kulda. Nearly singular magnetic fluctuations in the normal state of a high-tc cuprate superconductor. *Science*, 278(5342):1432–1435, 1997.

[80] A. J. Millis, Hartmut Monien, and David Pines. Phenomenological model of nuclear relaxation in the normal state of $yba_2cu_3o_7$. *Phys. Rev. B*, 42:167–178, Jul 1990.

[81] O. Gunnarsson, T. Schäfer, J. P. F. LeBlanc, E. Gull, J. Merino, G. Sangiovanni, G. Rohringer, and A. Toschi. Fluctuation diagnostics of the electron self-energy: Origin of the pseudogap physics. *Phys. Rev. Lett.*, 114:236402, Jun 2015.

[82] Wei Wu, Michel Ferrero, Antoine Georges, and Evgeny Kozik. Controlling feynman diagrammatic expansions: Physical nature of the pseudogap in the two-dimensional hubbard model. *Phys. Rev. B*, 96:041105, Jul 2017.

[83] D.J. Scalapino. The case for $d_{x^2-y^2}$ pairing in the cuprate superconductors. *Physics Reports*, 250(6):329 – 365, 1995.

[84] P. Monthoux and D. Pines. $yba_2cu_3o_7$: A nearly antiferromagnetic fermi liquid. *Phys. Rev. B*, 47:6069–6081, Mar 1993.

[85] P. Monthoux and D. Pines. Nearly antiferromagnetic fermi-liquid description of magnetic scaling and spin-gap behavior. *Phys. Rev. B*, 50:16015–16022, Dec 1994.

[86] Mengxing Ye and Andrey V. Chubukov. Hubbard model on a triangular lattice: Pseudogap due to spin density wave fluctuations. *Phys. Rev. B*, 100:035135, Jul 2019.

[87] Karlo Penc and Andreas M. Läuchli. *Spin Nematic Phases in Quantum Spin Systems*, pages 331–362. Springer Berlin Heidelberg, Berlin, Heidelberg, 2011.

[88] Andrew Smerald and Nic Shannon. Theory of spin excitations in a quantum spin-nematic state. *Phys. Rev. B*, 88:184430, Nov 2013.

[89] L. E. Svistov, A. I. Smirnov, L. A. Prozorova, O. A. Petrenko, A. Micheler, N. Büttgen, A. Ya. Shapiro, and L. N. Demianets. Magnetic phase diagram, critical behavior, and two-dimensional to three-dimensional crossover in the triangular lattice antiferromagnet $RbFe(MoO_4)_2$. *Phys. Rev. B*, 74:024412, Jul 2006.

[90] Luis Seabra and Nic Shannon. Competition between supersolid phases and magnetization plateaus in the frustrated easy-axis antiferromagnet on a triangular lattice. *Phys. Rev. B*, 83:134412, Apr 2011.

[91] M V Gvozdikova, P-E Melchy, and M E Zhitomirsky. Magnetic phase diagrams of classical triangular and kagome antiferromagnets. *Journal of Physics: Condensed Matter*, 23(16):164209, 2011.

[92] Andrey V. Chubukov and Oleg A. Starykh. Spin-Current Order in Anisotropic Triangular Antiferromagnets. *Phys. Rev. Lett.*, 110:217210, May 2013.

[93] Ru Chen, Hyejin Ju, Hong-Chen Jiang, Oleg A. Starykh, and Leon Balents. Ground states of spin-$\frac{1}{2}$ triangular antiferromagnets in a magnetic field. *Phys. Rev. B*, 87:165123, Apr 2013.

[94] Johannes Richter, Oliver Götze, Ronald Zinke, Damian J. J. Farnell, and Hidekazu Tanaka. The Magnetization Process of the Spin-One Triangular-Lattice Heisenberg Antiferromagnet. *Journal of the Physical Society of Japan*, 82(1):015002, 2013.

[95] Tommaso Coletta, Tamás A. Tóth, Karlo Penc, and Frédéric Mila. Semiclassical theory of the magnetization process of the triangular lattice Heisenberg model. *Phys. Rev. B*, 94:075136, Aug 2016.

[96] Y. Shimizu, H. Akimoto, H. Tsujii, A. Tajima, and R. Kato. Mott Transition in a Valence-Bond Solid Insulator with a Triangular Lattice. *Phys. Rev. Lett.*, 99:256403, Dec 2007.

[97] Oleg A. Starykh and Leon Balents. Excitations and quasi-one-dimensionality in field-induced nematic and spin density wave states. *Phys. Rev. B*, 89:104407, Mar 2014.

[98] R. Moessner and S. L. Sondhi. Resonating Valence Bond Phase in the Triangular Lattice Quantum Dimer Model. *Phys. Rev. Lett.*, 86:1881–1884, Feb 2001.

[99] Fa Wang and Ashvin Vishwanath. Spin-liquid states on the triangular and Kagomé lattices: A projective-symmetry-group analysis of Schwinger boson states. *Phys. Rev. B*, 74:174423, Nov 2006.

[100] David A. Huse and Veit Elser. Simple Variational Wave Functions for Two-Dimensional Heisenberg Spin-1/2 Antiferromagnets. *Phys. Rev. Lett.*, 60:2531–2534, Jun 1988.

[101] B. Bernu, C. Lhuillier, and L. Pierre. Signature of Néel order in exact spectra of quantum antiferromagnets on finite lattices. *Phys. Rev. Lett.*, 69:2590–2593, Oct 1992.

[102] Luca Capriotti, Adolfo E. Trumper, and Sandro Sorella. Long-Range Néel Order in the Triangular Heisenberg Model. *Phys. Rev. Lett.*, 82:3899–3902, May 1999.

[103] Steven R. White and A. L. Chernyshev. Neél Order in Square and Triangular Lattice Heisenberg Models. *Phys. Rev. Lett.*, 99:127004, Sep 2007.

[104] Th. Jolicoeur and J. C. Le Guillou. Spin-wave results for the triangular heisenberg antiferromagnet. *Phys. Rev. B*, 40:2727–2729, Aug 1989.

[105] P. Fazekas. *Lecture Notes on Electron Correlation and Magnetism*. Series in modern condensed matter physics. World Scientific, 1999.

[106] S. E. Korshunov. Chiral phase of the Heisenberg antiferromagnet with a triangular lattice. *Phys. Rev. B*, 47:6165–6168, Mar 1993.

[107] P. H. Y. Li, R. F. Bishop, and C. E. Campbell. Quasiclassical magnetic order and its loss in a spin-$\frac{1}{2}$ heisenberg antiferromagnet on a triangular lattice with competing bonds. *Phys. Rev. B*, 91:014426, Jan 2015.

[108] Wen-Jun Hu, Shou-Shu Gong, Wei Zhu, and D. N. Sheng. Competing spin-liquid states in the spin-$\frac{1}{2}$ Heisenberg model on the triangular lattice. *Phys. Rev. B*, 92:140403, Oct 2015.

[109] Zhenyue Zhu and Steven R. White. Spin liquid phase of the $s = \frac{1}{2}$ $J_1 - J_2$ heisenberg model on the triangular lattice. *Phys. Rev. B*, 92:041105, Jul 2015.

[110] Ryui Kaneko, Satoshi Morita, and Masatoshi Imada. Gapless Spin-Liquid Phase in an Extended Spin 1/2 Triangular Heisenberg Model. *Journal of the Physical Society of Japan*, 83(9):093707, 2014.

[111] Yasir Iqbal, Wen-Jun Hu, Ronny Thomale, Didier Poilblanc, and Federico Becca. Spin liquid nature in the heisenberg $J_1 - J_2$ triangular antiferromagnet. *Phys. Rev. B*, 93:144411, Apr 2016.

[112] A V Chubukov and D I Golosov. Quantum theory of an antiferromagnet on a triangular lattice in a magnetic field. *Journal of Physics: Condensed Matter*, 3(1):69, 1991.

[113] E.G. Batyev and L.S. Braginskii. Antiferrornagnet in a strong magnetic field: analogy with Bose gas. *Sov. Phys. JETP*, 60(4):781, 1984.

[114] E. G. Batyev. Antiferromagnet of arbitrary spin in a strong magnetic field. *Sov. Phys. JETP*, 62(1):173, 1986.

[115] Tommaso Coletta, M. E. Zhitomirsky, and Frédéric Mila. Quantum stabilization of classically unstable plateau structures. *Phys. Rev. B*, 87:060407, Feb 2013.

[116] K. Morita and N. Shibata. Field-Induced Quantum Phase Transitions in S = 1/2 J_1-J_2 Heisenberg Model on Square Lattice. *Journal of the Physical Society of Japan*, 85(9):094708, September 2016.

[117] Oleg A. Starykh, Wen Jin, and Andrey V. Chubukov. Phases of a Triangular-Lattice Antiferromagnet Near Saturation. *Phys. Rev. Lett.*, 113:087204, Aug 2014.

[118] R. M. Fernandes, A. V. Chubukov, J. Knolle, I. Eremin, and J. Schmalian. Preemptive nematic order, pseudogap, and orbital order in the iron pnictides. *Phys. Rev. B*, 85:024534, Jan 2012.

[119] Th. Jolicoeur, E. Dagotto, E. Gagliano, and S. Bacci. Ground-state properties of the S =1/2 Heisenberg antiferromagnet on a triangular lattice. *Phys. Rev. B*, 42:4800–4803, Sep 1990.

[120] Kenn Kubo and Tsutomu Momoi. Ground state of a spin system with two- and four-spin exchange interactions on the triangular lattice. *Zeitschrift für Physik B Condensed Matter*, 103(3):485–489, 1997.

[121] A. I. Coldea, L. Seabra, A. McCollam, A. Carrington, L. Malone, A. F. Bangura, D. Vignolles, P. G. van Rhee, R. D. McDonald, T. Sörgel, M. Jansen, N. Shannon, and R. Coldea. Cascade of field-induced magnetic transitions in a frustrated antiferromagnetic metal. *Phys. Rev. B*, 90:020401, Jul 2014.

[122] E. Wawrzyńska, R. Coldea, E. M. Wheeler, T. Sörgel, M. Jansen, R. M. Ibberson, P. G. Radaelli, and M. M. Koza. Charge disproportionation and collinear magnetic order in the frustrated triangular antiferromagnet agnio$_2$. *Phys. Rev. B*, 77:094439, Mar 2008.

[123] E. M. Wheeler, R. Coldea, E. Wawrzyńska, T. Sörgel, M. Jansen, M. M. Koza, J. Taylor, P. Adroguer, and N. Shannon. Spin dynamics of the frustrated easy-axis triangular antiferromagnet $2h$-agnio$_2$ explored by inelastic neutron scattering. *Phys. Rev. B*, 79:104421, Mar 2009.

[124] Luis Seabra and Nic Shannon. Supersolid phases in a realistic three-dimensional spin model. *Phys. Rev. Lett.*, 104:237205, Jun 2010.

[125] Luis Seabra and Nic Shannon. Competition between supersolid phases and magnetization plateaus in the frustrated easy-axis antiferromagnet on a triangular lattice. *Phys. Rev. B*, 83:134412, Apr 2011.

[126] Tetsuro Nikuni and Hiroyuki Shiba. Quantum fluctuations and magnetic structures of cscucl3 in high magnetic field. *Journal of the Physical Society of Japan*, 62(9):3268–3276, 1993.

[127] Christian Griset, Shane Head, Jason Alicea, and Oleg A. Starykh. Deformed triangular lattice antiferromagnets in a magnetic field: Role of spatial anisotropy and dzyaloshinskii-moriya interactions. *Phys. Rev. B*, 84:245108, Dec 2011.

[128] Rahul Nandkishore, L. S. Levitov, and A. V. Chubukov. Chiral superconductivity from repulsive interactions in doped graphene. *Nat Phys*, 8(2):158–163, 02 2012.

[129] Jörn W. F. Venderbos, Vladyslav Kozii, and Liang Fu. Odd-parity superconductors with two-component order parameters: Nematic and chiral, full gap, and majorana node. *Phys. Rev. B*, 94:180504, Nov 2016.

[130] Gregory Moore and Nicholas Read. Nonabelions in the fractional quantum hall effect. *Nuclear Physics B*, 360(2-3):362–396, 1991.

[131] Nicholas Read and Dmitry Green. Paired states of fermions in two dimensions with breaking of parity and time-reversal symmetries and the fractional quantum hall effect. *Physical Review B*, 61(15):10267, 2000.

[132] F. Wilczek. New kinds of quantum statistics. In B. Duplantier, J.M. Raimond, and V. Rivasseau, editors, *The Spin*, volume 55. Progress in Mathematical Physics, Birkhäuser Basel, 2009.

[133] A Yu Kitaev. Fault-tolerant quantum computation by anyons. *Annals of Physics*, 303(1):2–30, 2003.

[134] Chetan Nayak, Steven H Simon, Ady Stern, Michael Freedman, and Sankar Das Sarma. Non-abelian anyons and topological quantum computation. *Reviews of Modern Physics*, 80(3):1083, 2008.

[135] R. M. Lutchyn, E. P. A. M. Bakkers, L. P. Kouwenhoven, P. Krogstrup, C. M. Marcus, and Y. Oreg. Majorana zero modes in superconductor–semiconductor heterostructures. *Nature Reviews Materials*, 3(5):52–68, 2018.

[136] Stephen M. Winter, Ying Li, Harald O. Jeschke, and Roser Valentí. Challenges in design of kitaev materials: Magnetic interactions from competing energy scales. *Phys. Rev. B*, 93:214431, Jun 2016.

[137] Sae Hwan Chun, Jong-Woo Kim, Jungho Kim, H Zheng, Constantinos C Stoumpos, CD Malliakas, JF Mitchell, Kavita Mehlawat, Yogesh Singh, Y Choi, et al. Direct evidence for dominant bond-directional interactions in a honeycomb lattice iridate Na_2IrO_3. *Nature Physics*, 11(6):462, 2015.

[138] SC Williams, RD Johnson, F Freund, Sungkyun Choi, A Jesche, I Kimchi, S Manni, A Bombardi, P Manuel, P Gegenwart, et al. Incommensurate counterrotating magnetic order stabilized by Kitaev interactions in the layered honeycomb α-Li_2IrO_3. *Physical Review B*, 93(19):195158, 2016.

[139] K. W. Plumb, J. P. Clancy, L. J. Sandilands, V. Vijay Shankar, Y. F. Hu, K. S. Burch, Hae-Young Kee, and Young-June Kim. $\alpha - \mathrm{rucl}_3$: A spin-orbit assisted mott insulator on a honeycomb lattice. *Phys. Rev. B*, 90:041112, Jul 2014.

[140] Mitali Banerjee, Moty Heiblum, Vladimir Umansky, Dima E. Feldman, Yuval Oreg, and Ady Stern. Observation of half-integer thermal hall conductance. *Nature*, 559(7713):205–210, 2018.

[141] *Supplementary Material*.

[142] Ivar Martin and C. D. Batista. Itinerant electron-driven chiral magnetic ordering and spontaneous quantum hall effect in triangular lattice models. *Phys. Rev. Lett.*, 101:156402, Oct 2008.

[143] Zhihao Hao and Oleg A. Starykh. Half-metallic magnetization plateaux. *Phys. Rev. B*, 87:161109, Apr 2013.

[144] Maximilian L. Kiesel, Christian Platt, Werner Hanke, Dmitry A. Abanin, and Ronny Thomale. Competing many-body instabilities and unconventional superconductivity in graphene. *Phys. Rev. B*, 86:020507, Jul 2012.

[145] Subir Sachdev. Kagome- and triangular-lattice heisenberg antiferromagnets: Ordering from quantum fluctuations and quantum-disordered ground states with unconfined bosonic spinons. *Phys. Rev. B*, 45:12377–12396, Jun 1992.

[146] Andrey Chubukov. Order from disorder in a kagomé antiferromagnet. *Phys. Rev. Lett.*, 69:832–835, Aug 1992.

[147] R. Moessner. Magnets with strong geometric frustration. *Canadian Journal of Physics*, 79:1283–1294, November 2001.

[148] J.-C. Domenge, P. Sindzingre, C. Lhuillier, and L. Pierre. Twelve sublattice ordered phase in the $J_1 - J_2$ model on the kagomé lattice. *Phys. Rev. B*, 72:024433, Jul 2005.

[149] J. Lorenzana, G. Seibold, C. Ortix, and M. Grilli. Competing Orders in FeAs Layers. *Phys. Rev. Lett.*, 101:186402, Oct 2008.

[150] Vladimir Cvetkovic and Oskar Vafek. Space group symmetry, spin-orbit coupling, and the low-energy effective hamiltonian for iron-based superconductors. *Phys. Rev. B*, 88:134510, Oct 2013.

[151] Andrey V. Chubukov, M. Khodas, and Rafael M. Fernandes. Magnetism, superconductivity, and spontaneous orbital order in iron-based superconductors: Which comes first and why? *Phys. Rev. X*, 6:041045, Dec 2016.

[152] M. Khodas and A. V. Chubukov. Orbital order from the on-site orbital attraction. *Phys. Rev. B*, 94:115159, Sep 2016.

[153] Jason Alicea, Andrey V. Chubukov, and Oleg A. Starykh. Quantum Stabilization of the 1/3-Magnetization Plateau in Cs_2CuBr_4. *Phys. Rev. Lett.*, 102:137201, Mar 2009.

[154] Jian Kang, Xiaoyu Wang, Andrey V. Chubukov, and Rafael M. Fernandes. Interplay between tetragonal magnetic order, stripe magnetism, and superconductivity in iron-based materials. *Phys. Rev. B*, 91:121104, Mar 2015.

[155] S. Maiti and A. V. Chubukov. Superconductivity from repulsive interaction. In A. Avella and F. Mancini, editors, *American Institute of Physics Conference Series*, volume 1550 of *American Institute of Physics Conference Series*, pages 3–73, August 2013.

[156] Anatoley T. Zheleznyak, Victor M. Yakovenko, and Igor E. Dzyaloshinskii. Parquet solution for a flat fermi surface. *Phys. Rev. B*, 55:3200–3215, Feb 1997.

[157] Walter Metzner, Claudio Castellani, and Carlo Di Castro. Fermi systems with strong forward scattering. *Advances in Physics*, 47(3):317–445, 1998.

[158] Manfred Salmhofer. Continuous renormalization for fermions and fermi liquid theory. *Communications in Mathematical Physics*, 194(2):249–295, Jun 1998.

[159] Karyn Le Hur and T. Maurice Rice. Superconductivity close to the mott state: From condensed-matter systems to superfluidity in optical lattices. *Annals of Physics*, 324(7):1452 – 1515, 2009. July 2009 Special Issue.

[160] A. V. Chubukov, D. V. Efremov, and I. Eremin. Magnetism, superconductivity, and pairing symmetry in iron-based superconductors. *Phys. Rev. B*, 78:134512, Oct 2008.

[161] D. Podolsky, H.-Y. Kee, and Y. B. Kim. Collective modes and emergent symmetry of superconductivity and magnetism in the iron pnictides. *EPL (Europhysics Letters)*, 88(1):17004, 2009.

[162] A.V. Chubukov. Renormalization group analysis of competing orders and the pairing symmetry in Fe-based superconductors. *Physica C: Superconductivity*, 469(9):640 – 650, 2009. Superconductivity in Iron-Pnictides.

[163] Saurabh Maiti and Andrey V. Chubukov. Renormalization group flow, competing phases, and the structure of superconducting gap in multiband models of iron-based superconductors. *Phys. Rev. B*, 82:214515, Dec 2010.

[164] James M. Murray and Oskar Vafek. Renormalization group study of interaction-driven quantum anomalous hall and quantum spin hall phases in quadratic band crossing systems. *Phys. Rev. B*, 89:201110, May 2014.

[165] Y. Lemonik, I. Aleiner, and V. I. Fal'ko. Competing nematic, antiferromagnetic, and spin-flux orders in the ground state of bilayer graphene. *Phys. Rev. B*, 85:245451, Jun 2012.

[166] Laura Classen, Rui-Qi Xing, Maxim Khodas, and Andrey V. Chubukov. Interplay between Magnetism, Superconductivity, and Orbital Order in 5-Pocket Model for Iron-Based Superconductors: Parquet Renormalization Group Study. *Phys. Rev. Lett.*, 118:037001, Jan 2017.

[167] Rui-Qi Xing, Laura Classen, Maxim Khodas, and Andrey V. Chubukov. Competing instabilities, orbital ordering, and splitting of band degeneracies from a parquet renormalization group analysis of a four-pocket model for iron-based superconductors: Application to FeSe. *Phys. Rev. B*, 95:085108, Feb 2017.

[168] Andrey V. Chubukov, Rafael M. Fernandes, and Joerg Schmalian. Origin of nematic order in FeSe. *Phys. Rev. B*, 91:201105, May 2015.

[169] Yuxuan Wang and Andrey Chubukov. Charge-density-wave order with momentum $(2q, 0)$ and $(0, 2q)$ within the spin-fermion model: Continuous and discrete symmetry breaking, preemptive composite order, and relation to pseudogap in hole-doped cuprates. *Phys. Rev. B*, 90:035149, Jul 2014.

[170] Debanjan Chowdhury and Subir Sachdev. Feedback of superconducting fluctuations on charge order in the underdoped cuprates. *Phys. Rev. B*, 90:134516, Oct 2014.

[171] W A Atkinson, A P Kampf, and S Bulut. Charge order in the pseudogap phase of cuprate superconductors. *New Journal of Physics*, 17(1):013025, jan 2015.

[172] Yuxuan Wang, Daniel F. Agterberg, and Andrey Chubukov. Coexistence of charge-density-wave and pair-density-wave orders in underdoped cuprates. *Phys. Rev. Lett.*, 114:197001, May 2015.

[173] Yuxuan Wang, Daniel F. Agterberg, and Andrey Chubukov. Interplay between pair- and charge-density-wave orders in underdoped cuprates. *Phys. Rev. B*, 91:115103, Mar 2015.

[174] Daniel F. Agterberg, J. C. Séamus Davis, Stephen D. Edkins, Eduardo Fradkin, Dale J. Van Harlingen, Steven A. Kivelson, Patrick A. Lee, Leo Radzihovsky, John M. Tranquada, and Yuxuan Wang. The Physics of Pair Density Waves. *arXiv e-prints*, page arXiv:1904.09687, Apr 2019.

[175] Oleg Tchernyshyov. Noninteracting cooper pairs inside a pseudogap. *Phys. Rev. B*, 56:3372–3380, Aug 1997.

[176] KV Shajesh. Eikonal approximation. *http://www.nhn.ou.edu/ shajesh/eikonal/sp.pdf*.

[177] Hiroki Isobe and Liang Fu. Supermetal. May 2019.

[178] R Côté and A. M. S Tremblay. Spiral Magnets as Gapless Mott Insulators. *Europhysics Letters (EPL)*, 29(1):37–42, jan 1995.

[179] M. V. Sadovskiĭ. A model of a disordered system (A contribution to the theory of "liquid semiconductors"). *Soviet Journal of Experimental and Theoretical Physics*, 39:845, November 1974.

[180] M. V. Sadovskiĭ. Theory of quasi-one-dimensional systems undergoing peierls transition. *Sov. Phys. -Solid State v.16, 1632*, 1974.

[181] M. V. Sadovskiĭ. Exact solution for the density of electronic states in a model of a disordered system. *Zh. Eksp. Theor. Fiz. 77, 2070 (1979) [Sov. Phys. JETP 50, 989 (1979)]*, 1979.

[182] Sadovskii, M. V. *Diagrammatics: Lectures on Selected Problems in Condensed Matter Theory*. World Scientific Publishing Co, 2006.

[183] Ross H. McKenzie and David Scarratt. Non-fermi-liquid behavior due to short-range order. *Phys. Rev. B*, 54:R12709–R12712, Nov 1996.

[184] I. L. Aleiner and K. B. Efetov. Supersymmetric low-energy theory and renormalization group for a clean fermi gas with a repulsion in arbitrary dimensions. *Phys. Rev. B*, 74:075102, Aug 2006.

[185] P. Azaria, B. Delamotte, and T. Jolicoeur. Nonuniversality in helical and canted-spin systems. *Phys. Rev. Lett.*, 64:3175–3178, Jun 1990.

[186] A V Chubukov, S Sachdev, and T Senthil. Large-S expansion for quantum antiferromagnets on a triangular lattice. *Journal of Physics: Condensed Matter*, 6(42):8891, 1994.

[187] B. L Altshuler, A. V Chubukov, A Dashevskii, A. M Finkel'stein, and D. K Morr. Luttinger theorem for a spin-density-wave state. *Europhysics Letters (EPL)*, 41(4):401–406, feb 1998.

[188] Andrey V. Chubukov and Peter Wölfle. Quasiparticle interaction function in a two-dimensional fermi liquid near an antiferromagnetic critical point. *Phys. Rev. B*, 89:045108, Jan 2014.

[189] Andrey V. Chubukov and Dirk K. Morr. Electronic structure of underdoped cuprates. *Physics Reports*, 288(1):355 – 387, 1997.

[190] Andrey V. Chubukov and Karen A. Musaelian. Systematic 1/S study of the two-dimensional Hubbard model at half-filling. *Phys. Rev. B*, 50:6238–6245, Sep 1994.

[191] Andrey V. Chubukov and Karen A. Musaelian. Magnetic phases of the two-dimensional hubbard model at low doping. *Phys. Rev. B*, 51:12605–12617, May 1995.

[192] Ar. Abanov, Andrey V. Chubukov, and Jörg Schmalian. Fingerprints of spin mediated pairing in cuprates. *Journal of Electron Spectroscopy and Related Phenomena*, 117-118:129 – 151, 2001.

[193] Matthias Eschrig. The effect of collective spin-1 excitations on electronic spectra in high- tc superconductors. *Advances in Physics*, 55(1-2):47–183, 2006.

[194] E. J. Nicol and J. P. Carbotte. Phonon spectroscopy through the electronic density of states in graphene. *Phys. Rev. B*, 80:081415, Aug 2009.

[195] Andrey V. Chubukov and David M. Frenkel. Renormalized perturbation theory of magnetic instabilities in the two-dimensional hubbard model at small doping. *Phys. Rev. B*, 46:11884–11901, Nov 1992.

[196] Wang Zhu Xi and Guo Dun Ren. *Introduction to special functions*. China Press, 2000.